Statistical methods for vascular magnetic resonance fingerprinting : application to the epileptic brain

Fabien Boux

THÈSE

Pour obtenir le grade de

DOCTEUR DE L'UNIVERSITE GRENOBLE ALPES

Spécialité : **Mathématiques Appliquées**

Arrêté ministériel : 25 mai 2016

Présentée par

Fabien BOUX

Thèse dirigée par **Florence FORBES**, DR, Inria,
codirigée par **Emmanuel BARBIER**, DR, Inserm,
et coencadrée par **Julyan ARBEL**, CR, Inria.

préparée au sein du **Laboratoire Jean Kuntzmann**,
et du **Grenoble Institut des Neurosciences (GIN)**,
dans **l'École Doctorale Mathématiques, Sciences et Technologies de l'Information, Informatique**.

Méthodes statistiques pour l'imagerie vasculaire par résonance magnétique : application au cerveau épileptique

Thèse soutenue publiquement le **11 décembre 2020**,
devant le jury composé de :

Monsieur Ludovic DE ROCHEFORT
Chargé de recherche HDR, CNRS délégation Provence et Corse, Rapporteur
Monsieur Simon Keith WARFIELD
Professeur, Université Harvard Boston – États-Unis, Rapporteur
Monsieur Olivier FRANCOIS
Professeur des universités, Université Grenoble Alpes, Président
Monsieur Benoît MARTIN
Chargé de recherche HDR, CNRS délégation Bretagne Pays de Loire, Examinateur
Monsieur Benjamin MARTY
Docteur en sciences, Institut de Myologie - Paris, Examinateur
Monsieur Julyan ARBEL
Chargé de recherche HDR, Inria Centre de Grenoble Rhône-Alpes, Invité
Madame Lorella MINOTTI
Praticienne hospitalier, Centre Hospitalier Universitaire Grenoble Alpes, Invitée
Monsieur Emmanuel BARBIER
Directeur de recherche, Inserm délégation Alpes, Directeur de thèse
Madame Florence FORBES
Directrice de recherche, Inria Centre de Grenoble Rhône-Alpes, Directrice de thèse

Résumé

Méthodes statistiques pour l'imagerie vasculaire par résonance magnétique : application au cerveau épileptique

L'objectif de ce travail de thèse est l'exploration de l'imagerie par résonance magnétique (IRM) pour l'identification et la localisation des régions du cerveau impliquées dans l'épilepsie mésio-temporale. Précisément, les travaux visent 1) à optimiser un protocole d'IRM vasculaire sur un modèle animal d'épilepsie et 2) à concevoir une méthode de quantification de cartes IRM vasculaires basée sur la modélisation de la relation entre signaux IRM et paramètres biophysiques.

Les acquisitions IRM sur un modèle expérimental murin d'épilepsie mésio-temporale avec sclérose de l'hippocampe ont été effectuées sur un scanner 9.4 T. Les données collectées ont permis de quantifier sept cartes IRM cellulaires et vasculaires quelques jours après l'état de mal épileptique puis plus tard, lorsque les crises spontanées sont apparues. Ces paramètres ont été employés pour l'identification automatique des régions épileptogènes et des régions de propagation des crises. Afin d'augmenter la détection de petites variations des paramètres IRM chez les individus épileptiques, une méthode de quantification basée sur la résonance magnétique *fingerprinting* est développée. Cette méthode consiste à identifier, parmi un ensemble de signaux simulés, le plus proche du signal IRM acquis et peut être vue comme un problème inverse qui présente les difficultés suivantes : le modèle direct est non-linéaire et provient d'une série d'équations sans expression analytique simple ; les signaux en entrée sont de grandes dimensions ; les vecteurs des paramètres en sortie sont multidimensionnels. Pour ces raisons, nous avons utilisé une méthode de régression inverse afin d'apprendre à partir de simulation la relation entre l'espace des paramètres et celui des signaux. Dans un domaine largement dominé par les approches d'apprentissage profond, la méthode proposée se révèle très compétitive fournissant des résultats plus précis. De plus, la méthode permet pour la première fois de produire un indice de confiance associé à chacune des estimations. En particulier, cet indice permet de réduire l'erreur de quantification en rejetant les estimations associées à une faible confiance.

Actuellement, aucun protocole clinique permettant de localiser avec précision le foyer épileptique ne fait consensus. La possibilité d'une identification non-invasive de ces régions est donc un premier pas vers un potentiel transfert clinique.

Abstract

Statistical methods for vascular magnetic resonance fingerprinting: application to the epileptic brain

The objective of this thesis is the investigation of magnetic resonance imaging (MRI) for the identification and localization of brain regions involved in mesio-temporal lobe epilepsy (MTLE). Precisely, the work aims 1) at optimizing a vascular MRI protocol on an animal model of epilepsy and 2) at designing a method to quantify vascular MRI maps based on the modeling of the relationship between MRI signals and biophysical parameters.

MRI acquisitions on an experimental mouse model of MTLE with hippocampal sclerosis were performed on a 9.4 T scanner. The data collected allowed the quantification of seven cellular and vascular MRI maps a few days after the epileptic condition and later when the spontaneous seizures emerged. These parameters were used for the automatic identification of epileptogenic regions and regions of seizure propagation. To enhance the detection of small variations in MRI parameters in epileptic subjects, a quantification method based on magnetic resonance *fingerprinting* has been developed. This method consists in identifying, among a set of simulated signals, the closest one to the acquired signal. It can be seen as an inverse problem that presents the following difficulties: the direct model is non-linear, as a complex series of equations or simulation tools; the inputs are high-dimensional signals; and the output is multidimensional. For these reasons, we used an appropriate inverse regression approach to learn a mapping between signal and biophysical parameter spaces. In a field widely dominated by deep learning approaches, the proposed method is very competitive and provides more accurate results. Moreover, the method allows for the first time to produce a confidence index associated with each estimate. In particular, this index allows to reduce the quantification error by discarding estimates associated with low confidence.

So far no clinical protocol emerges as a consensus to accurately localize epileptic foci. The possibility of a non-invasive identification of these regions is therefore a first step towards a potential clinical transfer.

Contents

Nomenclature **7**

1 Introduction **11**

1.1 Context and objectives 11

1.2 Manuscript organization 15

2 State of the art **17**

2.1 Brain and epilepsy 17

2.1.1 Brain structure and function 18

2.1.1.1 Anatomy of the brain 18

2.1.1.2 Brain cells 19

2.1.1.3 Vascular system 21

2.1.1.4 Blood-brain barrier and capillaries 22

2.1.1.5 Neurogliovascular unit 23

2.1.2 Epilepsy 24

2.1.2.1 General overview 24

2.1.2.2 Neuronal activity 25

2.1.2.3 Glial and microvascular modifications 27

2.1.3 Experimental murine model 29

2.1.3.1 Kindling and status epilepticus models of epilepsy 29

2.1.3.2 Status epilepticus models: general presentation and behavioral manifestations 31

2.1.3.3 Status epilepticus models: electroencephalographic features and neuropathological changes 32

2.1.3.4 Status epilepticus models: imaging 34

2.2 Magnetic resonance imaging (MRI) 38

2.2.1 Nuclear magnetic resonance 38

2.2.1.1 Magnetization . . . 38
2.2.1.2 Bloch equations . . . 40
2.2.1.3 Basic types of MR signals . . . 41
2.2.2 Images and contrast . . . 42
2.2.2.1 T_1 and T_2 contrasts . . . 42
2.2.2.2 Spatial encoding . . . 43
2.2.2.3 k-space data . . . 45
2.2.2.4 Noise in MRI . . . 47
2.2.2.5 Clinical application . . . 48
2.3 Quantitative MRI . . . 49
2.3.1 Relaxation times . . . 50
2.3.2 Water diffusion . . . 51
2.3.3 Perfusion using arterial spin labeling . . . 54
2.3.4 Mapping vascular parameters using contrast agents . . . 56
2.3.4.1 Ultrasmall superparamagnetic iron oxide . . . 57
2.3.4.2 Gadolinium . . . 59
2.3.5 Conclusion . . . 61
2.4 Magnetic resonance fingerprinting (MRF) . . . 62
2.4.1 Basic principle . . . 62
2.4.1.1 Acquisition sequences . . . 63
2.4.1.2 Simulations . . . 65
2.4.1.3 Quantification . . . 65
2.4.2 Vascular MRF . . . 66
2.4.2.1 Acquisition sequence . . . 66
2.4.2.2 Simulations . . . 66
2.4.2.3 Quantification . . . 69
2.4.3 Evolution of MRF quantification methods . . . 70
2.5 Challenges and requirements . . . 76

3 Bayesian inverse regression for vascular MRF quantification 79
3.1 Introduction . . . 79
3.2 MRF as an inverse problem . . . 81
3.2.1 Dictionary-based matching (DBM) method . . . 82
3.2.2 Proposed dictionary-based learning (DBL) method . . . 82
3.2.3 Dictionary sampling strategy . . . 85

3.3 Analysis framework . . . 86
3.3.1 Signals . . . 86
3.3.1.1 Synthetic scalable signals . . . 86
3.3.1.2 Synthetic vascular MRF signals . . . 86
3.3.1.3 Acquired vascular MRF signals . . . 88
3.3.2 Analysis pipeline . . . 88
3.3.2.1 Dictionary design . . . 88
3.3.2.2 Dictionary-based analysis . . . 88
3.3.2.3 Closed-form expression fitting (CEF) analysis . . . 89
3.3.2.4 Performance evaluation . . . 89
3.4 Results . . . 90
3.4.1 Synthetic scalable signals . . . 90
3.4.1.1 Effect of sampling strategy on parameter accuracy . . . 90
3.4.1.2 Effect of noise addition on dictionary signals . . . 91
3.4.1.3 Impact of the dictionary size and SNR on parameter accuracy . . . 93
3.4.1.4 Boundary behavior . . . 96
3.4.1.5 Confidence index . . . 97
3.4.2 Vascular MRF signals . . . 98
3.4.2.1 Synthetic vascular MRF signals . . . 98
3.4.2.2 Acquired vascular MRF signals . . . 99
3.5 Discussion, conclusion and perspectives . . . 102

4 Statistical learning vs deep learning in generalized MRF applications 105
4.1 Introduction . . . 105
4.2 Analysis framework . . . 106
4.2.1 Model design . . . 106
4.2.1.1 Neural network architecture and training . . . 106
4.2.1.2 Calibration model parameter set and model sizes . . . 108
4.2.2 Signals and performance evaluation . . . 108
4.2.2.1 Standard MRF signal . . . 108
4.2.2.2 Aliasing noise as modulated Gaussian noise . . . 109
4.2.2.3 Analysis workflow . . . 110
4.2.2.4 Bias-variance analysis . . . 110
4.3 Results . . . 111

4.3.1 Synthetic scalable signals . . . 111
4.3.1.1 Model size: memory and simulation requirement . . . 111
4.3.1.2 Computational times . . . 112
4.3.1.3 Impact of the dictionary size and noise on parameter estimation accuracy . . . 113
4.3.1.4 Boundary behavior . . . 114
4.3.2 Standard MRF signals . . . 116
4.3.2.1 Estimate accuracy and noise . . . 116
4.3.2.2 Highly undersampled data . . . 117
4.3.2.3 Model variance . . . 117
4.3.3 Summary of results . . . 118
4.3.4 Ensemble learning . . . 121
4.4 Discussion, conclusion and perspectives . . . 123

5 Murine model study of MTLE **125**
5.1 Introduction . . . 125
5.2 Materials and methods . . . 126
5.2.1 Animals . . . 126
5.2.2 MTLE model . . . 126
5.2.3 MRI . . . 128
5.2.3.1 Animal preparation . . . 128
5.2.3.2 MRI acquisition . . . 129
5.2.3.3 MRI quantification . . . 130
5.2.4 Brain immunohistochemistry and quantifications . . . 131
5.2.5 Statistical analyses and classification . . . 132
5.2.5.1 Statistical analyses . . . 132
5.2.5.2 Classification . . . 132
5.3 Results . . . 132
5.3.1 Tracking hippocampal MRI changes post-KA and during spontaneous seizures . . . 132
5.3.2 Multiparametric analysis for the identification of epileptogenic and seizure-spreading hippocampi . . . 138
5.3.3 Dictionary-based learning vs. steady-state methods . . . 140
5.4 Discussion, conclusion and perspectives . . . 141

5.4.1 Multiparametric MRI to map the epileptic networks: clinical and experimental evidence . . . 141
5.4.2 Integrating imaging and histological evidence of neurovascular damage in MTLE . . . 142
5.4.3 Study limitations and conclusions . . . 143

6 Conclusion and perspectives **145**

Bibliography **151**

A *Curriculum vitae* **177**

B Co-supervision of a master's student internship **181**
B.1 Context . . . 181
B.2 Abstract: validation of MRI simulations . . . 181

C Supplementary material - chapter 3 **185**
C.1 Bias-variance analysis . . . 185
C.1.1 Frequentist analysis . . . 185
C.1.2 Bayesian analysis . . . 187
C.2 Data augmentation and noise modeling . . . 188

D Supplementary material - chapter 5 **195**

E Software **199**
E.1 Magnetic resonance fingerprinting package . . . 200
E.2 MP3: Medical software for Processing multi-Parametric images Pipelines 201
E.3 Vascular MRF module in MP3 software . . . 202

Nomenclature

Acronyms

ADC	Apparent diffusion coefficient
ASL	Arterial spin labeling
AUC	Area-under-curve
BBB	Blood-brain barrier
BVf	Blood volume fraction
CA	Contrast agent
CASL	Continuous arterial spin labeling
CBF	Cerebral blood flow
CEF	Closed-form expression fitting
CSF	Cerebrospinal fluid
CT	Computerized tomography
DB-DL	Dictionary-based deep learning
DB-SL	Dictionary-based statistical learning
DBL	Dictionary-based learning
DBM	Dictionary-based matching
DCE	Dynamic contrast enhanced
DL	Deep learning
DT	Decision tree
DTI	Diffusion tensor imaging
EEG	Electroencephalography
EPG	Extended phase graph
EZ	Epileptogenic zone
FA	Flip angle
FID	Free induction decay
FISP	Fast image with steady precession
FOV	Field of view

FT	Fourier transform
GABA	Gamma-aminobutyric acid
GE	Gradient echo
GFAP	Glial fibrillary acidic protein
GLLiM	Gaussian locally linear mapping
GM	Grey matter
IE	Inversion efficiency
IR	Inversion recovery
KA	Kainic acid *or* kainate
kNN	k-nearest neighbors
LDA	Linear discriminant analysis
MGE	Multi gradient echo
MGEFIDSE	Multiple gradient echo sampling of the free induction decay and spin echo
MRF	Magnetic resonance fingerprinting
MRI	Magnetic resonance imaging
MSME	Multi-spin multi-echo
MTLE	Mesial temporal lobe epilepsy
NB	Naive Bayes
NMR	Nuclear magnetic resonance
NN	Neural network
PASL	Pulsed arterial spin labeling
pCASL	Pseudo-continuous arterial spin labeling
PGSE	Pulsed gradient spin echo
QDA	Quadratic discriminant analysis
RF	Radio frequency
RMSE	Root mean square error
ROI	Region of interest
SE	Spin echo
SNR	Signal-to-noise ratio
SRS	Spontaneous and recurrent seizures
SSFP	Steady-state free precession
StO_2	Tissue oxygen saturation
SVD	Singular value decomposition
SVM	Support vector machine
TE	Echo time

TLE	Temporal lobe epilepsy
TR	Repetition time
TTP	Time-to-peak
USPIO	Ultrasmall superparamagnetic iron oxide
VSI	Vessel size index
WM	White matter

Mathematical notations

x or X	Variable
$\mathbf{x}$	Vector variable
$\mathbf{X}$	Tensor variable
$x_i, \ldots, x_k$	Sequence of k successive elements
(x, y)	Ordered pair
$+$	Addition
$-$	Subtraction
$\times$	Cartesian product
$/$	Division
$\propto$	'proportional to' symbol
$\sum$	Sum
$\in$	'in' a set symbol
$\{\cdot\}$	Set
$\mathbb{R}$	Set of real numbers
$\varnothing$	Empty set
f^{-1}	Inverse function
exp	Exponential function
ln	Logarithm base 2 function
log	Logarithm base 10 function
cos	Cosine function
sin	Sine function
$\arg\min$	Argument of the minimum
p	Probability distribution

$\mathcal{N}$	Gaussian distribution
$\mathbb{E}$	Expectation
Var	Variance

Chapter 1

Introduction

1.1 Context and objectives

There is not one but several epilepsies. Together, they are the third most common neurological disease, after migraine and dementia. In the public mind, epilepsy is associated with convulsive seizures, absences, muscular rigidity, etc. But each epileptic syndrome can manifest itself through a wide variety of symptoms and be accompanied by mood, cognitive and sleep disorders [1]. Each one is also associated with its own specific evolution. It is estimated that about 500 000 persons suffer from epilepsy in France. Nearly half of them are under 20 years old. Internationally, the disease affects over 50 million people with an estimate of 10 to 200 cases per 100 000 people depending on income level and the country's healthcare system [1]. Treatments for epilepsy are mostly drug-based. Their goal is to compensate alterations in the excitatory or inhibitory synaptic transmission and to limit the spread of seizures. Thanks to these treatments, the disease can be controlled, i.e. with absence of seizures in 60 to 70 % of cases [2]. When the patient develops resistance to the treatment and when there is clear identification of the area responsible for the seizures, surgery can be considered as long as the area is focal, unique and sufficiently distant from highly functional regions (e.g. involved in language, motor skills, etc). In this case, in-depth examinations are carried out to assess the benefit-risk ratio of such a surgery. When it is curative, the operation consists in removing or disconnecting the epileptogenic area. In practice, this is only possible in a minority of patients suffering from drug-resistant partial epilepsy but surgery is widely accepted as an effective therapy for refractory epilepsy [2]. For the others, palliative approaches using neurostimulation or vagus nerve stimulation methods are good options [3]. The objective is then to reduce the frequency of seizures. These approaches consist in acting directly

on the neuronal network responsible for the seizures, or in modulating its excitability [4]. In all these cases, the localization of the epileptic area is necessary to perform medical intervention, and the question of which method should be used to identify this area still is an important part of epilepsy research. Indeed, current means to locate the epileptic foci are invasive and not accurate. Another fundamental issue in epilepsy research is understanding how recurrent seizures (or chronic epilepsy) emerge. It is suggested that at least 10 % of the population experience at least one seizure during their life [5]. We already know that factors such as a metabolic abnormality (alterations of metabolic homeostasis, cerebral hypoxia, etc.), the use of drugs and toxic substances (alcohol, neuroleptics, medications used to treat mental disorders, some antidepressants, some analgesics, etc.), exposure to a toxic epileptogen (carbon monoxide, neurotoxic gases, etc.) or brain injury (trauma, stroke, tumor, etc.) may explain the occurrence of a single and unique epileptic seizure [6]. But when no such accidental cause is involved, it is not always possible to identify the origin of epilepsy. The onset of an isolated seizure does not necessarily lead to chronic epilepsy, which is the consequence of mechanisms leading to the formation of a neuronal network favorable to the emergence of epileptic seizures. From a research standpoint, the question is: what tool can be used to characterize the evolution of biological changes resulting or not in a condition of recurrent seizures? From a clinical standpoint, can these techniques be used as diagnostic tools to predict the emergence of new seizures in patients who recently had a seizure?

Nowadays, among diagnostic techniques, the electroencephalogram (EEG) is the most specific method for both diagnosis and monitoring of the disease in several epileptic symptoms [7]. It consists in recording the electrical activity of the brain using electrodes placed on the scalp. The behavior, frequency and topography of abnormalities recorded during seizures (spikes or spike-waves) or interictally helps to characterize the epileptic syndrome and/or to locate the brain area involved. However, a low-voltage discharge may not appear on the scalp EEG recording during seizure, especially if it is located deep in the brain. In such a case, particular attention is paid to a well-localized flattening of the EEG trace, or to the disappearance of well-localized interictal EEG abnormalities, which are both good indicators of the region of seizure origin [8]. Since the EEG is not a modality with a high spatial resolution, it cannot account for the whole brain area which is involved in the discharge but it can help for identifying the core region of the future implantation of deep invasive electrodes. Invasive EEG studies are associated with additional risks that are only justifiable if there is a good chance of obtaining essential localizing information on a potentially resectable area [7]. One problem with the use

of intracerebral EEG recordings is that the number of electrodes is limited (10-20) and most of the brain volume is not covered by the recording. Among other diagnostic techniques, magnetic resonance imaging (MRI) has an excellent spatial resolution and is already used to eliminate the lesional cause (traumatic, vascular, tumoral, dysplasia, inflammatory or infectious) in epilepsy. Patients can also exhibit sclerosis that results in an abnormal structural MRI, and the seizure types are classified as MRI-positive partial epilepsy. However, it is still unclear whether this method can be used to identify and delineate epileptogenic zones in cases when large modifications did not occur, such as in the presence of sclerosis.

This work, initiated in September 2017, therefore aims at answering some of these previous questions. In particular, can a vascular MRI protocol and associated quantification methods be designed to detect and characterize the evolution of a chronic epilepsy condition in an experimental animal model? Because MRI is already a routine procedure in epilepsy and because the number of MRI scanners is about a thousand in France, it could be an entry point to develop a robust method of localization and characterization of epileptic regions. In this context, the Grenoble Institute of Neurosciences (GIN) offers an adequate environment in terms of infrastructure, since it has a clinical and a preclinical MRI imaging platform, located close to the hospital, and in terms of expertise with the *functional neuroimaging and brain perfusion* team led by Emmanuel Barbier and the *synchronization and modulation of neural networks in epilepsy* team led by Antoine Depaulis. These expertises are particularly suitable for a collaboration with Nicola Marchi's *cerebrovascular and glia research* team at the Institute of Functional Genomics (IGF) in Montpellier. These collaborators designed the Epicyte (cerebrovascular dynamics in epilepsy, endothelial-pericyte interface) project funded by the French national research agency (ANR). The project targeted a clinical impact with the potential to deliver: 1) pericyte damage as a novel mechanism of disease; 2) pericyte signaling as a novel pharmacological target; and 3) specific vascular MRI read-outs matching cellular changes and of pre-operative diagnostic value.

During this work, I collected MRI data using an experimental murine model on the preclinical IRMaGe platform with the support of the staff, in particular Nora Collomb for animal preparation. This part was particularly challenging, requiring a training in MRI physics and animal handling. I took the animal experimentation course and obtained the related certification, which are skills somewhat distant from my initial engineering training in signal processing and computing (see my resume in appendix A). Histological imaging to assess cellular and vascular modifications and thereby validate

changes observed with MRI were performed by Emma Zub (IGF, Montpellier). Data processing and software development have also been an important part of the work, see appendix E.2. They were integrated into the development of a collaborative tool within the GIN team. The main line of research of this work is a methodological part on the reconstruction of quantitative MRI images. It has been identified that this development could be necessary for the MRI data analysis in order to be more sensitive to the small cellular and cerebrovascular changes observed in epilepsy. Inspired by the promising magnetic resonance fingerprinting (MRF) method, a quantitative MRI approach, Julyan Arbel and Florence Forbes from the *Statify* team at Inria provided and helped to develop innovative statistical approaches. It was thus possible to formalize the methodology and to develop high-performance statistical analysis methods for MRI reconstruction. My contributions were to overcome some of the limitations of this method and to contribute to the improvement of this new approach.

The work, initiated in September 2017, mainly focuses on these two aspects: on one hand, the collection of MRI data on the preclinical platform, and on the other hand, the development of statistical methods for data processing. The data collection was achieved at a frequency of about one week per month during the first two years, requiring regular implementations of data processing tools and improvements of experimentation protocols. However, the main part of data processing was completed during the third year together with the interpretation of the results. The methodological development was more extensive during the first two years but has continued uninterrupted since the beginning of the work. I also had the opportunity to co-supervise a master's student for a 6-month internship, which aimed at improving the performance of the simulation tool used in my work and to investigate the deployment of the tool on the university's computing grids to speed up simulations. This work is not presented in the manuscript but a summary of the master student's results is given in appendix B. Finally, I participated in several national and international congresses and conferences [9–13].

1.2 Manuscript organization

This manuscript is organized in 6 chapters including this introduction.

- **Chapter 2:** As the work has been conducted along two lines of research, the objective of this chapter is to provide sufficient information so that scientists in each field can appreciate the entire work. An effort has been made for clarity and conciseness. When necessary, illustrations are provided. In particular, this chapter covers the structures and functions of the brain through a neuropathological angle, epilepsy and experimental murine models of epilepsy. It also covers the principles of the MRI, quantitative MRI methods, in particular, cellular and vascular, and the MRF. In the section dedicated to MRF, we present the basic principles of MRF, the vascular MRF and the evolution of quantification methods. Finally, the chapter ends with the objectives of the thesis.

- **Chapter 3:** The first contribution is a quantitative MRI method based on MRF framework. We propose a dictionary-based learning approach for estimation split into three steps: 1) a quasi-random sampling strategy to efficiently produce an informative dictionary; 2) an inverse statistical regression model to learn from the dictionary a correspondence between magnetic resonance signals and physiological parameters; and 3) the use of this mapping to provide both parameter estimates and their confidence indices. This study is realized for the vascular application.

- **Chapter 4:** The previous analysis is completed by a comparison between the proposed method and a reference dictionary-based learning method using a neural network. This study is extended to standard applications and not restricted to vascular MRF. It involves addressing new specific issues including aliasing artifacts resulting from highly undersampled data and complex-valued signal samples. We discuss the differences between the two models and the strengths and weaknesses of each. Finally, we conclude on a possible combination of the two models to provide more accurate and robust methods.

- **Chapter 5:** The second contribution is an MRI analysis using data acquired with a 9.4 T scanner, to quantify a suite of cellular (relaxation times and diffusion) and cerebrovascular (blood volume, microvessel diameter, tissue oxygen saturation and blood-brain barrier permeability) parameters. Acquisitions were performed both

1) after status epilepticus and 2) at spontaneous seizure stage, in a mouse model of mesial temporal lobe epilepsy induced by a unilateral injection of kainate. We applied basic classification methods providing multi-parametric MRI scores to integrate all MRI information for automatic identification of regions involved in seizures.

- **Chapter 6:** The manuscript closes with a general conclusion and a discussion of possible perspectives.

Chapter 2

State of the art

2.1 Brain and epilepsy

This section is a compilation of epilepsy and MRI background information on both of which we relied during the acquisition and processing of data and during the interpretation of the results. This part is of particular interest for the understanding of chapter 5.

We first introduce the anatomical basis of the human and the mouse brains. This comparison is intended to highlight the important similarities between the two species, which justify the choice of the mouse as a standard animal model for many neuropathologies and epilepsy in particular. The objective is the presentation of the cellular environment that is altered and damaged in epileptic patients. Several *in vivo* observations were validated on the resected tissue using histology. However, this validation approach does not allow an extrapolation beyond the resected tissue. Animal models are thus essential for more extensive and detailed studies. There are indeed several animal models since there is not an animal model that replicates all characteristics of mesial temporal lobe epilepsy. We focus on the major murine models of mesio-temporal lobe epilepsy. In a final section, we summarize the main observations made with MRI in these experimental animal models.

2.1.1 Brain structure and function

2.1.1.1 Anatomy of the brain

The brain is composed of three main structures: the cerebrum, cerebellum and brainstem, see figure 2.1(a). The brainstem supports vital functions of the autonomic nervous system such as breathing, heartbeat and salivation. The cerebellum is involved in fundamental functions, sometimes referred to as reptilian, such as movement coordination, balance, learning motor functions, and controlling circadian and heart rhythms. Discoveries have also shown the involvement of this structure in higher level functions such as speech production and speech perception [14]. The cerebrum is separated into two parts: the right and left hemispheres that are connected by the corpus callosum, see figure 2.1(b). Each hemisphere is divided into four areas called lobes, themselves divided into sub-areas that serve specific functions, see figure 2.1(c).

Here some functions associated to each lobe in humans:

- Frontal lobe: control of voluntary movement (motor strip), attention, short term memory tasks, motivation, planning, problem solving, speech: speaking and writing (Broca's area)
- Parietal lobe: proprioceptive and mechanoceptive stimuli (sensory strip), language processing
- Occipital lobe: visual processing
- Temporal lobe: decoding sensory input into derived meanings for retention of visual memory and language comprehension (Wernicke's area).

Most of the functions involve different areas of the brain that can be located in different lobes, and there are very complex relationships between all of these areas. Some of them are better known than others e.g. Broca's and Wernicke's areas, represented in figure 2.1(c). A damaged Broca's area may result in a disability to speak and write but a preserved ability to read and understand spoken language, a phenotype known as Broca's aphasia [18]. A damaged Wernicke's area in the left temporal lobe can cause the person to speak in long sentences that have no meaning; add unnecessary words or even create new words. The person can speak but has difficulty in understanding speech and is therefore unaware of their own mistakes, a phenotype known as Wernicke's aphasia [19]. This is the typical areas avoided during surgery, especially in case of resection.

The brain, is crossed by four fluid-filled cavities called ventricles. Inside the ventricles circulates the cerebrospinal fluid that also circulates around the brain. The skull and cerebrospinal fluid help cushion the brain from injury, like a sponge in a jar full of water.

(a) Brain structures

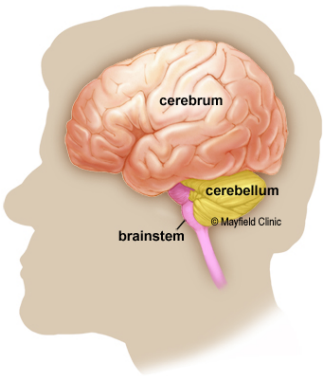

(b) Hemispheres

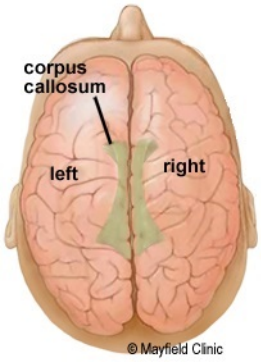

(c) Lobes and functional areas

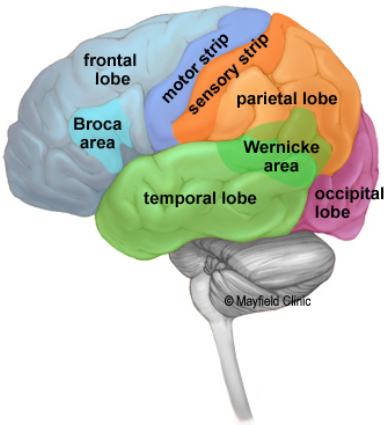

(d) Equivalent in mice

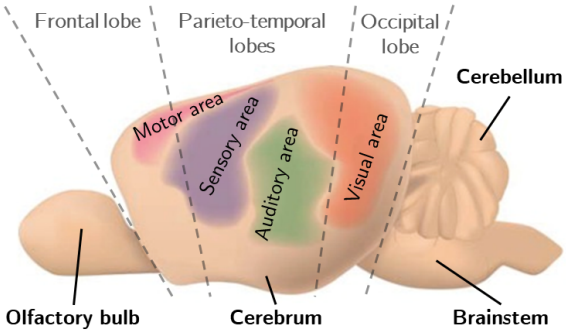

Figure 2.1 – Biological and functional segmentation of the human brain organ, adapted from [15], and equivalent areas in mice, adapted from [16, 17].
(a) The 3-structure brain. (b) The two hemispheres. (c) The lobes and brain areas in humans. (d) The 3-structure and brain lobes in mice.

There are many similarities in the structure and functional areas of the brain in mice (figure 2.1(d)). It should be noted that the images do not reflect the organs sizes: the human brain weight is approximately 1 300 g while it is 0.4 g for mice, i.e. an odds ratio of 3 000 [17]. This information is important for imaging since the proportion of brain volumes imaged is far from being equivalent for an identical spatial resolution.

2.1.1.2 Brain cells

In our study, we see the brain as composed of two major types of cells: neurons and glial cells. Neurons directly ensure the functional component of the brain through the transfer of information. The transmission of information from one neuron to another is usually done by the passage of the nervous message through the body of the first neuron called

axon, via the activation of different ion channels (neurotransmitters) at the synapse, the junction between neurons. These small molecules that ensure the transmission of messages from one neuron to the other at synapses, enable the activation of different receptors and ion channels located on the second neuron. A change in electrical activity is then generated on the second neuron, leading to the transmission of the neural signal. Figure 2.2 illustrates a neuron and the message delivery path.

Glial cells provide neurons with support and protection. In the central nervous system, glial cells include oligodendrocytes, astrocytes, ependymal cells and microglia. Oligodendrocytes provide support and insulation to neuron's axon by creating myelin sheath [20]. Astrocytes realize several functions such as providing the neurons part of the nutrients and chemicals required by transporting certain molecules in and out of the fluid between cells in the brain. Microglia are key cells in overall brain maintenance. They are constantly cleaning the central nervous system of damaged or unnecessary neurons and synapses, and infectious agents [21]. Finally, ependymal cells are involved in the production of cerebrospinal fluid and studies show that these cells act as a reservoir of cells in the forebrain, which can be activated after an injury [22]. Overall, glial cells are very reactive when an injury occurs.

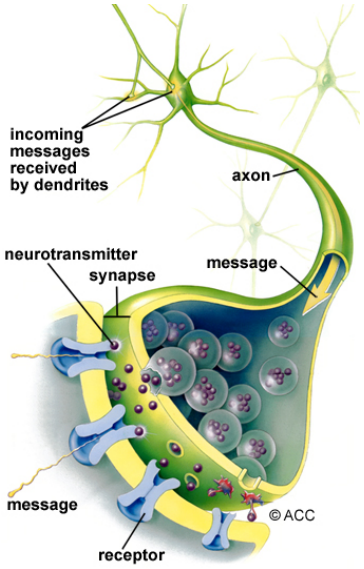

Figure 2.2 – Neuron, adapted from [15].
A neuron consists in a cell body, dendrites and axon. Neurons communicate with each other by exchanging neurotransmitters across synapses.

Non-invasive *in vivo* imaging of these cells would be ideal for the diagnosis and understanding of pathologies, but no such imaging is so far available. However, *ex vivo* imaging of these cells is possible and allows to establish a link between *in vivo* observations, with spatial resolution $> 100\,\mu m$ and *ex vivo* images, with spatial resolution $< 1\,\mu m$. After *in vivo* experiments, the animals may be euthanized and the imaged organs fixed. Tissue sections are realized in the organ at the level of the imaged slices and the cells are revealed by histological methods (figure 2.3). Specific antibodies are used for binding to the specific markers, highlighting the cell properties of interest in the histological section. These antibodies carry a visible or fluorescent probe to enable its imaging using a confocal microscope, see [23] for details.

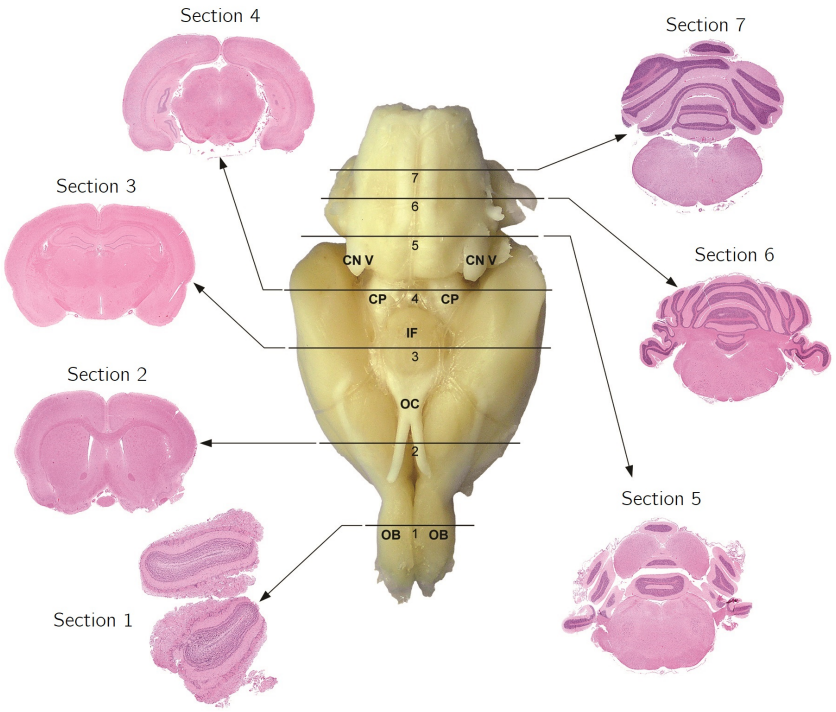

Figure 2.3 – *Ex vivo* cellular imaging, adapted from [24].
Seven transverse (coronal) hematoxylin and eosin-stained sections corresponding to the following anatomical landmarks: OB = olfactory bulb, OC = optic chiasm, IF = infundibulum (and/or median eminence), CN V = cranial nerve V (trigeminal), and CP = cerebral peduncle.

2.1.1.3 Vascular system

The blood brings materials for the brain cells to function properly: oxygen, carbohydrates, amino acids, fats, etc. The blood also removes materials from the brain: carbon dioxide, ammonia, lactate, neurotransmitter, etc. The brain blood supply is realized by two sets of branches: the vertebral arteries and the internal carotid arteries [25]. The internal carotid arteries split in two arteries: the middle and the anterior cerebral arteries (figure 2.4(a)). The vertebral arteries come together at the level of the brainstem to create the midline basilar artery. Finally, the basilar artery joins the blood supply from the internal carotids in a cerebral arterial circle named the circle of Willis that supplies blood to the brain via a multitude of arteries, see illustration in figure 2.4(a) and equivalent for mice in figure 2.4(b). Note that similarities are directly observable between the vascular trees. Then, these arteries split up into a network of increasingly smaller vessels until they reach few micrometers in diameter, the capillaries. The mean diameter is 6.47 µm in human brain [26], and diameters range from 4.6 to 5 µm in different rat cortical areas [27].

Capillaries are thus much smaller than imaging spatial resolution, both in human and in animals. Blood then flows in venules and veins drain blood back to the heart.

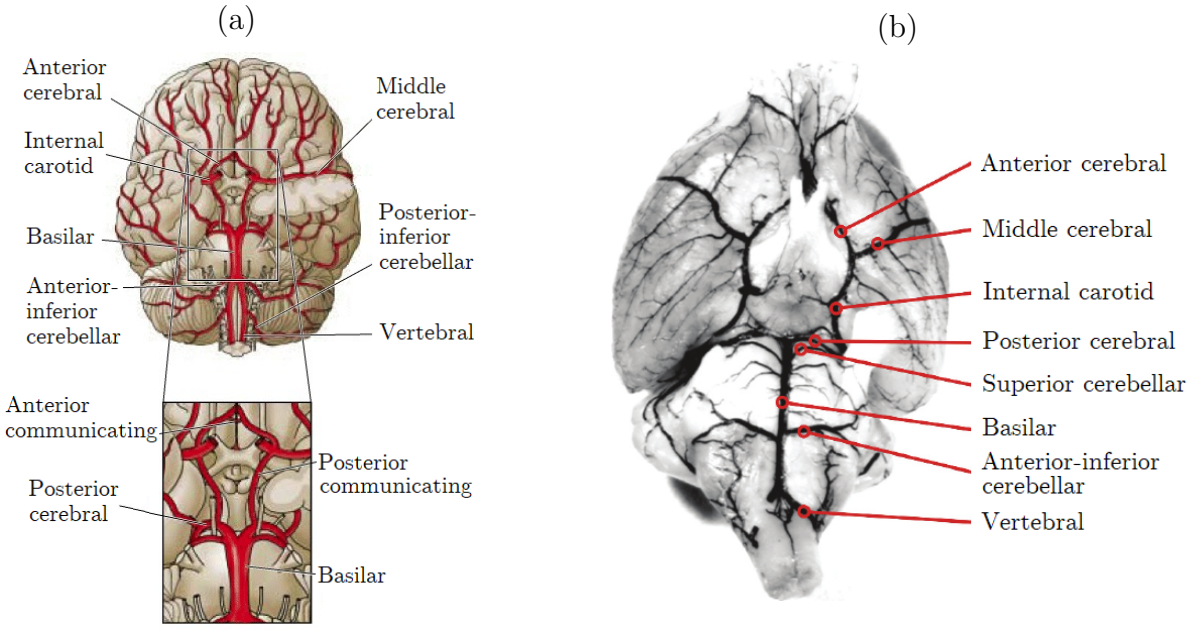

Figure 2.4 – Comparison of human and mouse brain arteries, adapted from [25] and [28]. Figures show the major arteries of the brain. (a) Human ventral view. The enlargement of the boxed area shows the circle of Willis. (b) Mouse ventral view.

2.1.1.4 Blood-brain barrier and capillaries

Except for gaseous exchanges that can be achieved at large vessel interface, all exchanges between the vascular system and the extravascular environment occur at capillary level. The wall of these capillaries is composed of multiple layers that form the blood-brain barrier (BBB). The total length of capillaries in the human brain is about 600 km and they represent a surface area of about 12 m^2 [29]. The BBB protects the brain from pathogens, toxins and hormones circulating in the blood. It is an extremely selective filter through which materials needed by the brain are transmitted and debris are removed. The first layer is composed of the endothelial cells saddled together by tight junctions, surrounded by the pericytes [30]. According to [31], these cells have contractile properties and play a role in the regulation of circulatory flow and the permeability of BBB capillaries [32]. In fact, the BBB is a several layers structure including endothelial and pericytes, but also a basal lamina (collagen) and the astrocyte feet that cover about 90 % of the BBB surface.

2.1.1.5 Neurogliovascular unit

The complex functional and anatomical structure of the endothelial cells, the basal lamina covered with pericytes and astrocytes, the microglia, the neurons, the oligodendrocytes, and the extracellular matrix, is known as the *neuro-glio-vascular unit* (figure 2.5), which particularly regulates regional cerebral blood flow and permeability of the BBB [33].

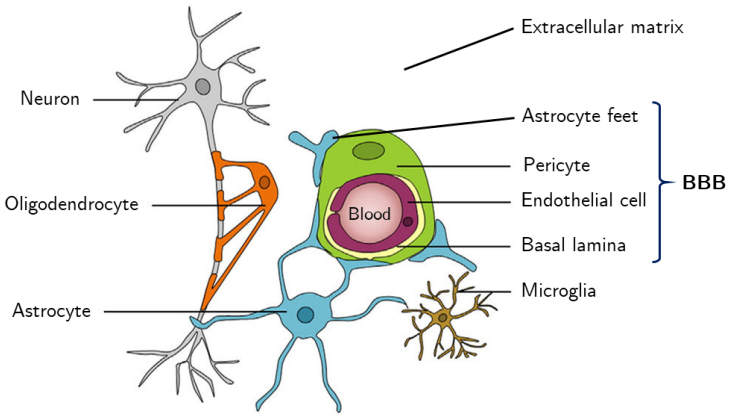

Figure 2.5 – Neurogliovascular unit, adapted from [34].
The neurogliovascular unit at the level of brain capillary is composed of vascular cells (pericytes and endothelial cells), glial (astrocytes, oligodendrocytes, and microglia), and neurons.

Most of the glial cells react to a large scope of injuries, which is known as *gliosis*. Gliosis involves the activation of glial cells that may proliferate and/or become hypertrophic to occupy the injured brain areas [35]. Once activated, reactive glial cells secrete neurohibitory factors to prevent neuronal growth and can eventually form a glial scar in lesional brain areas [36]. The series of morphological and functional changes of astrocytes is known as the *astrogliosis*. According to [37], astrogliosis includes a lot of reactivity including the upregulation of structural protein, hypertrophy of the cell body, elongation around the lesion core and release of inflammatory signals. Astrocytes interact with other cell types, in particular glial cells to form a complex glial scar. Activated microglia change their morphology, release pro- and anti-inflammatory factors, and enhance their mobility and phagocytic activity [38]. Pericytes have been shown to migrate away from brain microvessels in rapid response to hypoxia [39] and traumatic brain injury [40]; both of these conditions are associated with increased BBB permeability. In addition, the extracellular matrix also interacts with the cerebral microsvacular endothelium. Disruption of the extracellular matrix is associated with increased BBB permeability in pathological state [41]. Matrix proteins can influence expression of tight junction proteins [42].

2.1.2 Epilepsy

2.1.2.1 General overview

Epilepsy is the third most common neurological disease and despite the many findings in the field, the understanding of epilepsy remains a very important subject of study (6 524 PubMed entries for epilepsy in 2019). If in the popular mind it is often limited to episodic seizures, in reality it is a disease that includes various symptoms, the most spectacular of which are indeed these well-known seizures. Epilepsy has a high risk of disability, psychiatric comorbidity, social isolation and premature death [1]. Diseases associated with a primary pathology are now an integral part of epilepsy. In this context, the seizure would only be the visible part, with parallel neurobiological, cognitive, psychological and social consequences. In [43], the authors enumerate about 50 epilepsy syndromes. A few have a clear genetic background, but most are multifactorial in origin, linked to hereditary, lesional and/or environmental components. However, they share a common feature: a synchronized and abnormal excitation of a large neurons group in a particular brain area, which can secondarily spread to other areas of the brain. It results in a sudden and intense electrical activity which causes the symptoms during seizures (involuntary movements, auditory or visual hallucinations, absences, etc). The expression of these symptoms depends on the cerebral zones in which the neurons involved are located or the role of these neural cells in the systems that manage our motor skills, cognition, emotions or behaviors.

The most typical manifestation of epilepsy is thus the epileptic seizure. We can distinguish two seizure types: generalized and (multi-)focal seizures [44]. Generalized seizures are related to the excitation and synchronization of neurons originating from several spread regions over both cerebral hemispheres. They generally associate a transitory consciousness loss (absence of a few seconds to a few minutes) with tonic (muscle contractions), myoclonic (muscle shakes) or atonic (without muscle contraction) motor signs. Focal seizures originate from a specific area of the brain, referred to as the epileptogenic zone (EZ). Depending on the area, multiple manifestations result. The symptoms of a focal epileptic seizure are numerous: language disorders, emotional signs (fear, laughter, ecstasy, etc.), pain, vegetative signs (salivation, apnea, tachycardia, etc.), automatic gestures and often explosive motor behavior. A loss of consciousness (or contact with the outside world) is also often observed. The hyperexcitation of the focal seizure can spread and thus leads to a generalized seizure.

2.1.2.2 Neuronal activity

Epileptic seizures result from a transient abnormal synchronization of a population of neurons that disrupts normal brain activity. It is this disruption that causes the symptoms described in the previous section. The synchronization of neurons additionally produces a particular electrical activity that can be recorded by EEG, i.e. by a set of electrodes placed on the scalp. Within the EZ, seizures were assumed to originate from increased excitation or decreased inhibition based on a simplistic model that only involve communication between two neurons [45]. It has been shown that during a seizure, the level of the inhibitory neurotransmitter gamma-aminobutyric acid (GABA) at the synaptic level is lower than usual [46, 47], while the level of the excitatory glutamate neurotransmitter, most prevalent in the central nervous system is abnormally high [46]. Epilepsy was previously considered to be the result of an imbalance between these two neurotransmitters [48]. Today, this hypothesis alone is no longer sufficient: other cellular pathways are implicated in the genesis of seizures, described in the next section. The simplistic two-neuron communication model can be expanded to account for the presence of complex neuronal networks. These networks are interconnected allowing seizures to spread and different networks can be involved in the initiation, spread, or termination of seizures [49]. One can also observe in epileptic patients, brief synchronous activity of a group of neurons (duration of less than 70 ms) leads to inter-ictal spikes, which is distinct from a seizure [50]. Indeed, the site of inter-ictal spiking can be separate from the EZ. Transition from normal to epileptiform behavior is probably caused by greater spread and neuronal recruitment secondary to a combination of enhanced connectivity, enhanced excitatory transmission, a failure of inhibitory mechanisms, and changes in intrinsic neuronal properties [45].

The EEG is the key examination in epilepsy for both diagnosis and monitoring of the disease. The appearance, frequency and topography of abnormalities recorded outside of seizures (spikes, sharp waves and spike-wave discharges) help to characterize the epileptic syndrome and/or to locate the brain area involved [51], see figure 2.6(a). In fact during seizures, the synchronization of neurons result in a periodic signal characterized by specific frequency bands, see figure 2.6(b-c). In general, the EEG recording is decomposed using a time-frequency analysis in order to investigate the evolution of these frequency bands during seizures. For example, it is commonly accepted that regions showing transient fast oscillations (> 15 Hz) are related to the EZ [52]. In [53], authors have shown that EEG signal power in range 60-100 Hz increases after seizure onset in regions suspected of being part of the EZ. During focal seizures, it is suspected that

high-frequency oscillations ($> 100\,\text{Hz}$) are involved [54]. The same work has shown that these high-frequency oscillations are preceded by low-frequency oscillations ($< 20\,\text{Hz}$), which illustrates the need to get a temporal evolution of the frequency bands for the characterization of EEG recordings, see figure 2.6(c).

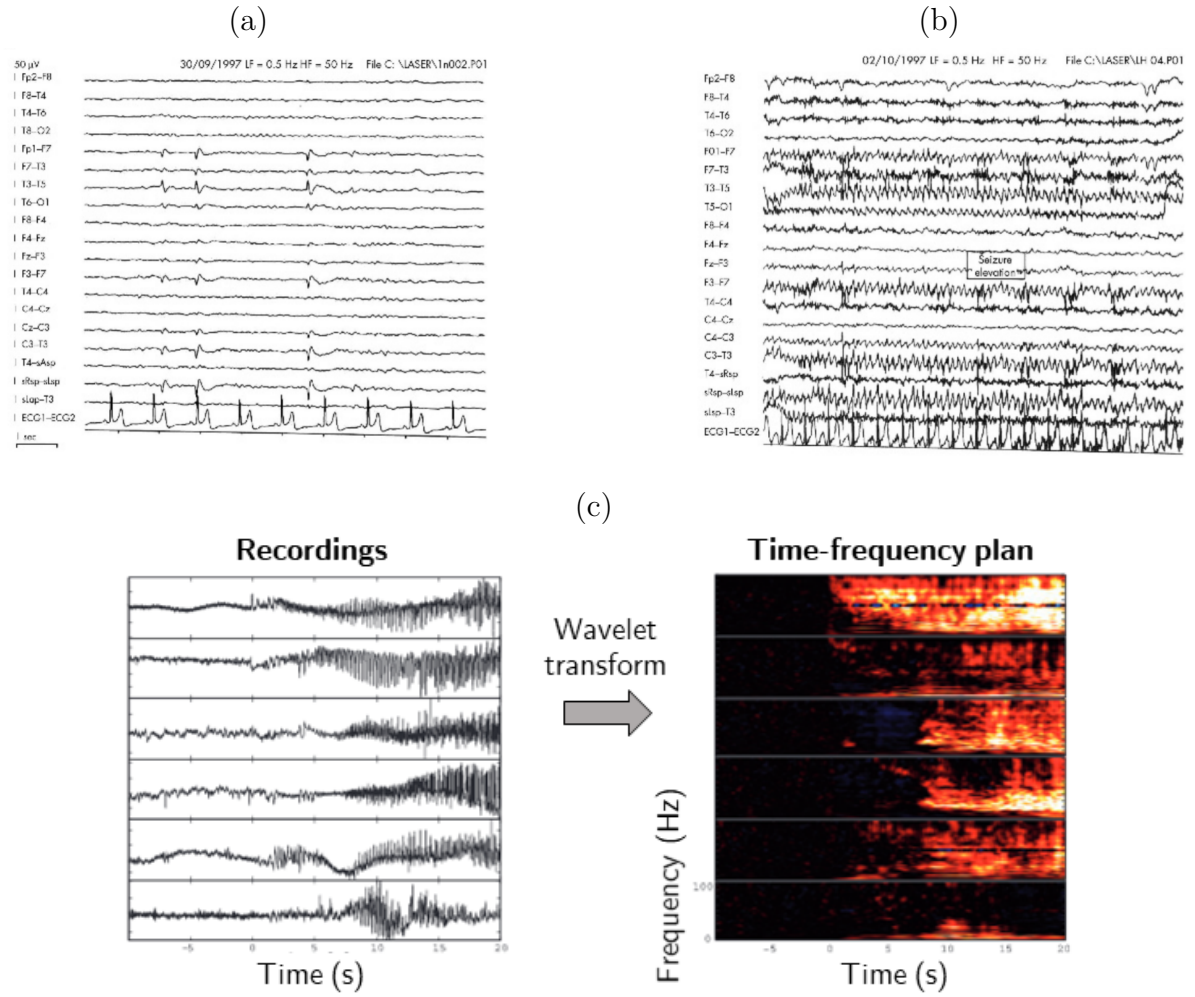

Figure 2.6 – Typical electroencephalography (EEG) recordings in epilepsy and time-frequency decomposition, adapted from [55] and [56].
(a) Interictal focal temporal discharges in left mesial temporal epilepsy. (b) Three per second spike and wave discharge during typical absence seizure. (c) Stereo-EEG recording and associated time-frequency decomposition.

The prolonged atypical electrical activity is associated with a neuronal loss [57], especially in the syndrome of temporal lobe epilepsy (TLE) associated with hippocampal sclerosis (figure 2.7).

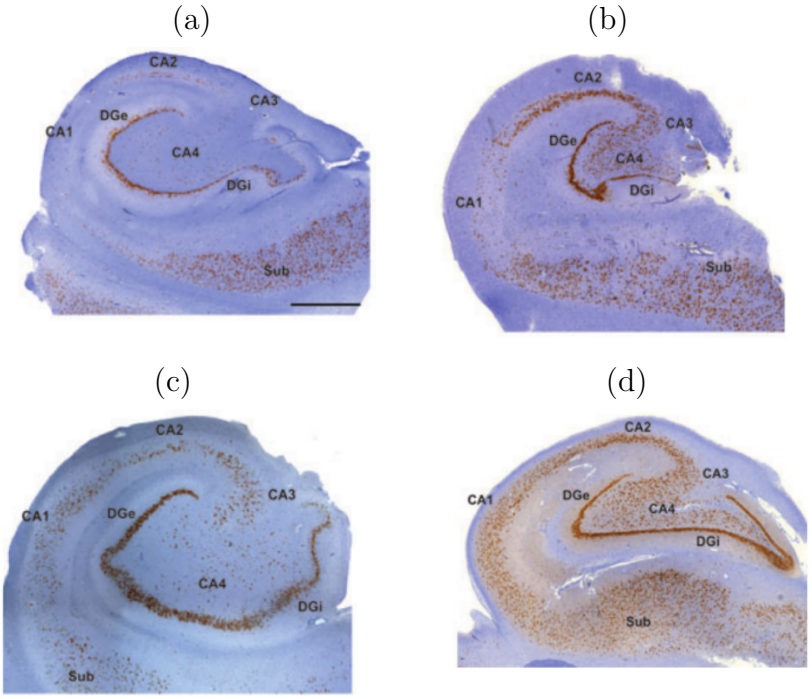

Figure 2.7 – Histopathologic subtypes of hippocampal sclerosis in patients with temporal lobe epilepsy (TLE), adapted from [58].
(a) ILAE hippocampal sclerosis (HS) type 1: pronounced pyramidal cell loss in both CA4 and CA1, variable but frequently visible damage to CA3 and CA2, and variable cell loss in the dentate gyrus. (b) ILAE HS type 2: CA1 predominant neuronal cell loss and gliosis. (c) ILAE HS type 3: CA4 predominant neuronal cell loss and gliosis. (d) No HS, gliosis only. All stainings represent NeuN immunohistochemistry with hematoxylin counterstaining using 4-µm–thin paraffin embedded sections. Scale bar in (a) = 1 000 µm (applies also to (b-d)).

2.1.2.3 Glial and microvascular modifications

A prominent feature of epileptic foci in patients is an abnormal glial environment including chronically activated astrocytes and microglia, and glial scars [59], see figure 2.8(a). This dysregulation of glial functions may cause seizures or promote epileptogenesis [60]. Indeed, perturbation in regulation of ions, water, and neurotransmitters can promote hyperexcitability and hypersynchrony [59]. Activated astrocytes and microglia lead to the release of pro-inflammatory mediators and could cause sustained inflammatory changes that facilitate epileptogenesis [61]. Therefore, the main mechanisms by which glial cells could facilitate the development of epilepsy and seizures include an increased excitability and inflammation.

As introduced in section 2.1.1.5, glial cells are also related to the microvascularization and contribute to BBB function. In TLE, a significant increase of vascular density in

the hippocampus of patients has been reported [62], see figure 2.8(b). The occurrence of an angiogenic process has been confirmed by high levels of vascular endothelial growth factor. This vessel proliferation is correlated with seizure frequency and altered BBB [62]. The increased vascularization overlapped with the loss of tight junction proteins. In [63], authors showed that BBB openings correlate to seizure development, see figure 2.8(c). There is evidence that an increase in BBB permeability promotes seizures, contributes to epileptogenesis, and favors seizure recurrence in epilepsy but whether this BBB dysfunction is the result or the origin of the seizures remains an open question [64].

These modifications have mostly been shown on resected tissue (figure 2.8). The challenge for diagnosis is to detect these changes in patients by imaging. To investigate this issue, most studies use animal models that allow the correlation between *in vivo* imaging and post-mortem analysis.

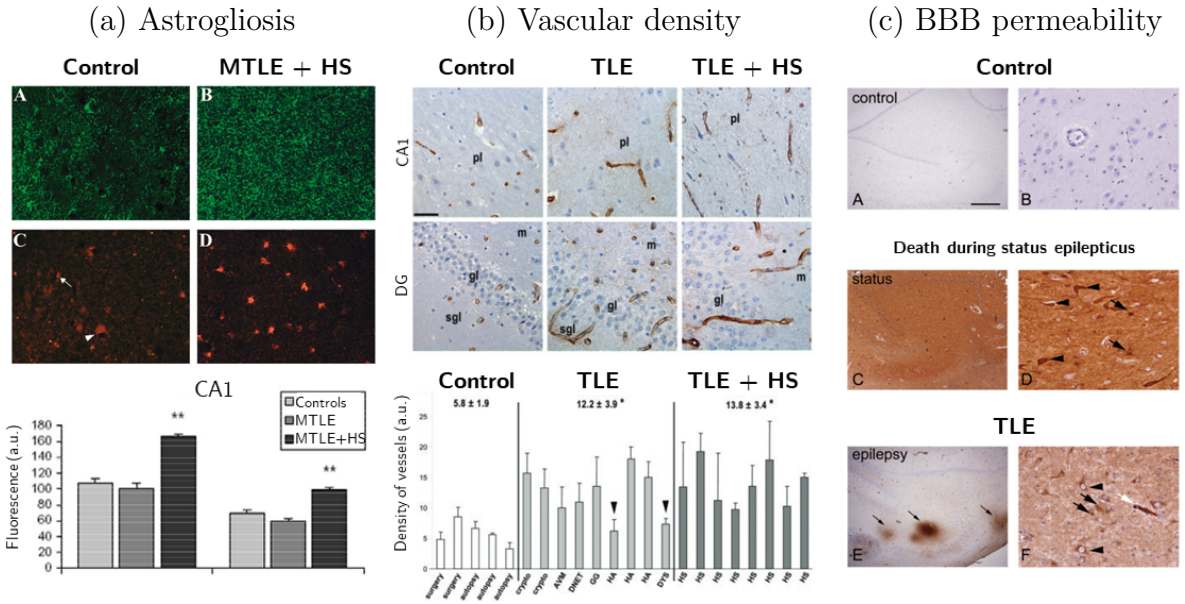

Figure 2.8 – Cellular and vascular changes in patients with temporal lobe epilepsy, adapted from (a) [65], (b) [62], and (c) [66].
TLE = temporal lobe epilepsy, HS = hippocampal sclerosis, and BBB = blood-brain-barrier.
(a) Astrocytic reaction in (1^{st} *column*) control and (2^{nd} *column*) TLE patient with HS.
(b) Vascularization in (1^{st} *column*) controls, (2^{nd} *column*) TLE patients, and (3^{rd} *column*) TLE patients with HS.
(c) Albumin extravasation through the BBB: (1^{st} *row*) controls, (2^{nd} *row*) patients that died during status epilepticus, (3^{rd} *row*) TLE patients.

2.1.3 Experimental murine model

In the following section, it should be understood that several models for seizures, epileptogenesis and chronic epilepsy have been developed in several animal species. Most of the time, each model allows a number of specific questions to be answered. Because our work is intended to detect epileptogenic regions for mesial temporal lobe epilepsy in an experimental murine model, a certain amount of works are omitted in the following. Among the introduced works, it was decided to consider both mouse and rat models because the rat was considerably more extensively used in MRI studies. However, we do not claim that these models are equivalent and despite the similarities, features of these two species are somewhat different (see [67]).

2.1.3.1 Kindling and status epilepticus models of epilepsy

Taken together, the clinical findings presented in the previous section have to be replicated in order to answer many unresolved questions. The identification of the seizure onset is especially important for surgical treatment of MTLE. Another point is the understanding of the epileptogenesis for establishing the evolution of the epileptic disorder. Models must therefore reproduce both the epileptogenesis period and the chronic period histopathological, electroencephalographic and behavioral features encountered in focal epilepsy.

Several experimental animal models provide high levels of similarity with human epilepsy, but there is no experimental model that reproduces all features of MTLE. The two most commonly used animal models of MTLE are kindling and status epilepticus models. With the first one introduced in 1967 by Goddard [68], spontaneous seizures are induced by repeated electrical simulations accompanied by stronger seizure responses until the animal reached standard seizure response. At this point, the stimulation must continue until the development of spontaneous crises (overkindling period in figure 2.9(a)). In the status epilepticus model, a status epilepticus condition (continual seizures) is inducted by chemical agents administration (among others, pilocarpine, kainate, pilocarpine-lithium, flurothyl) that terminates within several hours. Then, spontaneous seizures emerge after a latent period that lasts for weeks or months (figure 2.9(b)).

The advantages of the kindling model are the precise focal activation of brain sites, the development of chronic epiletogenesis and the fact that the pattern of seizure propagation and generalization is readily monitored [69]. In return, kindling experiments can be relatively labor intensive because the electrodes are implanted into the brain and a large

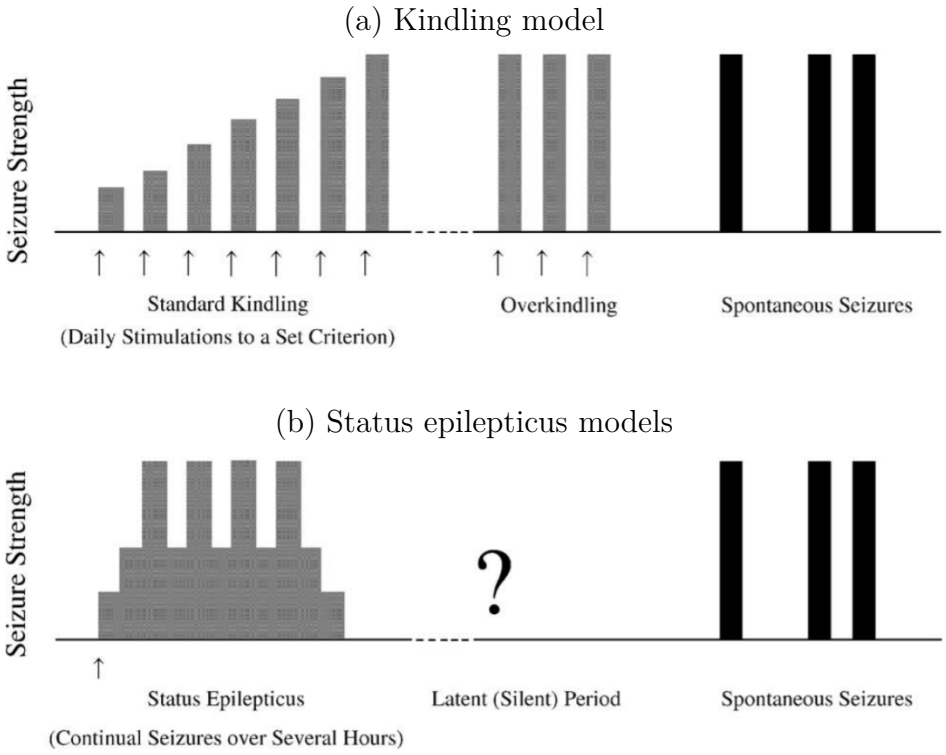

Figure 2.9 – The development of epileptogenesis and emergence of recurrent spontaneous seizures in (a) the kindling and (b) status epilepticus models, adapted from [69].
Arrows indicate electrical stimulation in the kindling model or the administration of chemical agents (e.g. kainate and pilocarpine) in the status epilepticus model. (a) In the kindling model, repeated stimulation triggers progressively stronger seizure responses. (b) In the status epilepticus model, there is typically one bout of status epilepticus that terminates within several hours. Spontaneous seizures appear after a latent (silent) period that lasts for weeks or months.

number of spaced simulations are required to develop spontaneous seizures. In contrast, status epilepticus models (e.g. kainate [70] or pilocarpine [71]) are easier to produce but more variable in their expression. The cytotoxic agents is usually administrated by systemic injections. Many animals can be injected at a time and it does not require to perform surgical procedures, which also means that surgical lesions are eliminated. In addition, morphological changes are very similar to those observed in human TLE. The disadvantages of status epilepticus models are that one has no control on the bio-availability of agents in the brain and some animals require multiple injections before status epilepticus and the mortality rate following systemic injections is high. However, mortality can be reduced by multiple low dose injections until status epilepticus or by stopping the status epilepticus by anesthetic substances administration [72].

Figure 2.10 shows the research activities of these models since their emergence. We observe that the pilocarpine and kainate (or kainic acid, KA) models have greatly overcome the kindling model in the last 10 years.

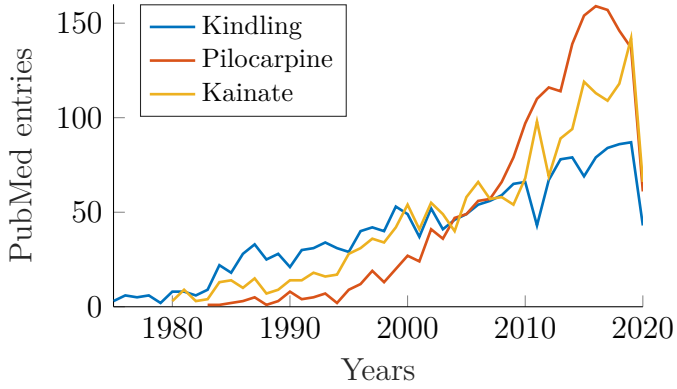

Figure 2.10 – Experimental rodent model of epilepsy research activities since their emergence.

2.1.3.2 Status epilepticus models: general presentation and behavioral manifestations

Status epilepticus models present a latent (or silent) period of weeks or months following status epilepticus, i.e. absence of spontaneous seizures. However, during this period, the presence of spikes and later spike clusters in EEG recordings, is associated with the progressive development of chronic epilepsy [73]. Structural and functional modifications occur leading to predisposition to synchronized neuron activity and thus contribute to the emergence of spontaneous seizures. According to [74], the status epilepticus models are usually used to study the transition of an episode of status epilepticus into chronic epilepsy; the mechanisms of neuronal injury and susceptibility; synaptic reorganization (sprouting); hippocampal sclerosis; seizure-changes in gene expression and neurogenesis; and the development of new anticonvulsant drugs. Epilepsy may develop because of an abnormality in brain wiring, an imbalance in inhibitory and excitatory neurotransmitters, or some combination of these factors. Glutamate is the primary excitatory neurotransmitter and GABA is the inhibitory neurotransmitter in the brain, to name a few. Chemoconvulsants that enhance glutamatergic neurotransmission or block GABAergic inhibition are then able to induce continuous seizures or status epilepticus (e.g. kainate model), while enhancing cholinergic neurotransmission can also trigger status epilepticus by cholinergic hyperactivation (e.g. pilocarpine model).

The status epilepticus induced by pilocarpine and the one induced by kainic acid are similar, leading to the development of spontaneous limbic motor seizures and mossy fiber sprouting in the dentate gyrus [75]. The pattern of neuronal damage is similar to KA model but pilocarpine induces greater neocortical damage, i.e. cell loss [76, 77]. One of the drawback of the pilocarpine-systemic administrated model compared to kainate model is the more extensive lesions observed [78], but systemic injections of KA also induce large damage out of the hippocampal regions. The mortality rate following systemic administration of KA in rats is between 5 and 30% [72], while the pilocarpine model is known to be more reliable because almost all treated rats will develop spontaneous seizures, independently of the duration of the status epilepticus. After the administration of KA, animals show automatisms and a catatonic posture that often progresses to myoclonic twitching of the head, forelimbs and rearlimbs. Typically, before and after the administration, KA-treated rats also develop wet-dog shakes.

For both of these models, the cytotoxic agent can be delivered via systemic or intracerebral administration (generally in the hippocampus [79, 80] and amygdala for KA [81]). In fact, the behavioral, electrographic and neuropathological alterations that follow intracerebral injection, are similar to those observed following systematic injection and the mortality following injection is drastically reduced [72, 79]. More generally, the variability of models is reduced. Using unilateral intrahippocampal KA administration, we observe cell loss and complete degeneration of the hippocampus with enlargement of the granule cell layer of the dentate gyrus weeks after injections. The intraamygdala administration of KA could induce bilateral hippocampal lesions [82]. These lesions, distant from the injection site, result from the propagation of the seizure activity. However, these models require a surgery, which increases the labor required to produce animals.

2.1.3.3 Status epilepticus models: electroencephalographic features and neuropathological changes

After injection and during status epilepticus typical EEG recordings are observed. Figure 2.11(a) shows the type of high amplitude, high frequency epileptiform EEG activity that repeatedly occurs up to more than 100 times following KA and which is associated with either limbic or generalized convulsive seizures. The activity observed in figure 2.11(b) can sometimes last for hours.

During the week that followed status epilepticus, spontaneous seizures are reported and hippocampal EEG shows paroxysmal discharges, see figure 2.11(c-d). Note that spontaneous focal and generalized convulsive seizures are very often indiscriminable

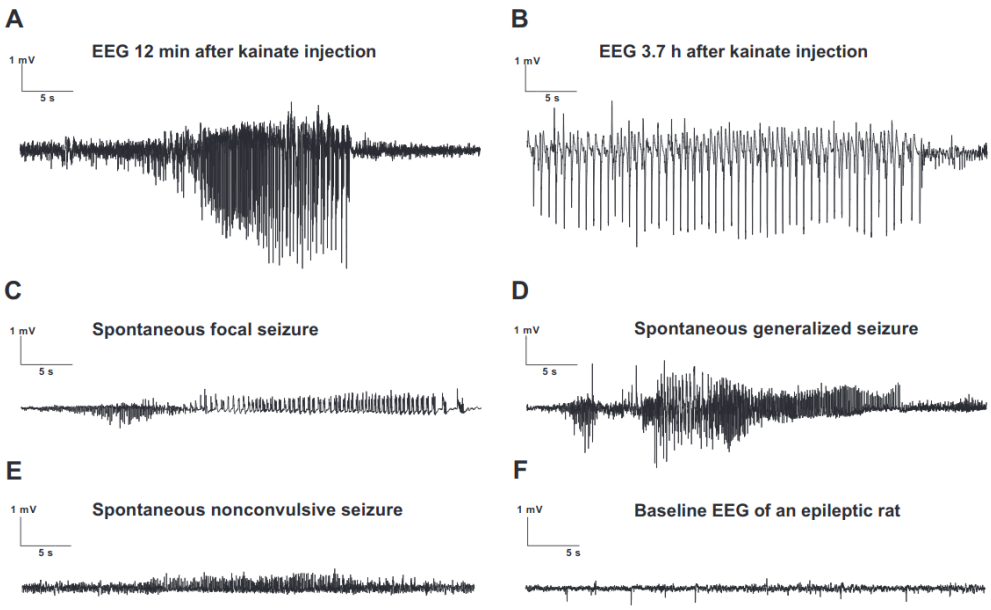

Figure 2.11 – Electroencephalograms (EEG) of rats kainate model, adapted from [83]. (A) First typical EEG seizure determined 12 minutes after kainate injection. (B) Typical epileptiform activity observed several hours after kainate. (C) Paroxysmal EEG activity during a spontaneous focal seizure. (D) Paroxysmal EEG activity during a spontaneous generalized convulsive seizure in an epileptic rat; (E) Atypical paroxysmal EEG activity during a spontaneous nonconvulsive seizure in an epileptic rat. (F) Baseline EEG between seizures in the chronic period of an epileptic rat.

in the EEG. Once spontaneous and recurrent seizures emerge, we observe around 6-7 generalizations per week [83]. Typically, the baseline EEG recordings of an epileptic rat show interictal spikes (figure 2.11(f)).

A large loss of neurons is reported in the ipsilateral CA1, CA3 and the dentate hilus, while the dentate gyrus is generally preserved. In the rat model, CA1 is less damaged. However, a slight dispersion of the granule cells of the dentate gyrus has already been reported, see figure 2.12. In the mouse model, proliferation and hypertrophy of astrocytes and microglia has been shown [84]. Authors also reported the formation of a pericyte-glial scar around hippocampus capillaries a few days after the status epilepticus, which persists at spontaneous seizure period. Note that existence of epileptic discharges has also been reported in contralateral hippocampus without cell loss [85]. According to [67], the intrahippocampal kainate model in mice displays features of MTLE that are somewhat different from those observed in rat using the same conditions but which offers closer similarities with clinical features such as occurrences of focal seizures with

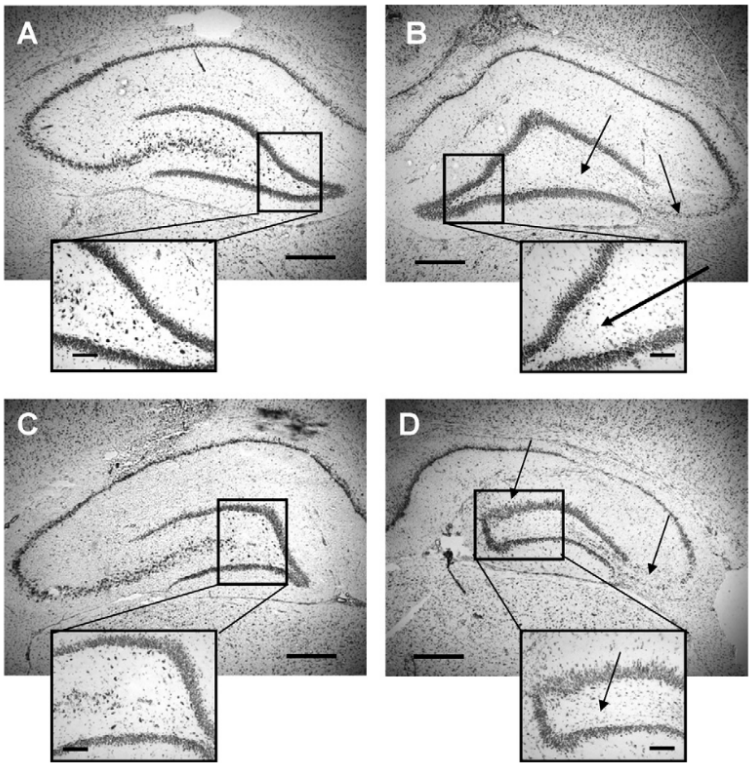

Figure 2.12 – Thionin-stained sections of rats kainate model, adapted from [83].
Thionin-stained sections of (B, D) the ipsi- and (A, C) contralateral hippocampus of two epileptic rats, which received intrahippocampal kainate injections into the right posterior CA3. Sections (A, B) are from the same rat, whereas (C, D) are from another rat. In each figure, the hippocampal formation is shown at ×25 magnification (scale bar = 1000 µm); inserts show the hilus at higher magnification (×100; scale bar = 250 µm). Note the severe neuronal damage in the ipsilateral CA3a and CA3c region and hilus (arrows) and dispersion of the ipsilateral granule cell layer (D, arrow). The extensive neuronal loss of hilus neurons is associated with reduced (shrunken) hilus volume. In (C, D), some neurodegeneration was also observed in CA1 (average score 1.5). If at all, only very discrete changes (score 1) were observed in the contralateral hippocampal formation.

mild behavioral component, EEG aspect of discharges and a characteristic pattern of hippocampal sclerosis.

2.1.3.4 Status epilepticus models: imaging

In epilepsy, the role of imaging in the evaluation of accurate or onset seizure is critical to exclude lesional causes, such as traumatic, vascular, tumoral, malformations, inflammatory or infectious. In the absence of preceding events, there is supporting evidence for MRI as the neuroimaging technique of choice due to better sensibility and specificity [86, 87].

However, computerized tomography scan (CT) can be preferred due to more widespread availability, rapidity of acquisition, and limited contraindications. In [86], authors indicated, however, that 8-12 % of patients with initial negative CT scans, present positive findings in MRI. Still, it is also possible for patients to have negative MRI. Classically, MRI is used to qualitatively assess for an atrophic hippocampus with hyperintense T_2 signals (described in the subsequent section 2.2.2.1), which is a defining trait of advanced hippocampal sclerosis [88, 89]. Although qualitative imaging remains the gold standard for diagnosis, there is a constant need to develop quantitative and automated methods to identify hippocampal and extra-hippocampal damages. MRI can provide a precise characterization of the internal architecture of the hippocampus, which allows better detection of more subtle changes. One of the main targeted development is the detection of the epileptogenic foci but one can also study the epileptic condition following the status epilepticus in experimental model to identify biomarkers of the development of a chronic condition. Of course, a robust method to reduce the number of negative MRI scans is also very valuable.

A step forward is the use of more complex MRI acquisitions such as functional, diffusion, perfusion with or without contrast agent administration among others. These MRI techniques are described in section 2.3 but we propose to summarize here the important findings associated with epilepsy. In fact, some parameters are very well documented while others are sometimes completely absent from the picture. We propose to report most of the last quantitative MRI findings in experimental status epilepticus models summarized in table 2.1. We also propose to interpolate from few longitudinal studies, the variations of the most documented MRI parameter values during the month following the status epilepticus in figure 2.13. This duration includes the entire epileptogenesis that ends with the establishment of a favorable environment for epileptic seizures. Note that the graph was produced from several models/scanners.

Regarding cellular related MRI parameters, several works reported hyperintensity in T_2-weighted images after status epilepticus [90], which matches increased T_2 values reported in quantitative studies [91]. In this work, authors also reported increased T_1 values. Usually, these parameters return to their initial values after 1-2 weeks [91]. Diffusion parameters are the most documented MRI parameters in epilepsy. Early diffusion decreased first days after status epilepticus is followed by an increase in diffusion at the chronic period [92–94]. Regarding vascular related MRI parameters, the blood flow first increases and then, decreases at one week [91, 95]. Finally, several works have shown a significant increase in BBB permeability [96–98].

MRI technique	**Ref**	**Experimental findings**	**Models** and **time after induction**	**Matching clinical outcomes**
Weighted imaging	[90]	- Hyperintensity in T_2-weighted images	Rats / KA (in striatum) 1 day	[88]
	[99]	- Hyperintensity in T_2-weighted images (40-70% in ipsilateral hippocampus and 20-50% in ipsilateral amygdala) from first hours to 7 days and reduced hyperintensity (30% in hippocampus and 0-10% in amygdala) at 21 to 120 days	Mice / KA (intrahippocampal injection) 1 h to 120 days	[88, 89]
Quantitative relaxometry	[91]	- Increase T_1 (5-12% in hippocampus) at 1 to 3 days and normal after 2 weeks	Rats / pilocarpine 0 to 21 days	[100]
	[91]	- Increase T_2 (15-20% in pyriform cortex, 20-35% in piriform cortex, 5-20% in hippocampus) at 1 to 3 days and normal after 1 week		
Diffusion	[92]	- Decrease diffusion (ADC) (30% in piriform cortex and 7% in hippocampus)	Rats / KA 1 day	[89]
	[93]	- Early increase ADC (10-30% in pyriform cortex, amygdala and hippocampus) at 3-5 minutes and decrease (9-30% in the same regions) at 15 to 120 minutes	Rats / pilocarpine 3 to 120 minutes	
	[94]	- Increase ADC (0-10%), at 4 days and (10-15%) at 21-50 days	Rats / electrical stimulation 1 to 250 days	[101]
Perfusion	[95]	- Increase cerebral blood flow (CBF) at 14 days in amygdala, no changes before	Rats / pilocarpine 2 and 14 days	[102]
	[91]	- Increase CBF (45-65% in hippocampus), at 1 to 2 days) and normal after - Decrease CBF (15-25% in parietal cortex and 5-30% in piriform cortex) at 3 to 14 days	Rats / pilocarpine 0 to 21 days	
Susceptibility-weighted	[103]	- Increase cerebral blood volume (rCBV) (100% in deep layers, to 200% in superficial layers in cingulate/parietal cortex, 106% in hippocampus, 150-500% in caudoputamen and thalamic nuclei)	Rats / pilocarpine 12 hours	[104–106]
Dynamic contrast-enhanced	[98]	- BBB breakdown only in the thalamus at 2 hours; it had disappeared by 6 hours. At 24 hours, edema was present in the amygdala, the piriform and entorhinal cortices; it disappeared over a 5-day period. In the hippocampus, the T2-weighted signal underscored the progressive constitution of atrophy and sclerosis, starting at 2 days	Rats / pilocarpine 2 hours to 9 weeks	[107]

MRI technique	**Ref**	**Experimental findings**	**Models** and **time after induction**	**Matching clinical outcomes**
Dynamic contrast-enhanced (*continued*)	[97]	- Damaged BBB in piriform, enthorhinal cortex, hippocampus and amygdala (gadolinium leakage is 1.5-4 times higher at 1 day than at 6 weeks)	Rats / KA 1 day to 6 weeks	
	[96]	- Increase volume with damaged BBB at 2/7 days in amygdala, cortex and piriform and reduction of the increase volume damaged BBB at 1 month	Rats / paraoxon 2 days to 1 month	

Table 2.1 – Overview of MRI findings in murine experimental models of epilepsy from status epilepticus to the establishment of the chronic condition favorable to the occurrence of spontaneous seizures .
When the injection site is not specified, the injection was not intracerebral. When the values were not provided in the text, they were manually measured in figures.

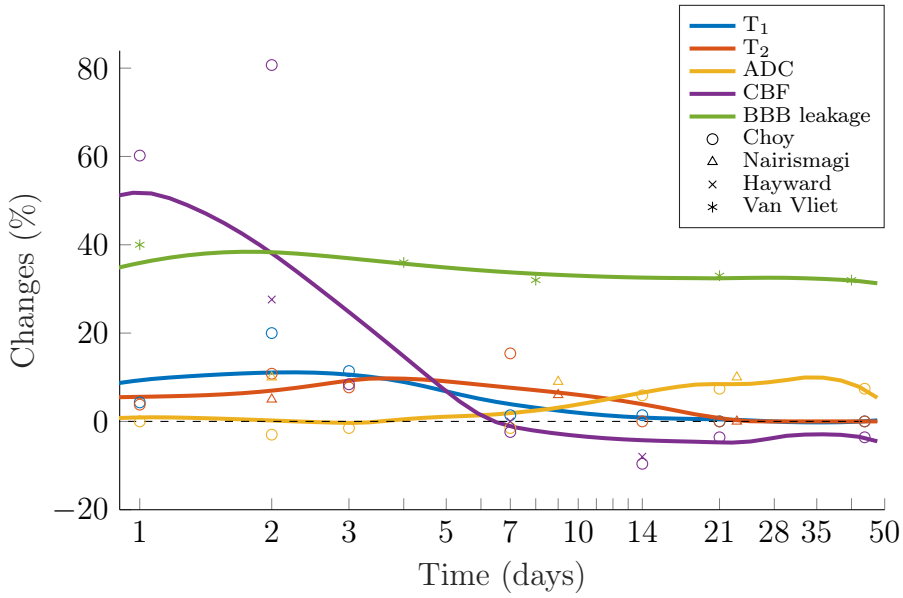

Figure 2.13 – Cellular and vascular MRI parameter evolutions after status epilepticus until chronic period.
Curves represent the evolution of cellular and vascular MRI parameters induced by status epilepticus: blue (T_1), red (T_2), yellow (apparent diffusion coefficient, ADC), purple (cerebral blood flow, CBF), and green (damaged blood-brain-barrier, BBB). Four longitudinal/multiparametric studies were used to interpolate these curves [91, 94, 95, 97] by modified Akima cubic Hermite interpolation after smoothing. Each marker represents a study: circle [91], triangle [94], cross [95], and asterisk [97].

2.2 Magnetic resonance imaging (MRI)

In this section, we briefly introduce how nuclear magnetic resonance (NMR) may be used to form images with different contrasts between tissues placed into a magnetic field. Different sources have been used to produce this section, in particular the two websites [108, 109] and other works referenced throughout the text.

The introduced notions will help understand the stakes of quantitative MRI and particularly magnetic resonance fingerprinting. First, the production of an MRI signal relies on a multitude of phenomena, most of them interfering with others. Models used in standard quantitative MRI are often based on many simplifying assumptions but complex simulations can be performed for more accurate quantification. Second, quantitative MRI is a time-consuming technique and is subject to many sources of image deterioration. The robustness of quantification methods to these deteriorations is therefore required and may eventually lead to accelerated acquisitions, detailed in a dedicated section.

2.2.1 Nuclear magnetic resonance

2.2.1.1 Magnetization

Placed into a magnetic field B_0, some nuclei become comparable to magnets, with an elementary magnetization. Under the action of a suitable radio-frequency (RF) pulse, these nuclei can absorb a certain amount of energy: this occurs when the RF pulse and elementary magnetization, are on resonance. In this work, the *spin* is assimilated to a macroscopic magnetization that can be analyzed according to the laws of classical electromagnetism rather than by those of quantum mechanics. For these nuclei, the interaction of B_0 with the spin generates a magnetic moment causing the spin to precess.

Exposed to a magnetic field B_0, the magnetization adopts a precession movement around the axis of the magnetic field characterized by a precession frequency ω_0, known as Larmor's frequency, proportional to the value of the field:

$$\omega_0 = \gamma B_0, \tag{2.1}$$

with γ the gyromagnetic ratio that is unique to each nucleus. In the following, we only focus on hydrogen since water molecules is the main component of human tissues (65-70 % in the body and 70-75 % in the brain [110]) and the target of standard clinical MRI. Note that the gyromagnetic ratio for the hydrogen nucleus is $\gamma = 2.67513 \times 10^8$ rad.s^{-1}.T^{-1}.

At thermal equilibrium, the macroscopic magnetization M resulting from spins, has a null transversal component since the phases of the spins are incoherent and a non-null longitudinal component. The macroscopic magnetization is therefore colinear and in addition, proportional to the magnetic field B_0, see figure 2.14(a).

In this state, an RF pulse noted B_1 applied perpendicular to B_0 can affect the equilibrium state of the spins. This phenomenon occurs if the frequency of B_1 is identical to the proton precession frequency, i.e. at resonance. Energy is thus delivered to the system that moves away from its state of equilibrium during excitation. After the end of B_1 emission, the system returns toward its equilibrium position. This equilibrium return period is called relaxation. The B_1 pulse may be characterized by the angle it can impose to the macroscopic magnetization. This angle depends on B_1 amplitude and B_1 application duration.

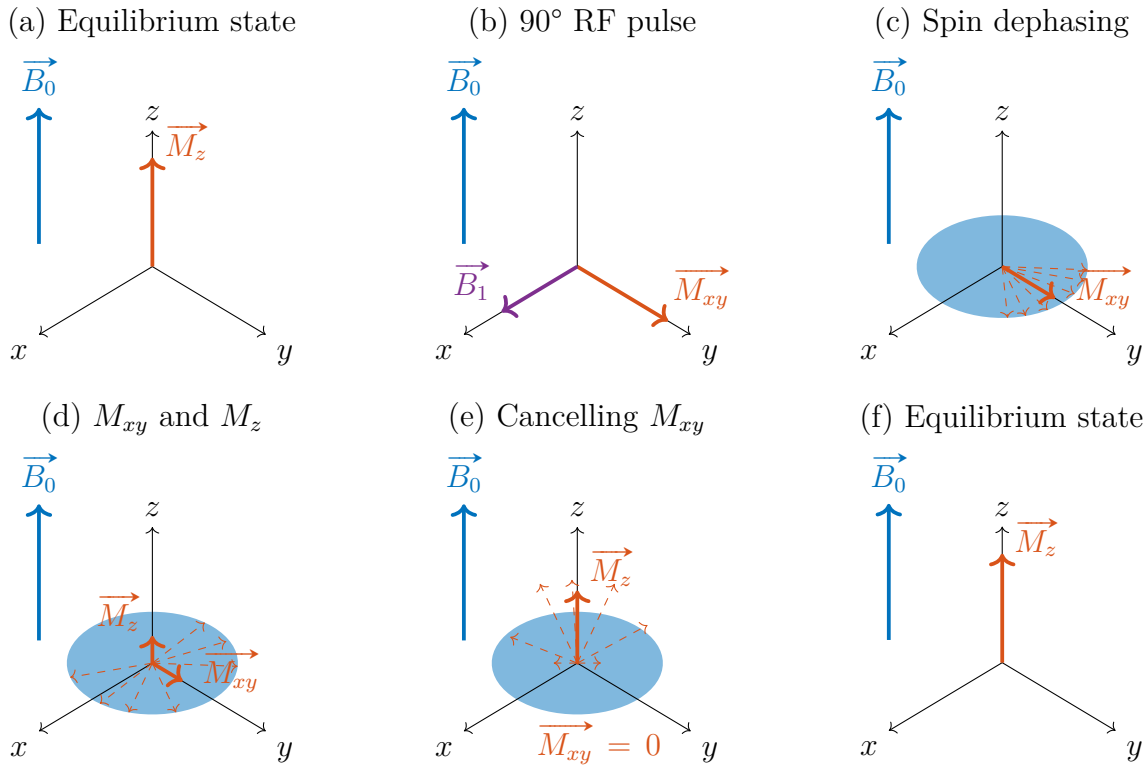

Figure 2.14 – Excitation and relaxation, using a 90° B_1 radio-frequency pulse in the rotating frame.
(a) Protons are placed into a magnetic field B_0 and (b) a 90° B_1 RF pulse is applied. (c-e) After the RF pulse ends, concomitant transverse and longitudinal relaxation processes. However, the order chosen for the figures results from the fact that the transverse relaxation process is shorter than the longitudinal relaxation process. Note that the blue disk represents the (xOy) plane. (f) At the end of the relaxation process, protons return to the state of equilibrium (a).

During an excitation with a 90° pulse, the magnetization flips to the plane orthogonal to B_0 (figure 2.14(b)). At the same time, the spins precess in phase and the transverse component of the magnetization increases and reaches its maximum value. During relaxation, the spin population returns to their thermal equilibrium level and spins dephase. Figure 2.14 illustrates the different steps of the relaxation process after a 90° excitation case.

2.2.1.2 Bloch equations

Felix Bloch introduced in 1946, a series of equations that describe the evolution over time of magnetization [111]. Note for the record that Edward Mills Purcell also independently described this same phenomenon of resonance and relaxation. They both obtained the Nobel Prize in Physics in 1952 for their work. Thus, in the laboratory frame where B_0 is aligned with the axis z and B_1 in the (xOy) plane, the magnetization $\mathbf{M}(t) = (M_x(t), M_y(t), M_z(t))$ is described by the following series of equations:

$$\frac{dM_x(t)}{dt} = \gamma\Big(M_y(t)B_z(t) - M_z(t)B_y(t)\Big) - \frac{M_x(t)}{T_2}, \tag{2.2}$$

$$\frac{dM_y(t)}{dt} = \gamma\Big(M_z(t)B_x(t) - M_x(t)B_z(t)\Big) - \frac{M_y(t)}{T_2}, \tag{2.3}$$

$$\frac{dM_z(t)}{dt} = \gamma\Big(M_x(t)B_y(t) - M_y(t)B_x(t)\Big) - \frac{M_z(t) - M_0}{T_1}, \tag{2.4}$$

where $\mathbf{B}(t) = (B_x(t), B_y(t), B_z(t))$ is the total magnetic field, $M_0 = M_z(t = t_{\text{eq}})$ is the longitudinal magnetization at thermal equilibrium, and the parameters T_1 and T_2 represent the relaxation times of the system.

In a frame rotating at the Larmor's frequency and after a 90° RF pulse, the solutions of Bloch's equations $M_{xy}(t)$ and $M_z(t)$ are:

$$M_{xy}(t) = M_0 \exp\left(-\frac{t}{T_2}\right), \tag{2.5}$$

$$M_z(t) = M_0\left(1 - \exp\left(-\frac{t}{T_1}\right)\right). \tag{2.6}$$

We observe that:

- The transverse magnetization follows an exponential decreasing law of characteristic time T_2. This time corresponds to the duration necessary for the transverse magnetization to reach 37 % of its initial value, i.e. $M_{xy}(t = T_2) = 0.37 \times M_0$.

- The longitudinal magnetization follows an exponential law characterized by relaxation time T_1. T_1 represents the time necessary for $M_z(t)$ to reach 63 % of its original value, i.e. $M_z(t = T_1) = 0.63 \times M_0$.

Note that the T_1 and T_2 time values depend on the intensity of the magnetic field B_0, and that transverse relaxation occurs faster than longitudinal relaxation. Therefore, T_2 is less than T_1 (can be equal e.g. in pure water).

2.2.1.3 Basic types of MR signals

The recorded MR signal $S(t)$ corresponds to an electromotive force produced by the precession of the magnetization $M(t)$ during resonance. This is a manifestation of Faraday's law of induction, wherein a changing magnetic field induces a voltage in a nearby conductor. In fact, only the transverse magnetization $M_{xy}(t)$ generates the current in the receiver coil.

After a 90° RF excitation, the resulting signal is called the free induction decay (FID), a damped sine wave, see figure 2.15(a). In practice, we observe that the decay is faster than expected by theory due to the inhomogeneities of the magnetic field. Therefore, the exponential decays with time constant T_2^* that reflects the combined effects of the T_2 relaxation and of phase dispersion due to magnetic field inhomogeneities ($T_2^* \leq T_2$). A clever manipulation of the FID signal begins by applying an external dephasing gradient field across the tissue. This gradient causes a calibrated change in local magnetic fields and hence alters the resonance frequencies slightly across the tissue. This results in accelerated dephasing of the FID. Then, the process is reversed by applying a rephasing gradient with the same magnitude but with the opposite polarity to the dephasing gradient. The resulting signal is called the gradient echo signal (GE), see figure 2.15(b). This process affects neither T_2 nor T_2^*. One can recover the level of the T_2 relaxation. For this, one adds a second excitation: a rephasing 180° pulse, after the 90°. This process can refocus dephased components of the original FID into a spin echo (SE) at twice the delay that separates RF pulses (figure 2.15(c)). We do not go into details on the spin echo, additional information can be found in [112].

These basic sequences are at the origin of the two major MRI contrasts, depending on the type of echo recorded: the SE sequences, characterized by the presence of a 180° RF rephasing pulse and the GE sequences, more sensitive to magnetic field inhomogeneities. Any other sequence is a sophisticated combination of RF pulses and gradients. The objectives for any sequence are to enhance the signal of a particular tissue (contrast), as

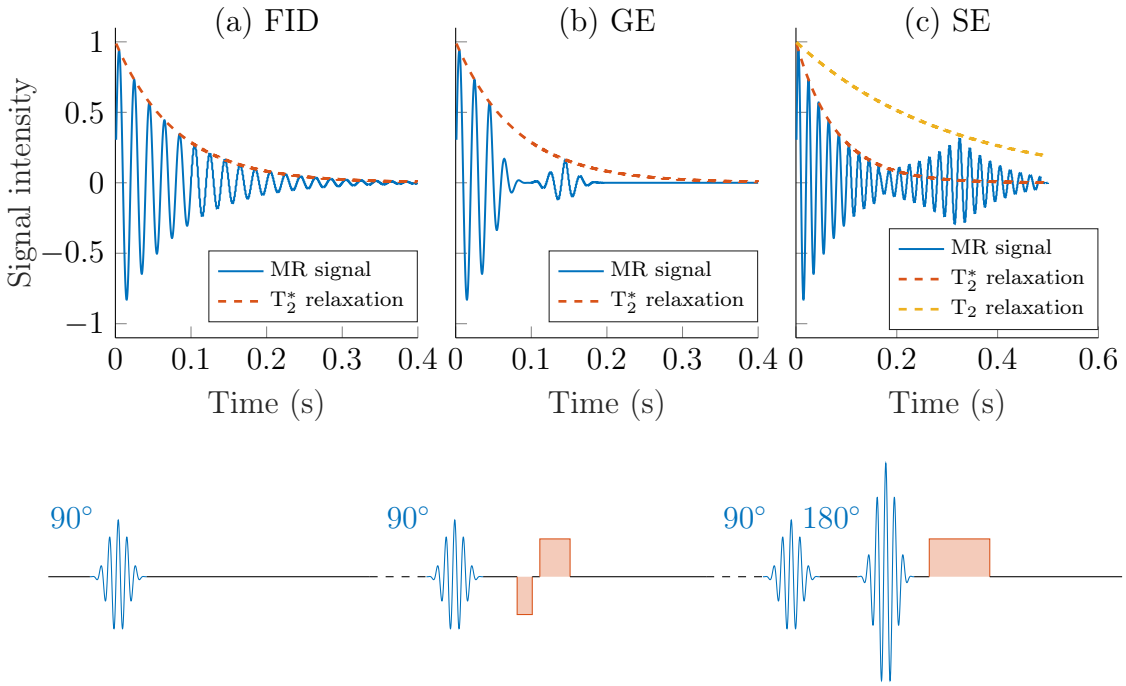

Figure 2.15 – Basic types of nuclear magnetic resonance signals.
(a) Free induction decay (FID) signal. (b) Gradient echo (GE) signal. (c) Spin echo (SE) signal. Corresponding chronograms are reported below with the RF pulses (*blue*) and the gradients (*red*).

fast as possible, while limiting artifacts and without altering the signal-to-noise ratio. This subject is further discussed later.

2.2.2 Images and contrast

2.2.2.1 T_1 and T_2 contrasts

In first approximation, two acquisition parameters can be specified in MR imaging: the echo time (TE) and the repetition time (TR) in order to generate a contrast between the tissues. The TE corresponds to the delay between the excitation pulse and the acquisition window, i.e. the transverse magnetization measurement time. The TR corresponds to delay between two excitation pulses. Depending on these acquisition parameters values, different magnetization values are obtained. As the magnetization is not the same for the different tissues, one can obtain different contrasts. In particular, intermediate TR ($TR \approx T_1$) and a short TE ($TE \ll T_2$) correspond to a T_1-weighted image while a long TR ($TR > T_1$) and a long TE ($TE > T_2$) correspond to a T_2-weighted image (figure 2.16).

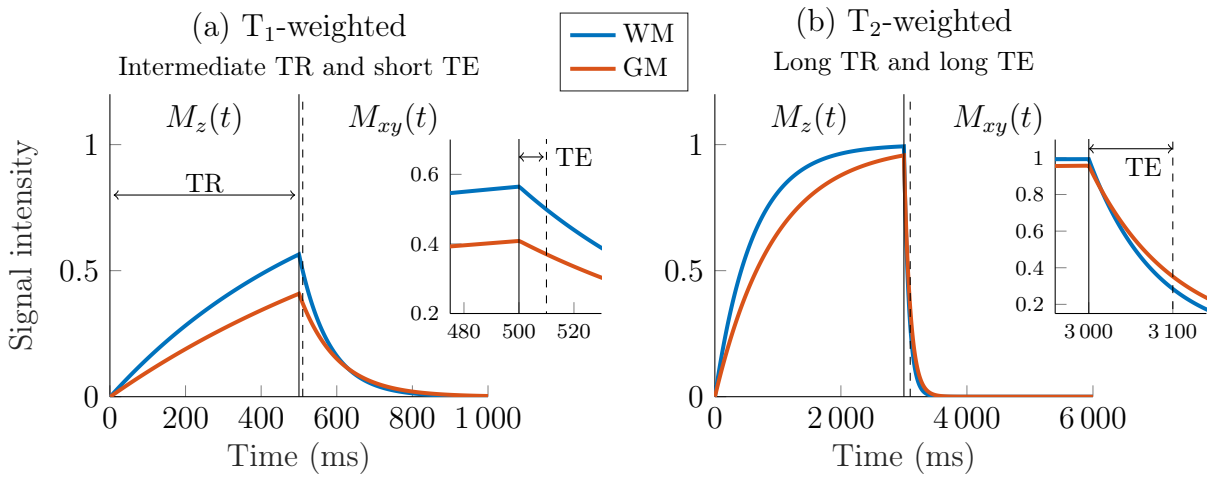

Figure 2.16 – Magnetization evolutions, using spin-echo sequence.
White matter (WM) and grey matter (GM) transversal M_{xy} and longitudinal M_z magnetizations for (a) T_1-weighted image, and (b) T_2-weighted image acquired at echo time (TE). $T_1/T_2 = 600/80$ ms for WM and 950/100 ms for GM. The smaller axes correspond to a zoom in on the delay TE between excitation (solid line) and acquisition time (dashed line).

At this point, we only obtain contrasts between tissues. These contrasts are related to the acquisition parameters and the quantification of T_1 and T_2 values (which are independent of the acquisition parameters) is not available at this point. We see in section 2.3.1 how to use the theory introduced in this section to quantify T_1 and T_2.

2.2.2.2 Spatial encoding

We have seen how to generate a signal/contrast using an RF excitation applied on protons in a volume but the spatial coding has so far been omitted. A typical magnetic resonance (MR) scan may contain million of voxels (generalization of the pixel in 3 dimensions), each generating its own MR signal. The location of all MR signals is encoded following a combination of different methods:

- Frequency encoding: magnetic field gradients are applied to locally modify the main magnetic field, causing the resonance frequency to vary as a function of position.
- Phase encoding: a gradient is applied to provide a gain or loss in phase that persists even after the gradient has been turned off.

We only describe 2D-multislice imaging, which consists in acquiring multiple $N_x \times N_y$ resolution images of N_z slices of tissue. This acquisition results in $N_x \times N_y \times N_z$ voxels. The size of these voxels depends on the size of the volume imaged and the matrix, i.e. the size of the organ imaged and the number of voxels. Typical fields of view (FOV) are

$25 \times 25\,\text{cm}^2$ for human brains and $2.5 \times 2.5\,\text{cm}^2$ for mouse brains, and a slice width of 1 mm for humans and 100 µm for mice (about 10 times smaller).

The first step in 2D-multislice imaging is to select the slice plane. Briefly, a slice-selection gradient is applied along the direction perpendicular to the plane of the desired slice. This gradient results in a linear variation of the resonance frequencies in that direction. An RF pulse is simultaneously applied, whose frequency band matches the range of frequencies contained in the desired slice. The combination of these two processes insures that only protons located in the desired plane are excited. We will see how to encode the localization according to the two directions of the plane.

The second step is to use a phase encoding gradient, let us say in the vertical direction. The phase-encoding gradient modifies the precession frequencies of the spins, which induces a phase shift. It persists when the gradient is stopped and until acquisition. Thereby, protons on the same line precess at the same frequency but with modified phases (figure 2.17(a)). To obtain an image, it is necessary to acquire multiple measurements with different phase shifts, incremented regularly. For a SE sequence with N_y lines, N_y acquisitions are realized, each with a different phase encoding gradient.

The last step in spatial encoding is to apply, during signal acquisition, a frequency gradient in the last direction (horizontal in our example). It modifies the precession frequencies in the horizontal direction throughout the duration of its application. It creates columns of protons, which have an identical precession frequency (figure 2.17(a)).

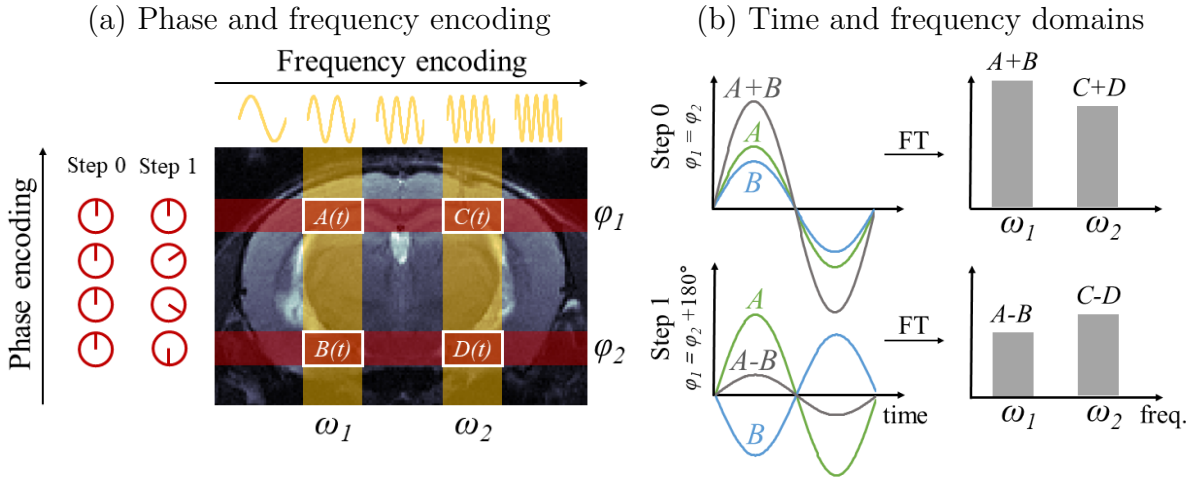

Figure 2.17 – Spatial encoding in MRI.
Figure (a) shows the phase and frequency encoding in 2D MRI. $A(t)$, $B(t)$, $C(t)$ and $D(t)$ are MR signals of volumes delimited by white rectangles in 2D. Figure (b) shows these signals in time and frequency domains during the two phase encoding steps.

We present in figure 2.17, an illustration of the spatial encoding in a 2D slice. Note that MR signals result from a population of protons contained in a volume. Figure 2.17(b) shows that MR signals of a vertical line contribute to the corresponding frequency magnitude. Considering a simple two-phase encoding: $A(t)$ and $B(t)$ for frequency ω_1 and $C(t)$ and $D(t)$ for frequency ω_2. In equation (2.7), we see that the combination of the signal $(A + B)$ results in a sine wave of the same base frequency ω_1, but with an averaged phase shift of $(\varphi_1 + \varphi_2)/2$.

$$\begin{aligned} S_0(t) &= A(t) + B(t) \\ &= \sin(\omega_1 t + \varphi_1) + \sin(\omega_1 t + \varphi_2) \\ S_0(t) &= 2\sin\left(\omega_1 t + \frac{\varphi_1 + \varphi_2}{2}\right)\cos\left(\frac{\varphi_1 - \varphi_2}{2}\right). \end{aligned} \tag{2.7}$$

From the single measurement $S_0(t)$, we cannot determine the phase contributions from $A(t)$ and $B(t)$ individually. However, in this simple 2-line phase encoding, the individual contribution can be obtained by performing a second acquisition $S_1(t)$:

$$S_1(t) = A(t) - B(t), \tag{2.8}$$

and it results that

$$\frac{S_0(t) + S_1(t)}{2} = \frac{(A(t) + B(t)) + (A(t) - B(t))}{2} = A(t), \tag{2.9}$$

$$\frac{S_0(t) - S_1(t)}{2} = \frac{(A(t) + B(t)) - (A(t) - B(t))}{2} = B(t). \tag{2.10}$$

This example is generalizable and it is therefore necessary to perform as many acquisitions as the desired line number N_y. The duration of a 2D acquisition $\mathrm{T_{acq}}$ is therefore:

$$\mathrm{T_{acq}} = \mathrm{TR} \times N_y \times N_R, \tag{2.11}$$

where N_R is the number of repetitions.

2.2.2.3 k-space data

In MRI, instead of solving the equation system (2.9) for N_y acquisitions, we use the Fourier transform (FT). The raw MR signal is acquired in the k-space (or Fourier plane, frequency space) and its complex values are stored in a matrix. This matrix is then used to form the 2D image using a 2D FT. Thus k-space holds raw data before reconstruction.

The filling of the entire k-space cannot be achieved at once but it can be achieved in any orders: popular methods include Cartesian (row-by-row), radial and spiral trajectories, see figure 2.18(a, d, e). The Cartesian method was used nearly exclusively at the beginning of MRI, but today all patterns are encountered. The major benefit of radial sampling is a lower sensitivity to motion artifacts [113]. In radial acquisitions, the center of k-space is oversampled and continuously updated due to the overlapping spokes that repeatedly pass through this region. This redundancy can be exploited to detect and correct for movement if the signal from the k-space center changes between views. In return, the principal advantage of Cartesian sampling is that data elements are regularly spaced and can be placed directly into standard array processors designed for efficient FT computations. Radial methods generate data points that do not fall into a rectangular matrix. To efficiently process such non-uniformly acquired data, these points must be morphed into a Cartesian format.

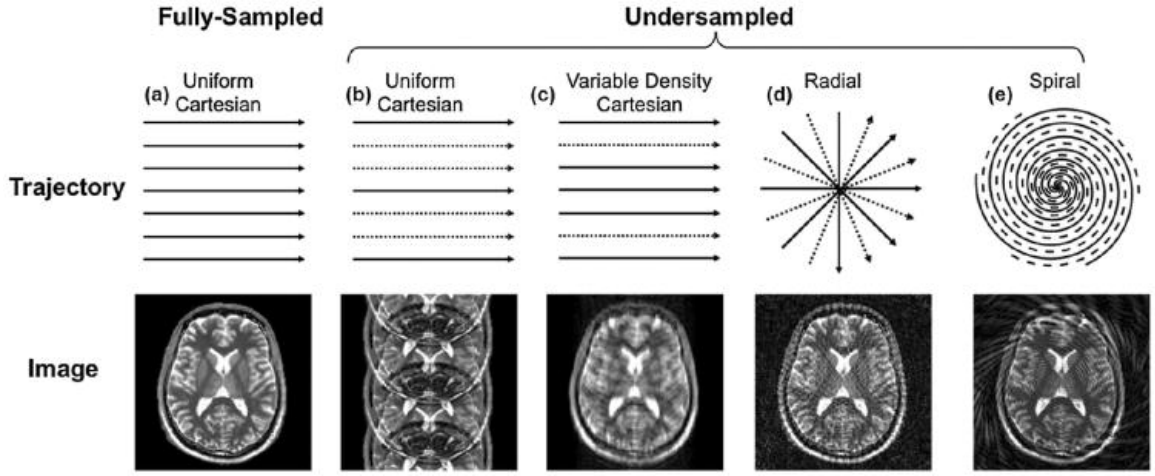

Figure 2.18 – Examples of different k-space trajectories and their associated aliasing artifacts, adapted from [114].
Acquired k-space data are indicated by solid lines, while missing data are depicted with dashed lines. (a) Fully-sampled Cartesian data produces a full FOV image. (b) Uniformly undersampled Cartesian k-space with an acceleration factor of $R = 3$ leads to coherent aliasing artifacts. (c) With variable density sampling, a higher concentration of lines is acquired near the k-space center, and the imaging artifacts are more diffuse. (d) Radial data can be undersampled by skipping radial spokes at regular intervals, which leads to diffuse streaking artifacts. (e) Spiral k-space can be undersampled by skipping spiral arms, which produces incoherent swirling artifacts.

To shorten scan time, some works have proposed to sample a smaller number of phase encoding lines in k-space; however, without further processing, the resulting images will be degraded by aliasing artifacts, see figure 2.18(b-e). It is also demonstrated that scan

time can be reduced using parallel imaging and simultaneous multislice. This subject is not addressed in this work, details can be found in [114]. However, artifacts related to spatial undersampling are of importance in magnetic resonance fingerprinting.

2.2.2.4 Noise in MRI

As opposed to acquisition artifacts, the noise is an unavoidable random signal that gets added to all of our acquisitions [115]. It results from the thermal fluctuations of our system: in the electronics and of the spins in the organ imaged. Johnson-Nyquist noise or thermal noise of an electronic system is given by [116]:

$$\sigma_{\text{thermal}} = \sqrt{4\, k_{\text{B}}\, R\, T\, \Delta\nu}, \tag{2.12}$$

where $k_{\text{B}} = 1.38.10^{-23} J.K^{-1}$ is the Boltzmann's constant, T is the temperature of the system in K, R is the resistance in Ω, and $\Delta\nu$ is the acquisition frequency band in s^{-1}.

The reduction of noise in signals therefore involves the reduction of one or more of these parameters e.g. MRI receivers can be cooled to cryogenic temperatures to reduce the temperature and thus noise (as was done in this work). Concerning the resistance, this value is the sum of the RF coils and associated electronic component resistances and the patient resistance. The composition of biological tissues and in particular the presence of ions causes the human body to act as a conductor. When a conductor is placed into a magnetic field, it creates currents, which dissipate slowly. These currents induced in the patient then induce currents in the coils that are picked up as noise [117]. This is called patient loading and for large magnetic fields (higher than 1 T) it is significantly larger than the intrinsic hardware noise. In fact, the patient loading is proportional to B_0^2. The acquisition frequency band is directly proportional to the FOV and depends on the sequence gradient used. Finally, the MRI signal is measured in k-space and consequently Fourier transform implies that every point in the original k-space affects every point in the image. Without going into technical details and according to [117], the noise's standard deviation is increased by a factor $\sqrt{N_x\, N_y}$.

Because this noise is added to the MR signal of interest, to estimate the deterioration of our signal by noise, the most meaningful measurement is the signal-to-noise ratio (SNR), which is defined as the ratio between the signal magnitude S_{m} and the noise's standard deviation. Note that the repetition of acquisition and averaging of signals leads to a reduction of noise's standard deviation by a factor $\sqrt{N_R}$. Overall and according to [115], SNr is proportional to the volume voxel and the square root of the acquisition

time:

$$\text{SNR} \propto V_{\text{voxel}} \sqrt{T_{\text{acq}}} \,, \tag{2.13}$$

where $\propto$ means *proportional to* and V_{voxel} is the volume of the voxel. In addition to the noise, motion artifact and undersampling artifact can also contribute to increase the apparent noise level.

2.2.2.5 Clinical application

The relevance of MRI for clinical applications depends on the following imaging characteristics:

- Imaging resolution: the size of voxels must be at least of the order of the observed anatomical structures.
- Quality of the signal: the noise and aliasing artifacts must be sufficiently small so as not to affect the estimation of the parameters carried out on the signals, i.e. smaller than the variations due to the physiological changes.
- Acquisition time: the image must be sufficiently fast to be considered for a routine clinical application.

Most of the parameters that can be adjusted at acquisition (i.e. FOV, N_x, N_y, TR, N_R), affect several or all of these characteristics. The improvement of one property generally leads to a deterioration of another and vice versa. For example, the reduction of the voxel size for a given FOV implies an increased acquisition time (equation (2.11)) and/or a decreased SNR (equation (2.13)). Most of the time, an MRI acquisition consists in finding the appropriate compromise between these characteristics. In the next sections, we describe how cellular and vascular biophysical properties can be quantified from well-designed MR signals.

2.3 Quantitative MRI

We saw in the previous section how to acquire MR images. These images are affected by a combination of different factors, some intrinsic to the tissue (e.g. T_1 or T_2) and some dependent on the specifics of the experiment (e.g. TR and TE). However, to compare subjects with each other or to apply statistical methods on cohorts, it is necessary to have access to quantified values. We regard an MRI study to be quantitative when we obtain maps of meaningful physical or biological parameters that can be measured in physical units and compared between tissue regions and among subjects. In this section, we explain how to obtain these quantitative maps using MRI. We only describe the sequences and parameters that have been investigated in the study of epilepsy. For simplicity, in this work, we only consider two MRI parameter categories: cellular and vascular. Even though it is not a perfect fit, we consider that the relaxation times are into cellular parameters since these parameters are mainly defined by the extravascular composition. Indeed, as the blood volume fraction is small ($< 5\,\%$; except when the voxel corresponds to a large vessel), more than $95\,\%$ of the MRI signal originates from cells (neurons, glia). We introduce these parameters in table 2.2.

	Parameter	Acronym	Page
Cellular	Longitudinal relaxation time	T_1	50
	Transverse relaxation time	T_2	50
	Apparent diffusion coefficient	ADC	51
	Fractional anisotropy	FA	51
Vascular	Cerebral blod flow	CBF	54
	Blood volume fraction	BVf	57
	Vessel size index	VSI	57
	Tissue oxygen saturation	StO_2	57
	Signal enhancement	ΔS	59
	Time-to-peak	TTP	59
	Area under the curve	AUC	59

Table 2.2 – Cellular and vascular parameters used for mesial temporal lobe epilepsy model experiments and described in this section.

For each parameter, we present the theory, the MR sequence acquisition used in this work and then the associated standard quantification method (we do not consider here more advanced quantification schemes). We propose a simple single line chronogram for each MR sequence. For illustration, we provide a map of each parameter using the data that we acquired on mice with a Bruker 9.4 T MRI scanner.

2.3.1 Relaxation times

In general, a known model of physical and physiological phenomena that describes the evolution of the magnetic signal after specific RF pulses is used. For example, in the case of the relaxation, we have seen that after a 90° pulse, the transverse magnetization $M_{xy}(t)$ and longitudinal magnetization $M_z(t)$ follow the equations (2.5) and (2.6), respectively. To obtain the temporal evolution, time-weighted images are acquired using a multi-echo SE sequence (figure 2.19(a)) and an inversion recovery (IR) sequence (figure 2.19(b)), which is the same sequence preceded by a 180° RF pulse. It is then sufficient to fit the temporal evolution of the signals with the models $S(t)$ to determine the T_1 or T_2 values, respectively (figure 2.19(b, c)):

$$S_{\text{IR}}(t) = C_{\text{IR}} \left(1 - \exp\left(-\frac{t}{T_1}\right)\right), \tag{2.14}$$

$$S_{\text{MSE}}(t) = C_{\text{MSE}} \exp\left(-\frac{t}{T_2}\right), \tag{2.15}$$

where C_{IR} and C_{MSE} are model constants.

(a) IR sequence

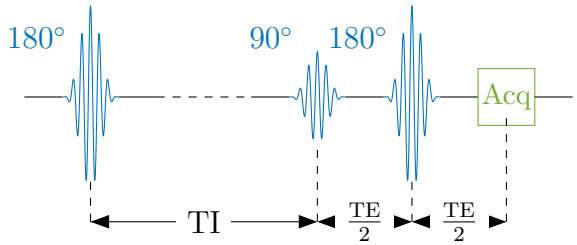

(b) Multi-echo SE sequence

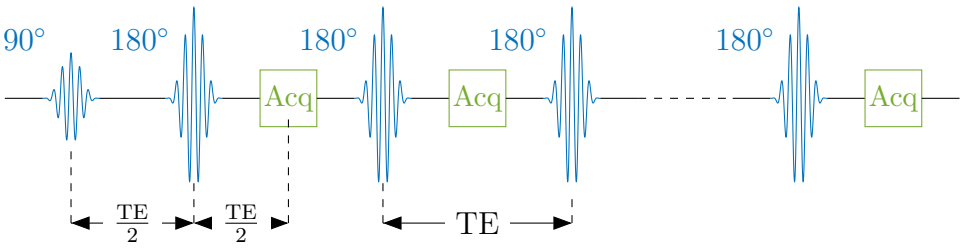

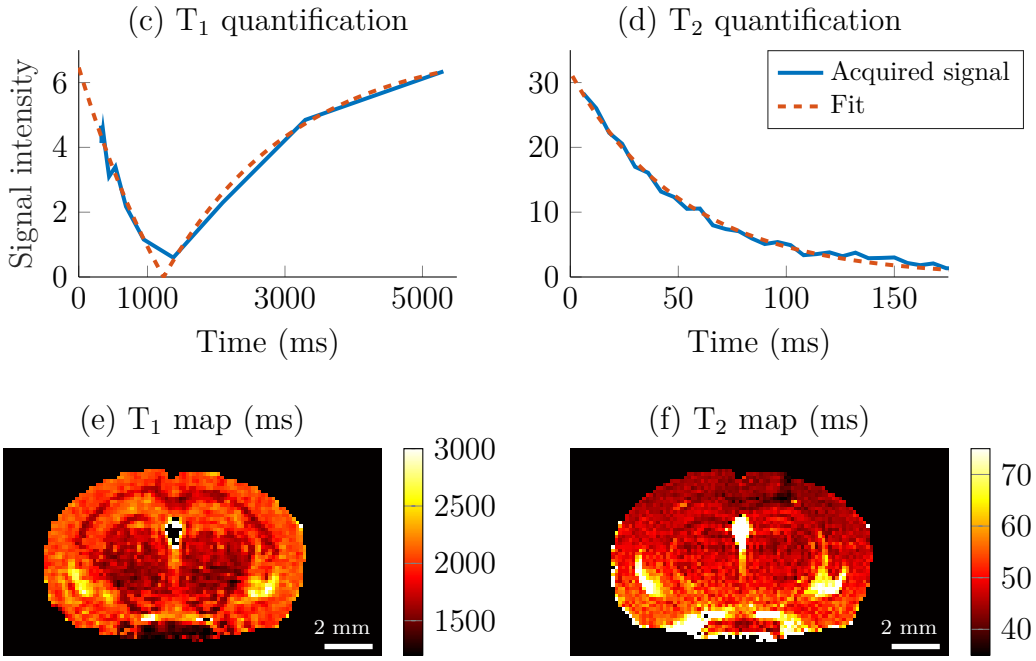

Figure 2.19 – Relaxation times MRI: T_1 and T_2.
(a) Inversion recovery (IR) and (b) multi-echo spin echo (SE) sequences, and (c, d) MR signals associated, respectively. A Levenberg-Marquardt solver of non-linear least squares problems is used on MR signals to fit (c) equation (2.14) and (d) equation (2.15). (e) T_1 and (f) T_2 maps. Data were acquired at 9.4 T on an adult mouse, using a spatial resolution of $136 \times 136 \times 700\,\mu m^3$. Note that one can observe an up-down spatial bias on (f) the T_2 map that suggests a proximity effect at the receiving antenna.

Relaxation times (or relaxivities: $R_1 = 1/T_1$ and $R_2 = 1/T_2$) are certainly the most used quantification and reflect tissue composition. Physiological parameters that can influence T_1 and T_2 include cell type, tissue water content and myelin content. It is also possible to perform more complex acquisitions or to inject contrast agents for quantification of physiological parameters as presented in the following sections.

2.3.2 Water diffusion

The mechanical interaction of particles or molecules with each other under the effect of thermal agitation produces pseudo-random movements at the microscopic level. The trajectories are qualified of Brownian. In 1855, Adolf Fick established the law describing the process of diffusion of molecules [118]. Fick's law expresses a linear relationship between the flow of a substance and the concentration gradient of this substance:

$$J = -D\,\nabla C\,, \tag{2.16}$$

with J the flux of substance in mol.m^{-2}.s^{-1}, D the diffusion coefficient in m^2.s^{-1} and ∇C the gradient of the local concentration in mol.m^{-4}. J measures the amount of substance that will flow through a unit area during a unit time interval. The diffusion of the molecules therefore occurs in the opposite direction of the concentration gradient, i.e. the diffusion tends to homogenize the concentrations of the molecules in the environment.

The conservation law, also called Fick's second law (in this case the equation (2.16) is called Fick's first law), describes the variation of concentration over time as a function of the second space derivative:

$$\frac{\partial C}{\partial t} = D\,\nabla^2 C\,, \tag{2.17}$$

with $\nabla^2 C$ the Laplacian of the local concentration in mol.m^{-5}. To obtain an MRI signal that is sensitive to the diffusion of water occurring in one direction of space, the pulsed gradient spin-echo (PGSE) sequence, an MRI sequence of the classical SE type but with diffusion gradients, was proposed in [119] and is still widely used today. Two magnetic field gradients of equal intensity G and equal duration δ are applied on both sides of the 180° refocusing RF pulse (figure 2.20(a)). If there is a diffusion process in the direction of these gradients during the period Δ that separates the two gradients, then the second phase shift does not fully compensate for the first and the attenuation of the signal may be related to the diffusion D. Torrey modified the Bloch equations (2.2) to take into account the diffusion process and solved these new Bloch-Torrey equations [120]:

$$S_{\text{PGSE}}(b) = S_0 \exp\left(-bD\right), \tag{2.18}$$

$$\text{with } b = (\gamma G \delta)^2 \left(\Delta - \frac{\delta}{3}\right), \tag{2.19}$$

where S_0 is the signal in the absence of diffusion gradients, G the gradient intensity in T.m^{-1}, δ the gradient duration and Δ the time between gradients in second. The b-value was introduced in [121] and represents the diffusion weighting. The equation (2.18) assumes that the compartment is isotropic and therefore requires the same diffusion coefficient in all directions.

The first and one of the most commonly used diffusion model is the diffusion tensor imaging (DTI). The model substitutes the diffusion coefficient D by a symmetrical positive-definite tensor $\mathbf{D}$ of order two. Thus to determine the tensor only 6 acquisitions are necessary. The previous equation (2.18) becomes:

$$S(\mathbf{g}, b) = S_0 \exp\left(-b\mathbf{g}^T\mathbf{D}\mathbf{g}\right), \tag{2.20}$$

where $\mathbf{g}$ is a gradient direction of norm 1 and $\mathbf{g}^T$ is its transpose. For a given value of b, 6 acquisitions for 6 different values of $\mathbf{g}$ are enough to determine $\mathbf{D}$. The diagonalization of this tensor allows to express the diffusion in a new referential where the eigenvalues (λ_1, λ_2 and λ_3) represent the diffusion values in the 3 principal diffusion directions. From this eigenvalue decomposition, different quantitative values can be calculated, such as the apparent diffusion coefficient (ADC) and the fractional anisotropy (FA):

$$\mathrm{ADC} = \frac{\lambda_1 + \lambda_2 + \lambda_3}{3}, \tag{2.21}$$

$$\mathrm{FA} = \sqrt{\frac{(\lambda_1 - \lambda_2)^2 + (\lambda_2 - \lambda_3)^2 + (\lambda_1 - \lambda_3)^2}{2\,(\lambda_1{}^2 + \lambda_2{}^2 + \lambda_3{}^2)}}. \tag{2.22}$$

The apparent diffusion coefficient is usually given in $\mu m^2.s^{-1}$. This value is a good indicator of the mobility of water molecules within a voxel. FA (between zero and one) describes the degree of anisotropy of the diffusion process. A value of zero means that diffusion is isotropic, i.e. it is equally restricted in all directions. A value of one means that diffusion occurs only along one axis and is fully restricted along all other directions.

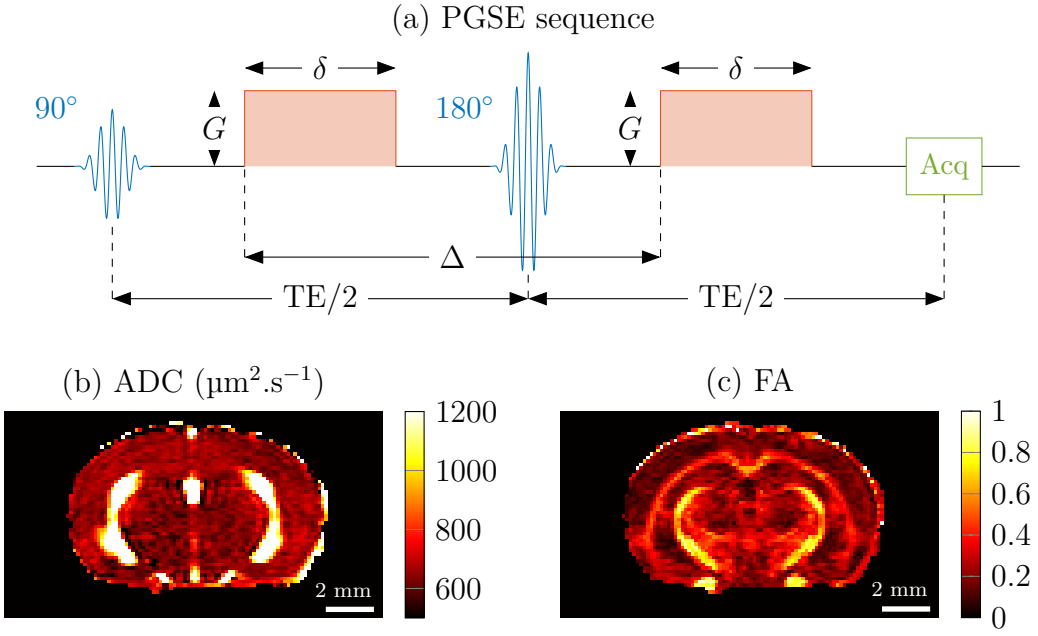

Figure 2.20 – Diffusion MRI.
(a) Diffusion MR sequence. (b) Apparent diffusion coefficient (ADC). (c) Fractional anisotropy (FA). Data were acquired at 9.4 T on an adult mouse, using a spatial resolution of $136 \times 136 \times 700\,\mu m^3$.

Complex diffusion images that reflect various diffusion properties of a tissue can be produced using the eigenvalues and eigenvectors. However, most of the time, we only use the regular diffusion-weighted imaging to produce ADC images (figure 2.20(b)) but FA images can also be computed (figure 2.20(c)). A more complex modeling of water diffusion process exist but is beyond the scope of this thesis.

2.3.3 Perfusion using arterial spin labeling

Perfusion is the tissue irrigation by blood, at capillary levels. To measure the perfusion, it is necessary to use tracers of blood circulation. These tracers can be of two natures: endogenous or exogenous. In this part, we present the tracking of endogenous tracers in the blood, i.e. hydrogen protons. This method, known as arterial spin labeling (ASL), is particularly valuable for its non-invasive aspect compared to the contrast agent injection perfusion methods described in the following sections.

In an ASL sequence, an RF pulse and a magnetic field gradient are used upstream of the imaged volume. The idea is to « mark » the spins contained in the blood, which then modify the magnetic signal when perfusing the imaged brain volume. The subtraction of the images in the absence (called control images) and in the presence (called label images) of labeled spin allows to remove the signal originating from the static tissues and to reveal the changes caused by blood circulation. These changes depend on blood volume and flow rate, which are the parameters known as cerebral blood volume or blood volume fraction (BVf) and cerebral blood flow (CBF). In practice, ASL imaging produces a very low signal close to the noise level and only the repetition of the acquisitions provides, by averaging label-control image pairs, a correct signal-to-noise level.

Numerous ASL sequences have been proposed in recent years [122]. Among these sequences, two main types of methods appear: pulsed ASL (PASL) and continuous ASL (CASL). PASL sequences use very short RF pulses over large labeling areas, while CASL sequences, initially proposed by [123], jointly implement continuous labeling using long RF pulses located at the carotids (a few seconds) and a gradient in the direction of flow. CASL sequences allow a higher perfusion contrast but have two major drawbacks: magnetization transfer effects and high energy deposition in the tissues. The pseudo-continuous ASL (pCASL) method, presented below, combines the advantages of both CASL and PASL sequences.

Indeed, the works [124, 125] introduce the pCASL method using very short ($\approx 400\,\mu m$) repeated RF pulses as pseudo-continuous labeling. During the labeling period, positive gradients are applied during the pulses and negative gradients between pulses such that

the mean value corresponds to the gradient used in CASL. During the control period, the average value of the magnetic field gradient is set to zero. As it induces limited magnetization transfer effects, the pCASL sequence allows the acquisition of several imaging slices (figure 2.21(a)).

The CBF can be computed using equation (2.23) and ΔM, the signal difference between control and label acquisitions averaged over repetitions:

$$\mathrm{CBF} = \frac{\lambda \Delta M \exp\left(\frac{\omega}{\mathrm{T_{1b}}}\right)}{2\,\mathrm{IE}\,\mathrm{T_{1app}}\,M_{0\mathrm{t}}\left(1-\exp\left(\frac{-\tau}{\mathrm{T_{1app}}}\right)\right)}, \tag{2.23}$$

$$\text{with IE} = \left|\frac{M_\mathrm{C} - M_\mathrm{L}}{2M_\mathrm{C}}\right|, \tag{2.24}$$

where $\lambda = 0.9$ mL.g^{-1} is the blood-brain partition coefficient of water, τ is the labeling duration, ω is the post-labeling delay, $M_{0\mathrm{t}}$ is the equilibrium magnetization of arterial blood, $\mathrm{T_{1app}}$ is the apparent $\mathrm{T_1}$ of tissue and $\mathrm{T_{1b}}$ is the $\mathrm{T_1}$ of blood. IE is the inversion efficiency that is computed using control M_C and label M_L complex signals. These last signals are measured in carotids using a specific sequence (figure 2.21(c)).

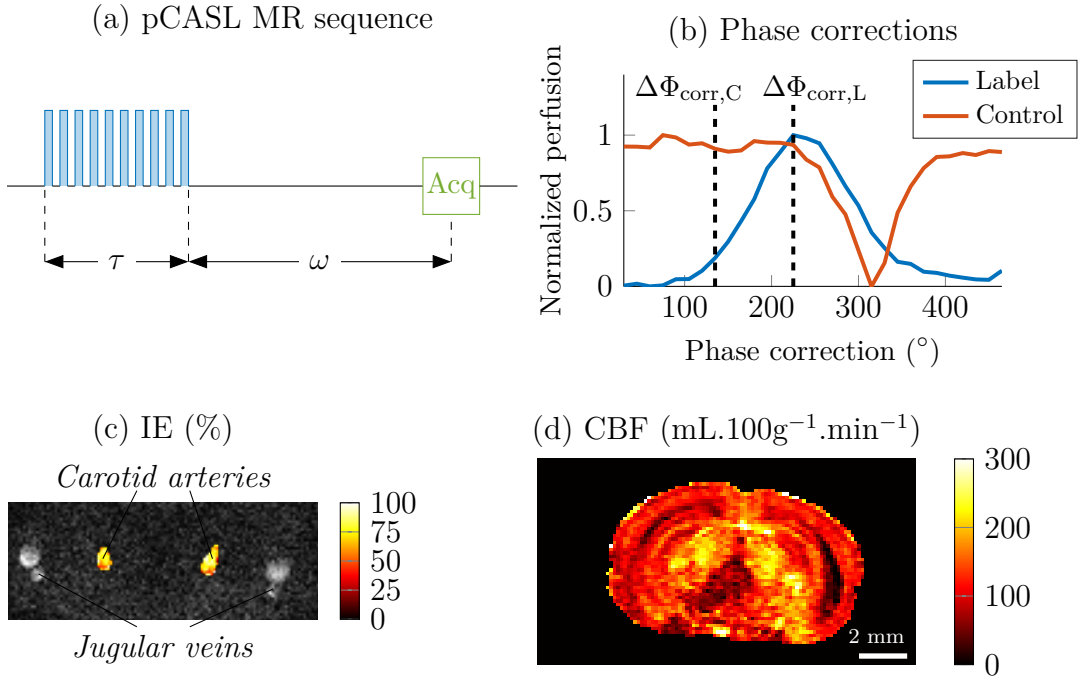

Figure 2.21 – Perfusion MRI using arterial spin labeling.
(a) pCASL MR sequence, (b) label and control phase corrections, (c) inversion efficiency (IE), and (d) cerebral blood flow (CBF). Data were acquired at 9.4 T on an adult mouse, using a spatial resolution of $136 \times 136 \times 700\,\mu\mathrm{m}^3$.

The pCASL sequence has its own limits, and in particular pCASL is very sensitive to field inhomogeneities that are present at the labeling slice and this effect increases with the magnetic field. In practice, at high fields, a correction is necessary in order to be able to freely position the labeling slice [126]. Label and control interpulse phase increments are optimized separately by means of two pre-scans. The mean perfusion is measured for several phase combinations to determine the interpulse phase corrections ($\Delta\Phi_{\mathrm{corr,L}}$ and $\Delta\Phi_{\mathrm{corr,C}}$) that maximize the perfusion signal. This correction is then applied to acquire the pCASL sequence (figure 2.21(b)).

2.3.4 Mapping vascular parameters using contrast agents

Exogenous contrast agents (CA) include intravenously administered substances that modify the contrast of blood and organs. CA are not directly visible but are imaged because they shorten the relaxation times T_1 and T_2 or because they increase the magnetic susceptibility differences between blood vessels and surrounding tissues. In this last case, the induced long-range magnetic field perturbations extend to adjacent tissues and increase the transverse relaxation rates R_2 and R_2^*. Therefore, a CA is characterized by its magnetic susceptibility and its relaxivities (r_1 and r_2), i.e. its ability to locally modify the magnetic field and the relaxation times of the molecule around, and also by its size, charge, or hydrophilicity that determines the locations where it goes. We used two main classes of CA (main characteristics given in Table 2.3):

- superparamagnetic iron oxide particles, used for their susceptibility effect and in particular result in a decrease T_2^*-weighted signal.
- gadolinium chloride, paramagnetic, with the principal effect of signal enhancement in T_1-weighted imaging.

Currently, gadolinium-based CAs are the most commonly used in MRI and particularly in clinical MRI, whereas ultrasmall superparamagnetic iron oxides (USPIO) are rather limited to a pre-clinical application.

Contrast agent	**Relaxivities** ($s^{-1}.mM^{-1}$)		**Hydrodynamic size** (nm)
	r_1	r_2	
Gd-Dota (Gadolinium)	3.3	4.1	1
P904 (USPIO)	4.0	92.0	25-30

Table 2.3 – Superparamagnetic iron oxide particle and gadolinium chloride contrast agents characteristics. Given for 37 °C, 4 % human albumin serum and 4.7 T [127, 128].

2.3.4.1 Ultrasmall superparamagnetic iron oxide

The first contrast agent presented induces magnetic susceptibility and relaxivity effects. When such a CA is compartmentalized within a voxel, these effects result in a decrease of the MR signal in an inhomogeneous magnetic field. This is what happens at vessel-tissue interfaces, since CA is distributed only in the vascular compartment. This paramagnetic substance acquires, in the magnetic field, a magnetization different from that of the surrounding environment: on each vessel surface, and over few microns, a magnetic field gradient appears [129]. This increase in the heterogeneity in the magnetic field of the voxel yield a decrease in signal intensity due to an increased spin-spin dephasing (T_2 relaxation). In a first approximation and when the blood volume fraction is small, the decrease of the signal observed in a voxel depends on the concentration of the tracer in vessels (i.e. the blood volume fraction), and on the fraction of blood in the volume. Going a little further, we can also show that this signal decrease depends on the number of vessels and their diameter [130]. Figures 2.22(b, c) show an example of T_2^*-weighted images before and after the injection of USPIO. On these images, it is easy to distinguish (in black because of signal decrease) the important vascular structures.

Using a multiple gradient echo sampling of the free induction decay and spin echo (MGEFIDSE) sequence (cf. below), it is possible to directly evaluate two parameters: the blood volume fraction (BVf) and the vessel size index (VSI), which are the proportion of blood in the volume imaged in % and a weighted mean vessel radius [131], respectively. VSI is computed as:

$$\mathrm{VSI} = \left(\frac{\sum_{i=1}^{R} r_i^{\frac{4}{3}}}{\sum_{i=1}^{R} r_i^2} \right)^{-\frac{3}{2}}, \tag{2.25}$$

where r_i is the radius of the i^{th} vessel, and R the total number of vessels in the voxel.

MGEFIDSE sequence is composed of a first 90° RF pulse and then a 180° RF pulse. Gradient echos collected after the first pulse capture information about the relaxation rate R_2^* (inverse of T_2^*) while the information acquired around twice the time between the two pulses capture information about the relaxation rate R_2 (inverse of T_2). The theory for determining BVf and VSI is presented in [132]. The changes in relaxation rates ΔR_2^* and ΔR_2 induced by the injection of USPIO are computed using gradient echo (GE) and spin echo (SE) signal intensities, respectively. The pre- and post-injection relaxation times $T_{2,\mathrm{pre}}^*$ and $T_{2,\mathrm{post}}^*$ are obtained by fitting the GE signal intensities to an exponential function, see section 2.3.1. It allows to compute ΔR_2^*, while ΔR_2 is directly calculated

from the two SE signal intensities (pre-injection: $S_{\mathrm{SE,pre}}$; and post-injection: $S_{\mathrm{SE,post}}$):

$$\Delta \mathrm{R}_2^* = \frac{1}{\mathrm{T}_{2,\mathrm{post}}^*} - \frac{1}{\mathrm{T}_{2,\mathrm{pre}}^*}, \tag{2.26}$$

$$\Delta \mathrm{R}_2 = \frac{1}{\mathrm{TE}} \ln\left(\frac{S_{\mathrm{SE,pre}}}{S_{\mathrm{SE,post}}}\right). \tag{2.27}$$

Then, these changes in relaxation rates are used to compute BVf and VSI using the following equations:

$$\mathrm{BVf} = \frac{3}{4\pi\,\gamma\,B_0\,\Delta\chi_{\mathrm{USPIO}}}\,\Delta \mathrm{R}_2^*, \tag{2.28}$$

$$\mathrm{VSI} = 0.424\left(\frac{\mathrm{ADC}}{\gamma\,B_0\,\Delta\chi_{\mathrm{USPIO}}}\right)^{\frac{1}{2}}\left(\frac{\Delta \mathrm{R}_2^*}{\Delta \mathrm{R}_2}\right)^{\frac{3}{2}}, \tag{2.29}$$

where $\Delta\chi_{\mathrm{USPIO}}$ is the increase in blood susceptibility due to USPIO. Note that VSI depends on the diffusion parameter ADC introduced in section 2.3.2.

(a) MGEFIDSE sequence

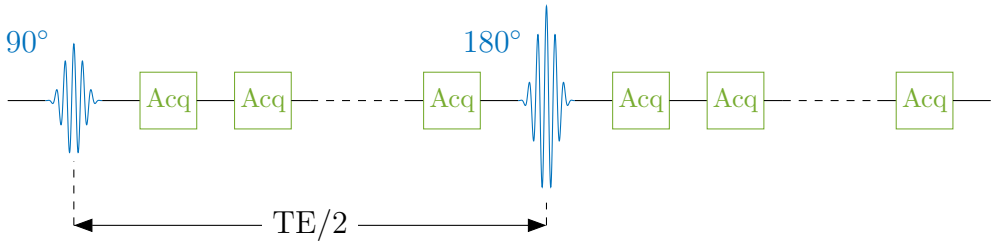

(b) T_2^*-weighted pre-injection image

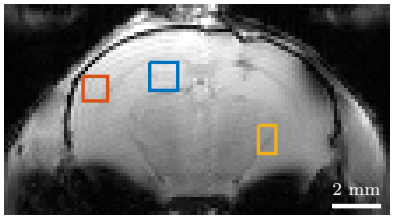

(c) T_2^*-weighted post-injection image

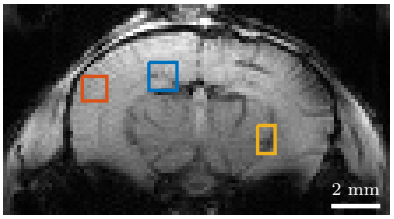

(d) MR signals

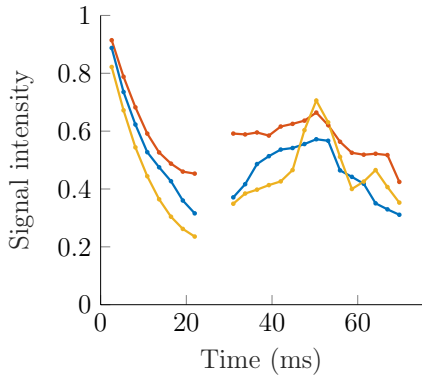

(e) BVf (%)

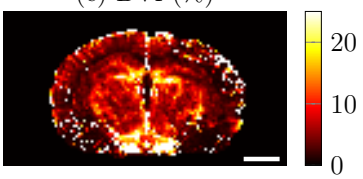

(f) VSI (µm)

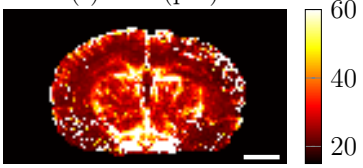

Figure 2.22 – Vascular structure MRI using USPIO.
Example of T_2^*-weighted images of a mouse brain (a) before and (b) 1 minute after the 200 µmol Fe.kg^{-1} body weight injection of USPIO. Data were acquired at 9.4 T on an adult mouse: spatial resolution of $136 \times 136 \times 700\,\mu m^3$ and spin echo at 50 ms. The average MR signals for the 3 regions (rectangles) are provided in (c). Each point of the curves correspond to one *'Acq'* on the chronogram represented in (a) (the blank corresponds to the 180° pulse).

The tissue oxygen saturation (StO_2) parameter is estimated using the quantitative approach described in [133]. First, the relaxation time T_2 is computed, see section 2.3.1. Equation (2.30) is then fitted to the MR signal decay of the mutli gradient echo sequence (MGE), which is given by:

$$S_{\mathrm{MGE}}(t) = S_0 \exp\left(-\frac{1}{T_2}\, t - \frac{4}{3}\pi\, \gamma\, B_0\, \Delta\chi_0\, Hct\, BVf\, (1 - StO_2)\, t\right), \tag{2.30}$$

where $\Delta\chi_0$ is the difference between the magnetic susceptibilities of fully oxygenated and fully deoxygenated hemoglobin, which is set to 3.32 ppm (SI unit), and *Hct* is the microvascular hematocrit, which is set to 0.357 (see [134]). S_0 is a constant.

2.3.4.2 Gadolinium

Dynamic contrast enhanced (DCE) imaging measures changes in relaxation time T_1 over time following an injection of Gadolinium. Immediately after the CA injection, gadolinium circulates throughout organs and extravasates (i.e. leaks out of the vessels into the surrounding area) in most of them with the exception of the healthy brain. Indeed, Gadolinium does not cross the BBB except in pathological conditions where it may be damaged. In this case, there is an extravasation of the CA, which reduces the T_1 of tissues. In practice, acquisition starts before the injection in order to observe changes induced by CA over time. The figure 2.23(a, b) shows T_1-weighted images during the acquisition and three examples of typical curves that can be observed.

There are two main groups of approaches to quantitatively analyze DCE MRI, namely, parametric (analytical) techniques and nonparametric (model-free). Parametric approaches aim to quantify kinetic parameters directly by fitting pharmacokinetic models to the concentration curves. Pharmacokinetic models are based on different assumptions and simplifications, see [135]. The advantage is that parameters are physiologically interpretable but the underlying model assumptions may not be applicable to all tissues or to damaged tissue. In addition, these approaches require the preliminary quantification of the arterial input function and the conversion of signal evolution into the CA concentration

evolution. Nonparametric approaches, on the other hand, derive empirical parameters that characterize directly the shape of signal evolution. All these steps add noise and can reduce reliability of the estimates. Empirical parameters correlate with physiological pharmacokinetic parameters [136] but it is difficult to estimate the tissue's physiological quantities, such as vascular permeability. Examples of such parameters are shown in figure 2.23(c) and computed from signal $S_{\mathrm{DCE}}(t)$ by:

- Signal enhancement (ΔS) is the difference between the maximum signal intensity $S_{\max}$ and the baseline S_0: $\Delta \mathrm{S} = S_{\max} - S_0$.
- Time-to-peak (TTP) is the delay between the CA arrival and the peak, i.e. signal intensity reaches its maximum value: $S_{\mathrm{DCE}}(t = \mathrm{TTP}) = S_{\max}$.
- Area-under-curve (AUC_T) for a time T in seconds (typically, 180):

$$\mathrm{AUC}_T = \int_0^T (S_{\mathrm{DCE}}(t) - S_0)\,\mathrm{dt}\,. \tag{2.31}$$

In chapter 5, the term BBB permeability ($\mathrm{BBB_p}$) is used for AUC_{600}, for sake of clarity.

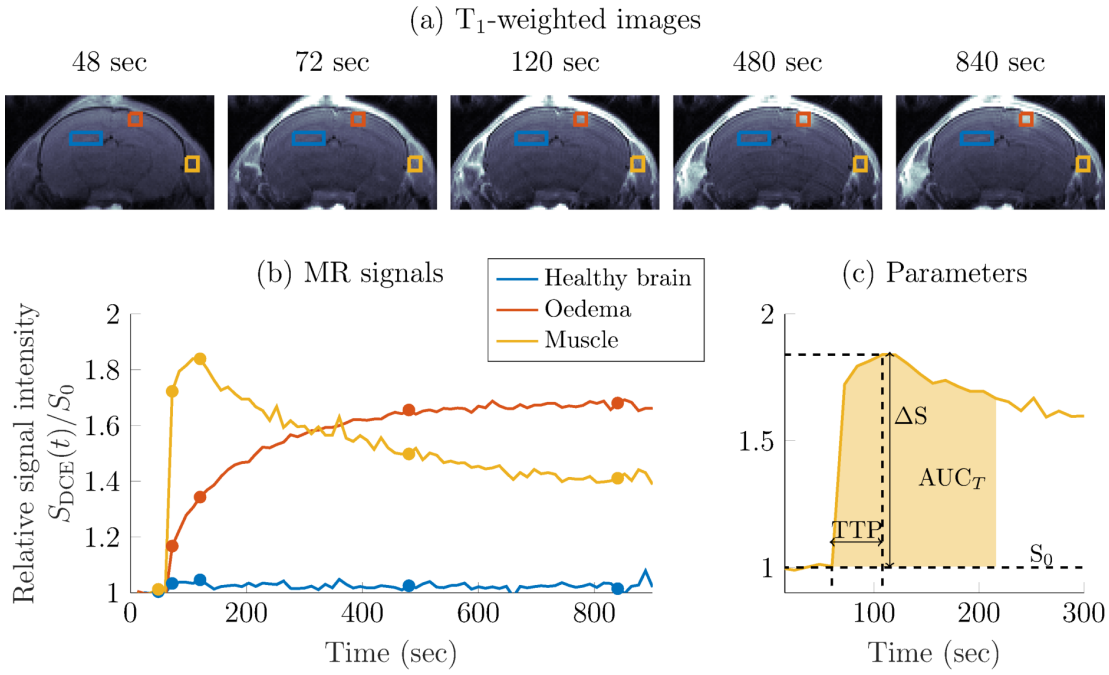

Figure 2.23 – Dynamic contrast enhanced MRI using gadolinium injection.
(a) Example of $\mathrm{T_1}$-weighted images of a mouse brain at 5 different times after the beginning of the acquisition. The gadolinium (200 µmol.kg^{-1}) was injected at 60 seconds. Data were acquired at 9.4 T on an adult mouse, using a spatial resolution of $136 \times 136 \times 700\,\mu\mathrm{m}^3$. The average MR signals over time for the 3 regions (colored rectangles) are provided in (b). The markers on curves indicate the values corresponding to the weighted images in (a). This mouse presents an edema in the cortex (red rectangle). (c) Nonparametric parameters: time-to-peak (TTP), signal enhancement (ΔS) and area-under-curve (AUC_T).

2.3.5 Conclusion

Conventional MRI, i.e. weighted imaging, is limited to reveal large morphological abnormalities resulting in regional differences in signal intensities within an acquired image. It means that MRI is intrinsically insensitive to subtle global changes that may affect the entire brain. In this case, quantitative MRI that allows the comparison of measurements in a single subject with normal values acquired in a healthy population is required. Conventional MRI also depends on the clinician's expertise in images interpretation and the absence of quantities is not optimal for using mathematical methods, e.g. classification.

However, most of quantitative MRI methods employed typically provide information on a single parameter at a time. The acquisition of several quantitative parameters thus require significant scan time. Moreover, these quantitative maps are often highly sensitive to system imperfections [137]. Because of these scan time limits and a high sensitivity to the measurement setup and experimental conditions, robust quantitative multiparametric MRI remains an important research focus in MRI.

2.4 Magnetic resonance fingerprinting (MRF)

In this section, we introduce the concept of MRF and the sequences that were developed. We then introduce vascular MRF and the simulation tool used in this study. We finally propose an overview of current quantification methods and current challenges. For more details, two complete reviews have been proposed in 2017 [138] and 2019 [139]. Figure 2.24 illustrates the recent apparition of MRF and its rapid development. The attractiveness of the method derives from its flexibility to address a wide range of MRI applications (e.g. vascular in our case) and the resulting scientific activity emerges from the multiple possible improvements.

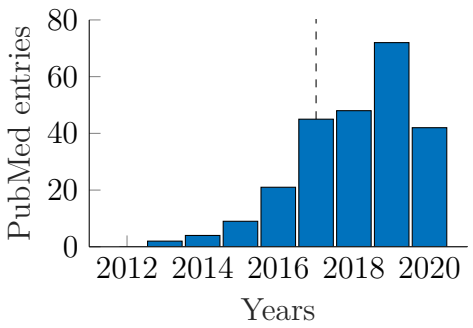

Figure 2.24 – PubMed entries for magnetic resonance fingerprinting from 2010 to 2020 (June).
The dashed line indicates the beginning of the thesis.

2.4.1 Basic principle

As explained in section 2.3, the standard quantification in MRI consists in fitting the signal evolution acquired with biophysical models using minimization algorithms (e.g. in this work, the Levenberg–Marquardt nonlinear least squares algorithm [140]). We refer to this quantification method as the closed-form expression fitting (CEF) method. The CEF method is often restricted to the measurement of a single parameter at a time, using a time-consuming acquisition. Thus, the acquisition time of a large set of parameters rapidly becomes impractical, particularly in clinical MRI. In 2013, Dan Ma et al. introduced a new paradigm, called magnetic resonance fingerprinting (MRF) that overcomes these constraints by taking a completely different approach to both data acquisition and data quantification [137]. The standard MRF quantification was introduced as an alternative to the least squares model fitting and thereby allows the use of more sophisticated biophysical models.

2.4.1.1 Acquisition sequences

Instead of using a repeated, serial acquisition of data for the characterization of individual parameters of interest (here, T_1 and T_2), MRF uses pseudorandomized acquisition parameters (here, TE, TR and flip angles), see figure 2.25 A-B. The term pseudorandom refers to the reasonable flexibility in the choice of acquisition parameters since the quantification is not driven by a biophysical model as with CEF, but by simulations. However, for accurate quantification, one should limit the choice of acquisition parameters to a range of values that allows the sequence to be sensitive to the biophysical parameters under investigation. Then, the sampling of acquisition parameters can be randomly generated [137] or based on other considerations, such as improving patient comfort by encoding acquisition parameters from a music file in order to provide pleasing sounds during acquisition [141]. Repeated acquisitions with variable acquisition parameters cause the signals from a specific material or tissue to have a unique temporal evolution or *fingerprint* from successively different system states. Note that the signal is called fingerprint to refer to its uniqueness and this uniqueness of fingerprints seems to be provided by a sufficiently large number of system states. In practice, a few minutes of acquisition is enough to provide a sufficiently typical signal evolution to quantify several parameters. However, to our knowledge, no theoretical framework has yet demonstrated the uniqueness of fingerprints. In this work, we thus prefer to refer to a fingerprint simply as an MRF signal. This signal, denoted by $\mathbf{y}$, is a function of the multiple parameters under investigation, denoted by $\mathbf{x}$.

In the original work of [137], a major strength of MRF was that MRF acquisitions were extremely spatially undersampled using a spiral trajectory (only $1/48^{\text{th}}$ of full k-space dataset was acquired for each time point). This contributed to the reduction of acquisition time. In return, the undersampling results in severe artifacts in the image associated to each individual time point (figure 2.25 C). Despite these spatial artifacts, the signal evolution (figure 2.25 F) could still be used for MRF because high quality individual time point images are not explicitly sought.

In the initial implementation, [137] proposed to used an inversion recovery–prepared balanced steady-state free precession (IR-bSSFP) sequence. This sequence is known to be sensitive to three parameters: T_1, T_2, and off-resonance frequency, which make IR-bSSFP suitable to estimate relaxation times with MRF. However, MRF has been adapted for other sequences in subsequent works, to overcome certain limitations, to confer additional advantages or to measure additional tissue properties. For example, in [142], authors utilized the SSFP sequence that is insensitive to B_0 inhomogeneity, eliminates banding

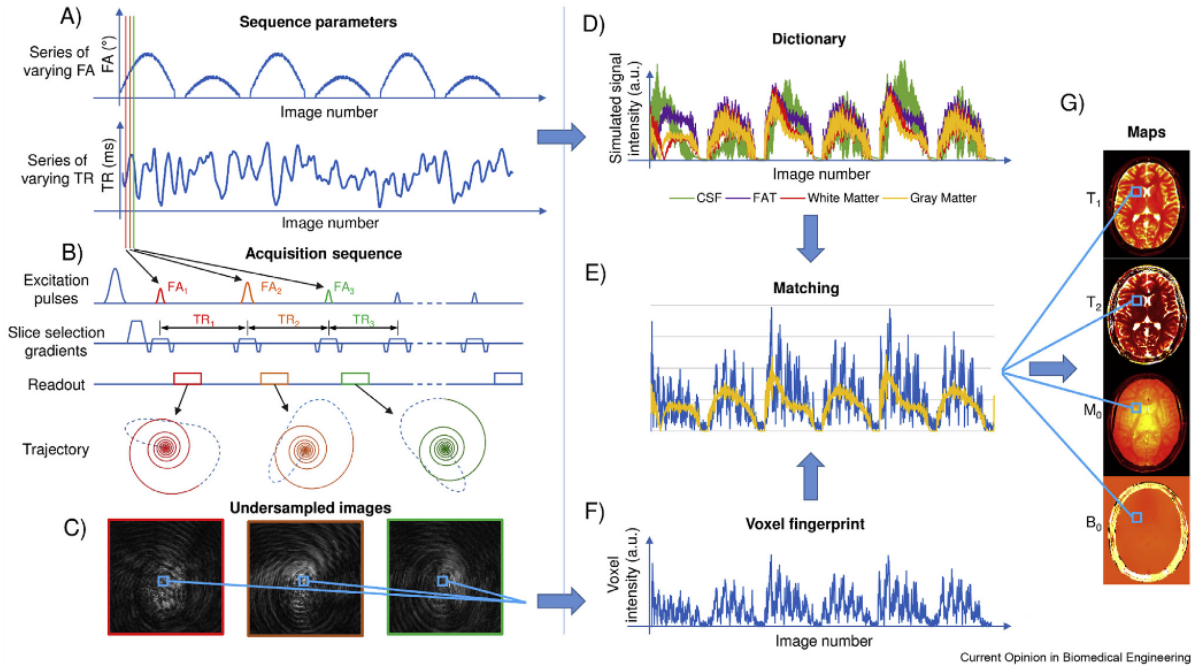

Figure 2.25 – Illustration of the MRF method, adapted from [138].
The flowchart shows an overview of the MRF framework as used for MR-True Fast Imaging with Steady State Precession (TrueFISP) acquisition. (A) An example of variable flip angles (FA) and repetition times (TR) used for this acquisition. (B) Sequence diagram showing the excitation pulses, slice selection gradients, readout and k-space trajectory for each TR. (C) Three undersampled images acquired in different TR. (D) Examples of four dictionary entries representing four main tissues; cerebrospinal fluid (CSF) ($T_1 = 5\,000$ ms, $T_2 = 500$ ms), fat ($T_1 = 400$ ms, $T_2 = 53$ ms), white matter ($T_1 = 850$ ms, $T_2 = 50$ ms) and gray matter ($T_1 = 1\,300$ ms, $T_2 = 85$ ms). (E) Pattern matching of the voxel fingerprint with the closest entry in the dictionary, which allows to retrieve the tissue features represented by that voxel. (F) Intensity variation of a voxel across the undersampled images. (G) Parameter maps obtained by repeating the matching process for each voxel. M_0 corresponds to the signal amplitude. B_0 is the main magnetic field intensity.

artifacts seen with bSSFP and can be readily adapted for body applications (i.e. large FOV with high B_0 inhomogeneities). In [143], authors adopted a pseudo steady-state free precession (pSSFP) sequence to improve the spin-echo like signal properties of a bSSFP based MRF acquisition and thereby reduce the effects of B_0 inhomogeneity on estimated tissue properties within a limited range of B_0. Authors in [144] incorporated an EPI based data acquisition approach into the MRF framework and a variation in TE for simultaneously estimating T_1 and T_2^*. A complete review of all MRF techniques can be find in [145].

Other works focused on the method for other parameters, such as Su et al. [146] that modified an ASL sequence (section 2.3.3) by using a variable labeling duration time for

each TR, removing the post-labeling delay and ordering the labeling-control pairing in a pseudorandom fashion. The MRF framework has also been extended to characterize the properties associated with the microvascular network. In [147], the authors adapted the MRF to measure BVf, mean vessel radius and StO_2. We will return to this in a next section.

2.4.1.2 Simulations

The original implementation of MRF used a simple Bloch simulation of a single isochromat (i.e. spin) [137]. This approximation is very fast, but becomes inaccurate in the presence of inhomogeneities of B_0 inside the voxel that cause dephasing. To take this gradient dephasing into consideration, the Bloch model can be extended by averaging over an ensemble of spins, but this is computationally expensive and still an approximation. The extended phase graph (EPG) model [148] is an alternative approach that has been used previously in fast image with steady precession (FISP) signal simulations [142]. The EPG method describes the spin system as several discrete configuration states using the FT. This provides more accurate signal evolution compared to Bloch simulation when the spin system is affected by inhomogeneous magnetic fields.

The challenge for simulation tools is generally the balance between complexity and time, since in MRF, we observed that the number of simulations is of the order of 10^5-10^6 (10-100 values per parameters). For GPU implementation, the snapMRF tool (fully parallel EPG) allows the simulation of 10^5 signals in less than 10 seconds [149]. In CPU implementations, EPG-X [150] and PnP-MRF [151] tools allow the simulation of the same 10^5 signals in 10^4 and 10^2 seconds [149].

2.4.1.3 Quantification

To estimate the parameters of interest, a large database, referred to as a *dictionary*, and containing a large number of possible signal evolutions, is simulated using the introduced biophysical model for a pseudorandomized acquisition (figure 2.25 D). The simulated dictionary is noted $\mathcal{D}_f$, where f is the model. A search is performed by comparing one acquired signal $\mathbf{y}_{\text{obs}}$ and all the simulated signals $\mathbf{y} = f(\mathbf{x})$ in the dictionary to find the best match according to an objective function $\mathrm{d}(\cdot, \cdot)$, usually a standard distance or dissimilarity measure (e.g. in MRF, the dot product). The tissue parameters are then estimated as the combination of parameter values $\mathbf{x}$ that generated the best signal

evolution match (figure 2.25 E), i.e. that minimizes the objective function:

$$\hat{\mathbf{x}} = \underset{\mathbf{x} \in \mathcal{D}_f}{\arg\min}\, \mathrm{d}(\mathbf{y}_{\mathrm{obs}}, f(\mathbf{x})). \tag{2.32}$$

Because, this data processing is particularly robust to high noise levels, its combination with the highly spatially undersampled data acquisition enables the fast acquisition of multiple parameters (figure 2.25 G) [137]. Additionally, the simulation can include the contribution of system imperfections (e.g. B_0 inhomogeneities) and thus overcome this bias during quantification. Together, these aspects of MRF contributed to the attractiveness of the framework for quantitative MRI and we will see how this framework has evolved.

2.4.2 Vascular MRF

Christen et al. have shown the possibility of applying MRF to directly quantify BVf, mean vessel radius and StO_2 [147]. The authors called this framework vascular magnetic resonance fingerprinting. We propose to reproduce the previous figure 2.25 for vascular MRF in figure 2.26 in order to illustrate similarities and differences.

2.4.2.1 Acquisition sequence

In this work, the full MGEFIDSE signal samples were exploited compared to the classic CEF approach introduced in section 2.3.4, which only used the samples before the 180° RF pulse and the spin echo sample. Authors proposed to use the ratio of the pre- and post-USPIO injection MGEFIDSE signal evolutions (section 2.3.4) as the fingerprint, which reduced the effect of B_0 inhomogeneities and T_2's effect on signals (figure 2.26 A). For the moment, no other sequences have been used in vascular MRF.

The MRF implementation to vascular signals required more sophisticated simulation tools than Bloch's equations that are used for relaxation times related works.

2.4.2.2 Simulations

Using Bloch's equations as a simulation model, the magnetization is homogeneous within the voxel since the voxel itself is characterized by a single T_1 and a single T_2 values, and placed into a constant magnetic field (figure 2.27(a)). For vascular MRF applications, the voxel needs to be segmented into a vascular compartment and an extravascular compartment, which results in an inhomogeneous magnetization through the voxel

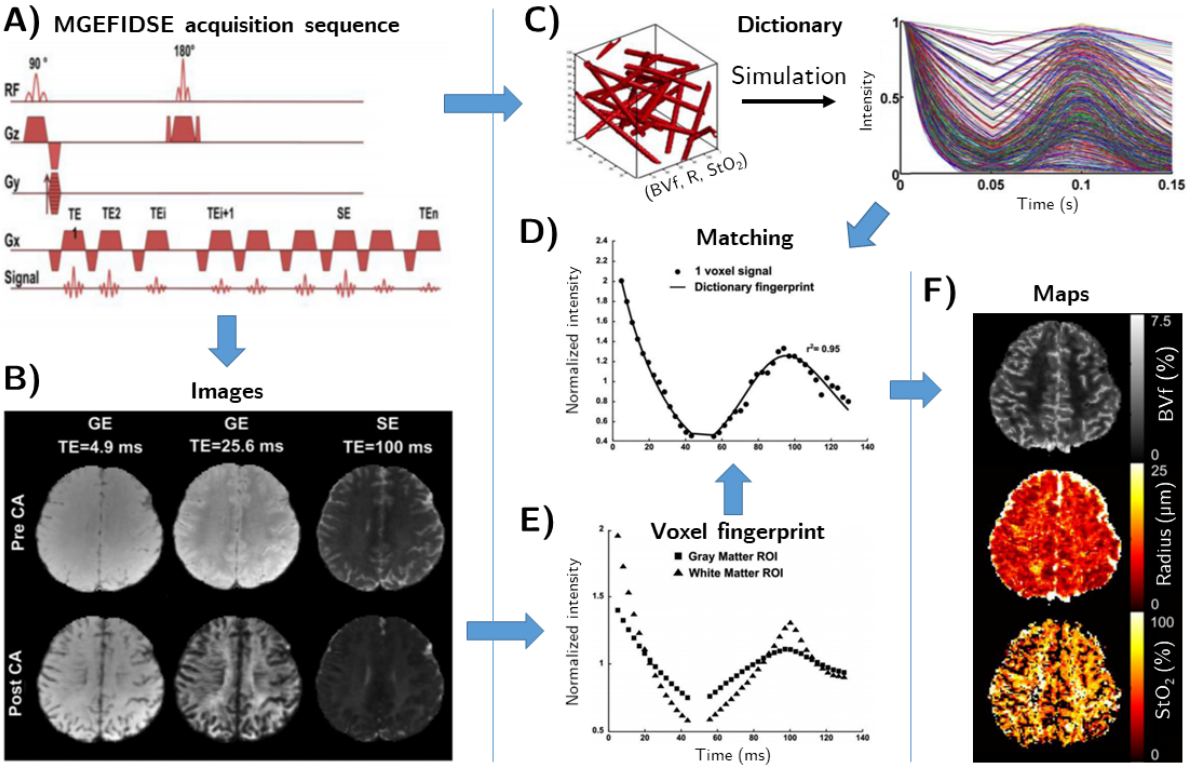

Figure 2.26 – Illustration of the vascular MRF method, inspired by [138] and composed with images from [147].
The flowchart shows an overview of the vascular MRF framework as used for MGEFIDSE pre- and post-USPIO contrast agent acquisitions. (A) MGEFIDSE sequence. (B) Three images acquired in different TE and pre/post-USPIO injection. (C) Typical virtual voxel used for simulation of the dictionary signals. (D) Pattern matching of the voxel fingerprint with the closest entry in the dictionary, which allows to retrieve the tissue features represented by that voxel. (E) Normalized intensity variation of two ROI across the images. (F) Parameter maps obtained by repeating the matching process for each voxel.

(figure 2.27(b)). The complexity of the task calls for more sophisticated simulation tools than those based on Bloch's equations only.

Such a tool has been developed by Pannetier et al. [152]. This particularly complete tool accounts for the intrinsic relaxations, the magnetic field perturbations induced by susceptibility interfaces (vessels), the diffusion of the water protons and the compartmentalization of the contrast agent within the vessels (figure 2.27(c)). The resulting model can be used to produce signals considering a large number of input parameters. Some of the input parameters of the model are reported in figure 2.27(c). This simulation tool opens the possibility of simultaneously quantifying T_1, T_2, ADC, BVf, VSI and StO_2 but this would probably require the optimization of a new sequence sensitive to all these parameters.

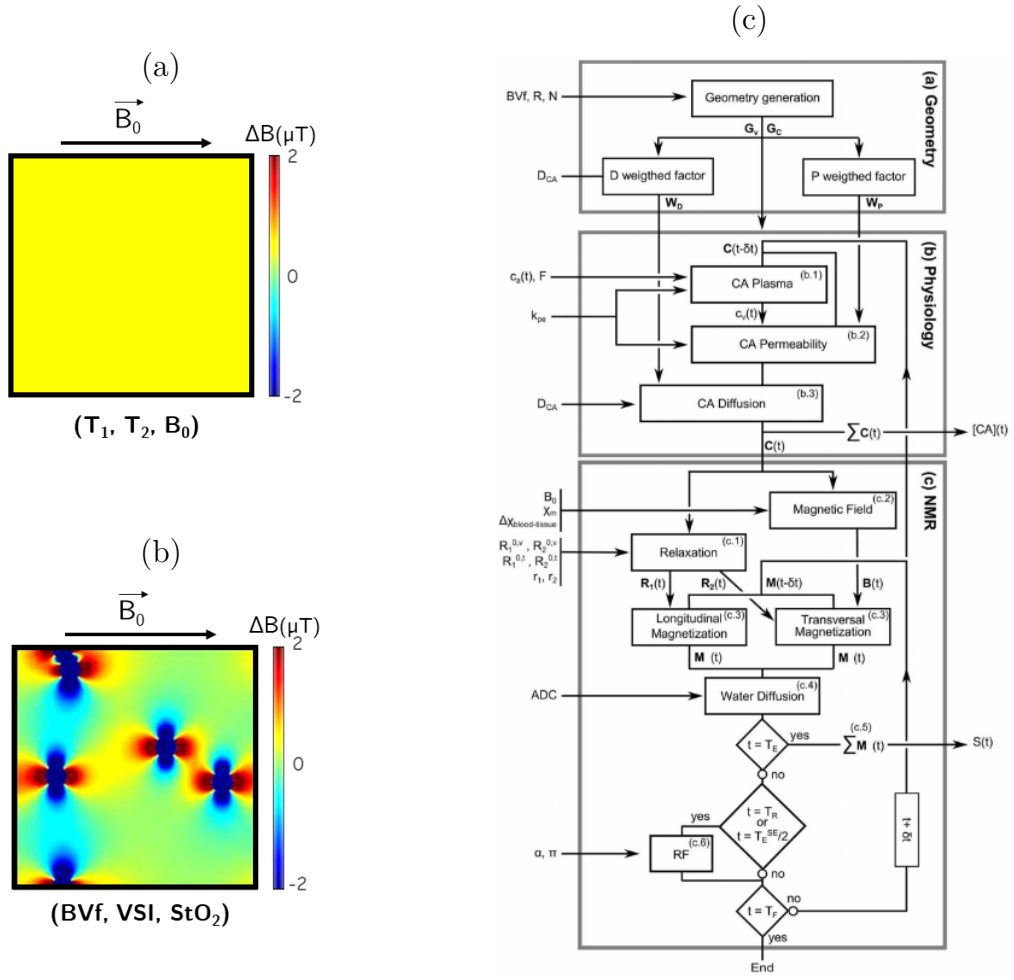

Figure 2.27 – Sketch of the simulation algorithm, adapted from [152].
(a) Typical magnetization in a pixel using Bloch's equations. (b) Typical magnetization in a pixel using the vascular simulation tool. (c) Sketch of the simulation algorithm. In (c), only the most important parameters have been represented. Data on the left of the gray boxes are inputs to the model. Data on the right are outputs of the simulation. The simulation is organized in three blocks. Geometry block initializes the geometry. Physiology block describes the contrast agent behavior over time. NMR block estimates the MR signal.

In this version of vascular MRF, a dictionary was designed based on relatively simplistic models for blood vessels and oxygen distribution (figure 2.26 C). Specifically, the authors modeled the blood vessels as straight cylinders, with no preferential directions, and with uniform oxygenation across the network, similar to those used in classic approach's mathematical models. In addition, the image volume is reduced to a 2-dimensional plane. A major improvement on vascular MRF can be to take greater heterogeneity into account to increase the vascular characterization in a 3-dimensional volume. This process would

certainly even overcome the proposed vascular MRF implementation as it has been shown by [153]. In this work, authors used real mouse angiograms and physiological values as the substrate for the MR simulations. However, the generation of a dictionary for each mouse angiogram took 70 hours on a computer cluster [153].

The consequence of using this simulation tool is that the simulation times are considerably increased compared to Bloch simulation. For vascular MRF, authors report that a single signal simulation took about 2.5 seconds on a desktop computer and the largest dictionary of the study, composed of about 1 150 000 entries, was generated on a 30-node cluster in about 24 hours [154] (about 8-9 days with a 4-core computer). Compared to the CPU implementation of the PnP-MRF tool on a desktop computer, it took about 75 times longer on a cluster. The processing of this amount of data is already almost impossible on a desktop computer and the addition of a single parameter would make the study impossible even on high-performance hardware.

At this point, we understand that the simulation constraints are very different between the two MRF applications. For simple simulations, the stakes of standard MRF only consist in managing the large volume of data simulated during quantification (i.e. time and memory), whereas in vascular MRF, the simulation time is already a concern.

2.4.2.3 Quantification

Concerning quantification, the procedure remains the same as the one of standard MRF. The parameter values that generate the vascular signal that minimizes the equation (2.32) is used as estimate (figure 2.26 D).

While it has not been clearly shown that the vascular MRF method can improve estimates on BVf and mean radius, this is mainly due to the lack of a validation solution. It is most likely that the use of all signal samples should provide this improvement. What is certain is that the method allows, in addition to BVf and mean radius, the quantification of StO_2, which is achieved by acquiring other sequences using CEF method. This results in a reduction of the scan time. The main limit to be addressed to extend the vascular MRF and quantify more parameters and/or acquire longer sequences, is the extensive simulation times. An acceleration of the simulation tool can be considered (out of the scope of this work) but one could also investigate the optimization of the reconstruction methods in order to reduce the need for dictionary entries, i.e. for simulations.

2.4.3 Evolution of MRF quantification methods

In this section, we first summarize introduced quantitative MRI workflows. Then, we briefly review the progress achieved in MRF quantification.

Prior to the voxel-by-voxel CEF quantification, data are derived from fully (or at least sufficiently sampled) acquired k-space data. Then signal evolutions are fitted with a biophysical model, see figure 2.28(a). The MRF quantification, was introduced as an alternative to least squares fitting approach and thereby allows the use of more sophisticated models via matching procedure. As CEF, the MRF quantification is a voxel-by-voxel quantification performed after FT and considering complex-valued signals. The MRF requires a dictionary to perform quantification, which is why we named the MRF quantification methods *dictionary-based methods*. The dictionary $\mathcal{D}_f$ is composed of N entries of coupled S-sample fingerprint and P-dimensional parameters $(\mathbf{x}, \mathbf{y})$. The $\{\mathbf{y}_1, \ldots, \mathbf{y}_N\}$ are generated by running a simulation model f for N different values of the magnetic and physiological parameters $\{\mathbf{x}_1, \ldots, \mathbf{x}_N\}$.

In the original dictionary-based matching (DBM) method, a grid is generated with sampled values in a pre-set interval for each parameter. The dimension of the grid corresponds to the number of parameters. Then, to invert an observed $\mathbf{y}_{\text{obs}}$, it is compared with the signals in $\mathcal{D}_f$ to find the best match according to the objective function $\mathrm{d}(\cdot, \cdot)$. With $\mathcal{D}_f = \{(\mathbf{x}_n, \mathbf{y}_n = f(\mathbf{x}_n)),\, n = 1{:}N\}$, $\mathbf{x}$ is thus estimated as the argument of the minimization introduced in equation (2.32). Solutions are sought within the discrete $\mathcal{D}_f$ only, while in non-constrained optimization, the minimization is performed by considering the whole continuous space of parameter values. This DBM method is in particular suitable for highly noisy and artifacted data, which means that one can undersample the k-space during the acquisition, see figure 2.28(b). The performance of the DBM method directly depends on the space discretization, i.e. the choice of the number of dictionary entries and the number of parameters. The larger the number N of entry $(\mathbf{x}_n, \mathbf{y}_n)$, the more accurate the estimates but the larger the simulation time to produce the dictionary and the memory requirement to store the dictionary. Even for a moderate number of parameters, the required number of elements in the dictionary renders grid search intractable on a desktop computer.

Additionally, each new $\mathbf{y}_{\text{obs}}$ requires the computation and comparison of N matching scores $\mathrm{d}(\mathbf{y}_{\text{obs}}, \mathbf{y}_n)$. This can be costly if N is very large and if many inversions are desired (e.g. many voxels). When the dictionary is large, this might be problematic for storage and memory. Another issue is that the exhaustive matching process, when coupled with a large dictionary, can take too much time to compute. However, as spatial undersampling

artifacts from a highly accelerated MRF scan can be severe, it is advantageous to develop methods that bypass these limitations, preserve the main advantages of MRF and handle these artifacts without sacrificing acquisition speed. Different works proposed the use of singular value decomposition (SVD) to compress the dictionary and thus reduce its size in the time dimension of fingerprints [156]. It was also proposed to project the dictionary in smaller subspaces mainly to speed-up quantification [157–159]. However, the calculation of the SVD can be difficult on a desktop computer when the dictionary is very large. A randomized SVD approach can be applied to approximate the singular vectors of the dictionary in this case [160], but this decreases the accuracy of the estimates. Since the pattern matching used to find the best dictionary match is exhaustive, a group matching strategy was proposed in [161]. All these accelerated DBM methods, e.g. compressed dictionary, group matching, etc., belong to the workflow (figure 2.28(b)). Iterative

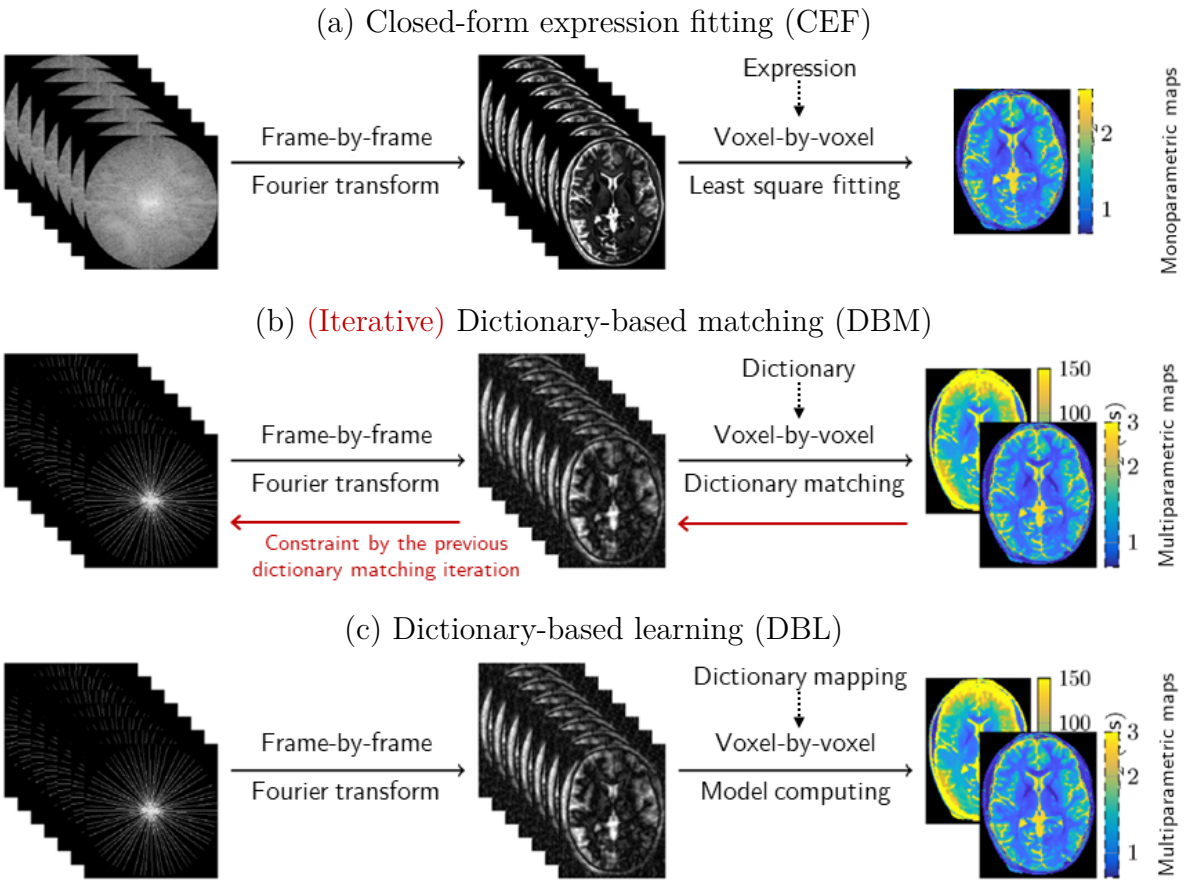

Figure 2.28 – Comparison of the different quantification methods in quantitative MRI, freely adapted from [155].
(a) Closed-from expression fitting (CEF). (b) Dictionary-based matching (DBM). (c) Dictionary-based learning (DBL).

DBM methods have also been proposed [157, 162–164] to push toward the solving of the optimization problem, which has improved estimation performance. Note that the first iteration of these methods is strictly equivalent to the standard DBM [164].

Other works, including us, have decided to take an alternative strategy by directly learning the mappings between the tissue property and the signal evolution. The compact representation of the mapping and the quantification speed allow these methods to overcome previous constraints associated with large dictionaries. In return, an additional (exhaustive) procedure is required. However, the learning is done only once and the mapping can be reused for each new inversion. Mappings were approximated by machine learning approaches, usually neural networks. Different architectures have been proposed using either fully connected [165] or convolutional networks [166, 167]. We refer to these methods as dictionary-based learning (DBL) methods, see figure 2.28(c). A non-exhaustive summary of different DBM and DBL methods for MRF can be found in table 2.4. For each work, we first describe the experiment conditions, i.e. sequence, parameters and the number of dictionary entries. Then, we report when possible the performance gains in quantification time, storage memory and estimate accuracy. Note that the parameter M_0 (proton density) is not mentioned in the table because this parameter is not obtained using a dictionary but by a simple computation of the signal norm.

Beyond fast matching strategies, few works have focused on reducing the number of dictionary entries required for accurate quantification of tissue properties. In DBM, a coarse version of the dictionary in the tissue property dimension was used, meaning that the step size in properties such as T_1 and T_2 is relatively large [160]. Pattern matching was first performed using the coarse dictionary. The dictionary was projected to a low-rank subspace where a polynomial interpolation was applied to determine more accurate T_1 and T_2 values. By applying interpolation to the coarse dictionary, the coarse discretization of the tissue properties can be circumvented. A similar idea was proposed in [159], using linear interpolation between dictionary entries to overcome the large dictionary step size during quantification. In DBL, models allow a continuous representation of values by approximating the mapping between signal and the parameter spaces. Yet, among DBL works, Cohen et al. [165] is the only one to investigate the impact of the sampling density of the parameter space. We suspect that works to reduce the number of dictionary entries have not yet emerged because the current performance of simulation tools for the most commonly used sequences in MRF (bSSFP, FISP) allows very fast dictionary generation. We understand that the numerical simulations in

	Ref & Focus	Dictionary			Performance gains		
		N	S	P	Time	Memory	Accuracy
DBM	[161] Group matching for accelerating quantification	196 000	1 000 (FISP)	3 (T_1,T_2,ΔB_0)	70	1	0.98
	[156] Dictionary compression to speed up the pattern recognition algorithm	363 624	1 000 (bSSFP)	3 (T_1,T_2,ΔB_0)	3.4	5	≈ 0.99 $\approx 0.78^{(n)}$
		10 169	1 500 (FISP)	2 (T_1,T_2)	4.8	60	≈ 1
	[160] Tractable dictionary compression in large scale problems and polynomial dictionary fitting for increased accuracy	3 312 coarse: 119	500 (bSSFP)	3 (T_1,T_2,ΔB_0)			0.82
		5 970 coarse: 1 585	3 000 (FISP)	2 (T_1,T_2)			0.97
	[157] Low-rank alternating directions method of multipliers quantification	24 921	841 (pSSFP)	2 (T_1,T_2)	12		
DBL	[165] Fully connected NN for fast, accurate and robust to noise quantification	79 900	600 (FISP)	2 (T_1,T_2)	5 000		1 $1.3^{(n)}$
		1 150	600 (FISP)	2 (T_1,T_2)			3 $1.1^{(n)}$
	[168] Complex-valued NN for more accuracy than real-valued NN	100 000	500 (bSSFP)	3 (T_1,T_2,ΔB_0)	20		5.8 $1.2^{(n)}$
	2-channel real/imaginary				70		3.1 $1.2^{(n)}$
	[166] Convolutional NN to overcome time and storage limitations	8 750	3 000 (FISP)	2 (T_1,T_2)	30 GPU: 100	105	
	[169] Noise addition and random parameter space sampling for optimal NN training in high parameter dimension	396 550	1 000 (bSSFP B_1)	4 (T_1,T_2, ΔB_0,B_1^+)	40		5.2
		164 475	1 000 (FISP B_1)	3 (T_1,T_2,B_1^+)	11		4

Table 2.4 – Overview of MRF quantification methods.
The focus of each work is summarized and the dictionary design is then provided i.e. number of dictionary entries N of S-sample signal and P-parameter combinations, and the MR sequence. Performance gains are the quantification time acceleration, reduction of memory requirement and estimation accuracy. $\approx$ indicate coarse approximations from figures, other values have been extracted directly or computed from the results provided in papers. Note that gains >1 (resp. <1) indicate increased (resp. reduced) performance. $^{(n)}$ indicates accuracy gains on noisy data. Abbreviations: ΔB_0: static field inhomogeneity, B_1^+: B_1 excitation RF field.

vascular MRF are specifically computationally expensive, but a compact and accurate fingerprint representation is of key importance in MRF. In [165], authors reduced the initial dictionary density (69 000 entries and 2 parameters) from 2 to 60 fold, see the impact on estimate errors in figure 2.29. Using noiseless signals, the NN is more robust to the decreased dictionary density than DBM, the ratio of root mean square errors (RMSE) obtained using $1/2^{\text{th}}$ and $1/60^{\text{th}}$ of the dictionary entries, are 6 for T_1 and 4.5 for T_2, while for DBM the ratio are 14.6 for T_1 and 11.3. Using 1 % noise level corrupted signals, the NN ratio are 1.6 for T_1 and 1.1 for T_2 and the DBM ratio are 1.2 for T_1 and 1.1 for T_2. These results therefore suggest that DBL methods are more promising than the standard DBM approach for reducing the size of the dictionary.

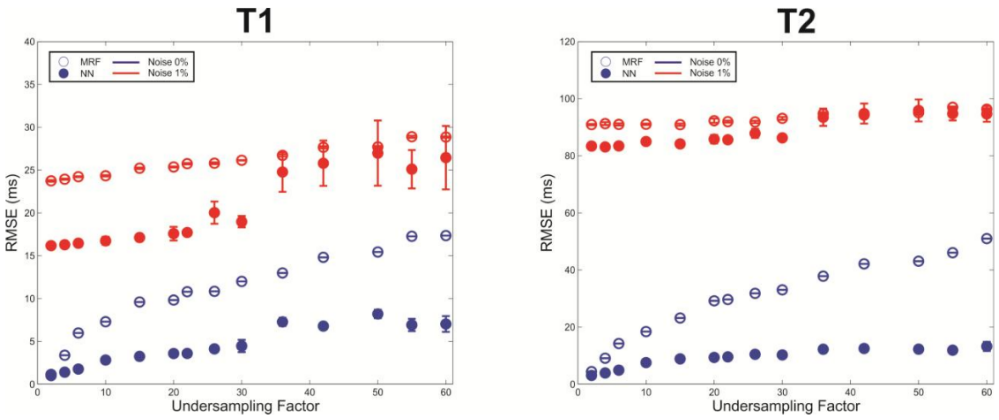

Figure 2.29 – Impact of dictionary reduction on T_1 and T_2 MRF estimation accuracy, adapted from [165].
RMSE of the MRF dictionary matching (open circles) and NN quantification (closed circles) for the different undersampling factors and noise levels tested. For the noiseless acquisition (blue curves) the error in the NN quantification was 2 fold smaller for T_1 and 4 fold smaller for T_2 at the largest undersampling factor tested. For the noisy acquisition (red curves) only tissues with $T_2 > 11$ ms were included in the error calculation for the MRF dictionary matching whereas all tissues were included in the NN quantification error. Nevertheless, the NN quantification error was still smaller or equal to the MRF error for all undersampling factors tested.

By considering the latest developments in MRF quantification, one can improve the estimation relying on MRF quantification methods that require less dictionary entries to perform accurate and fast estimation. Accuracy appears to be achievable through continuous data representation, spatial considerations and complex-valued data processing. Compression or learning of the dictionary seems to be the most effective approach to limit extensive quantification time and excessive memory requirements. To optimize and implement MRF in large scale or in time-consuming simulation (e.g. vascular), it is

therefore required to design a method that maintains a good parameter quantification accuracy but reduces significantly the number of dictionary entries. However, very few works address this issue.

2.5 Challenges and requirements

The main stake of this thesis is to develop an MRI acquisition and data processing protocol for the identification and characterization of MRI changes induced by an epileptic condition in an experimental animal model.

We decided to work with two kainate-induced status epilepticus models. The first model, induced by intraperitoneal kainate injection, is easier to produce and allows the imaging of animals early after status epilepticus. To investigate the early modifications, the animals may be imaged over time (typically, from 24 hours to 1 week). The second model, induced by intrahippocampal kainate injection, is less variable in its expression and causes an hippocampal sclerosis, which allows the investigation of chronic condition, after the emergence of spontaneous seizures. Again, animals may be imaged over time to characterize the epileptogenesis period and, at least 4 weeks after injection, to characterize the period when chronic seizure occurs. The validation of the epileptic condition can be done early by identifying the symptoms (automatisms and a catatonic posture, myoclonic twitching of the head, forelimbs and rearlimbs) a few hours after injection, i.e. during status epilepticus. One can also identify specific EEG patterns or hippocampal sclerosis on anatomical MRI images for the intrahippocampal injection model.

Both cellular and vascular MRI parameter changes have been reported, among these parameters, relaxation times T_1 and T_2, diffusion, perfusion, vascular density, and BBB leakage. However, most of the MRI vascular findings are related to large vessel while changes at the capillary levels have only been reported using *ex vivo* imaging or resection tissues in patients. One can add to the well-documented cellular protocols, acquisitions with iron oxide based contrast agents to determine the fraction of blood volume as well as the size of the capillaries, as observed using histology. Concerning the BBB integrity, MRI findings were obtained after long gadolinium infusion. One can also investigate imaging changes in BBB permeability by injecting a bolus of gadolinium to reduce acquisition time and perform the acquisitions necessary for the quantification of all the parameters in a time compatible with the duration of animal anesthesia, i.e. less than two hours.

As small variations of these parameters are expected, methodological developments for the processing are conducted in parallel. The MRF approach promises to provide better accuracy in estimating parameters and thus facilitate the detection of small changes and this point has to be confirmed. The objective is to develop a method that allows the accuracy of very fine grids to be achieved with no more than a few hours of simulations for the dictionary, i.e. in vascular MRF, about 10^4 signals. To be viable, the method should

provide a reconstruction of a multi-slice acquisition (about 10^6 voxels) in a few minutes on a desktop computer. The method must preserve as much as possible the advantages of MRF, i.e. robustness to thermal noise and undersampling artifacts, flexibility and ease of use, etc.

With these objectives in mind, we therefore performed MRI experiments on epileptic mouse models and develop MRF methods in parallel. MRI Data were analyzed using the existing and the proposed methods, as developed in the next chapters.

Chapter 3

Bayesian inverse regression for vascular MRF quantification

To reach a good accuracy, the matching MRF quantification requires an informative dictionary whose cost, in terms of design, storage and exploration, is rapidly prohibitive for even moderate numbers of parameters. In this study, we develop a robust and scalable multi-parametric dictionary-based reconstruction to measure vascular parameters. Our proposed method is compared to MRF matching on two types of synthetic signals: scalable and vascular MRF signals. A manuscript has been submitted to the journal *IEEE Transactions on Medical Imaging* [170]. Here the manuscript has been adapted.

3.1 Introduction

Magnetic resonance fingerprinting (MRF) is a novel approach to quantitative magnetic resonance imaging that allows the estimation of multiple tissue properties in a single acquisition [137, 171]. The acquisition, which consists in repeating measurements with varying experimental conditions, generates a signal evolution (or *fingerprint*) that depends on the parameters of the studied tissue. To estimate these parameters, a large database, referred to as a *dictionary* and containing a large number of possible signal evolutions, is simulated from biophysical models. A comparison is performed between an acquired signal and the signals in the dictionary to find the best match according to an objective function. The tissue parameters are then estimated to the values that generated the best signal evolution match. In MRF, parameter estimation accuracy therefore depends on the number of dictionary entries, which increases exponentially with the number of parameters. For applications with many parameters such as vascular MRF [147], the

required memory size and simulation time as well as the parameter estimation time (or quantification time) quickly become a limit.

To compress the dictionary while limiting the loss of information, several authors have used singular value decomposition to project the dictionary in a well-chosen subspace [156–161]. However, this compression procedure generally decreases parameter accuracy. It has also been proposed to directly find a mapping from the fingerprints to the parameter space using kernel regression [172] or neural network approaches [165–169, 173–175]. The resulting compact representation offers the advantage over the discrete MRF grid of a continuous exploration of parameter values. These approaches significantly reduce the quantification time, but not the simulation time due to the need to span a high dimensional fingerprint space. To limit the simulation time, Cohen et al. [165] studied a mapping obtained from a sparse set of dictionary entries. The study, carried out with only two parameters, led to a modest reduction of dictionary entries (up to 60). Consider a dictionary of 10×10 entries simulated in 1 hour. If the number of parameters increases from 2 to 7 parameters, and always considering 10 values per parameter, then the dictionary computation time increases from 1 hour to more than 11 years. In this case, an approach that greatly reduces the need for simulation, continuously represents the parameters without loss of precision, relies on an explainable model and reduces the quantification time becomes highly desirable [9].

To reach this goal, we adopt in this work a mapping approach that circumvents the difficulty of learning a *high-to-low* mapping from a high dimensional fingerprint space to a low dimensional parameter space, learning instead the much less problematic *low-to-high* reverse mapping from parameters to fingerprints. More specifically, we use the Gaussian locally linear mapping (GLLiM) model [176], which allows both a tractable learning of the low-to-high mapping and a subsequent analytical expression of the high-to-low or signal-to-parameter mapping. Furthermore, unlike most other regression methods that focus on pointwise predictions, GLLiM provides a full posterior distribution per fingerprint. This distribution can then be used to compute an estimated value and a confidence index for each parameter, using respectively the posterior expectation and standard deviation.

In this vascular MRF study, the proposed dictionary-based learning (DBL) method and the standard dictionary-based matching (DBM) method are compared. Synthetic scalable signals are first used to assess quantitatively the methods' performance while increasing the number of parameters. Vascular MRF signals are then considered both through simulations and real data acquired in tumor bearing rats.

3.2 MRF as an inverse problem

In inverse problems, the overall issue is to provide information on some parameters of interest $\mathbf{x}$ given an observed signal $\mathbf{y}$, using a known *direct* or *forward model* that describes how the parameters $\mathbf{x}$ translate into a signal $\mathbf{y}$ (figure 3.1). Among inverse problems, MRF exhibits the following difficulties: 1) the direct model is (highly) non-linear, as a (complex) series of equations or simulation tools; 2) the $\mathbf{y}$'s are high-dimensional signals and 3) many $\mathbf{y}$'s need to be inverted (one for each voxel in an image); 4) the vector of parameters $\mathbf{x}$ is multidimensional and predicting each component of $\mathbf{x}$ independently is likely to be sub-optimal.

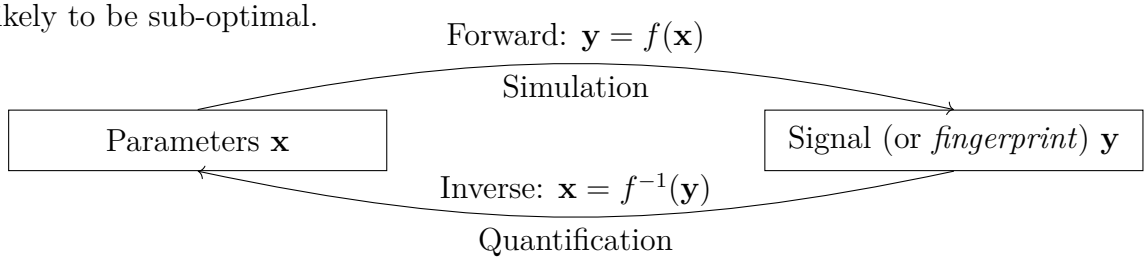

Figure 3.1 – Magnetic resonance fingerprinting as an inverse problem.

To account for possible sources of uncertainty, we focus on a statistical modeling assuming that the forward model is described by a likelihood and a prior distribution. The likelihood function is linking parameter values $\mathbf{x}$ to a probability of observing signal $\mathbf{y}$, $\mathcal{L}_{\mathbf{x}}(\mathbf{y}) = p(\mathbf{y}|\mathbf{x})$. A natural assumption is that $\mathcal{L}_{\mathbf{x}}(\mathbf{y})$ is a Gaussian distribution $\mathcal{N}(\mathbf{y}; f(\mathbf{x}), \mathbf{\Sigma})$ centered at $f(\mathbf{x})$ where f is the known simulation function that links the physical and physiological parameters to the fingerprint and $\mathbf{\Sigma}$ is a covariance matrix accounting for measuring or modeling imperfections. The parameter prior distribution, denoted by $p(\mathbf{x})$, encodes in turns information on the possible parameter values. Standard MRF uses a finite grid of values, which corresponds to a very particular discrete prior. This probabilistic point of view allows, with the Bayesian framework, to derive a posterior distribution $p(\mathbf{x}|\mathbf{y}) = p(\mathbf{y}|\mathbf{x})p(\mathbf{x})/p(\mathbf{y})$, which provides for any given $\mathbf{y}$, a characterization of $\mathbf{x}$ by a probability density function more informative than a single point prediction of $\mathbf{x}$. It corresponds to a richer inverse model but is not usually available in closed-form and requires approximations to be usable in practice.

More generally, most methods to solve inverse problems can be classified into two main categories, optimization-based and learning-based methods. In the next section, we refer to standard MRF as a matching method. We show that it can be seen as a penalized optimization, which does not require statistical modeling, while the method we propose next belongs to statistical learning approaches.

3.2.1 Dictionary-based matching (DBM) method

MRF requires a large database $\mathcal{D}_f$, referred to as a dictionary [137]. It is made of N entries of coupled fingerprint and parameters $(\mathbf{x}, \mathbf{y})$. The S-dimensional fingerprints $\{\mathbf{y}_1, \ldots, \mathbf{y}_N\}$ are generated by running the simulation model f for N different values of the P-dimensional magnetic and physiological parameters $\{\mathbf{x}_1, \ldots, \mathbf{x}_N\}$. In the DBM method, a P-dimensional grid is generated with sampled values in a pre-set interval for each parameter. Then, to invert an observed $\mathbf{y}_{\text{obs}}$, it is compared with the signals in $\mathcal{D}_f$ to find the best match according to an objective function $\mathrm{d}(\cdot, \cdot)$, usually a standard distance or dissimilarity measure (e.g. in MRF, the dot product). With $\mathcal{D}_f = \{(\mathbf{x}_n, \mathbf{y}_n = f(\mathbf{x}_n)),\ n = 1{:}N\}$, $\mathbf{x}$ is thus estimated as the argument of the following minimization:

$$\hat{\mathbf{x}} = \underset{\mathbf{x} \in \mathcal{D}_f}{\arg\min}\ \mathrm{d}(\mathbf{y}_{\text{obs}}, f(\mathbf{x}))\,. \tag{3.1}$$

Solutions are sought in $\mathcal{D}_f$ only, while in a non-constrained optimization the minimization is over the whole continuous space of parameter values. The performance of the method depends directly on the space discretization, i.e. the choice of the number of dictionary entries and the number of parameters. The larger the number N of entry $(\mathbf{x}_n, \mathbf{y}_n)$, the more accurate the estimates but the larger the simulation time and memory requirement. Even for moderate number of parameters, the required number of elements in the dictionary renders grid search intractable on a desktop computer. In addition, each new $\mathbf{y}_{\text{obs}}$, requires the computation and comparison of N matching scores $\mathrm{d}(\mathbf{y}_{\text{obs}}, \mathbf{y}_n)$, which can be costly if N is very large and if many inversions are desired. The regression or learning method that we propose in the next section is more efficient with respect to these aspects.

3.2.2 Proposed dictionary-based learning (DBL) method

In contrast to the DBM method, regression and learning methods can adapt to handle massive inversions of high dimensional data. The main principle is to transfer the computational cost, from 2-signal matchings to the learning of an inverse operator $\mathcal{F}^{-1}$. Equivalently, the goal is to learn a mapping from the fingerprint space to the parameter space, for any $\mathbf{y}$, with cost-less evaluation of $\mathcal{F}^{-1}(\mathbf{y})$. The dictionary $\mathcal{D}_f$ can be used to estimate $\mathcal{F}^{-1}$. Learning or regression methods adapted to high dimensions include inverse regression methods, i.e. sliced inverse regression [177], partial least squares [178], approaches based on mixtures of regressions with different variants, e.g. Gaussian locally linear mapping (GLLiM) [176], mixtures of experts [179], cluster weighted models [180],

and kernel methods [172]. Inverse regression methods are flexible in that they reduce the dimension in a way optimal to the subsequent mapping estimation task that can itself be carried out by any kind of standard regression tool. In that sense, the inverse regression methods are said to be non-parametric or semi-parametric. Similarly, in [172], the authors propose a regression with an appropriate kernel function to learn the non-linear mapping. The procedure has the advantage to be semi-parametric but a serious limit is that the components of f are optimized in each dimension separately. As regards application to MRF, the learning strategy has also been proposed by several groups using deep learning tools [165–169, 173–175]. A major limitation of these methods is that they require a large number of training points to learn many model parameters without overfitting.

In the same vein as [172], and in contrast to deep learning approaches, we propose to use the GLLiM method that exploits Gaussian mixture models [176]. Compared to other regression methods that focus on providing point-wise estimates, GLLiM provides a full probability distribution selected in a family of parametric models, e.g. mixture of Gaussian distributions, where the parameters are denoted by $\boldsymbol{\theta}$. The inversion operator is defined as $\mathcal{F}^{-1}(\mathbf{y}) = p(\mathbf{x}|\mathbf{y};\boldsymbol{\theta})$, where $\boldsymbol{\theta}$ is estimated from the dictionary. More specifically, GLLiM handles the modeling of non-linear relationships with a piecewise linear model. Each $\mathbf{y}$ is seen as the noisy image of $\mathbf{x}$ obtained from a K-component mixture of affine transformations. This is modeled by introducing a latent variable $z \in \{1, \dots, K\}$ such that

$$\mathbf{y} = \sum_{k=1}^{K} \delta_k(z) \left(\boldsymbol{A}_k \mathbf{x} + \boldsymbol{b}_k + \boldsymbol{\epsilon}_k\right), \tag{3.2}$$

where $\delta_k(z)$ indicates membership in the region k of $\mathbf{x}$, having the value 1 if it belongs to the region and the value 0 otherwise. $\boldsymbol{A}_k$ is a $P \times S$ matrix and $\boldsymbol{b}_k$ a vector in $\mathbb{R}^P$ that characterize an affine transformation. Variable $\boldsymbol{\epsilon}_k$ corresponds to an error term in $\mathbb{R}^P$ which is assumed to be zero-mean and not correlated with $\mathbf{x}$, capturing both the modeling noise and the quantification error due to the affine approximations. In GLLiM, $\boldsymbol{\epsilon}_k$ follows a Gaussian distribution $\mathcal{N}(\mathbf{0}, \boldsymbol{\Sigma}_k)$ and $\mathbf{x}$ follows a mixture of K Gaussian distributions defined by $p(\mathbf{x}|z=k) = \mathcal{N}(\mathbf{x}; \boldsymbol{c}_k, \boldsymbol{\Gamma}_k)$, and $p(z=k) = \pi_k$. It follows that

$$p(\mathbf{y}|\mathbf{x};\boldsymbol{\theta}) = \sum_{k=1}^{K} w_k(\mathbf{x})\, \mathcal{N}(\mathbf{y}; \boldsymbol{A}_k\mathbf{x} + \boldsymbol{b}_k, \boldsymbol{\Sigma}_k), \tag{3.3}$$
$$\text{with } w_k(\mathbf{x}) = \frac{\pi_k\, \mathcal{N}(\mathbf{x}; \boldsymbol{c}_k, \boldsymbol{\Gamma}_k)}{\sum_{j=1}^{K} \pi_j\, \mathcal{N}(\mathbf{x}; \boldsymbol{c}_j, \boldsymbol{\Gamma}_j)},$$

and $\boldsymbol{\theta} = \{\pi_k, \boldsymbol{c}_k, \boldsymbol{\Gamma}_k, \boldsymbol{A}_k, \boldsymbol{b}_k, \boldsymbol{\Sigma}_k\}_{k=1:K}$ is the set of parameters defining the model. The conditional probability distribution of interest can be derived as

$$p(\mathbf{x}|\mathbf{y};\boldsymbol{\theta}) = \sum_{k=1}^{K} w_k^*(\mathbf{y})\,\mathcal{N}(\mathbf{x};\boldsymbol{A}_k^*\mathbf{y}+\boldsymbol{b}_k^*,\boldsymbol{\Sigma}_k^*)\,, \tag{3.4}$$
$$\text{with } w_k^*(\mathbf{y}) = \frac{\pi_k\,\mathcal{N}(\mathbf{y};\boldsymbol{c}_k^*,\boldsymbol{\Gamma}_k^*)}{\sum_{j=1}^{K}\pi_j^*\,\mathcal{N}(\mathbf{y};\boldsymbol{c}_j^*,\boldsymbol{\Gamma}_j^*)}\,,$$

and a new parameterization $\boldsymbol{\theta}^* = \{\boldsymbol{c}_k^*, \boldsymbol{\Gamma}_k^*, \boldsymbol{A}_k^*, \boldsymbol{b}_k^*, \boldsymbol{\Sigma}_k^*\}_{k=1:K}$ easily expressed as an analytical function of $\boldsymbol{\theta}$. The mixture setting provides some guaranties that when choosing K large enough it is possible to approximate any reasonable relationship [179]. Automatic model selection criteria can also be used to select K (see [176]).

The $p(\mathbf{x}|\mathbf{y};\boldsymbol{\theta})$ distribution provides both estimates of the parameters $\mathbf{x}$ and information about the confidence to be placed in these estimates. In this work, estimates are defined through the expectation and the confidence indices as the square root of the covariance matrix diagonal element vector:

$$\hat{\mathbf{x}} = \mathbb{E}\left[\mathbf{x}|\mathbf{y};\boldsymbol{\theta}\right], \tag{3.5}$$
$$\text{CI} = \sqrt{\text{diag}\left(\text{Var}\left[\mathbf{x}|\mathbf{y};\boldsymbol{\theta}\right]\right)}, \tag{3.6}$$

with $\mathbb{E}\left[\mathbf{x}|\mathbf{y};\boldsymbol{\theta}\right] = \sum_{k=1}^{K} w_k^*(\mathbf{y})(\boldsymbol{A}_k^*\mathbf{y}+\boldsymbol{b}_k^*)$, and

$$\begin{aligned}\text{Var}\left[\mathbf{x}|\mathbf{y};\boldsymbol{\theta}\right] = &\sum_{k=1}^{K} w_k^*(\mathbf{y})\left[\boldsymbol{\Sigma}_k^* + (\boldsymbol{A}_k^*\mathbf{y}+\boldsymbol{b}_k^*)(\boldsymbol{A}_k^*\mathbf{y}+\boldsymbol{b}_k^*)^T\right]\\ &- \left(\sum_{k=1}^{K} w_k^*(\mathbf{y})(\boldsymbol{A}_k^*\mathbf{y}+\boldsymbol{b}_k^*)\right)\left(\sum_{k=1}^{K} w_k^*(\mathbf{y})(\boldsymbol{A}_k^*\mathbf{y}+\boldsymbol{b}_k^*)\right)^T,\end{aligned}$$

where diag$(\cdot)$ denotes the function returning the diagonal elements of a matrix. For the CI, computed from the estimated posterior $p(\mathbf{x}|\mathbf{y};\boldsymbol{\theta})$, to be a good indicator of the parameter estimation error, it is required that the inverted $\mathbf{y}$ follows the same model used to computed $\boldsymbol{\theta}$. The use of a unique $\boldsymbol{\theta}$ parameter for all inversions provides a great gain when massive inversions are required but it also assumes that the same model is valid for all fingerprints and that the dictionary $\mathcal{D}_f$ is a good representation of them. In practice, acquired fingerprints may come with different noise levels. An interesting feature of GLLiM is to adapt to this case at a very low cost. When the observed $\mathbf{y}$ comes with some covariance matrix $\boldsymbol{\Sigma}_\eta$ corresponding to a centered Gaussian noise variable $\boldsymbol{\eta}$, the initial dictionary $\mathcal{D}_f$ may not be fully adapted if it has not been generated with this same additional measurement error. Another training set should be simulated and used instead, with a corrected likelihood corresponding to $\mathcal{N}(\mathbf{y}; f(\mathbf{x}), \boldsymbol{\Sigma} + \boldsymbol{\Sigma}_\eta)$. Fortunately, it is straightforward to check that the structure of the Gaussian mixture approximation avoid the re-learning of the GLLiM model. Indeed, it suffices to change the estimated $\boldsymbol{\Sigma}_k$'s into $\boldsymbol{\Sigma}_k + \boldsymbol{\Sigma}_\eta$ and to report this change when computing $\boldsymbol{\theta}^*$.

Because S is much larger than P in MRF applications, it is important that the model (3.3) involving $\boldsymbol{\theta}$ is estimated first and then used to derive model (3.4) that has a similar structure. The number of trainable coefficients $\boldsymbol{\theta}$ can be drastically reduced by choosing constraints on covariance matrices $\boldsymbol{\Sigma}_k$ without inducing oversimplifications on the target model (3.4). In this work, equal diagonal covariance matrices are used as they yield the best results: for $1 \leq k \leq K$, $\boldsymbol{\Sigma}_k = \mathbf{D}_S$, where $\mathbf{D}_S \in \mathbb{R}^{S \times S}$ is a diagonal matrix. For example, with $S = 100$, $P = 3$ and $K = 50$, the number of trainable coefficients $\boldsymbol{\theta}$ is equal to 20 600 while a direct estimation of $\boldsymbol{\theta}^*$ would involve 272 703 trainable coefficients (see [176] for more details).

3.2.3 Dictionary sampling strategy

The dictionary design depends on the sampling strategy of the parameter space. In MRF, regular grids of P-dimensional parameter values are generally considered. In [169], authors show that in a regression context, the random sampling strategy provides better estimation of the parameters than the use of a regular grid. However, this strategy entails a risk of imperfectly covering the parameter space coverage.

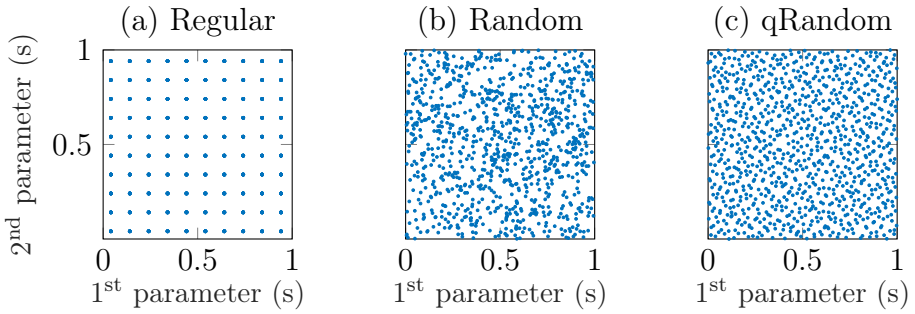

Figure 3.2 – Illustrations of the sampling strategies.
Figure shows the 2-dimensional projection of $N = 1\,000$ dictionary entries of the 3-dimensional parameter space ($P = 3$) obtained from (a) a regular grid sampling, (b) a random sampling and (c) a quasi-random sampling obtained from scrambled Sobol sequence.

Figure 3.2(a) shows a two-dimensional projection of $N = 1\,000$ points from a uniform grid in the 3D-hypercube ($P = 3$). Each parameter is described by 10 separate values. Note that with 1 000 points in 3D, only 100 distinct combinations appear in the 2D projection plane, each representing 10 different values of the third variable. This sampling scheme is not optimal in terms of information content. A significant improvement over the grid can be achieved by scrambled nets [181, 182]. In this paper, the Sobol sequence is generated [183] and scrambled [184]. We show the projection of $N = 1\,000$ points from

the scrambled Sobol sequence (figure 3.2(c)) referred to as quasi-random in the remainder of the manuscript.

3.3 Analysis framework

3.3.1 Signals

3.3.1.1 Synthetic scalable signals

The sensitivity of the MRF signals to each parameter is variable. In addition, parameters cannot readily be added to the simulation tool that produces the MRF or the vascular MRF signals. To produce signals that are equally sensitive to each parameter and dependent on a variable number of parameters (i.e. P may be set to any value), scalable signals that mimic MRF signals are introduced in equation (3.7). The parameters of the synthetic scalable signal have physical units to help understand their structure but no physical meaning,

$$\mathbf{y} = \left| \sum_{i=1}^{P} \sin\left(50\,\phi_i\,t\right) \exp\left(-\frac{t}{x_i}\right) \right|, \tag{3.7}$$

where x_i are the elements of $\mathbf{x}$, t varies from 10 to 1 000 ms in 10 ms steps ($S = 100$), the $\boldsymbol{\phi}_i$ values are between 0.1 and 1 and $|\cdot|$ is the absolute value function. The values of parameters $\mathbf{x}$ are in the range of 10 to 1 000 ms. The vector $\boldsymbol{\phi}$ is defined randomly such that none of the terms are equal. This makes the parameters x_i non-exchangeable: permutations of the $\mathbf{x}$ elements cannot lead to the same signal $\mathbf{y}$. Note that the relationship between $\mathbf{x}$ and $\mathbf{y}$ is non-linear. Examples of synthetic scalable signals are given in figure 3.3.

To create a noisy signal, a Gaussian zero-mean random variable with standard deviation σ_{noise} is added to the complex signal $\mathbf{y}$. The absolute value of the noisy signal is then considered. The signal-to-noise ratio is defined as: $\text{SNR} = I_{\max}/\sigma_{\text{noise}}$, where $I_{\max}$ is the maximum signal intensity. The same procedure is used to add noise to the following signals.

3.3.1.2 Synthetic vascular MRF signals

Vascular MRF signals are ratio of the gradient echo sampling of the free induction decay and spin echo (MGESFIDSE) signals measured pre- and post-injection of ultrasmall superparamagnetic iron oxide particles (USPIO) [147]. Eight sampled time points are obtained after the 90-degree pulse and 24 sampled time points after the 180-degree pulse

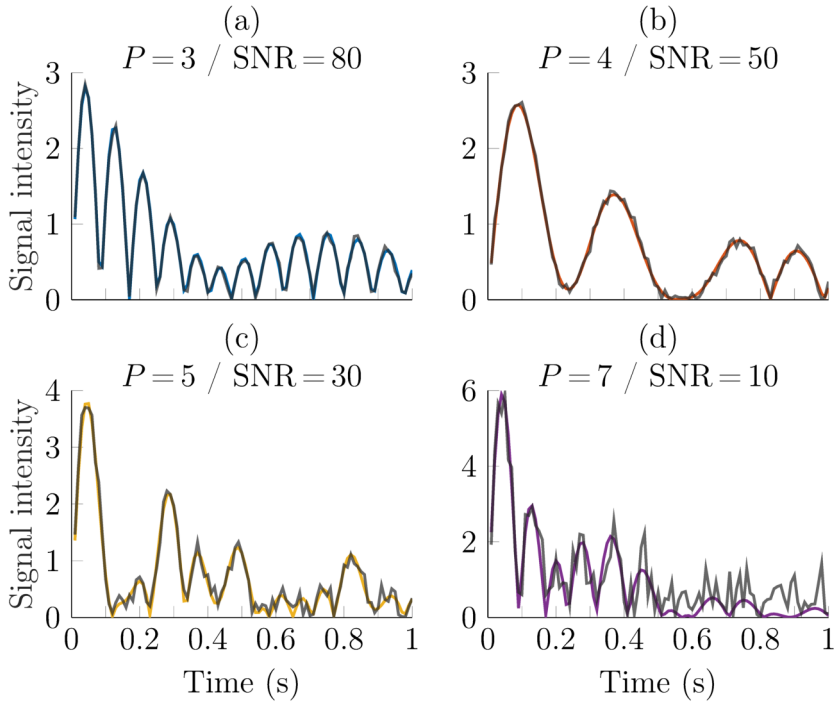

Figure 3.3 – Synthetic scalable signals for different number of parameters and SNR levels.
Color curves represent synthetic scalable signals randomly generated with different number of parameters (a) $P = 3$, (b) $P = 4$, (c) $P = 5$, and (d) $P = 7$. Black curves represent these signals once noise has been added according to (a) SNR $= 80$, (b) SNR $= 50$, (c) SNR $= 30$, and (d) SNR $= 10$.

($S = 32$). These signals mainly depend on the vascular properties of the tissues, which in our application are specified by three parameters ($P = 3$): blood volume fraction (BVf), vessel size index (VSI) and tissue oxygen saturation (StO_2). The simulation tool [152] takes into account intrinsic relaxations, magnetic field perturbations induced by susceptibility interfaces (vessels), water proton diffusion and compartmentalization of the contrast agent in the vessels. Due to the complexity of the tool, simulations are extremely time-consuming. Simulation of a single synthetic vascular MRF signal takes about 10 seconds and a dictionary of 100 000 signals is generated on a 32-node high-performance computer (*Intel Xeon Gold 6130*, 2.1 GHz) in about 67 hours.

3.3.1.3 Acquired vascular MRF signals

Experimental data were acquired at 4.7 T (Bruker Biospin, Ettlingen, Germany) and have been introduced in [154]. The field of view was 30×30 mm^2 and the voxel size was $234 \times 234 \times 800$ µm^3. A turbo spin-echo sequence was acquired to identify anatomical structures and tumor tissues. Then, two GESFIDSE sequences ($S = 32$) were acquired, before and after injection of UPSIO. For details on the conditions of animal preparation and data acquisition, see original data work [154].

3.3.2 Analysis pipeline

The simulated and acquired data are processed using custom code developed in the Matlab environment (The MathWorks Inc., Natick, Ma, USA). This code and the numerical experiment scripts are available[1], see appendix E.1 for details. Data from tumor bearing rats are processed using the *Medical software for Processing multi-Parametric images Pipelines*[2] [185], see appendices E.2 and E.3 for details.

3.3.2.1 Dictionary design

The dictionary is generated in two steps. First, combinations of parameter values in the parameter space are sampled using one of the sampling strategies in section 3.2.3. Then, for each combination of parameter values, the associated fingerprint is simulated using either equation (3.7) for synthetic scalable signals or the simulation tool described in section 3.3.1.2 for vascular MRF signals. For the DBL method, a low level, zero-mean Gaussian noise (typically, SNR = 60) is added to the dictionary signals as this improved our results (see section 3.4.1.2).

3.3.2.2 Dictionary-based analysis

The dictionary is fully stored for the DBM method or summarized by a parametric model $\boldsymbol{\theta}$ for the DBL method. To obtain this model, we use the GLLiM regression described in section 3.2.2. The model learning, a potentially time-consuming step, is performed only once, just after the production of the dictionary. The model requires only the setting of the K calibration value. In practice, the precise K value is not critical and different K values give similar results as long as they are sufficiently large compared to number of dictionary entries ($K \geq 50$ in our study).

[1] https://github.com/nifm-gin/DBL-qMRI
[2] https://github.com/nifm-gin/MP3

In DBM, given an observed signal $\mathbf{y}_{\text{obs}}$, an estimate $\hat{\mathbf{x}}$ of the true $\mathbf{x}_{\text{obs}}$ is calculated as the minimization argument of equation (3.1) among the couples $(\mathbf{x}, \mathbf{y})$ in the dictionary. The observed signal and the signals in the dictionary are previously normalized to have unit Euclidean norm. The parameters are normalized to have a mean of zero and unit variance using scaling and translating factors that are then used to rescale the estimates.

In DBL, an estimate $\hat{\mathbf{x}}$ of $\mathbf{x}_{\text{obs}}$ is computed using equation (3.5) and a confidence index (CI) using equation (3.6). To obtain an accurate CI, an estimation of the signal noise variance is required. This estimate can be derived from the data SNR and then used as explained in section 3.2.2 to update $\boldsymbol{\theta}$ adequately. We present in details, the relation between the CI and the root mean square error in appendix C.1.

3.3.2.3 Closed-form expression fitting (CEF) analysis

Vascular MRF signals can also be analyzed by fitting of a non linear biophysical model [132, 147]. The closed-form expression fitting (CEF) analysis method refers to this multiple-operation procedure. First, relaxation rates are extracted by fitting the intensities of MRI signals (synthetic or acquired). Then, these relaxation rates are used to compute the BVf and VSI parameters using equations (2.28) and (2.29).

3.3.2.4 Performance evaluation

To compare the method performance in parameter estimation, a set of M test signals is generated in the same way as for the dictionaries. The parameters values are randomly sampled in the parameter space and then the associated signals are computed. For each parameter, we compute the root mean square error (RMSE) as the square root of the quadratic mean of the differences between the estimated and the true parameter values.

3.4 Results

3.4.1 Synthetic scalable signals

3.4.1.1 Effect of sampling strategy on parameter accuracy

We investigate the impact of three parameter sampling strategies, regular, random and quasi-random, using synthetic scalable signals and the DBL method. We consider successively $P = 3$, 5, and 7, for each sampling strategy, leading to a total of 9 conditions. The numbers of entries in the dictionary are $N = 216$, 1 024, and 2 187, respectively. For each value of P, $M = 1\,000$ test signals are generated from parameters randomly sampled in the parameter space. The RMSE between the estimated and the true parameter values is then computed (see section 3.3.2.4) and divided by the number of parameters to obtain the average RMSE. To characterize the distribution of the average RMSE, the whole procedure was repeated 500 times (figure 3.4).

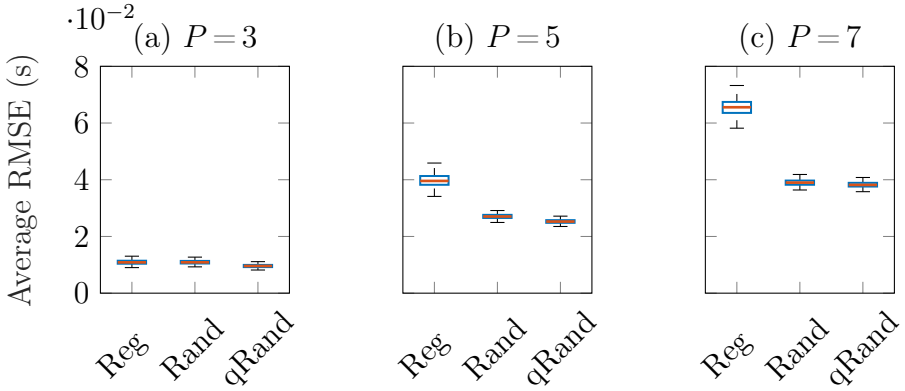

Figure 3.4 – Effect of sampling strategy on the dictionary-based learning (DBL) method, using synthetic scalable signals.
Figure shows the average RMSE ($M = 1\,000$ test signals) on the parameter estimates obtained using the DBL method for the three sampling strategies and (a) $P = 3$, (b) 5, and (c) 7 parameters. For each box, the red central mark indicates the median; the lower and upper edges indicate the 25$^{\text{th}}$ and 75$^{\text{th}}$ percentiles, respectively. The whiskers extend to the minimum and maximum values.

Regardless of the sampling strategy, the average RMSE increases with P, the number of parameters. As reported previously, for the same number of signals in the dictionary, random sampling gives a lower average RMSE than regular sampling, whatever the number of parameters [169]. This observation is also valid for other conditions presented in table 3.1. Note that when using the DBM approach instead of DBL, regular sampling yields a lower average RMSE than the random or quasi-random sampling (table 3.1).

Dictionaries		**DBM**			**DBL**		
P	N	Regular	Random	qRandom	Regular	Random	qRandom
3	512	36.9 ± 0.5	48.1 ± 1.0	43.0 ± 0.8	11.0 ± 0.8	11.0 ± 0.8	9.6 ± 0.6
3	1 728	24.9 ± 0.3	31.9 ± 0.6	28.8 ± 0.5	8.1 ± 0.4	8.7 ± 0.4	8.1 ± 0.4
3	4 096	18.7 ± 0.3	23.9 ± 0.4	21.5 ± 0.4	7.6 ± 0.3	8.1 ± 0.4	7.8 ± 0.3
5	1 024	74.8 ± 0.8	88.3 ± 1.2	84.3 ± 1.0	39.8 ± 2.3	27.1 ± 0.2	25.3 ± 0.7
5	3 125	60.6 ± 0.7	70.3 ± 0.9	68.0 ± 0.8	30.3 ± 1.2	22.5 ± 0.6	21.8 ± 0.6
5	7 776	51.0 ± 0.6	58.5 ± 0.7	56.6 ± 0.8	25.2 ± 0.7	21.0 ± 0.5	20.6 ± 0.5
7	2 187	98.6 ± 0.9	112.3 ± 1.2	111.3 ± 1.2	65.6 ± 2.9	39.0 ± 1.2	38.3 ± 1.0
7	16 384	75.1 ± 0.7	83.5 ± 0.8	82.1 ± 0.8	45.3 ± 1.8	31.1 ± 0.7	30.57 ± 0.7

Table 3.1 – Effect of parameter sampling strategies on the dictionary-based methods (DBL and DBM), using synthetic scalable signals.
Average RMSE ($M = 1\,000$ test signals) on the parameter estimates obtained using the DBM and DBL methods for the three sampling strategies: grid (regular), random and quasi-random (qRandom) obtained from scrambled Sobol sequence, and 8 combinations of P and N values.

The quasi-random sampling further reduces the average RMSE up to 12.4 %. Altogether, there is a reduction of 12.3 %, 36.4 % and 41.7 % in average RMSE between regular and quasi-random sampling for $3, 5,$ and 7 parameters, respectively. Therefore, in the following, a regular sampling is used for the DBM method and a quasi-random sampling is used for the DBL method.

3.4.1.2 Effect of noise addition on dictionary signals

To investigate the impact of noise addition on the DBL method robustness, we generate four scalable signals dictionaries: $N = 500$ and $2\,000$ (for $P = 3$), and $N = 2\,000$ and $10\,000$ (for $P = 5$). We consider three data augmentation approaches (or *data improvement* since the amount of data is not necessarily increased), using various noise levels. We used the initial matrix $\mathbf{Y}_{\text{dico}}$ of dictionary signals to build the matrix $\mathbf{Y}_{\text{augmented}}$ used to train mapping according to one of the three following data augmentation procedures [186]:

- The dictionary fingerprints $\mathbf{Y}_{\text{dico}}$ is substituted by its noisy version $\mathbf{Y}_{\text{noisy,1}}$ according to $\text{SNR}_{\text{dico,1}}$, see equation (3.8).
- $\mathbf{Y}_{\text{dico}}$ is doubled in size with the noisy signals $\mathbf{Y}_{\text{noisy,1}}$, see equation (3.9).
- $\mathbf{Y}_{\text{dico}}$ is augmented twice in size by noisy signals $\mathbf{Y}_{\text{noisy,1}}$ and $\mathbf{Y}_{\text{noisy,2}}$ according to $\text{SNR}_{\text{dico,1}}$ and $\text{SNR}_{\text{dico,2}}$, see equation (3.10).

$$\mathbf{Y}^{(1)}_{\text{augmented}} = \mathbf{Y}_{\text{noisy},1}, \tag{3.8}$$

$$\mathbf{Y}^{(2)}_{\text{augmented}} = \begin{pmatrix} \mathbf{Y}_{\text{dico}} \\ \mathbf{Y}_{\text{noisy},1} \end{pmatrix}, \tag{3.9}$$

$$\mathbf{Y}^{(3)}_{\text{augmented}} = \begin{pmatrix} \mathbf{Y}_{\text{dico}} \\ \mathbf{Y}_{\text{noisy},1} \\ \mathbf{Y}_{\text{noisy},2} \end{pmatrix}. \tag{3.10}$$

Note that the size of $\mathbf{X}_{\text{dico}}$ is also increased by replicating the matrix one or two times to match the length of $\mathbf{Y}_{\text{augmented}}$. The noise on dictionary signals is added in the same manner as the noise on the test signals.

We compare data augmentations (1-3) with $\text{SNR}_{\text{dico},1} = 60$ and $\text{SNR}_{dico,2} = 10$. For SNR_{test} between 3 and 100, we compute the RMSE gain (ratio between the RMSE in absence of data augmentation and the RMSE obtained using the data augmentation procedure for $M = 10\,000$ test signals) in the 4 experiment conditions (figure 3.5(a)). Then, to search the optimal SNR_{dico} for the data augmentation (1), we evaluated values of SNR_{dico} between 10 and 250 for three SNR_{test} (15, 30 and 45), see figure 3.5(b).

All data augmentations increase the robustness of the method (gain > 1) for SNR_{test} below a certain value and deteriorate it above, which is expected but is of minor importance since the purpose of this section is to improve the noise robustness for low and moderate SNR_{test} (i.e. about $\text{SNR}_{\text{test}} \leq 60$). Data augmentations (1) and (2) provide similar results, except for large SNR_{test} for which the data augmentation (2) provides larger RMSE gains. Data augmentation (3) yields significantly higher RMSE gains for SNR_{test} between 5 and 18 but in return significantly lower elsewhere.

For all SNR_{test}, the data augmentation (1) increases the robustness of the method for SNR_{dico} above a cut-off value and deteriorates it below. This cut-off value depends on SNR_{dico}, SNR_{test}, the number of parameters and the number dictionary entries. Cut-offs (mean $\pm$ standard deviation) are: 11.7 ± 0 for $\text{SNR}_{\text{test}} = 15$, 15.4 ± 8.5 for $\text{SNR}_{\text{test}} = 30$ and 22.8 ± 11.0 for $\text{SNR}_{\text{test}} = 45$. RMSE gains after the cut-off are: 1.28 ± 0.04, 1.22 ± 0.05 and 1.26 ± 0.04, for $\text{SNR}_{\text{test}} = 15$, 30 and 45, respectively. For $\text{SNR}_{\text{dico}} = 60$, the mean RMSE gains is 1.34 ± 0.15 considering these three SNR_{test} values and using the four dictionaries.

In the following, we use the data augmentation (1) since it provides increased robustness method and does not increase the dictionary size and therefore the mapping learning time. SNR_{dico} is set to 60. An extended study of the effect of noise addition in which we also investigate the benefit of modeling the noise during the learning is proposed in appendix C.2.

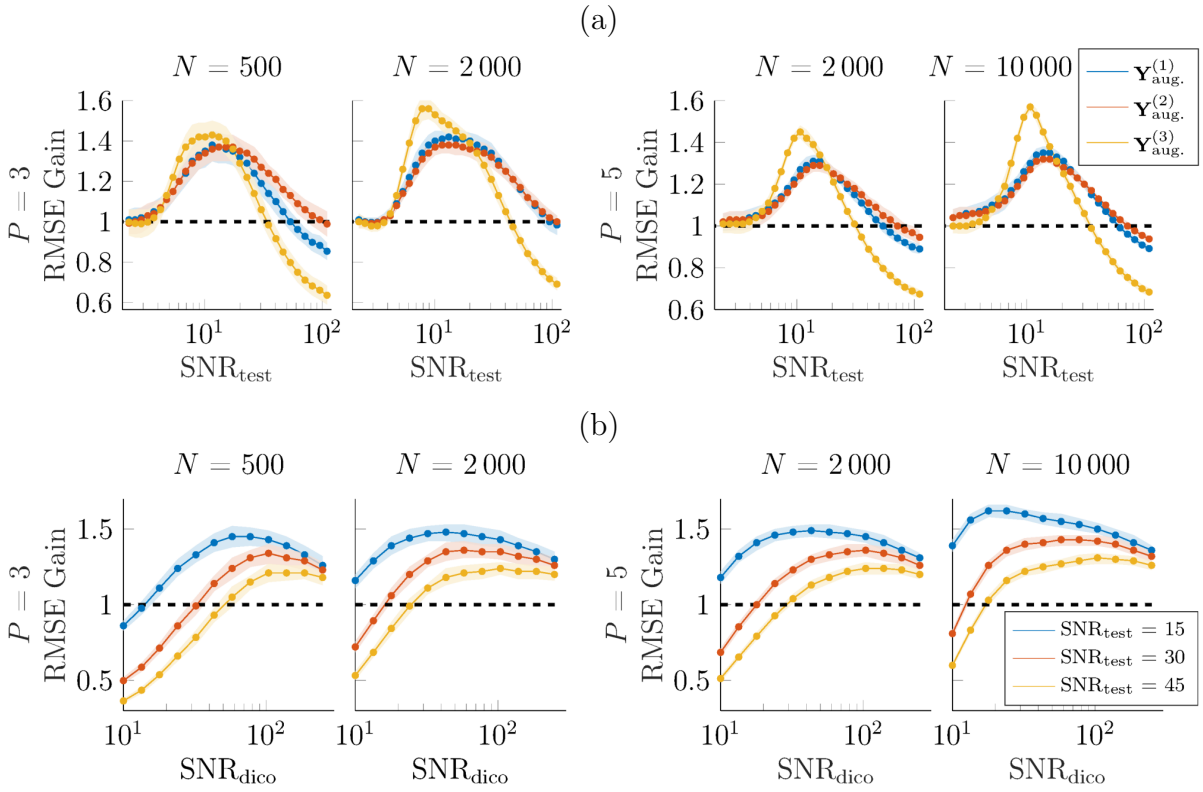

Figure 3.5 – RMSE gains for different data augmentations and noise levels on dictionary signals.
(a) RMSE gains for three data augmentations and different noise levels on test signals. The first two figures show the $P=3$ parameter experiments ($N=500$ and 2 000 signals) and next figures show the $P=5$ parameter experiments ($N=2\,000$ and 10 000 signals). (b) RMSE gains for different noise levels on dictionary signals and three different noise levels on test signals: 15, 30 and 45. The first two figures show the $P=3$ parameter experiments ($N=500$ and 2 000) and the next figures show the $P=5$ parameter experiments ($N=2\,000$ and 10 000). RMSE is computed for $M=10\,000$ test signals and then, the experiment is repeated 20 times. Markers are the mean RMSE through these 20 repetitions and the area represents the standard deviation. The dashed line represents the symbolic gain equal to 1, above the line the error is smaller than without data augmentations and inversely below.

3.4.1.3 Impact of the dictionary size and SNR on parameter accuracy

To study this impact for DBM and DBL, we generate four scalable signals dictionaries for $P=5$ and 7 parameters (a total of 8 conditions). The number of dictionary entries N was chosen so as to keep similar densities, i.e. a constant number of values per parameter (for $P=5$: $N=3^5$, 4^5, 5^5, and 6^5 and for $P=7$: $N=3^7$, 4^7, 5^7, and 6^7). For each condition, we evaluate the average RMSE, using $M=10\,000$ signals. To characterize the impact of SNR, the procedure is repeated for test signals with SNR between 10 and 110 (figure 3.6).

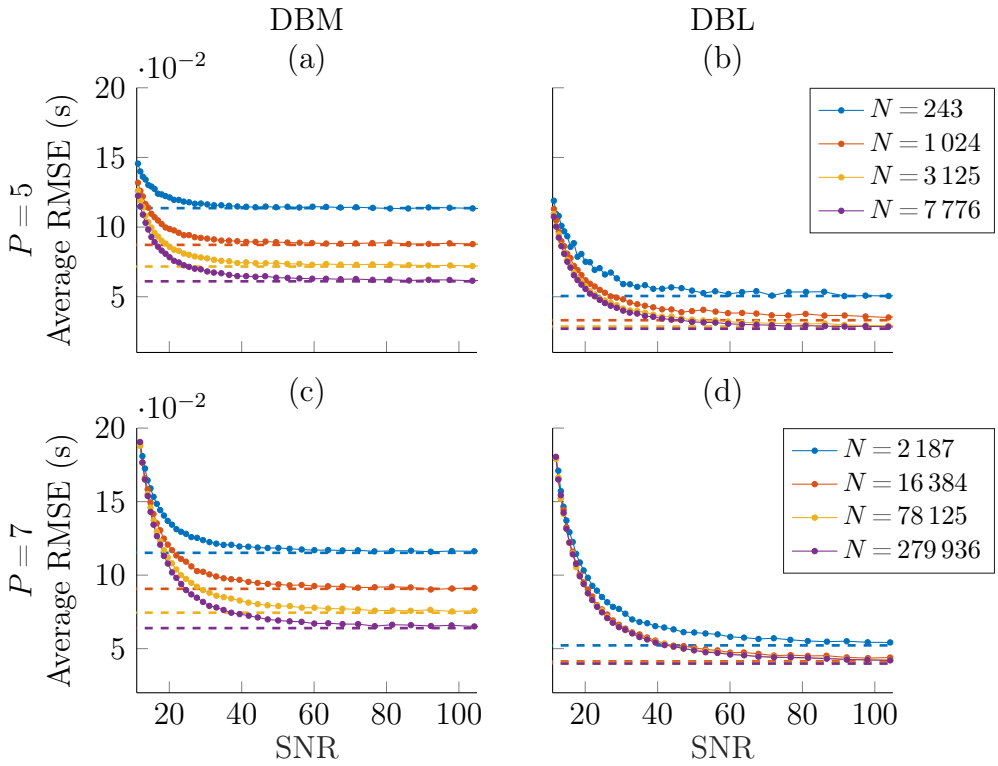

Figure 3.6 – Impact of dictionary size and SNR on DBM and DBL methods, using synthetic scalable signals.
Average RMSE are given with respect to the SNR for different numbers of parameters and dictionary entries. Average RMSE ($M = 10\,000$ test signals) for the DBM (a, c) and DBL (b, d) methods. The upper row (a, b) shows the results for $P = 5$ parameters, and the lower row (c, d) for $P = 7$ parameters. The dashed lines represent the average RMSE in the absence of noise on the test signals. The calibration value K (DBL method) is set to 50, except for $N = 243$ where $K = 20$.

As expected for the DBM method, the average RMSE decreases as the number of entries N increases. The average RMSE decreases as the SNR increases to about SNR = 60 and then plateaus near the value obtained in absence of noise. For the DBL method, the average RMSE also decreases as the SNR increases but up to about SNR = 90. Again, the highest SNR yields an average RMSE close to that obtained in the absence of noise. For the DBM method, the average RMSE is comparable between 5 and 7 parameters. The average RMSE obtained with the DBL method are lower than those obtained with the DBM method: $50.0 \pm 10.0\,\%$ lower for $P = 5$ and $38.0 \pm 12.3\,\%$ lower for $P = 7$, whatever the number of dictionary entries. N has a lower impact for DBL than for DBM. Between the smallest and the largest dictionary size, the average RMSE decreases by $38.0 \pm 9.5\,\%$ for the DBM method, while it decreases by only $18.3 \pm 5.2\,\%$

for the DBL method. Moreover, the two highest N yield similar average RMSE for the DBL method (difference smaller than 0.5 %), suggesting that an increase in the number of entries would not further improve the average RMSE. Altogether, compared to the DBM method, the DBL method reduces the average RMSE by 13.1 ± 5.2 % (12.3 ± 4.3 %, respectively) while reducing the number of entries by a factor of 32 (respectively 128) for 5 parameters (7 parameters, respectively). Same experiment for additional P and N values have been performed (17 conditions in total). The average RMSE is always lower for DBL than for DBM (39.2 ± 15.9 % lower).

Dictionaries		**DBM**		**DBL**		
P	N	Estimation (s)	Memory (Mo)	Learning (s)	Estimation (s)	Memory (Mo)
4	625	0.10 ± 0.02	0.52	1.12 ± 0.26	1.59 ± 0.21	4.21
4	1 296	0.18 ± 0.02	1.08	4.26 ± 1.21	1.52 ± 0.20	4.21
5	1 024	0.15 ± 0.02	0.86	2.59 ± 0.76	1.80 ± 0.23	4.26
5	3 125	0.39 ± 0.03	2.63	22.55 ± 4.66	1.81 ± 0.29	4.26
5	7 776	0.92 ± 0.06	6.53	89.18 ± 26.50	1.86 ± 0.32	4.26
6	729	0.11 ± 0.02	0.62	1.21 ± 0.34	1.99 ± 0.25	4.30
6	4 096	0.50 ± 0.04	3.47	34.68 ± 8.14	1.94 ± 0.31	4.30
6	15 625	1.84 ± 0.17	13.25	361.16 ± 83.55	1.90 ± 0.35	4.30
6	46 656	5.49 ± 0.48	39.56	1 816.3 ± 259.15	1.84 ± 0.32	4.30
7	2 187	0.29 ± 0.04	1.87	10.70 ± 2.75	2.13 ± 0.29	4.35
7	16 384	2.01 ± 0.08	14.03	432.32 ± 88.30	2.17 ± 0.40	4.35
7	78 125	9.17 ± 0.63	66.88	4 283.80 ± 861.72	2.12 ± 0.37	4.35
7	279 936	28.60 ± 2.57	239.63	12 130.11 ± 2 018.90	2.04 ± 0.20	4.35
4	1 296	0.30 ± 0.07	1.08	7.85 ± 2.14	2.64 ± 0.46	4.21
5	7 776	1.40 ± 0.25	6.53	158.90 ± 42.84	2.83 ± 0.44	4.26
6	46 656	5.72 ± 0.04	39.56	1 766.90 ± 89.53	2.33 ± 0.14	4.30
7	279 936	-	-	-	-	-

Table 3.2 – Computational times and memory requirements of dictionary-based matching (DBM) and dictionary-based learning (DBL) methods, using synthetic scalable signals. Computational estimation times of $M = 10\,000$ signals and learning times (DBL only: time to generate the regression model) and memory requirements to store the dictionary (DBM) and to store the model (DBL). Results are given for different combinations of number of parameters (P between 4 and 7) and number of dictionary entries (N between 625 and 279 936). The first part of the table (the first 13 lines) shows results for the processing of data on 32-core high performance computer (*Intel Xeon Gold* 6130, 2.1 GHz, 384 Go system memory) and the second part of the table (the last 4 lines) shows results for the processing on a 4-core desktop computer (*Intel Core* i7-4770, 3.4 GHz, 32 Go system memory). The case $P = 7$ and $N = 279\,936$ cannot be computed on that computer because the dictionary uses more memory than available.

By eliminating the costly dictionary matching operation, DBL can greatly reduce computation time when N increases. For 7 parameters and $N = 78\,125$, inverting 10 000

test signals takes 2.0 ± 0.1 seconds with DBM and 2.2 ± 0.4 seconds with DBL. When N increases to 279 936, the estimation time increases to 28.6 ± 2.6 seconds for DBM while it remains stable at 2.0 ± 0.2 seconds for DBL. In terms of memory, these dictionaries require 66.9 ($N = 78\,125$) and 239.6 Mo ($N = 279\,936$) whereas A complete comparison of the performance of the methods in terms of speed and memory is given in table 3.2. We observe that the number of dictionary entries has no effect on the estimation time or on the memory size once the model is learned.

3.4.1.4 Boundary behavior

The DBL method estimates parameter values using a continuous function that is not limited to the parameter space covered by the dictionary entries. To investigate the behavior of DBM and DBL methods outside the limits of this parameter space, we define a dictionary ($N = 10\,000$) composed of two disjoint patches in the parameter space, generate $M = 2\,000\,000$ test signals and evaluate the average RMSE for each parameter value.

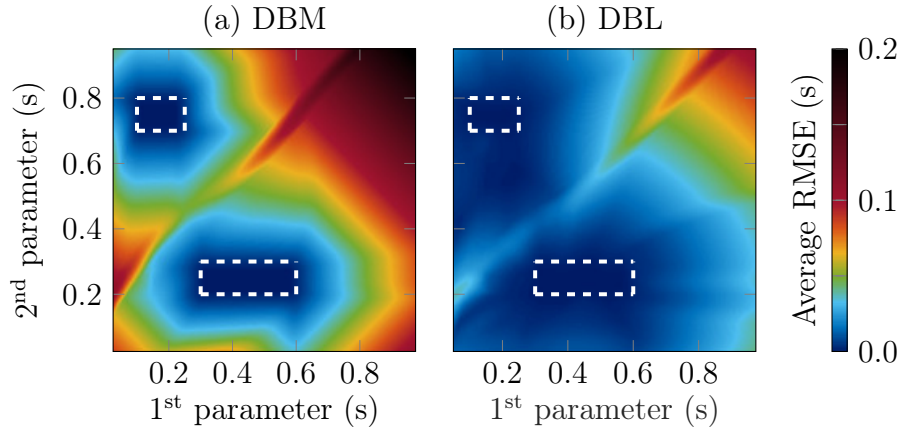

Figure 3.7 – Estimation accuracy outside the limits of the parameter space covered by the dictionary, using synthetic scalable signals.
Average RMSE ($M = 2\,000\,000$ test signals) in the parameter space ($P = 2$) obtained (a) with the DBM and (b) with the DBL method. The white dashed lines delimit the subspace covered by the dictionary. The average RMSE is computed from signals in a 50×50 ms sliding window, moving in 5 ms steps in the parameter space.

The two methods yield similar estimation accuracy in the subspace covered by the dictionary entries (figure 3.7). Outside that subspace, the average RMSE obtained with the DBM method increases with the distance to the subspace. For the DBL method, the average RMSE remains below 100 ms, well beyond the limit of the dictionary subspace.

3.4.1.5 Confidence index

We investigate the relationship between the CI, available with the DBL method, and the RMSE. We generate $N = 10\,000$ dictionary entries and $M = 10\,000$ test signals. We then add different noise levels to the test signals to obtain a SNR = 20, 30, 40, 60 and 100. A single initial regression model is computed. For each SNR, this model is then updated based on the noise level (denoted by η) which corresponds to the SNR values of the test signals (see section 3.2.2). We compute the RMSE and CI for the initial model (*i.e.* without accounting for the noise level) and $\text{RMSE}_{\boldsymbol{\eta}}$ and $\text{CI}_{\boldsymbol{\eta}}$ using the updated model. For each SNR value, the experiment is repeated 100 times. Figure 3.8(c), shows that the non-updated CI is proportional to but not equal to the RMSE in the SNR value range. Figure 3.8(c) also shows that the scaling factor between RMSE and non-updated CI depends on the added noise level.

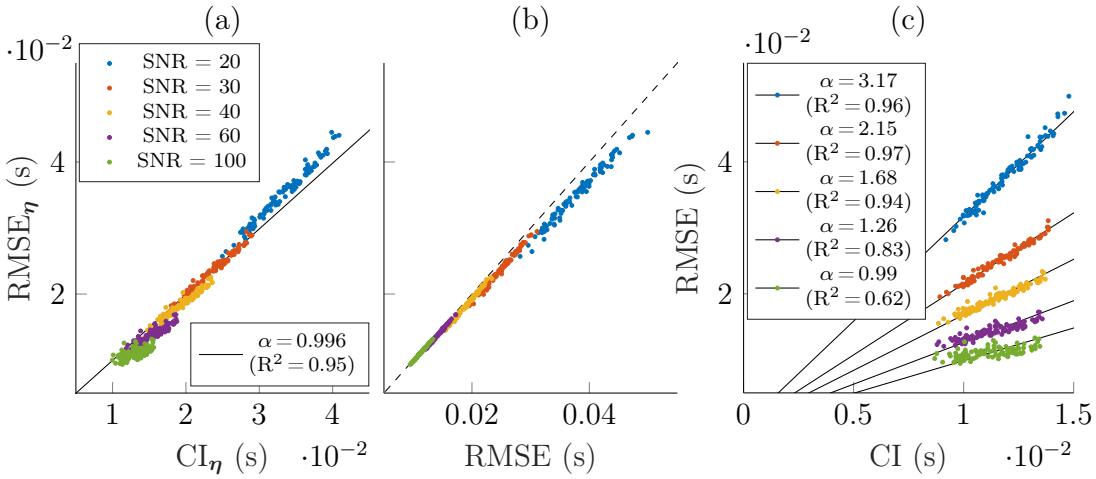

Figure 3.8 – Impact of model noise modelization on RMSE and confidence index (CI). $\text{RMSE}_{\boldsymbol{\eta}}$ ($M = 10\,000$ test signals) versus (a) confidence index ($\text{CI}_{\boldsymbol{\eta}}$) and (b) RMSE (non-updated model), using synthetic scalable signals. (c) RMSE as a function of the CI. SNR = 20, 30, 40, 60, and 100. (a,c) The black line represents the proportional regression coefficient α between $\text{RMSE}_{\boldsymbol{\eta}}$ and $\text{CI}_{\boldsymbol{\eta}}$ for all SNR values. (b) The dashed black line is the identity function. R^2 is the coefficient of determination.

As expected, $\text{RMSE}_{\boldsymbol{\eta}}$ and $\text{CI}_{\boldsymbol{\eta}}$ increase as the SNR decreases (figure 3.8(a)). $\text{RMSE}_{\boldsymbol{\eta}}$ and $\text{CI}_{\boldsymbol{\eta}}$ are proportional and comparable in the SNR value range (slope: 0.99, $R^2 = 0.95$). Note that $\text{CI}_{\boldsymbol{\eta}}$ may slightly under or over-estimate the $\text{RMSE}_{\boldsymbol{\eta}}$ (mean difference: 7.8 %). Overall, $\text{CI}_{\boldsymbol{\eta}}$ appears to be a good indicator of the $\text{RMSE}_{\boldsymbol{\eta}}$. Interestingly, the inclusion of noise in the model slightly improves the estimation accuracy. On average, the $\text{RMSE}_{\boldsymbol{\eta}}$ is 4.11 % lower than the RMSE (figure 3.8(b)). In the following, for DBL, RMSE and CI refer to $\text{RMSE}_{\boldsymbol{\eta}}$ and $\text{CI}_{\boldsymbol{\eta}}$ (updated model).

3.4.2 Vascular MRF signals

3.4.2.1 Synthetic vascular MRF signals

We compare the two dictionary-based methods and the CEF method on synthetic vascular MRF signals. The dictionaries (grid and quasi-random sampling) are simulated with a BVf between 0.25 and 30 %, a VSI between 0.5 and 50 µm and a StO_2 between 30 and 95 %. Among the 170 100 combinations, some signals cannot be produced, due to simulation constraints (e.g. a very large BVf cannot be produced with distant, small, vessels or small BVf with large vessels). The obtained N values reduce then to $N = 164\,524$ for the grid and to $N = 167\,216$ for quasi-random sampling.

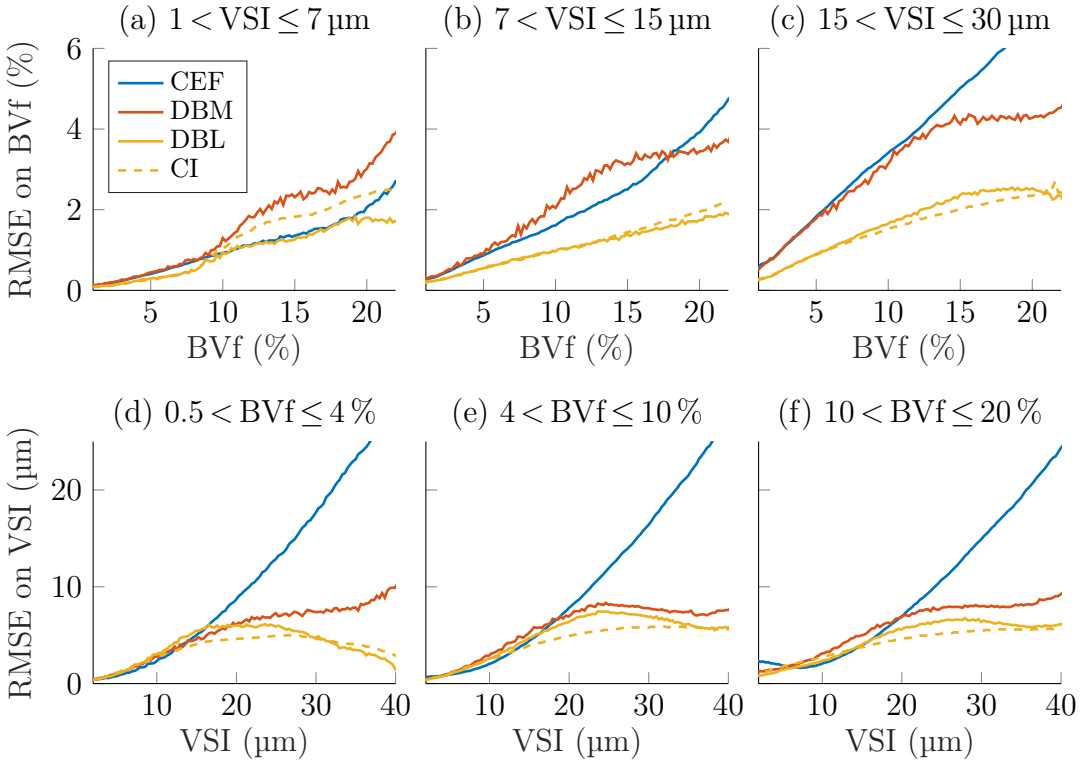

Figure 3.9 – Comparison of the RMSE on BVf and VSI obtained with the two dictionary-based methods (DBM and DBL) and with the closed-form expression fitting (CEF) method, using synthetic vascular MRF signals.
Figures (a, b, c) show RMSE ($M = 100\,000$ test signals) on BVf for three ranges of VSI, and figures (d, e, f) show the RMSE on VSI for three ranges of BVf. The dashed lines represent the average confidence indices (CI) on BVf (first row) and VSI (second row) obtained with DBL. The data are shown after 1D sliding window filtering (3 % for BVf and 5 µm for VSI). The dictionary dimensions are $P = 3$, $S = 32$, and $N = 164\,524$ for DBM and $N = 167\,216$ for DBL.

For each method, $M = 100\,000$ test signals (SNR = 100) are generated. To analyze the BVf RMSE, test signals are divided into three parts: small, medium and large vessel sizes. To analyze the VSI RMSE, test signals are divided into three parts: low, medium and large blood volumes.

For all vessel diameters, the RMSE on BVf tends to increase with BVf (figure 3.9). The DBM and CEF methods yield similar RMSE for BVf values below 10 %. For medium and large vessels and large BVf values, the CEF method yields the highest errors. The DBL method always yields the lowest error with an RMSE of 2.38 % for CEF, 2.68 % for DBM and 1.30 % for DBL.

For VSI values smaller than 15 µm, the behavior of the RMSE is similar in all three methods for the three BVf ranges. Above 15 µm, the CEF method yields larger errors than the two dictionary-based approaches and the RMSE obtained with CEF is linearly correlated with the VSI value ($R^2 \geq 0.99$). This linear behavior has already been reported in [187]. DBL yields a 25 % smaller RMSE than DBM, on average with an RMSE of 12.46 µm for CEF, 6.11 µm for DBM, and 4.50 µm for DBL. The CI appears again to be a good indicator of the RMSE, with maximum differences between CI and RMSE of 1.07 % for BVf and 2.36 µm for VSI and average differences of 0.25 % and 0.75 µm.

3.4.2.2 Acquired vascular MRF signals

The DBL method is then applied to acquired vascular MRF signals collected from rats bearing 9L and C6 tumors. We quantify BVf, VSI and StO_2 with both dictionary-based methods (DBM and DBL) and using two numbers of dictionary entries. The large dictionary ($N = 170\,100$) is the one used previously in section 3.4.2.1. The small dictionary ($N = 4\,320$) is simulated with BVf between 0.33 and 12 %, VSI between 1 and 20 µm and StO_2 between 40 and 90 %.

All methods yield consistent estimates (figure 3.10), in which the tumor and the large vessels can be easily depicted on BVf and VSI maps. StO_2 appears constant in healthy tissues. However, for DBM, there are many isolated high values, suggesting noisy maps. In [154], the authors proposed to remove the last 8 signal samples and apply a spatial Gaussian filtering to increase the SNR. Using the DBM method, these additional steps allowed them to produce less noisy maps. Interestingly, with the DBL method, these steps are no longer required. Our approach is therefore more likely to preserve small structure information, which may be otherwise removed by an additional spatial filtering.

For the large dictionary, the mean BVf and VSI obtained in tumor with the DBM and DBL methods are similar but with the DBL method, we can differentiate different

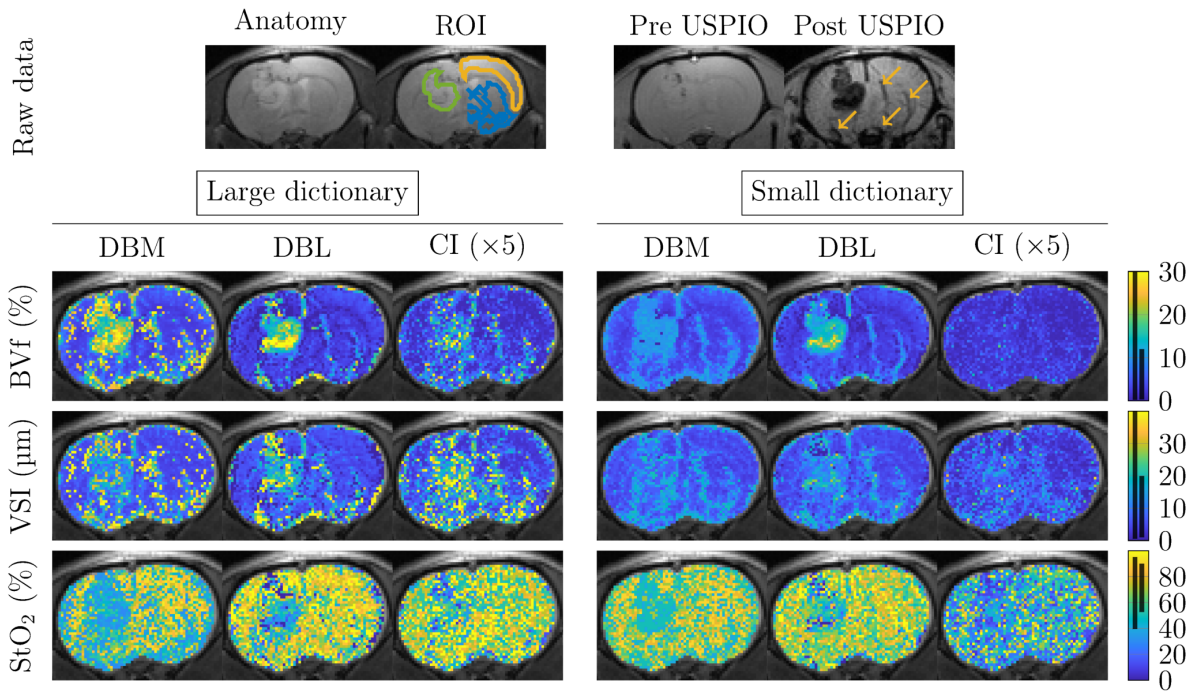

Figure 3.10 – Maps of vascular parameter estimates of a 9L rat tumor model.
The first row shows the anatomical image and regions of interest (left) and the MGEFIDSE pre and post USPIO injection (right) for the second echo time (6.3 ms). The tumor, cortex and striatum are respectively delineated with green, yellow and blue lines. The arrows on the post-USPIO injection image indicate large vessels. The estimated maps for BVf, VSI and StO_2 are shown below, using DBM (first and fourth columns) and DBL (second and fifth columns). The third and sixth columns show the DBL confidence index (CI) maps. In the color bars, the black lines represent the parameter ranges covered by the two dictionaries: the short (resp. long) line for the small (resp. large) dictionary. Large dictionary: $N = 164\,524$ for DBM; 70 values for BVf between 0.25 and 30 %, 90 values for VSI between 0.5 and 50 µm and 27 values for StO_2 between 30 and 95 % and $N = 167\,216$ for DBL. Small dictionary: $N = 4\,218$ for DBM; 36 values for BVf between 0.33 and 12 %, 20 values for VSI between 1 and 20 µm and 6 values for StO_2 between 40 and 90 % and $N = 4\,119$ for DBL.

subregions within the lesion. Mean values and standard deviations are 20.20 ± 6.14 %, 15.90 ± 7.79 µm for DBM and 18.22 ± 9.34 %, 19.91 ± 11.76 µm for DBL. For StO_2, the DBL method provides significantly larger values, closer to the expected values for healthy tissue [188]. Values for striatum are 62.67 ± 21.73 % for DBM and 74.46 ± 18.96 % for DBL. Overall, DBM and DBL yield comparable values. For the small dictionary, the contrasts are similar. The estimates obtained by the DBM method are limited to the space spanned by the dictionary, while the DBL method yields estimates outside this range and closer to the parameter values obtained with the large dictionary. In the tumor, the mean BVf is 13.66 % while the maximum dictionary value is 12 %.

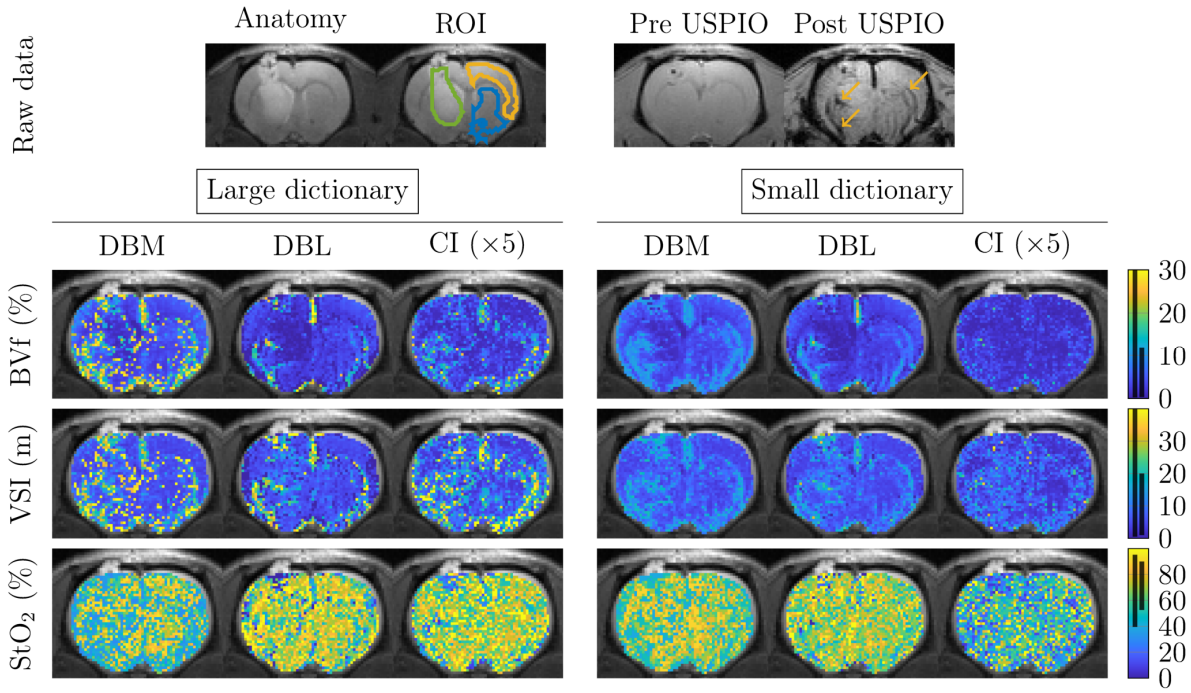

Figure 3.11 – Vascular parameter estimate maps of a C6 rat tumor model.
See figure 3.10 for caption.

A second example of a C6 rat tumor model is given in figure 3.11. The results are similar to those observed for the 9L tumor. DBL and DBM produce comparable physiological parameter values. With DBL, however, parameter maps are less noisy and additional CI maps can be produced. Figure 3.12, shows an evaluation by region of interest (ROI) (8 animals: 4 from each tumor model). The DBL method with a small dictionary produces estimates similar to those obtained with a large dictionary, except for the largest values which are underestimated. This results in a slight reduction in mean ROI values. The average differences between the mean ROI values obtained by the DBL method with the large and small dictionaries are 1.17 % for BVf, 3.50 µm for VSI and 1.62 % for StO_2.

The mean CIs in the tumor are 2.36 % for BVf, 4.90 µm for VSI and 12.22 % for StO_2, while in the cortex the mean CI are 0.81 % for BVf, 1.96 µm for VSI and 14.81 % for StO_2. These results are in agreement with previous results that pointed better estimates for BVf than for VSI and low signal sensitivity to StO_2 [154]. Confidence in the estimates is therefore on average 5 to 6 times lower in the tumor than in the cortex for BVf and VSI but is similar for StO_2. This is an interesting contribution of our DBL method as to our knowledge, it is the first time that such error maps are provided for BVf, VSI, and StO_2.

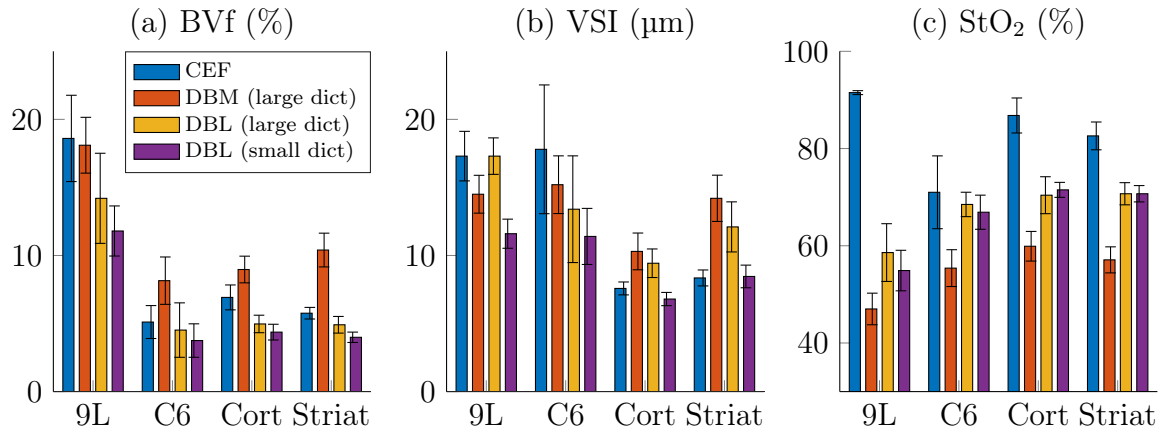

Figure 3.12 – Mean estimates by regions of interest of the vascular parameters. (a) BVf, (b) VSI and (c) StO_2 computed performing 3 methods: the closed-form expression fitting (CEF), the dictionary-based matching (DBM) and the dictionary-based learning (DBL) using 2 different numbers of dictionary entries. The colored bars are the average values of the mean vascular parameters by regions of interest (9L and C6 lesions: 4 rats, cortex (Cort) and striatum (Striat): 8 rats) and error bars are the standard deviations centered on the average values.

3.5 Discussion, conclusion and perspectives

This work presents a method for estimating vascular MRF parameters based on dictionary learning. It preserves the main advantages of the MRF method, i.e. robustness, speed and flexibility, and meets the challenge of producing accurate estimates from a small dictionary, even when the dimension of the parameters is large.

Regarding the design of the dictionary, we observe as [169] that random sampling of the parameter space gives more accurate estimates than grid sampling, when an inverse regression model is used. We further show that quasi-random sampling gives even better estimates. However, when the DBM method is used, the grid remains the most efficient sampling strategy. The appropriate dictionary design depends thus on the chosen inversion approach (grid matching vs statistical learning). The results obtained with the DBL method suggest that the simulation of a few patches (with quasi-random sampling) in the parameter space could save even more time in the construction of the dictionary (section 3.4.1.4). This result seems specific to the regression method. Indeed, a study using neural networks [165] rather reported increased deviations from the true values at the boundaries of the training dictionary. This is likely due to the vanishing gradient of the activation function in these regions. This patch approach could be implemented by combining a set of parameter values corresponding to healthy tissues and one or

more sets corresponding to damaged tissues (e.g. tumorous tissues). If needed, a few additional dictionary entries can be generated to fill gaps between patches (investigated in the next chapter, section 4.3.1.4).

Regarding the quality of the inversion, the regression approach usually involves calibration. In GLLiM, the number of Gaussian distributions K is the only calibration value that needs to be adjusted. This can be done automatically using a standard information criterion such as AIC or BIC [189, 190], as illustrated in [176], but this may result in additional learning time. We have observed that our results have little dependence on K. In contrast, neural networks [165–169, 173–175] used to solve similar inverse problems are very sensitive to their many complex calibration settings: architecture, batch sizes, learning rates, among others. The adjustment of all these calibration settings is usually performed by learning the model for a large number of calibration value combinations, which represents a higher computational cost than determining a single calibration value as in GLLIM. This difference in calibration cost makes the DBL method more flexible in case of change in dictionary design (extension of the parameter range, additional parameters, etc.). In addition, GLLiM has the advantage of providing a richer information. Here, we make use of the full posterior parameter distribution provided by GLLiM to derive a CI for each estimate. We observe that this CI matches the RMSE in cases where a ground truth is available (synthetic scalable; section 3.4.1.5 and synthetic vascular MRF signals; section 3.4.2.1). Interestingly, this CI reports both signal and model errors (derived from the dictionary) and thus reflects the whole DBL procedure.

Regarding the acquired vascular MRF signals, we observe that the number of dictionary entries can be divided by about 40 using the DBL method and still lead to accurate maps. The maps produced with the DBL method are significantly less noisy than those obtained with the DBM method and some structures, not observed with DBM, appear in the lesions. The additional tissue contrast provided by DBL could therefore contribute to improved tumor characterization [191].

In conclusion, this first evaluation of the DBL method appears promising. It reduces the simulation time and the memory required for dictionary storage, improves parameter accuracy, reduces the estimation time, and provides a first confidence index on parameter estimates. The DBL method could become even more efficient as the number of parameters to be estimated increases, which can happen when considering all the possible contributions of the tissues and the scanner to the signal. In addition, the flexibility of the proposed approach opens the door to further improvements. In particular, future work should include the adaptation and optimization of the dictionary sampling strategy

with respect to the targeted range of parameters to estimate. In addition, MRI produces complex-valued data but machine learning methodologies are generally designed for real-valued data. Dealing with complex-valued data could boost the performance of DBL [168]. This requires an adjustment of the inverse regression method also left to future work.

Chapter 4

Statistical learning vs deep learning in generalized MRF applications

This study is in line with the previous one. The objective is to compare the performance of the proposed dictionary-based learning method (chapter 3) with a DBL method using a neural network. Part of this study was presented during the 2020 congress of the *International Society for Magnetic Resonance in Medicine* (ISMRM) [13]. This section also extends the previous study to further investigations using standard MRF signals to estimate relaxation times T_1 and T_2, and off-resonance. This results in investigating highly undersampled data issues and complex-valued signal considerations.

4.1 Introduction

A major reason for the popularity of the dictionary-based matching (DBM) method is its flexibility since it does not require specific adjustment depending on the application (e.g. signal length, number of parameters, complexity of the mapping...). Potentially, the user may choose a different distance (or dissimilarity) function in equation (2.32) but in practice the dot product works sufficiently well. Instead, when using a dictionary-based learning (DBL) approach, a model is used to approximate the mapping between signal and parameter spaces. The choice of the model is therefore critical. It must be able to accurately approximate the mapping between these spaces and, if that relationship is complex (i.e. highly non-linear), the model is required to have a very high modeling power. Then, a larger model generally demands a greater number of dictionary entries in order to be properly trained and therefore implies an increase in computational costs. The

purpose of this study is to compare two different DBL methods to model the mapping: a deep learning model (DB-DL), and a statistical model (DB-SL).

We compare the model size, learning and quantification times, estimation accuracy, robustness to both thermal noise and spatial aliasing noise, number of dictionary entries requirement, and model generalization ability for the DB-DL and the DB-SL methods. The standard DBM method is also used to provide reference results obtained in the absence of dictionary learning. Performances were compared on synthetic signals: scalable signals that can scale across parameter dimensions and standard MRF signals. Finally, we perform a last study in order to briefly investigate ensembles of DBL methods to provide more accurate estimates.

4.2 Analysis framework

4.2.1 Model design

4.2.1.1 Neural network architecture and training

For the DB-DL method based on neural networks (NN), we use the architecture proposed in [165], i.e. a fully-connected NN. The first and last layers are the S-node input and P-node output layers which match the sizes of the input signal $\mathbf{y}$ and the output parameters $\mathbf{x}$, respectively. There are also H hidden layers of Z nodes. We present the architecture in figure 4.1. In [165], authors used $H = 2$ hidden layers of $Z = 300$ nodes. This implementation was not a very deep or large network. We therefore choose $H = 6$ and reduce Z to 100 in order to limit the number of trainable parameters and avoid overfitting.

The original activation functions were hyperbolic tangent functions for the hidden layers and sigmoid functions for the output layer. These activation functions are particularly susceptible to the vanishing gradient problem [165], i.e. the hyperbolic tangent function squishes a large input space into a small input space between -1 and 1. Therefore, a large change in the input of the sigmoid function may result in a small change in the output. Hence, the derivative becomes small. A small gradient means that the weights and biases of the initial layers will not be updated effectively at each gradient descent step. Since these initial layers are often crucial to recognizing the core elements of the input data, it can lead to overall inaccuracy of the whole network despite the training algorithm seemingly converging. Consequently, other activation functions such as ReLU, more robust to this issue, are used instead of the original functions.

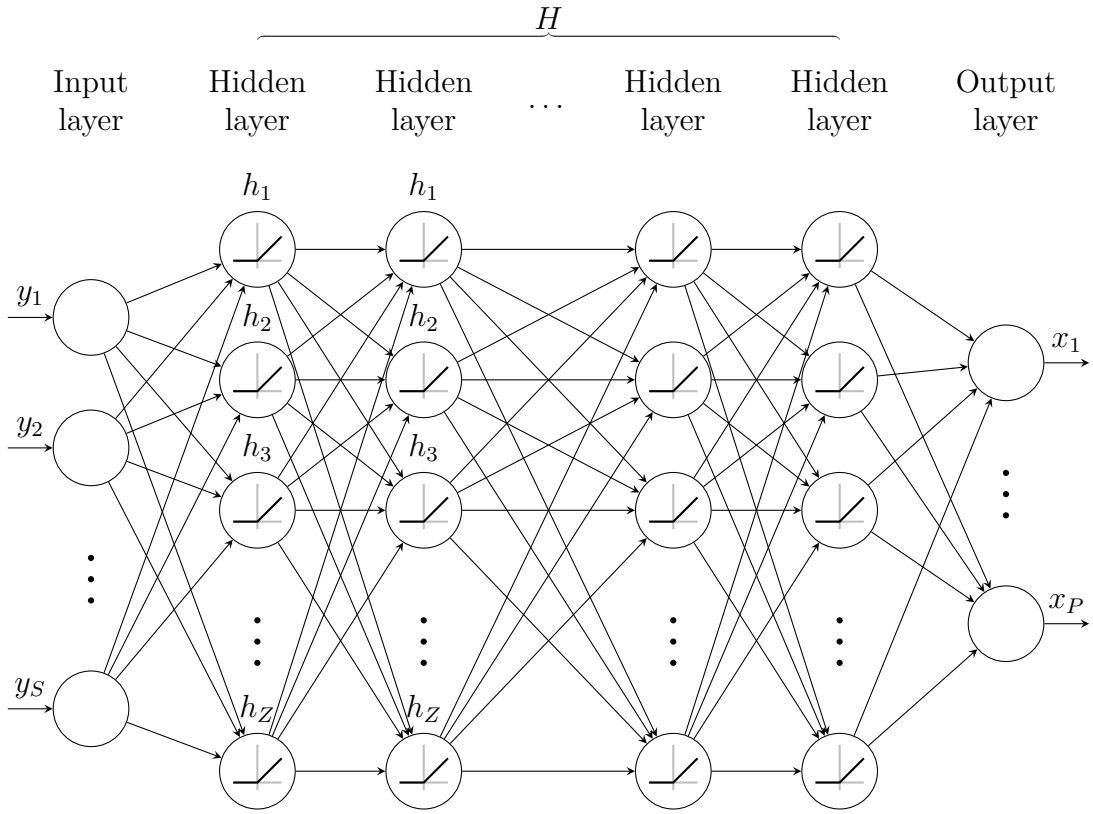

Figure 4.1 – Fully-connected neural network architecture.
The circles represent the nodes and the arrows the connections between these nodes. ReLU activation functions are displayed in circles. Input is the MR signal $\mathbf{y} = (y_1, \ldots, y_S) \in \mathbb{R}^S$ and output is the vector of parameters $\mathbf{x} = (x_1, \ldots, x_P) \in \mathbb{R}^P$.

As previously exhibited with DB-SL method, Gaussian noise is added to dictionary signals to promote robust learning. The network is trained by the ADAM stochastic gradient descent algorithm, the learning rate is set to 0.001 and the loss function defined as the mean square error. The maximum number of iterations is set to 2 000 to ensure convergence and we use mini-batches of 16 dictionary entries at each epoch. The neural network was designed and trained using the *deep learning toolbox* in Matlab environment (The MathWorks Inc., Natick, Ma, USA).

4.2.1.2 Calibration model parameter set and model sizes

An increase in model size is commonly combined with an increase in the number of dictionary entries and computational cost. However, the model must maintain a good expressivity to handle non-linear mappings. For example, linear and generalized linear regressions (e.g. least-square affine regression, perceptron, etc.) have a small model size $\mathcal{O}(SP)$ but do not handle non-linear mappings[1]. In contrast, fully connected deep NN exhibit very high modeling power but the model size is $\mathcal{O}(HS^2)$ (considering $Z = S$). This quadratic size is also observable with second order polynomial regressions that have a model size in $\mathcal{O}(PS^2)$. Note that n^{th} order polynomial regressions have model sizes in $\mathcal{O}(PS^n)$. A reduction of the size of these models is possible by performing a reduction/projection of the input signals. For example for NN, one can choose $Z \ll S$ to reduce model size to $\mathcal{O}(ZS)$. However, this reduction leads to a loss of information (i.e. reduction of explained variance). This loss is more or less important depending on the complexity of the input data structure.

$\mathcal{C}$ is the set of model calibration variables. Using the NN method, we identify two model calibration variables: $\mathcal{C} = \{Z, H\}$. In this case, the model size is $(H-1)(Z^2+Z) + Z(S+1) + P(Z+1) = \mathcal{O}(HZ^2)$. Using the GLLiM model, we identify one model calibration variable: $\mathcal{C} = \{K\}$ and the model size is $K(P + P^2 + 1 + SP + S) + S = \mathcal{O}(KSP)$ with equal diagonal covariance matrices. Note that using the original DBM method, $\mathcal{C} = \varnothing$. One can roughly see the cardinal of $\mathcal{C}$ as an indication of model flexibility: it represents the number of parameters to be tuned for a new sequence.

4.2.2 Signals and performance evaluation

4.2.2.1 Standard MRF signal

To evaluate the proposed reconstruction methods on a standard relaxometry application of magnetic resonance fingerprinting (MRF) [137], we use an MRF acquisition scheme based on an inversion-recovery balanced steady state free-precession sequence to generate synthetic MRF signals. According to [137], after an initial inversion pulse, the flip angle is a series of repeating sinusoidal curves with a period of 250 repetition times (TR) and alternating maximum flip angles (FA). In the odd periods, the FA is calculated as $\text{FA}_t = 10 + 50 \times \sin\left(\frac{2\pi}{500}t\right) + \text{rand}(2)$, where t varies from 1 to 250 and rand(2) is a function to generate normally distributed random numbers (mean is zero) with a

[1] $\mathcal{O}$ is a mathematical notation that describes the limiting behavior of a function, here, the model size function.

standard deviation of 2. In the even periods, we divide the previous period's FA by two. A 50-TR delay is added between each period. The TR pattern, between 10.5 and 14 ms, is generated following a procedural noise. This procedure yields pseudorandom acquisition parameters. We consider $S = 1\,000$ samples. FA and TR patterns as well as example magnitude synthetic MRF signals are shown in figure 4.6(a-c). The parameters of interest ($P = 3$) are the relaxation times T_1 (between 200 and 3 000 ms) and T_2 (between 20 and 300 ms), and the off-resonance Δf (between -200 and 200 Hz). Signals are generated using the simulation tool[2] described in [157].

Note that compared to the vascular MRF signals used in the previous study, standard signals are vectors of complex-valued samples. For the DBM method, the scalar product extends to complex data. However, to consider these complex samples using the two DBL methods, signals are doubled in size and composed of the real and imaginary parts of the initial signals [167, 168].

4.2.2.2 Aliasing noise as modulated Gaussian noise

In [192], authors introduce a tool to rapidly assess the efficiency of an MRF sequence in the presence of both normal and aliasing noise. In MRI, the acquired signal contains both Gaussian noise $\boldsymbol{\eta}_{\text{thermal}}$ as the result of thermal contributions (section 2.2.2.4), and correlated aliasing noise $\boldsymbol{\eta}_{\text{aliasing}}$ due to spatial undersampling artifacts (section 2.2.2.3). According to this work, the aliasing noise can be modeled as proportional to the signal at each sample, with a coefficient of proportionality that is taken to be zero-mean Gaussian noise. It results that a noisy signal $\mathbf{y}_{\text{noisy}}$ is computed from an original signal $\mathbf{y}$ as:

$$\mathbf{y}_{\text{noisy}} = \mathbf{y} + \boldsymbol{\eta}_{\text{thermal}} + |\mathbf{y}|\,\boldsymbol{\eta}_{\text{aliasing}}\,. \tag{4.1}$$

In our experiments on aliasing artifacts, we focus on the case where aliasing noise is dominant so that $\boldsymbol{\eta}_{\text{thermal}} = 0$. In addition, we have empirically determined the relationship between the standard deviation σ_{aliasing} of $\boldsymbol{\eta}_{\text{aliasing}}$ and the undersampling factor R (validity range 1-50) as $\sigma_{\text{aliasing}} = (3R - 2)/100$. This entire procedure provides typical undersampled MRF signals, see examples in figure 4.7(d-f).

[2] https://bitbucket.org/asslaender/nyu_mrf_recon/src/master/

4.2.2.3 Analysis workflow

In this study, we repeat the framework described in section 3.3. We remind that:

1. N vectors $\mathbf{x}$ of P parameters are sampled according to a grid (for the DBM method) or to a quasi-random sampling (for DB-SL and DB-DL methods) in the parameter space.
2. S-sample signals $\mathbf{y}$ are simulated from $\mathbf{x}$ according to a simulation function f (i.e. equation (3.7) for scalable signals and the simulation tool described in [157] for standard MRF signals, see section 4.2.2.1) to build the dictionary $\mathcal{D}_f$.
3. For DB-SL and DB-DL methods only, $\mathcal{D}_f$ is used to learn the model that maps the relation between the signal and the parameter spaces, using the GLLiM model for DB-SL and the NN for DB-DL. The learning is done according to $\mathcal{C}$.
4. M vectors $\mathbf{x}$ of P parameters are sampled according to a random sampling in the parameter space and then, S-sample signals are simulated using $\mathbf{x}$ and the simulation function f.
5. Prior to parameters estimation and depending on the experiment, thermal or aliasing noise at a specific level may be added using equation (4.1).

4.2.2.4 Bias-variance analysis

In [164], authors proposed to investigate the statistical properties of the reconstruction methods using a bias-variance analysis. We propose to conduct a similar analysis here. M test signals are simulated and for each signal, $I = 100$ random Gaussian noises are applied, according to a fixed SNR. To compare the bias, variance and RMSE, the following quantities are computed for the m^{th} test signal $\mathbf{y}_m$:

$$\text{Bias}_m = \hat{\mathbb{E}}\left[\mathbf{y}_m - \hat{\mathbf{y}}_m\right] , \tag{4.2}$$

$$\text{Var}_m = \hat{\mathbb{E}}\left[(\hat{\mathbf{y}}_m - \hat{\mathbb{E}}\left[\hat{\mathbf{y}}_m\right])^2\right] , \tag{4.3}$$

where $\hat{\mathbb{E}}\left[\,\cdot\,\right]$ is the empirical mean for the 100 Monte Carlo simulations: we have $\hat{\mathbb{E}}\left[\hat{\mathbf{y}}_m\right] = \sum_i^I \mathbf{y}_{m,i}$. Note that

$$\text{RMSE}_m = \hat{\mathbb{E}}\left[(\mathbf{y}_m - \hat{\mathbf{y}}_m)^2\right] = \sqrt{\text{Bias}_m^2 + \text{Var}_m} , \tag{4.4}$$

is the error used in the previous study, chapter 3. We provide supplemental details about bias-variance analysis in appendix C.1.

4.3 Results

4.3.1 Synthetic scalable signals

4.3.1.1 Model size: memory and simulation requirement

We investigate the model size growth as a function of the experimental conditions and model calibration. For different calibration variable values: $Z = 100$, 300, 500, and $Z = S$ and $H = 2$, 3, 5, and 10 for DB-DL and $K = 50$, 75, 100, and 200 for DB-SL. We present the model sizes as a function of the signal length S up to 3 000 samples (figure 4.2(a-c)). Then, the model sizes for the proposed implementation calibration variable values are show in figure 4.2(d). For our applications, we have in vascular MRF $S = 100$, in standard MRF $S = 1\,000$, and $S = 2\,000$ when concatenating the real and imaginary parts.

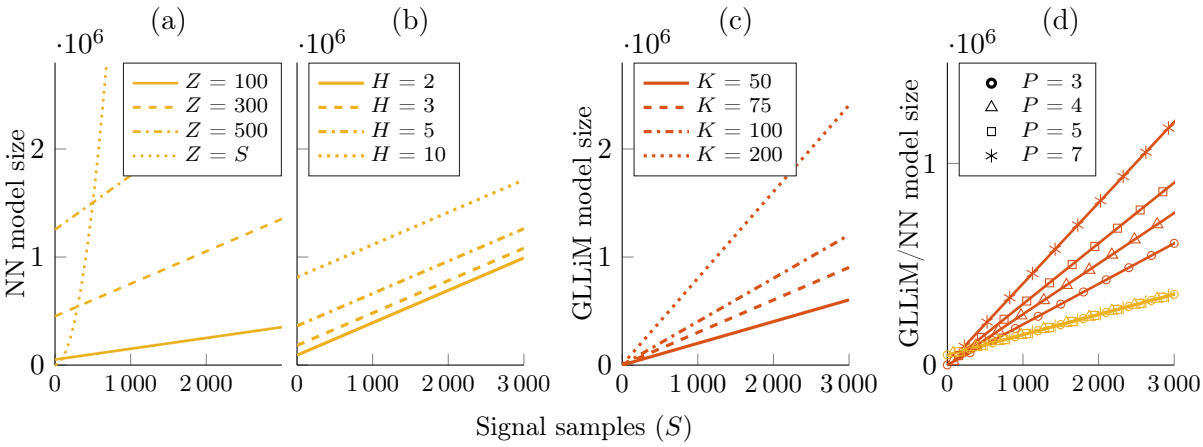

Figure 4.2 – Relation between calibration variables and model sizes of GLLiM and NN models.
Plots show the model sizes: Gaussian locally linear mapping (GLLiM) in red and neural network (NN) in yellow as a function of the number of signal samples S. Plots (a) and (b) show the NN model size depending on the number of nodes Z ($H = 2$) and depending on the number of hidden layers H ($Z = 300$), respectively. Plot (c) shows the GLLiM model size depending on the number of Gaussian distributions K. In (a-c), P is set to 3. Plot (d) shows the GLLiM and NN model sizes for different number of parameters (3, 4, 5, and 7) with the implementations, used in the following, i.e. $K = 50$ for DB-SL and $H = 6$ and $Z = 100$ for DB-DL.

For DB-DL, we observe that, when setting Z to a specific value, the model scales when S increases, when $S \ll Z$ a dimension reduction is performed while $Z = S$ leads to a quadratic growth of the model size. H has a minor influence on the model size, values in the range 1-6 are generally chosen. For DB-SL, the model size growth is linearly dependent on K and P. As proposed (i.e. Z fixed), the DB-DL better scales when

increasing the number of parameters, because the model size marginally depends on P (figure 4.2(d)) while DB-SL model size does.

Once the model is learned, the memory required to store this model is fixed and does not depend on the number of dictionary entries. For the proposed implementations, $S = 100$ and $P = 3$, the methods require the storage of 60 903 and 20 750 coefficients for DB-DL and DB-SL models, respectively. Numbers of model parameters are 150 903 for DB-DL and 201 650 for DB-SL with $S = 1\,000$.

4.3.1.2 Computational times

We investigate the impact of dictionary size (number of entries) on estimation time for DBM and both DBL methods, and on learning time for DBL methods. We consider successively $P = 3$, 4, 5, and 7 parameters and use synthetic scalable signals ($S = 100$). The number of dictionary entries N vary between 10^2 and 10^6 (figure 4.3). The grid sampling and the quasi-random sampling are used for DBM method and DBL method, respectively. The quantification time is given for $M = 10\,000$ test signals. Note that we execute both CPU-based and GPU-based implementations for the DB-DL method.

Concerning quantification times, we observe that the DBM method quantification time is proportional to N and independent of P. Linear regression provides a proportionality coefficient of 15.40×10^6 s/dictionary entries ($R^2 = 0.998$). Both DBL method quantification times do not depend on N, but depend on P, especially for the DB-SL method. For $P = 3$, the average reconstruction time is 670.4 ± 32.9 ms and 48.8 ± 12.0 ms for DB-SL and DB-DL methods, respectively. Using a GPU-based implementation (not available for DB-SL), the average reconstruction time decreases to 25.5 ± 0.5 ms for the DB-DL method (about twice faster).

Concerning the dictionary learning times, for $N \leq 25\,000$ the DB-SL is faster than the DB-DL (CPU-based implementations). Above this value, the DB-DL method learning is the fastest and both methods learning times are proportional to N ($R^2 = 0.956$ and $R^2 = 0.995$ for DB-SL and DB-DL, respectively). For $N \geq 25\,000$, the GPU-based implementation provides a 4.17 ± 0.49 speed gain in our simulation conditions.

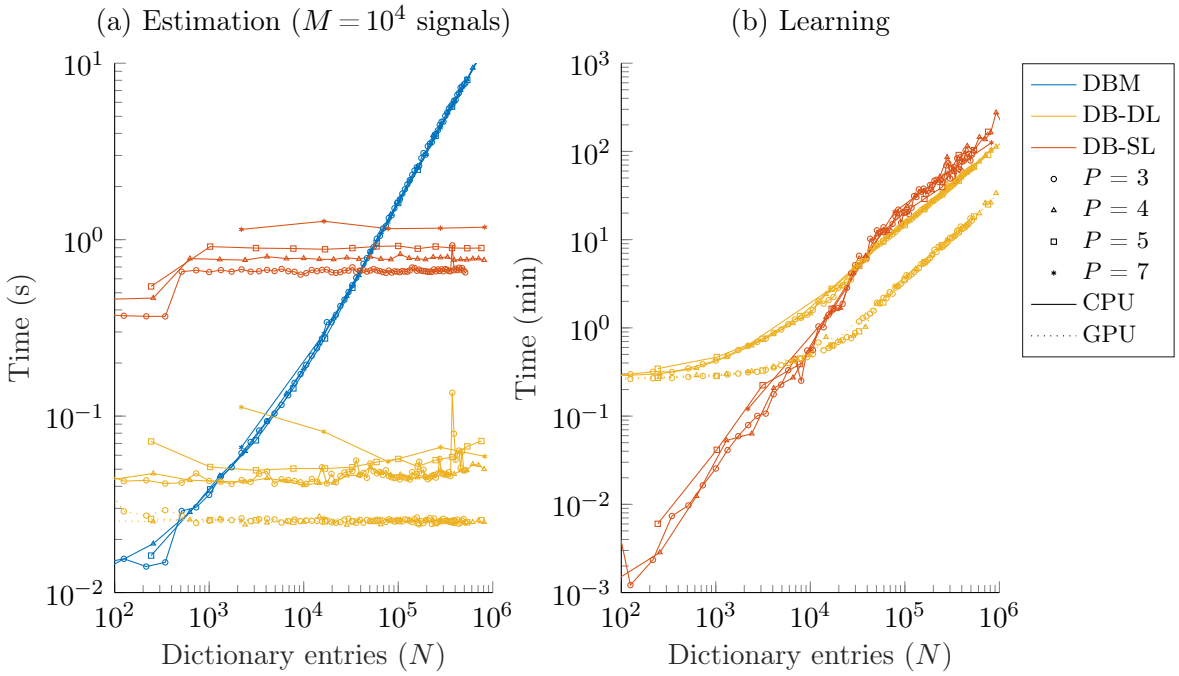

Figure 4.3 – Estimation and learning computational times for DBM, DB-SL and DB-DL methods.
Figure (a) shows $S = 100$-sample signal estimation times (in seconds for $M = 10\,000$ test signals) for the tree methods, and figure (b) shows learning times (in minutes) for DB-SL and DB-DL methods only. Different values of P are used (3, 4, 5 and 7). Computer hardware is a 32-CPU *Intel Xeon Gold* 6130, 2.1 GHz, 384 GB system memory with a *GPU Nvidia RTX2080 Ti*, 4352 CUDA cores, 11 GB memory.

4.3.1.3 Impact of the dictionary size and noise on parameter estimation accuracy

We investigate the impact of dictionary size reduction and SNR on estimate accuracy, using the same four previous conditions (on P and N) and synthetic scalable signals (see section 3.3.1.2). For each condition, we compute the average RMSE, using $M = 10\,000$ test signals. To characterize the effect of thermal noise, two noise levels (SNR = 20 and SNR = 100) are added (figure 4.4).

As already shown in section 3.4.1.3, we observe that with the DBM method and with low noise level (SNR = 100), the RMSE decreases as the dictionary size increases (linear relations between log-values; $R^2 \geq 0.994$). While for DBL methods, the RMSE decreases when increasing the number of dictionary entries and then plateaus. We observe that RMSE are similar between the DB-SL and DB-DL methods with a slight improvement for the DB-DL method (the mean RMSE decrease of DB-DL compared to DB-SL is 8.31 ± 4.62 % including all conditions). For SNR = 20, we observe that the errors of all

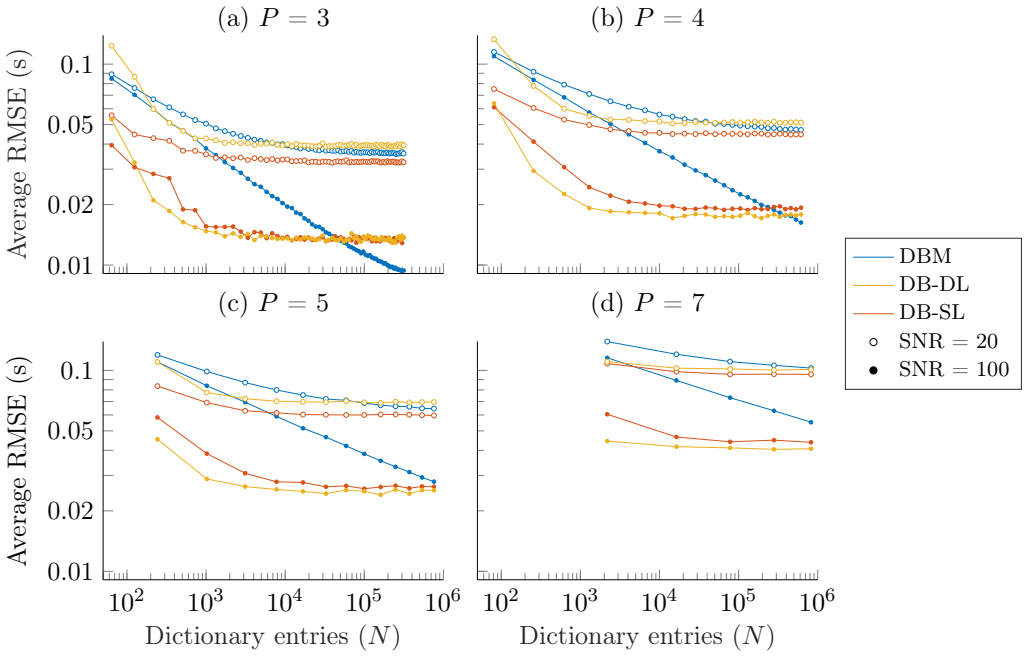

Figure 4.4 – Impact of dictionary size and noise level on DBM, DB-SL and DB-DL methods.
Average RMSE are given with respect to the number of dictionary entries N for two noise levels: SNR = 20 (empty circle) and SNR = 100 (filled circle). Average RMSE ($M = 10\,000$ test signals) for (a) $P = 3$, (b) 4, (c) 5, and (d) 7 parameters.

methods are increased. The DB-SL method RMSE is always the smallest (the mean RMSE increase of DB-DL compared to DB-SL is $15.11 \pm 7.47\,\%$ including all conditions).

4.3.1.4 Boundary behavior

To investigate the behavior of methods outside the limits of the parameter space covered by the dictionary, we define a dictionary ($N = 10\,000$) composed of two disjoint patches in the parameter space, generate $M = 2\,000\,000$ test signals in the entire parameter space and evaluate the average RMSE for each parameter value (figure 4.5(a-c)). Then, we repeat the experiment adding 3 more signals to the dictionary distant from the initial patches in the parameter space (figure 4.5(d-f)).

Compared to the DBM method, DBL methods allow accurate estimates (RMSE < 0.1 s) between patches. In addition for DB-SL method, estimates remain accurate (RMSE < 0.1 s) in a large bands around patches. We refer to this model property as the *generalization*, i.e. the ability of the model to react to new data outside the dictionary space.

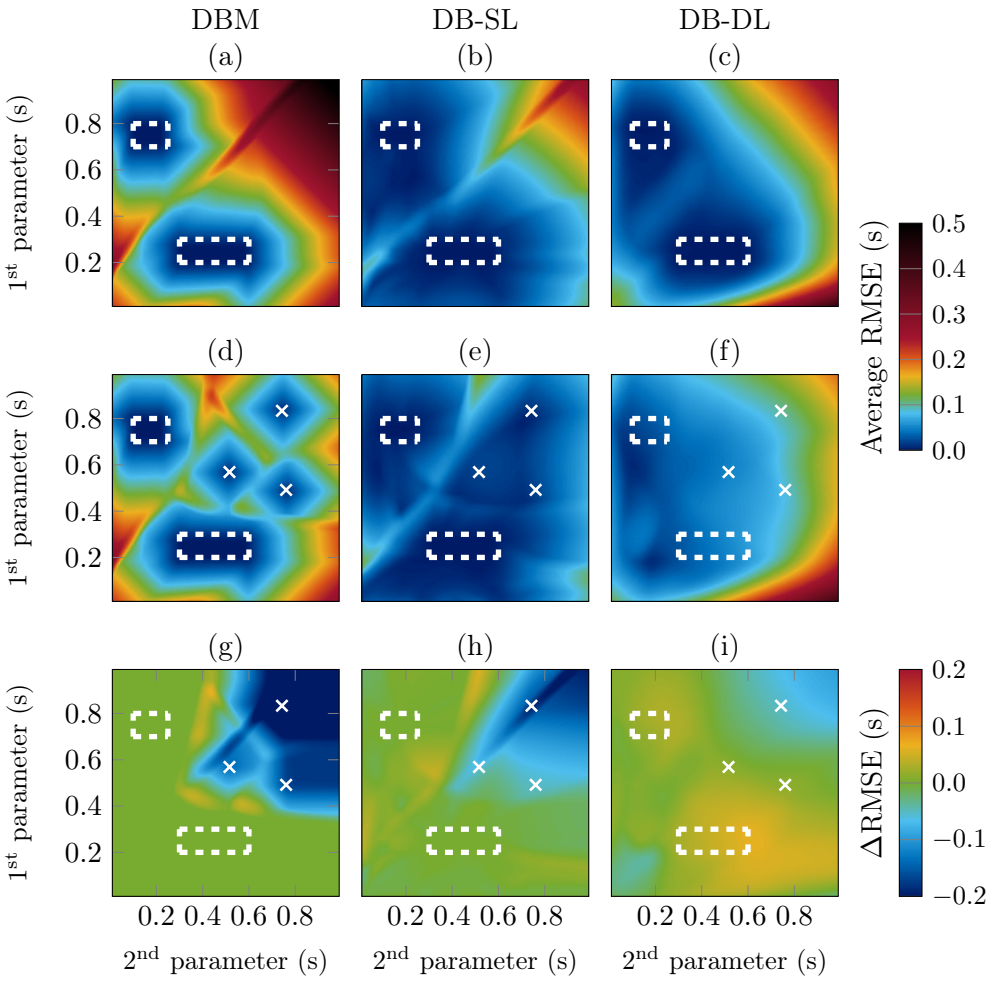

Figure 4.5 – Estimation accuracy outside the limits of the parameter space covered by the dictionary.
Average RMSE ($M = 2\,000\,000$ test signals) in the parameter space ($P = 2$) obtained (a, d) with the DBM, (b, e) with the DB-SL, and (c, f) with the DB-DL. The white dashed lines delimit the subspace covered by the dictionary. In figures (d-f), 3 additional signals (white marks) are added to the dictionary in figures (a-c). Figures (g-i) show the difference between the RMSE using additional entries in (d-f) and original RMSE in (a-c). Blue indicates decreased RMSE while yellow indicate increased RMSE. Green corresponds to the absence of change. The average RMSE is computed from signals in a 50×50 ms sliding window, moving in 5 ms steps in the parameter space.

Few additional dictionary entries allow to extend the band space coverage for DB-SL method, but not for the DB-DL method and even this leads rather to a deterioration of the estimate accuracy in the space covered by the patches (yellow in RMSE difference maps, figure 4.5(g-i). It demonstrates relative instability of the DB-DL quantification compared to DBM and DB-SL methods that do not exhibit changes away from the new entries.

4.3.2 Standard MRF signals

4.3.2.1 Estimate accuracy and noise

To compare dictionary-based methods on synthetic standard MRF signals, without spatial undersampling noise, we generate two dictionaries of $N = 4\,096$ (small dictionary) and $N = 226\,981$ entries (large dictionary) according to properties given in section 4.2.2.1. We evaluate the average RMSE on $M = 10\,000$ test signals, for thermal noise and SNR values between 10 and 110 (figure 4.6).

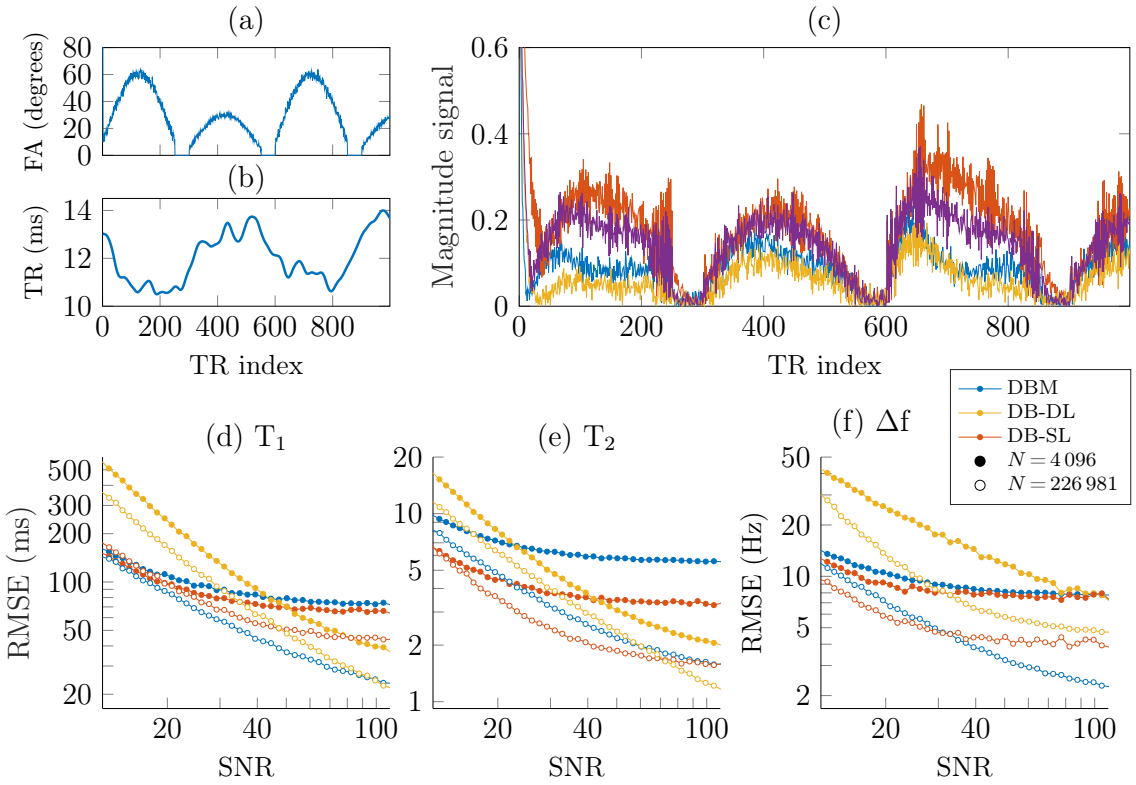

Figure 4.6 – Comparison of dictionary-based matching (DBM) and learning (DB-SL and DB-DL) methods for different noise levels, using synthetic MRF signals.
Figures (a, b) show the acquisition sequence settings: flip angles (FA) and repetition times (TR). Figure (c) shows the signal evolution of four synthetic MRF signals ($S = 1\,000$). Figures (d-f) show the RMSE ($M = 10\,000$ test signals) on relaxation times (T_1 and T_2) and off-resonance (Δf) parameters ($P = 3$) using the DBM and the two DBL methods with $N = 4\,096$ and $N = 226\,981$ dictionary entries.

For SNR < 40 and all parameters, DB-SL method is always better than DB-DL method, whatever the number of dictionary entries. For SNR > 70, DB-DL method is better than DB-SL method for T_1 and T_2 estimates. Then, similarly for $N = 4\,096$, considering SNR ≤ 55, RMSE are T_1: 216.3 ms, T_2: 7.3 ms, Δf: 22.6 Hz for DB-DL and

T_1: 93.6 ms, T_2: 4.4 ms, Δf: 9.0 Hz for DB-SL. For SNR > 55, RMSE become T_1: 44.2 ms, T_2: 2.2 ms, Δf: 8.4 Hz for DB-DL and T_1: 66.1 ms, T_2: 3.4 ms, Δf: 7.6 Hz for DB-SL.

4.3.2.2 Highly undersampled data

To investigate the estimation accuracy of dictionary-based methods with highly undersampled data, we use the two previous dictionaries. A 4-region human brain phantom is generated, resolution is 128×128 (figures 4.7(a-b)). In each region T_1 and T_2 values are sampled according to a normal distribution around a central value (1 000, 1 400, 1 800 and 2 200 for T_1 and 60, 120, 180 and 240 for T_2). An off-resonance map (Δf) is generated by linear increase following each direction, between -200 and 200 Hz, figure 4.7(c). This phantom results in $M = 7\,622$ test signals. Noise is added to test signals according to equation (4.1), with undersampling factor between 1 and 50. Examples of resulting signals for 3 undersampling factors (8, 16 and 48) are shown in figures 4.7(d-f).

We observe that the RMSE increases significantly with the undersampling factor. For T_1, RMSE remain below 300 ms ($\approx 10\,\%$) until undersampling factors of 10 for DB-DL and 22 for DB-SL. For T_2, RMSE remain below 30 ms ($\approx 10\,\%$) until undersampling factors of 46 for DB-DL and 38 for DB-SL. Note that the impact of the number of entries in the dictionary is no longer visible when the aliasing noise increases.

4.3.2.3 Model variance

To investigate the statistical properties of the methods, we conduct a bias-variance analysis (section 4.2.2.4). The model used is the one computed using the $N = 4\,096$ dictionary entries. 100 random noises are generated according to SNR = 40 for each value of the previous brain phantom ($M = 7\,622$). Bias, variance and RMSE are computed according to equations (4.2), (4.3) and (4.4), respectively. Resulting maps are presented in figure 4.8(a-c). Mean values for each map and those obtained with the $N = 226\,981$ dictionary entries, are given in table 4.8(d).

For T_1 and T_2, we observe that the DB-DL method is the less biased method with a mean bias about twice smaller than the one of the DB-SL method, but exhibits larger variance. Consequently, DB-DL RMSE are higher for both T_1 and T_2 than DB-SL RMSE, see table 4.8(d). We observe that compared to the DBM method, DBL methods provide errors that depend on underlying parameter maps such that we can distinguish brain structures in error maps.

For off-resonance Δf, the DBM provides the smallest RMSE. We suppose that complex-valued computation could be the reason of this better estimate accuracy compared to DBL methods. Interestingly, the grid sampling of the dictionary can be visualized as diagonal error lines. Black lines (corresponding to a small error) are located at the dictionary values. DB-SL provides significantly larger error on Δf.

4.3.3 Summary of results

We summarize results obtained in the previous sections in table 4.1. In this table, cells are colored according to the performance of methods e.g. it is arbitrarily consider that the estimation of an MRI image (about 10^6 voxels) should ideally be done in less than 5

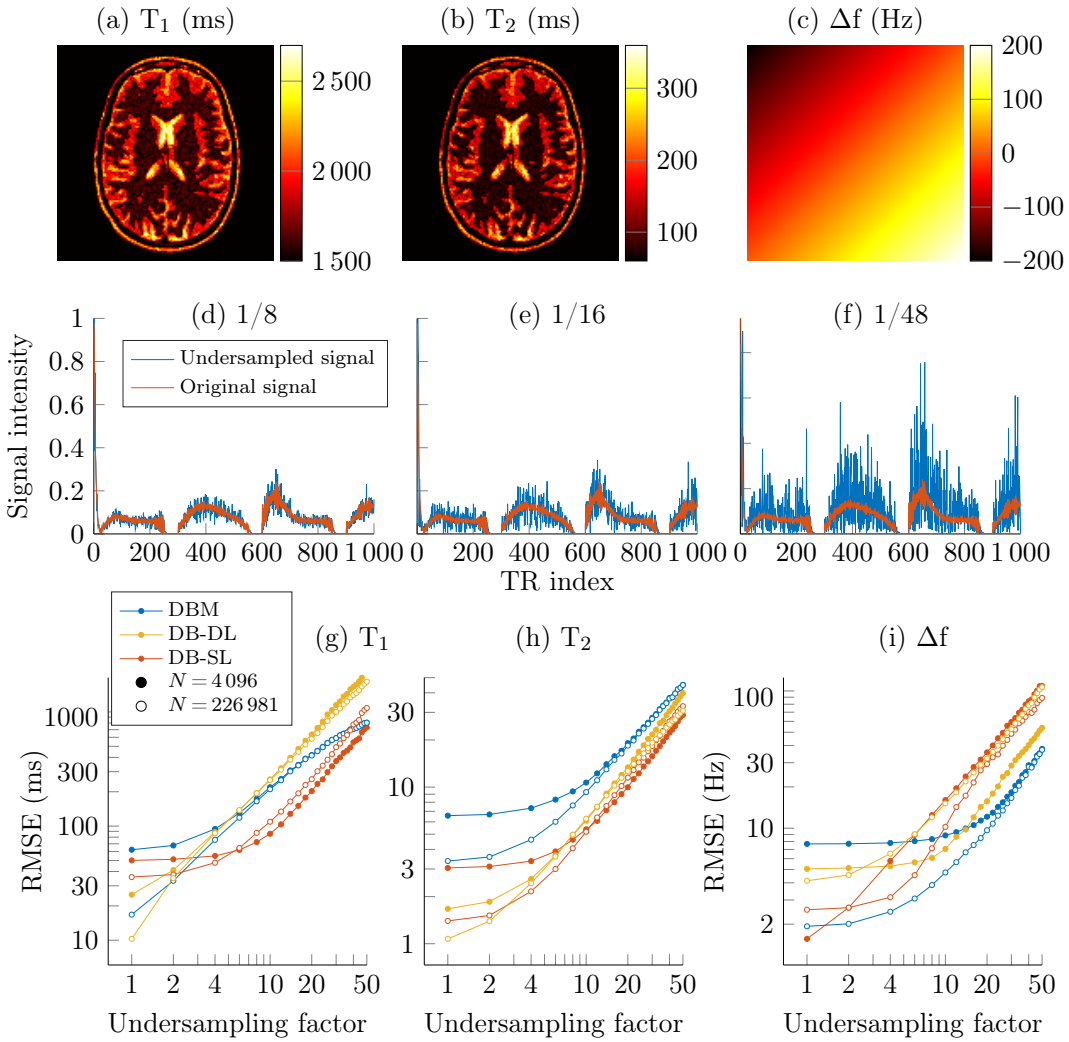

(caption of the figure on the next page)

Figure 4.7 – Robustness to data undersampling of dictionary-based methods, using synthetic MRF signals (*on previous page*).
Figures (a-c) show parameter maps ($P = 3$: T_1, T_2 and Δf) used for simulating the $M = 7\,622$ test signals. Figures (d-f) show an example of a signal altered by undersampling according to factors 8, 16 and 48. Figures (g-i) show RMSE on estimated parameters for the three dictionary-based methods using $N = 4\,096$ and $N = 226\,981$ dictionary entries. RMSE are given as a function of the undersampling factor.

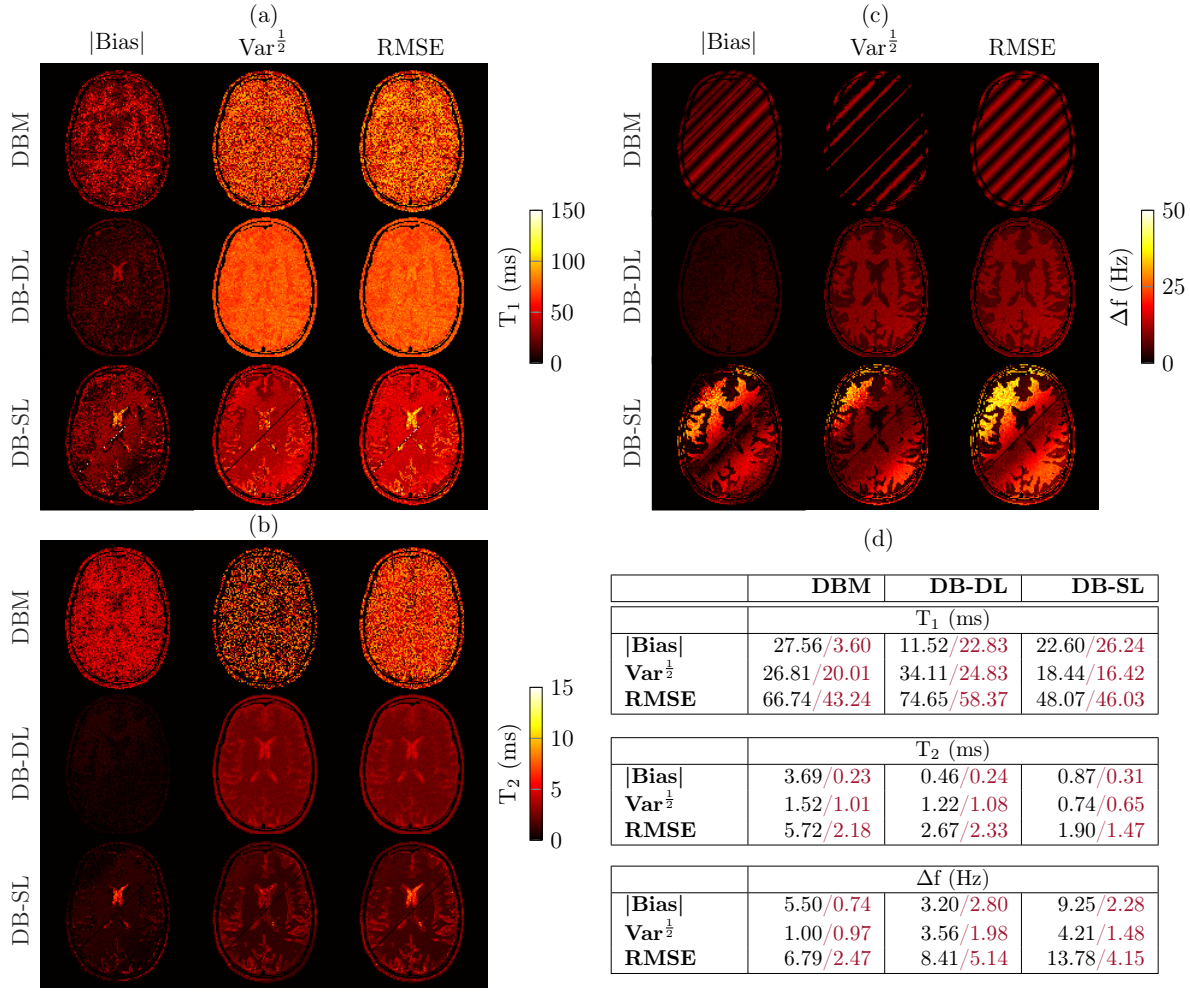

	DBM	DB-DL	DB-SL
	T_1 (ms)		
|Bias|	27.56/3.60	11.52/22.83	22.60/26.24
Var$^{\frac{1}{2}}$	26.81/20.01	34.11/24.83	18.44/16.42
RMSE	66.74/43.24	74.65/58.37	48.07/46.03
	T_2 (ms)		
|Bias|	3.69/0.23	0.46/0.24	0.87/0.31
Var$^{\frac{1}{2}}$	1.52/1.01	1.22/1.08	0.74/0.65
RMSE	5.72/2.18	2.67/2.33	1.90/1.47
	Δf (Hz)		
|Bias|	5.50/0.74	3.20/2.80	9.25/2.28
Var$^{\frac{1}{2}}$	1.00/0.97	3.56/1.98	4.21/1.48
RMSE	6.79/2.47	8.41/5.14	13.78/4.15

Figure 4.8 – Bias-variance analysis for dictionary-based methods, using synthetic MRF signals.
Figures (a-c) show bias, variance and RMSE maps ($M = 7\,622$) for the dictionary-based methods on (a) T_1, (b) T_2 and (c) Δf ($P = 3$), using $N = 4\,096$ dictionary entries. Table (d) reports mean values throughout the maps. In this table, values in red, were computed using the $N = 226\,981$ dictionary.

minutes (yellow color, red above) and that a map generation in less than one minute would be a very good performance (green color).

	Small dictionary ($N \approx 4\,000$)			**Large dictionary** ($N \approx 200\,000$)		
	DBM	DB-DL	DB-SL	DBM	DB-DL	DB-SL
Resources						
(*)**Memory** (.10^3 doubles)	412-428	60-62	**20-43**	20 600-21 400	60-62	**20-43**
(*)**Estimation time** (s) for 10^6 acquisitions	9	**4-11**	67-114	391	**5-7**	66-116
Estimate accuracy (%)						
Standard data (SNR = 50-100)	2.2	**1.7**	1.8	**0.8**	1.0	1.1
Thermal noise (SNR = 20-40)	3.0	5.7	**2.4**	**2.0**	3.7	**2.0**
Aliasing noise ($1/24^{\text{th}}$-$1/48^{\text{th}}$)	8.9-17.1	13.8-36.4	**5.6-15.0**	**8.7-17.0**	12.4-31.3	**7.9-22.1**
Others						
Bias-variance trade-off (ratio bias/variance$^{\frac{1}{2}}$)	3.0	0.5	1.5	0.4	0.8	1.2
Flexibility (Card ($\mathcal{C}$))	**0**	2	1	**0**	2	1
(*)**Generalization**	No	Few	**Yes**	No	Few	**Yes**

Table 4.1 – Performance of the three dictionary-based methods: matching and learning. (*) indicate performance evaluated using synthetic scalable signals. The others were obtained using MRF standard signals. For synthetic scalable signals, range of values represents the performance for $P = 3$ to $P = 7$. Cells are colored according to the associated performance. Green, yellow and red cells indicate very good, good/correct and bad performance, respectively. Best results are highlighted in bold.

We observe that each method has its own specific domains of application. Briefly, DBM is very flexible and achieves very good performance with good noise robustness for large dictionary entries but requires considerable resources (time and memory). DB-DL is extremely fast but exhibits low performance with high noise levels both thermal and aliasing. DB-SL provides good estimate accuracy even in noisy conditions and has the ability to preserve good accuracy outside the space covered by the dictionary. It is interesting to note that DB-SL is the best performing method for the small dictionary.

4.3.4 Ensemble learning

To produce more accurate estimates, we propose to combine the two DBL models to get an ensemble model with better performances [193]. We investigate here two ensemble learning approaches. The *bagging* learns models independently from each other in parallel and combines them following a deterministic averaging process (figures 4.9(a)). The *boosting* learns them sequentially, i.e. each model depends on the previous ones (here, DB-SL then DB-DL, figure 4.9(b)). The way to combine models has to be adapted to their types. Briefly, we can say that bagging will mainly focus at getting an ensemble model with less variance than its model components whereas boosting will mainly try to produce strong models less biased than their components (even if variance can also be reduced).

For each combination, we try two strategies: a first, standard, using only estimates and as the confidence index (CI) is correlated to the RMSE, we investigate its consideration in combination in figure 4.10(a). For the bagging, first, we compute standard mean and then, we compute a weighted mean using the CI, i.e. $w_{\text{DB-SL}} = (\text{CI}_{\text{max}} - \text{CI})\,/\text{CI}_{\text{max}}$ and $w_{\text{DB-DL}} = 1 - w_{\text{DB-SL}}$, where CI_{max} is the maximum CI value. It results that the smaller the CI, the more weight is given to the DB-SL method and the larger the CI, the more weight is given to the DB-DL method. For the boosting, first, we use the DB-SL estimate as the input of the DB-DL and them, we use both the estimate and CI as the inputs of the DB-DL in figure 4.10(b).

We observe that when computing the mean estimates from DB-SL and DB-DL estimates, the RMSE decreases so that the mean RMSE is better than both individual RMSE. In particular, whatever the SNR, the combined RMSE is always smaller than the DB-DL RMSE. Regarding the serial combination, the mean RMSE is also better than individual RMSE and in particular, the RMSE of the ensemble mdoel is always better than the DB-SL RMSE. Considering the CI does not improve much the results.

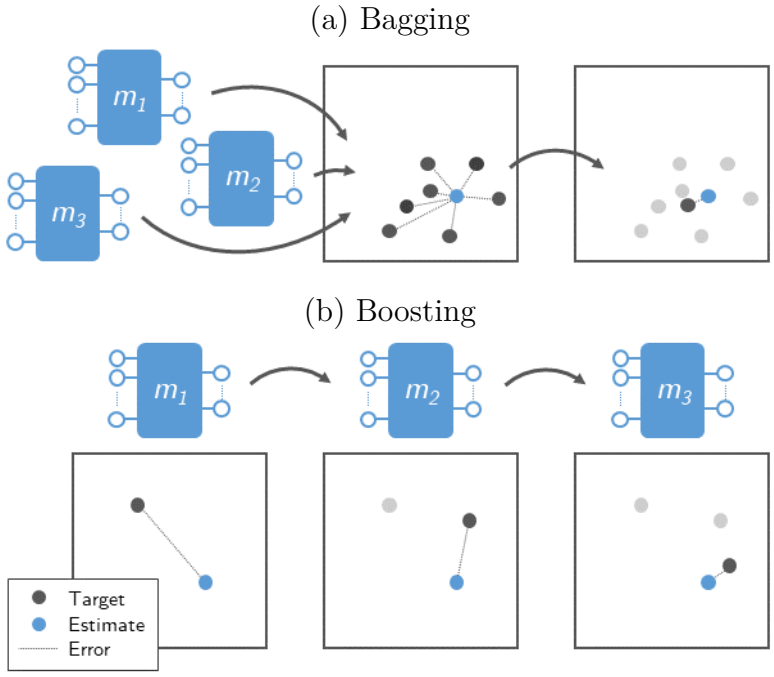

Figure 4.9 – Illustrations of ensemble learning model combinations.
(a) Bagging ensemble learning. (b) Boosting ensemble learning.

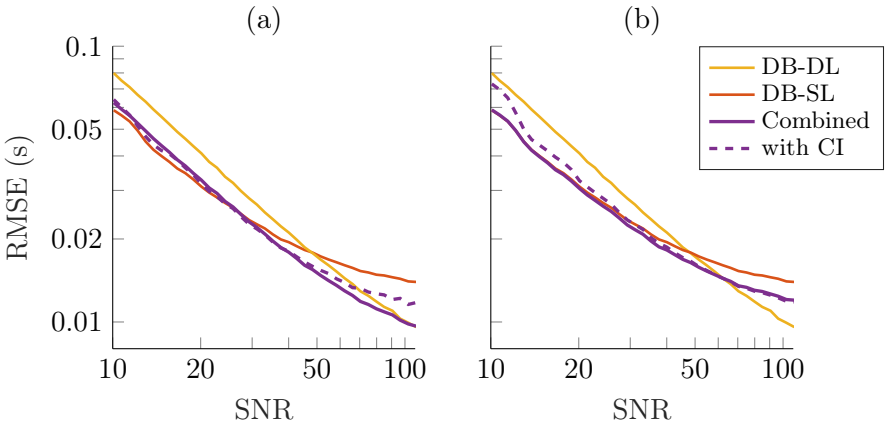

Figure 4.10 – Combination of statistical and deep learning methods, using synthetic scalable signals.
Figure (a) shows RMSE ($M = 10\,000$) obtained computing the mean estimates (*Combined*) and the confidence index weighted mean estimates (*with CI*) of DBL methods. Figure (b) shows RMSE resulting from the use of DB-SL estimates as input of DB-DL (*Combined*) and the estimates and confidence index as input of DB-DL (*with CI*). In both figures, RMSE obtained using only DB-SL and only DB-DL methods are plotted.

4.4 Discussion, conclusion and perspectives

This study presents a comparison of three methods for estimating standard MRF parameters (T_1, T_2 and off-resonance) based on dictionary matching and dictionary learning methods. We have shown that DBL methods provide scalability as compared to DBM method, while preserving DBM accuracy on a standard application when using large dictionaries and increasing accuracy when using small dictionaries (consistent with the previous chapter). DBL methods produce parameter maps much faster with quantification times not related to the size of the dictionary. In terms of speed, the DB-DL is 10-100 times faster than DB-SL and even faster with GPU implementations. The proposed DB-SL method is as robust as DBM to both thermal and aliasing noises while the DB-DL method faces some difficulties with noisy data. In addition, the DB-SL method exhibits good generalization performance as compared to DB-DL, i.e. DB-DL biased towards the sample distribution, while DB-SL model is smoother. Moreover, few additional distant entries in the dictionary allows a large improvement of the DB-SL accuracy in the neighborhood of these new entries while it leads to a general degradation in the whole space for the DB-DL. This behavior is not yet completely understood but other works reported the fully-connected NN tendency to overfit due to the huge number of parameters [167]. This could be a first clue.

Regarding the architecture of the neural network, further investigations could certainly find a design that provides better results. However, compared to the initial implementation proposed by Cohen et al. in [165], we have already modified both the number and composition of hidden layers, and activation functions in order to increase performance. Note that experiments on synthetic signals have first been realized with the initial architecture of [165], resulting in almost as good performance (results not shown). Additionally in both [173] and [174], authors reported that the fully connected NN introduced by Cohen et al. is more accurate in terms of RMSE than the convolutional NN introduced by Hoppe et al. [166] in both white matter and gray matter. Considering that mainly convolutional networks have been proposed for MRF [166, 194, 195], this is reassuring about the impact of choosing fully connected NN instead. However, other networks have been proposed such as recurrent NN [167, 196] and are not presently compared. In the last table, we reported the flexibility of the methods and consider only the setting once the architecture has been fixed (i.e. fully-connected). We assume that a constant number of nodes per layer is used. Considering all possible NN architectures would result in an unreasonable number of possibilities and can be seen as a limitation

of this approach. Although we cannot claim to have used the best possible design, the time spent in tuning the NN parameters was considerably higher than the time spent on tuning the DB-SL, which consisted only in the choice of the covariance matrices constraints and the selection of the number of Gaussian distributions in the mixture model.

In this study, we extended our approach to complex-valued signals by splitting the real and imaginary parts resulting in twice larger input signals as proposed in other works [167, 168]. However, such a representation could not respect the phase information that is captured by complex algebra [168]. In this work, authors thus introduce a new complex activation function for complex NN and showed that complex-valued NNs outperform 2-channel NNs. An adaptation of GLLiM for complex-valued data, which is possible, could improve the estimation of parameters from complex signals. Interestingly, both 2-channel and complex-valued NNs do not reach the DBM accuracy in estimating B_0 as observed in this study and in agreement with other work [168]. This may still be a limitation as compared to the initial DBM method.

An interesting point that, to the best of our knowledge, has not been discussed is the structure of the error on maps found in the majority of DBL works, including ours, see figure 4.8. Indeed, we observe that in RMSE maps using DBL methods, most of the brain structures can be distinguished while it does not when using DBM. It may be interesting to keep this in mind when interpreting the results since it means that we do not have a constant error across the estimated maps (e.g. white noise). Interestingly, using the DB-SL method, this information can be found in CI maps. We believe that knowing the average performance of a method is very valuable, but being able to predict it on new estimates has a totally different impact. Now that we have shown that it is possible to have access to such information, an optimization in this direction could be an opportunity for improvement.

In conclusion, this method irrefutably highlights the interest of learning methods as compared to matching ones. This comparison of the DBL methods shows that the proposed statistical learning method outperforms the fully-connected deep learning approach in standard MRF conditions, i.e. thermal noise and highly spatial aliasing noise. Nevertheless, there may still be a need to improve the DB-SL implementation in order to accelerate quantification. The real and imaginary 2-channel DB-SL method can handle complex-valued data but cannot directly capture complete complex algebra while some DB-DL method can [168]. This requires an adjustment of the inverse regression model, which is left as a short term future work.

Chapter 5

Murine model study of MTLE

To investigate the identification of the epileptogenic zone and associated seizure spreading regions, we use a multi-parametric MRI analysis at 9.4 T. We examined, elaborated and combined multiple cellular and neurovascular MRI parameters as imaging biomarkers of the epileptogenic and seizure propagating regions. Analyses were performed longitudinally in an experimental model of mesial temporal lobe epilepsy (MTLE). The previous proposed quantitative DB-SL method is compared with the CEF method.

5.1 Introduction

Defining the epileptogenic zone and the anatomical boundaries of seizure spreading networks in experimental or clinical focal epilepsies requires a complex clinical toolkit that includes magnetic resonance imaging (MRI) [89, 101, 105, 107]. Novel imaging approaches are based on the analysis of the multiple cellular and cerebrovascular dynamics that unfold during seizures, particularly blood-brain barrier permeability [197–199], perfusion modifications [200, 201], pathological neurovascular cell remodeling [84, 202], angiogenesis [62], and glial cells inflammation [203]. Cellular changes can translate into T_1, T_2, or diffusion modifications [91–93, 100], while cerebrovascular damage can be examined using gadolinium-based MRI [96, 204], with an extension to hemodynamic measurements such as cerebral blood flow or cerebral blood volume [105, 205], see details in section 2.1.3.4. However, no clear consensus has emerged on a single clinically applicable MRI parameter that would significantly improve the identification of the epileptogenic zone and the associated seizure propagating regions.

Here, we developed a multi-parametric MRI approach based on the quantification of four cerebrovascular (blood volume, microvessel diameter, tissue oxygen saturation

and BBB permeability) and three cellular (T_1, T_2, and diffusion contrast) parameters, allowing the acquisition of data within an examination session in each animal. Using a model of mesio-temporal lobe epilepsy (MTLE) elicited by a unilateral intra-hippocampal kainic acid (KA) injection [85, 206], we tracked the MRI modifications in the ipsilateral epileptogenic [207] and in the contralateral seizure propagating hippocampi. We mapped all MRI parameters with equal spatial resolution to obtain multiple values per image pixel. To derive an integrated information, we used standard statistical approaches (nearest neighbors, discriminant analysis, support vector machine, naive Bayes and decision tree) to classify the multi-parametric pixels, with the goal of discriminating the ipsilateral from the contralateral hippocampi, and comparing to sham animals.

5.2 Materials and methods

5.2.1 Animals

C57BL/6J male mice (8-10 weeks, Janvier LABS, Saint Berthevin, France), were housed in individual cages after surgery with food and water ad libitum and maintained in a 12-hour light-dark cycle (room temperature: 22 ± 1°C). All animal procedures were performed in accordance with the European Committee Council Directive 2010/63/EU after validation by our local ethical committee and authorization from the French Ministry of Research (#8804-2014121714272897 v6).

5.2.2 MTLE model

A stereotaxic injection into the right dorsal hippocampus of 50 nL of a 20 mM solution of KA (i.e. 1 nmol; Sigma, Lyon, France) was performed under general anesthesia (4 % chloral hydrate), as previously described and used by different groups [84, 85, 206, 208], while sham mice received 0.9 % NaCl. After KA injection, asymmetric clonic movements of the forelimbs and head deviations, rotations, and periods of immobility were observed for several hours [85]. After surgery, the mortality rate was 10.7 %. Animals that did not exhibit any of these signs were excluded from the study. These archetypical behavioural modifications lead to electrographic spontaneous seizures, as we and others previously showed by using intrahippocampal recordings [84, 85, 206, 209] (see figure 5.1). Furthermore, animals that did not present hippocampus sclerosis on the anatomical image acquired during the MRI sessions at 4-6 weeks were excluded (see figure 5.2). The experimental protocol and group sizes are summarized in figure 5.3.

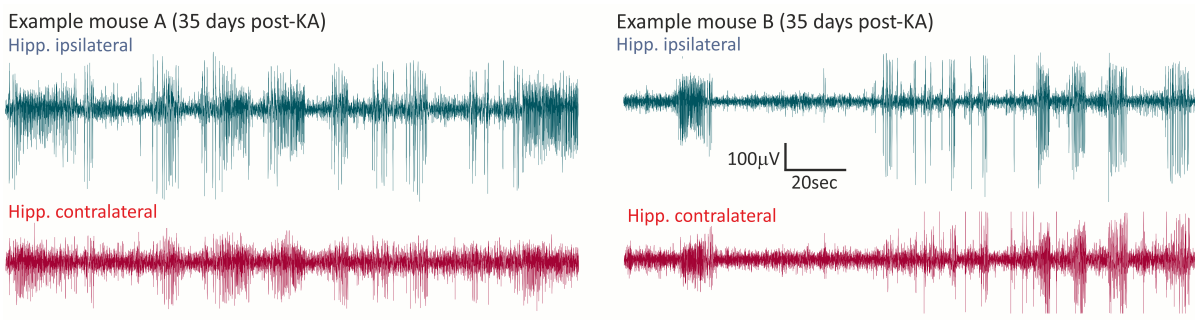

Figure 5.1 – Contra and ipsilateral electroencephalogram recordings performed 35 days post-kainate.
In blue, ipsilateral hippocampus electroencephalogram (EEG) recordings and in red associated contralateral EEG recordings in two mice examples.

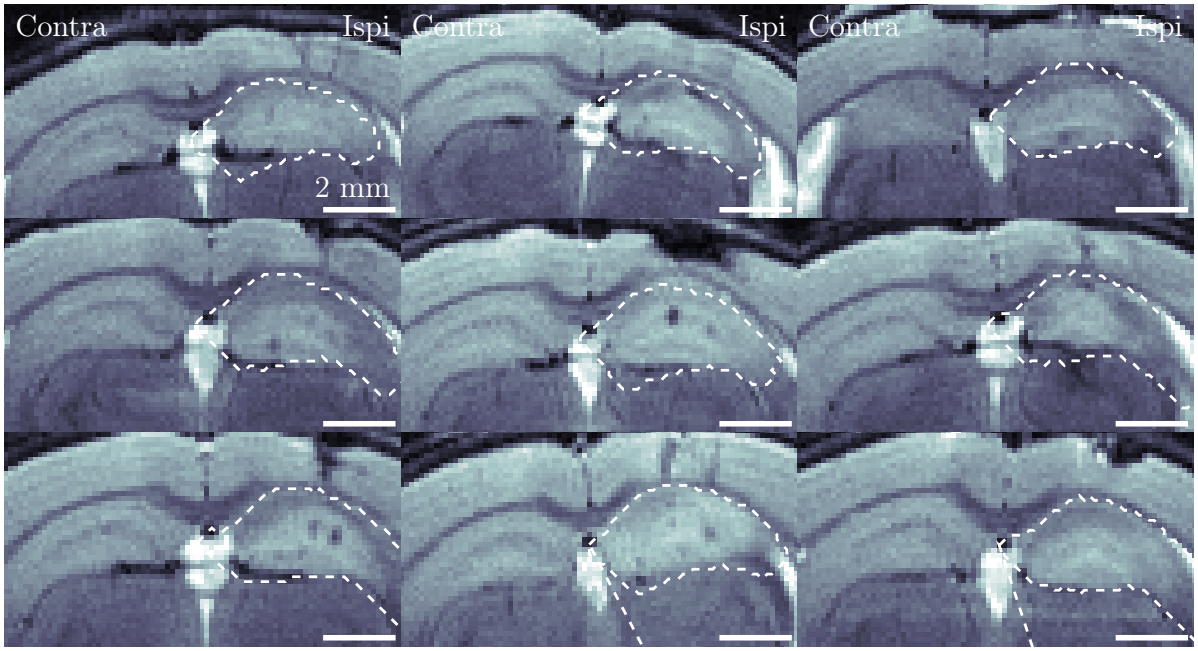

Figure 5.2 – Hippocampal sclerosis on MRI images from 9 different animals, 4-6 weeks after kainate.
Anatomical images were obtained from a T_2-weigted MRI acquisition. Sclerosis are visible in the ipsilateral hippocampus, i.e. the loss of hippocampal internal structure as described in [210]. White dashed lines indicate the sclerotic hippocampus.

A

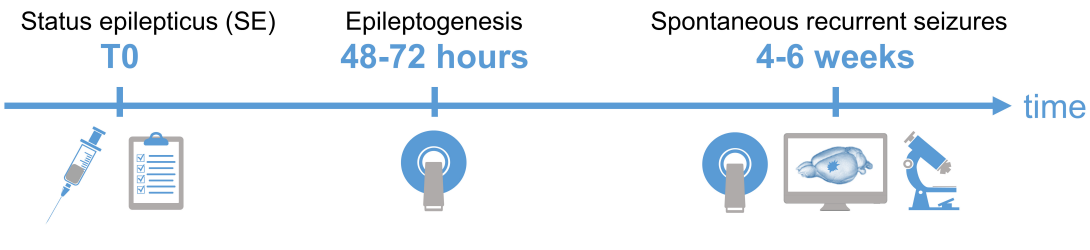

B

Protocol	Time after SE	Groups	
		Sham	KA-MTLE
NaCl / KA injection & symptoms	0-3 hours	40	34
MRI acquisitions & HS	48-72 hours	11	10
MRI acquisition & HS	4-6 weeks	20	20
Immunohistochemistry	4-6 weeks	6	6

Figure 5.3 – Experimental protocol.
(A) Workflow of the study. (B) Number of animals used at each step of the protocol. Among the 40 sham animals, 11 had a complete MRI at 48-72 hours and 20 at 4-6 weeks. Animals for which the contrast agent was not properly injected were discarded from the study. Moreover, 5 animals imaged at 48-72 hours were imaged again at 4-6 weeks. Histology was performed on 6 animals imaged at 4-6 weeks.
Among the 34 KA-MTLE animals, 10 had a complete MRI at 48-72 hours and 20 at 4-6 weeks. Animals for which the contrast agent was not properly injected were discarded from the study. Moreover, the 10 animals imaged at 48-72 hours were imaged again at 4-6 weeks. Histology was performed on 6 animals imaged at 4-6 weeks.

5.2.3 MRI

5.2.3.1 Animal preparation

The mouse tail vein was equipped with a catheter to deliver contrast agents. Anaesthesia was induced using 5 % isoflurane/air (IsoFlo, Abbot Laboratories Ltd, Berkshire, UK) and maintained through a facial mask using 1.5-2.5 % isoflurane in a mixture 75 % Air: 25 % O_2. Throughout all imaging procedures, the level of isoflurane was adjusted to maintain respiration rate between 40-70 bpm. Animals were maintained at 37°C by using a heating blanket.

5.2.3.2 MRI acquisition

Experiments were performed using a 9.4 T Biospec animal imager (Paravision 6.0.1; Bruker, Ettlingen, Germany) with an actively decoupled cross-coil setup: volume coil transmit and surface, four-channels, cryo-cooled coil reception. The voxel size was $78 \times 78 \times 350\,\mu m^3$ for the anatomical images and $136 \times 136 \times 700\,\mu m^3$ for the quantitative maps. The complete MRI session lasted approximately 2 hours including animal preparation, acquisitions and contrast agent injections.

Anatomical T_2-weighted (T_2w) images were acquired using a turbo spin-echo MRI sequence (TR/TE = 2 500/36 ms). The anatomical images were used to first visually identify the hippocampus sclerosis and second, to delineate the following regions of interest: contralateral and ipsilateral hippocampus, and contralateral cortex. These regions were automatically obtained after a non-linear registration between the anatomical images and the atlas described in [211], using a procedure described in [212]. Note that the atlas was manually modified to separate the regions of interest between the two hemispheres.

Relaxation times T_1 and T_2 were obtained using a flow-sensitive alternating inversion recovery (FAIR) and multi-spin-multi-echo (MSME) MRI sequences, respectively: (T_1: TR/TE = 10 s/15 ms and T_2: TR/ΔTE = 2 s/6 ms). The apparent diffusion coefficient (ADC) was derived from diffusion images, acquired using a diffusion-weighted, spin-echo, single-shot, echo-planar imaging (TR/TE = 3 s/23.17 ms). Blood volume fraction (BVf), vessel size index (VSI) and tissue oxygen saturation (StO_2) were obtained from a gradient echo sampling of the free induction decay and spin echo sequence and a multi spin echo sequence (MGEFIDSE) [132, 187]. Relaxations ΔR_2 and ΔR_2^* images were acquired using a gradient echo sampling of the free induction decay and spin echo sequence: (TR/ΔTE = 4 s/2.77 ms). Eight sampled time points were measured after the 90° RF pulse and 24 sampled time points after the 180° RF pulse. Ultrasmall superparamagnetic iron oxide (USPIO) particles (Guerbet, Aulnay-sous-Bois, France; 200 µµmol Fe.kg^{-1}) were injected via the tail vein and the previous scan was repeated 1 minute after the injection. Using a dynamic contrast enhanced approach, T_1-weighted images were acquired during 15 minutes (one each 12 seconds) using multiple T_1-weighted images (total 75) acquired performing a rapid acquisition with relaxation enhancement sequence (TR/TE = 800/5.05ms). A gadolinium bolus (200 µmol.kg^{-1}) was injected via the tail vein 1 minute after the beginning of the sequence acquisition. Note that interactions between CAs has been studied by authors in [213].

5.2.3.3 MRI quantification

Quantitative parameter maps were computed pixel-by-pixel using previously published methods and the Medical software for Processing multi-Parametric images Pipelines tool[1] in the Matlab environment (Mathworks, MA, USA), see appendix E.2. Seven parameter maps were obtained: relaxation times T_1 and T_2, apparent diffusion coefficient (ADC), blood volume fraction (BVf), vessel size index (VSI), tissue oxygen saturation (StO_2) and BBB permeability (BBB_p).

T_1 and T_2 maps were derived from the FAIR and MSME data respectively, using a non-linear fitting algorithm (section 2.3.1). ADC maps were computed as the mean of the ADCs observed in each of three orthogonal directions (section 2.3.2). BVf, VSI and StO_2 maps were estimated using the vascular MRF approach proposed in chapter 3. Combinations of parameters for simulation were obtained for BVf between 0.5 and 25 %, VSI between 1 and 100 µm, and StO_2 between 50 and 90 %. The susceptibility difference between blood in the presence and absence of USPIO, was set to 0.14×10^{-6} (CGS) [214] and hematocrit was set to 0.357. Other simulation settings (i.e. magnetic field, sequence acquisition) matched experiment conditions. Finally, after spatial Gaussian filtering (3×3), BBB_p was estimated as the area under the curve over the 10 minutes following the injection (AUC_{600}, section 2.3.4.2). In the brain, an increase of this quantity indicates an accumulation of the gadolinium in the extravascular compartment and therefore a reduction in the BBB permeability [188].

To reduce the possible contribution of biases inherent to the acquisition set-up (e.g. position of the receiver coil, dose of contrast agent), parameter maps were normalized by a region where no significant MRI changes are observed in these experimental conditions, e.g. the thalamus [211]. To allow a direct evaluation and graphical comparisons across read-outs, all parameter ratios were centered using the mean normalized sham ratio as reference. For each parameter and each animal, the following ratio R was calculated:

$$R = \frac{H}{T} - \frac{1}{S}\sum_{n=1}^{S}\frac{H_n}{S_n}\,, \tag{5.1}$$

where H and T are the mean parameter values in the hippocampus and thalamus of one animal, respectively. S is the number of sham mice and $\sum_{n=1}^{S} H_n/S_n$ is the sum of the ratios of hippocampus and thalamus mean parameter values for all the sham mice. This representation of the MRI parameters constitutes the normalized MRI parameter.

[1] https://github.com/nifm-gin/MP3

5.2.4 Brain immunohistochemistry and quantifications

Analyses were performed using sham (n = 6) and KA-MTLE (n = 6) mice after completion of the 4-6 weeks MRI session. Immunohistochemistry was performed on frozen brain slices as previously described by [84, 85].

After intracardiac perfusion with PBS, brains were dissected and fixed in PFA 4 % solution. Fixed brains were immersed in sucrose 15 % for 24 hours followed by sucrose 30 %. Brains were then snap frozen and stored at -80°C. Slices (20 µm) were obtained using a cryostat. Immunohistochemistry was performed after PBS washes. Slices were added with blocking solution (PBS, triton 0.5 %, horse serum 20 %) at room temperature for 1 hour. Primary antibodies (table 5.1) were diluted in blocking solution and slices incubated overnight at 4°C. After PBS washes, secondary antibody (table 5.1) was added in PBS for 2 hours at room temperature. Slices were then mounted using Vectashield containing DAPI. 20× Z-stack images (12-15 planes of 1 µm) were analyzed using Fiji. Two or three slices were examined for each mouse to quantify signals in constant regions of interest CA1, CA2 and CA3 identified by DAPI maps. Prior to analysis, all Z-stacks images were combined (Z-project, sum) using Fiji. GFAP quantification: images were converted to RGB stack format. Signal threshold was adjusted to 200 units for each image. Area of GFAP signal was calculated setting threshold sensitivity equal for each image. GFAP data are expressed as a percentage of ROI total pixels. CD13 quantification: a skeleton plug-in was used to track CD13 and CD31 signals. Branch length was calculated as pixels from Fiji "branch length" after smoothing (< 10 pixels objects).

Primary antibodies	**Host**	**Vendor / Reference**	**Dilution**
Anti-GFAP	Anti-chicken	Abcam / Ab4674	1/300
Anti-CD13	Anti-rat	Abcam	1/100
DAPI	Vectashield: mountain medium for fluorescence with DAPI	Vector Laboratories H-1200	[DAPI] = 1.5 µg.ml^{-1}
Anti-CD31	Anit-rat	Abcam / Ab56299	1/400
Secondary antibodies	**Host**	**Vendor / Reference**	**Dilution**
IBA1	Donkey anti-rabbit Alexa Fluor 488	Jackson ImmunoResearch 711-545-152	1/500
GFAP	Donkey anti-chicken Alexa Fluor Cy3	Jackson ImmunoResearch 703-165-155	1/500
CD13/CD31	Donkey anti-rat Cy3	Jackson ImmunoResearch 712-165-153	1/500

Table 5.1 – Antibodies used for immunohistochemistry imaging.

5.2.5 Statistical analyses and classification

5.2.5.1 Statistical analyses

Histological data were analyzed using Prism 8.3.1. Depending on normality (Shapiro-Wilk) data were analyzed using a two-tailed t-test or a non-parametric Mann-Whitney test. Results are reported as violin box with single points and indicating median, interquartile ranges and min-max range (figure 5.6). Significance threshold was set at $p < 0.05$.

MRI data were analyzed in the Matlab environment. Data were analyzed using a non-parametric Mann-Whitney test. Results are reported as a box. On each box, the central mark indicates the median, and the bottom and top edges of the box indicate the 25^{th} and 75^{th} percentiles, respectively. Whiskers extend to the most extreme data points.

5.2.5.2 Classification

We applied automatic classifications to MRI data considering 3 groups (sham, KA-MTLE contralateral, and KA-MTLE ipsilateral). To evaluate the impact of the classification method, different approaches are performed: k-nearest neighbors (kNN), linear and quadratic discriminant analysis (LDA and QDA), support vector machine (SVM), Naïve Bayes (NB), and Decision Tree (DT). Each approach was evaluated using a "leave-one-out" cross-validation strategy, specifically each classification model was trained using all animals except one. The omitted animal was then classified using the trained model. The procedure was repeated for all animals and the mean classification accuracy was reported. To examine whether it is more accurate to use one or several MRI parameters to classify the experimental groups, we performed the classification procedure considering 1) each MRI parameter individually, 2) all MRI parameters or 3) the subset of MRI parameters that yields to the highest classification accuracy. All possible parameter combinations were tested.

5.3 Results

5.3.1 Tracking hippocampal MRI changes post-KA and during spontaneous seizures

Anatomical imaging performed after status epilepticus (48-72 hours post-KA) indicated the unilateral cortical lesion and edema corresponding to the kainate injection route (figure 5.4 A2-A4, D2 and H2).

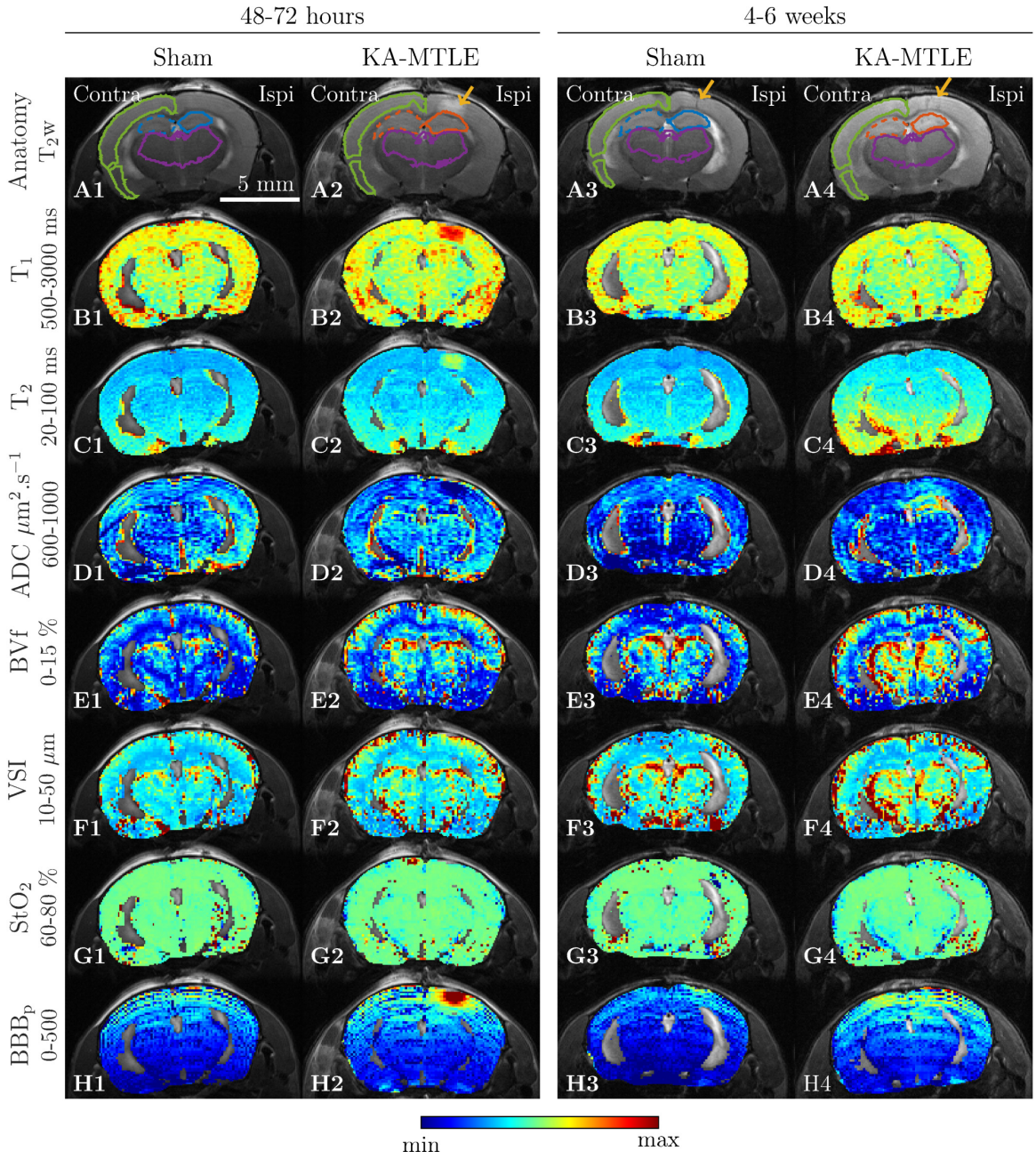

Unilateral hippocampal sclerosis was detected, consisting of a 16.22 % and 10.12 % volume reduction as compared to contralateral ($p = 0.007$) and sham ($p = 0.080$) hippocampi. Examination of the MRI data showed a T_1 (+6.49 %, $p < 0.001$) and BBB_p (+12.28 %, $p = 0.001$) increase in the MTLE ipsilateral, epileptogenic, hippocampi after status epilepticus as compared to sham (figure 5.5(a) A1-B1). Re-testing performed during spontaneous seizures indicated the persistence of BBB_p (+10.40 %, $p < 0.001$) along with an increase of ADC (+9.99 %, $p < 0.001$) and BVf (+19.91 %, $p = 0.001$) as compared

Figure 5.4 – Examples of MRI acquisitions *(on previous page).*
Anatomical images (**A1**-**A4**) with ROI overlaid and the seven quantitative parameter maps (horizontal arrangement) for each mouse model and each time-point (vertical arrangement). sham (**A1**-**H1**) at 48-72 hours and (**A3**-**H3**) at 4-6 weeks post-surgery; (**A2**-**H2**) epileptic mouse at 48-72 hours post-KA; (**A4**-**H4**) KA-MTLE mice at 4-6 weeks. MRI data are: (**A**) T_2-weighted anatomical image (not quantitative), (**B**) T_1 relaxation time, (**C**) T_2 relaxation time, (**D**) ADC: apparent diffusion coefficient, (**E**) BVf: blood volume fraction, (**F**) VSI: vessel size index, (**G**) StO_2: tissue oxygen saturation, and (**H**) BBB_p: blood-brain-barrier permeability. On the T_2-weighted images, the neocortex is delineated in green. The hippocampi are delineated in blue for sham mice and orange for epileptic mice (dashed lines for the contralateral and solid lines for the ipsilateral hippocampus). The thalamus, used for data normalization, is delineated in magenta. Yellow arrows indicate the lesions caused by the intra hippocampal injection. Minimum (min) and maximum (max) values are reported on the left side of each per row, except for the first row, which does not show quantitative image.

to sham, suggesting enduring cellular and vascular alterations (figure 5.5(a) B1-B2). The MRI outcome was paralleled by significant cellular level modifications, as shown by the increased hippocampal GFAP reactivity (figure 5.6 F), CD31 angiogenesis (figure 5.6 H, D1-D2) and CD13 pericyte remodelling (figure 5.6 J, E1-E2), examined in the ipsilateral epileptogenic hippocampi.

Subsequently, we studied the contralateral MTLE hippocampus, a non-lesional region characterized by significant EEG seizure propagation [215] (see figure 5.1). 48-72 hours post-KA, MRI changes consisted of increased T_1 (+2.85 %, $p = 0.032$) and decreased T_2 (-2.06 %, $p = 0.012$; figure 5.5(b) A1, A2). 4-6 weeks post-KA, ADC (+1.99 %, $p = 0.029$) and BVf (+13.14 %, $p = 0.010$) were increased in MTLE mice, as compared to sham (figure 5.5(b) B1, B2). The contralateral cortex exhibited discrete modifications, specifically ADC (-1.06 %, $p = 0.037$) and VSI (-4.82 %, $p = 0.001$; figure 5.5(c)).

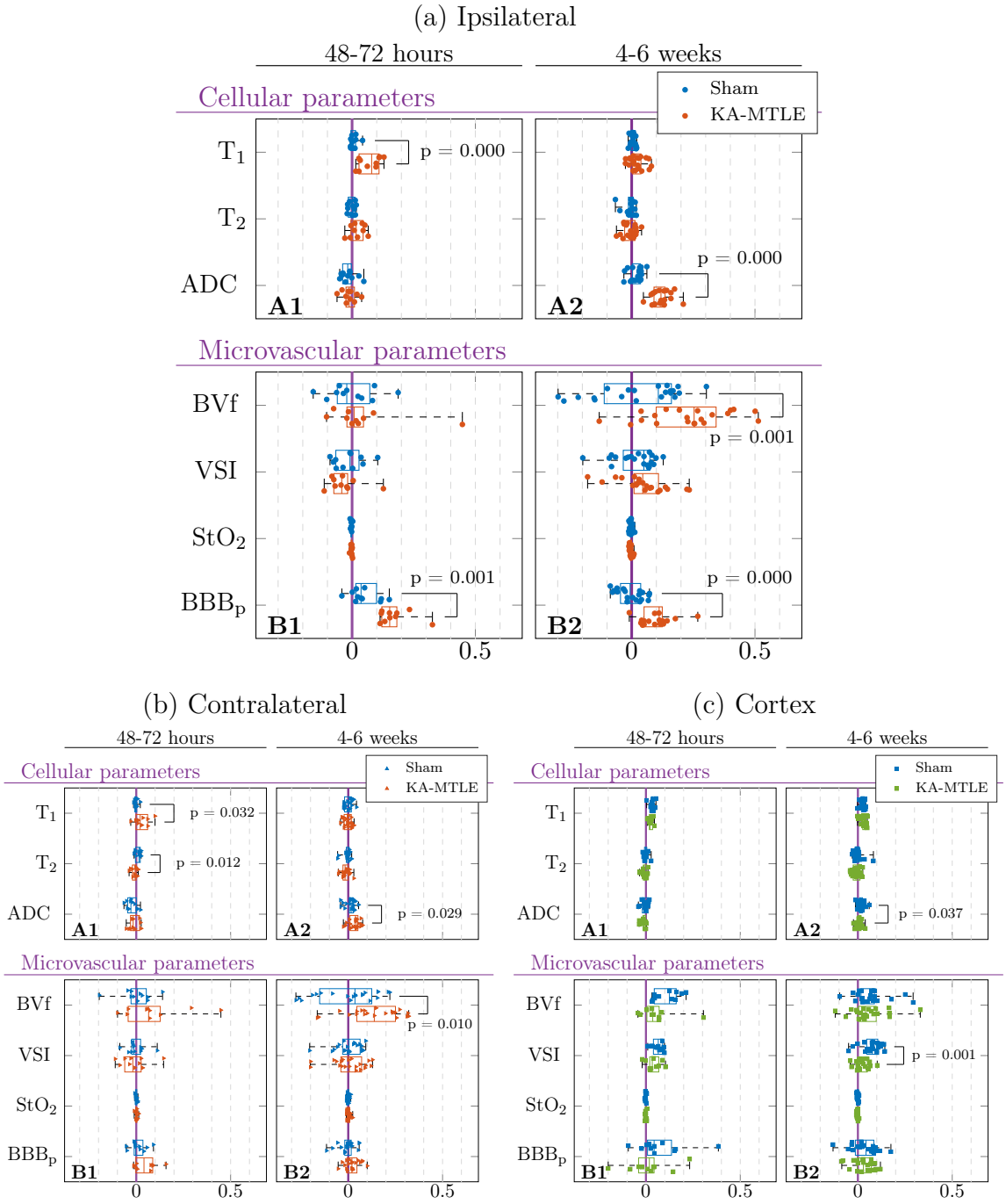

Figure 5.5 – Contralateral and ipsilateral hippocampus, and cortex MRI parameters. Normalized MRI parameter values (equation (5.1)) obtained from the analysis of the ipsilateral hippocampi 48-72 hours post-KA (sham n = 11; KA-MTLE n = 10) and at 4-6 weeks (sham n = 21; KA-MTLE n = 21). Absolute MRI parameter values are reported in appendix figures D.1 and D.2. (**A1**, **B1**) correspond to 48-72 hours and (**A2**, **B2**) to 4-6 weeks post-KA mice. Top-down: (**A**) T_1 and T_2: relaxation times, ADC: apparent diffusion coefficient; (**B**) BVf: blood volume fraction, VSI: vessel size index, StO_2: tissue oxygen saturation, BBB_p: blood-brain-barrier permeability. For each parameter, a Mann-Whitney test was performed between sham and KA-MTLE mice. Significant p-values ($p < 0.05$) are reported.

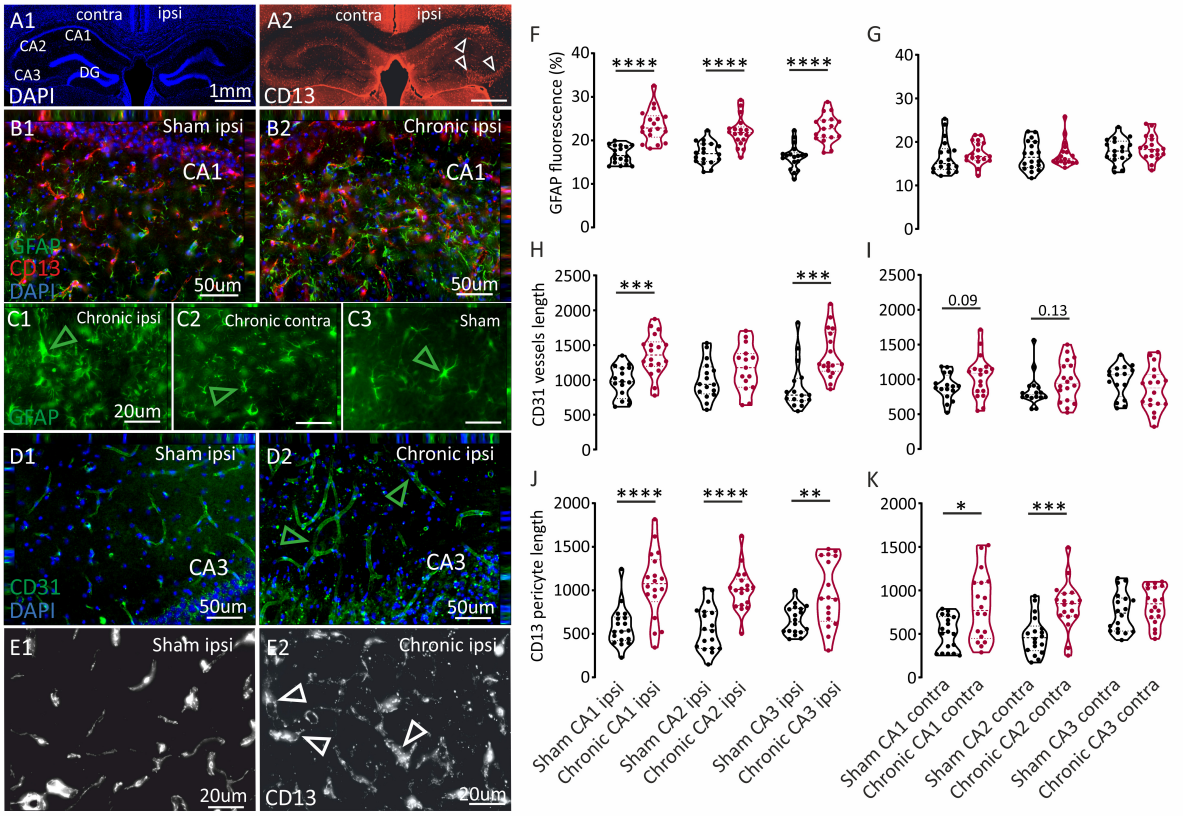

Figure 5.6 – Histological neurovascular changes in the ipsi and contralateral hippocampi during chronic seizures.
(**A1**, **A2**) DAPI and CD13 pericyte maps of the whole dorsal hippocampi (ipsi and contralateral) during chronic seizures (4-6 weeks). Arrowhead in A2 show gross pericyte abnormality in the CA regions. (**B1**, **B2**) Examples of GFAP reactivity during SRS in the ipsilateral CA1 hippocampus as compared to sham. (**C1**, **C3**) Examples of astrocyte morphological changes during chronic seizures (arrowhead, ipsi and contra-lateral) as compared to sham. (**D1**,**D2**) Example of CD31 angiogenesis during chronic seizures. Arrowheads in D2 indicate large and looping abnormal vessels. (**E1**, **E2**) Example of CD13 pericyte modification and hypertrophy during chronic seizures (arrowheads in E2). (**F**, **G**) Quantification of sub-hippocampal GFAP fluorescence, ipsi and contralateral. (**H**, **I**) Quantification of sub-hippocampal CD31 vessel length, ipsi and contralateral. (**J**, **K**) Quantification of sub-hippocampal CD13 pericyte length, ipsi and contralateral. Depending on normality (Shapiro-Wilk) data were analyzed using a two-tailed t-test. Panel G CA2 contra, panel H CA3 ipsi, panel I CA2 contra, panel K CA1 contra that were instead analyzed using non-parametric Mann-Whitney. Data refers to $n = 6$ mice/group, 2-3 slices/mouse. * $p < 0.05$, ** $p < 0.01$, and *** $p < 0.001$.

Histological analysis of the contralateral hippocampi indicated distinct cellular level changes, less apparent as compared to the lesional ipsilateral hippocampus (figure 5.6). In particular, CD13 pericyte (figure 5.6 K) and CD31 capillary (figure 5.6 I) length was trending or significantly increased as compared to sham, suggesting angiogenesis

in this region. Total GFAP reactivity was unchanged (figure 5.6 G), although discrete morphological modifications were observed (figure 5.6 C1-C3). We next correlated MRI measures with the histological read-outs as measured in each animal (figure 5.7). We report significant linear correlations between ADC and GFAP immunoreactivity ($r = 0.66$), BVf and VSI correlated with CD31 vessel length ($r = 0.61$ and 0.65, respectively; figure 5.7). Collectively, these results indicate specific MRI changes occurring in the epileptogenic and seizure propagating hippocampi, with an extension and a link to cellular histopathological modifications.

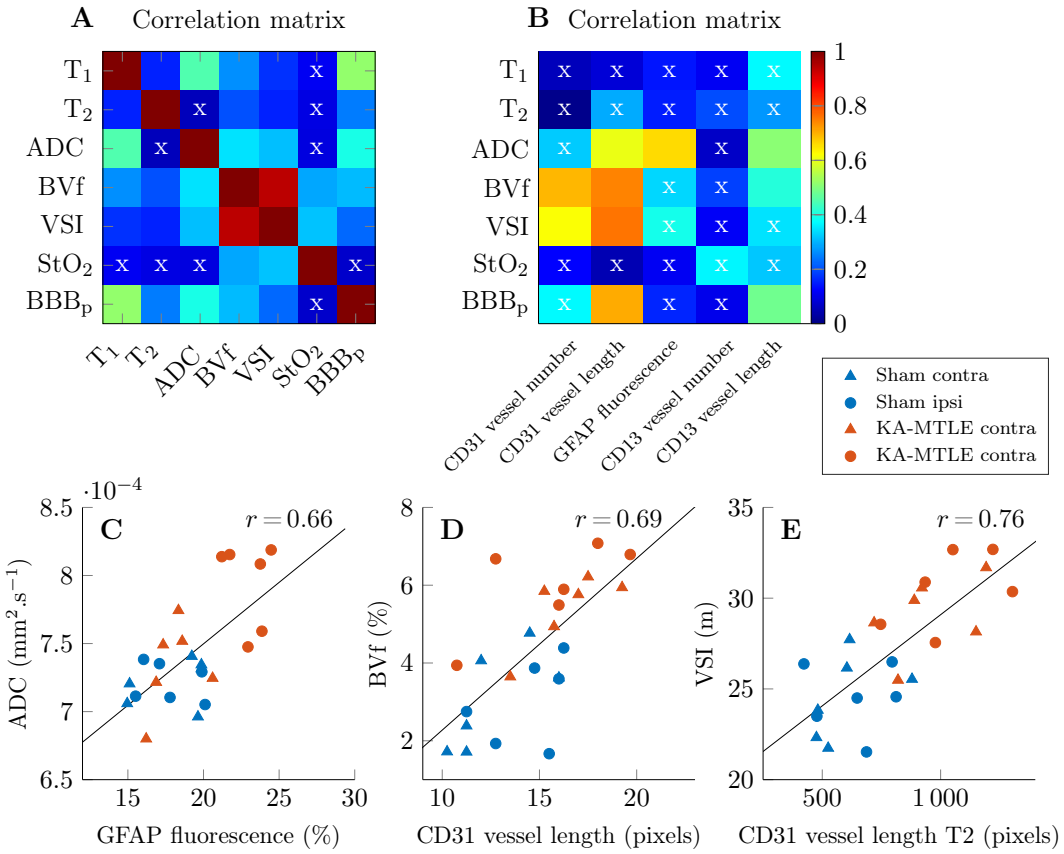

Figure 5.7 – Relation between MRI normalized parameters and immunohistochemistry parameters.
(**A**) Correlations between MRI parameters. (**B**) Correlations between MRI parameters and immunohistochemistry parameters. White crosses correspond to non-significant correlations ($p > 0.05$). (**C**) Apparent diffusion coefficient (ADC) vs. GFAP fluorescence. (**D**) Blood volume fraction (BVf) vs. CD31 vessel length. (**E**) Vessel size index (VSI) vs. CD31 vessel length. The Pearson correlation coefficient r is indicated in the top right corner.

5.3.2 Multiparametric analysis for the identification of epileptogenic and seizure-spreading hippocampi

We initially tested whether redundancy existed among all MRI parameters examined. Correlations below 0.5, except for BVf and VSI ($r = 0.88$; figure 5.7), ruled out interdependence between the MRI parameters, indicating that MRI parameter variations can be combined without redundant information. Furthermore, the correlation level between MRI parameter values and hippocampal volumes was low or not significant, indicating that quantitative MRI provides integrating data to hippocampus sclerosis (figure 5.2). We then examined the effectiveness of multiparametric analyses to separate our experimental groups. To this end, MRI data acquired from all animals underwent six classification analyses (see section 5.2.5.2; figure 5.8 A1-A2, B1-B2). Initially, we classified two experimental conditions, specifically ipsilateral MTLE and sham hippocampi, considering one MRI parameter at a time (figure 5.8 A1-A2). 48-72 hours post-KA, we obtained the highest classification accuracies using T_1, T_2 and BBB_p (93.0 %, 81.2 % and 89.2 %, respectively; MTLE: $n = 10$ and sham: $n = 22$). During spontaneous seizures (4-6 weeks), the best classification was obtained using ADC, BVf and BBB_p (98.3 %, 83.3 % and 89.2 %, respectively; MTLE: $n = 20$ and sham: $n = 40$). When we considered all seven MRI parameters, the accuracy score was 92.5 % post-KA and 96.7 % during spontaneous seizures. When screening and selecting the subset of MRI parameters that provides the highest accuracy score, we found that the combination of T_1, T_2, ADC and BBB_p delivers an accuracy of 100 % post-KA, while the combination of ADC, BVf, VSI and BBB_p delivers an accuracy of 99.2 % during spontaneous seizures. These results were obtained using QDA and SVM classification methods. The mean (across parameters) standard deviation (across classification methods) of accuracy was 2.15 ± 1.46 %, suggesting that the classification methods led to close results.

Next, we attempted classifying three experimental conditions, specifically MTLE ipsilateral, MTLE contralateral, and sham hippocampi (figure 5.8 B1-B2). 48-72 hours post-KA and considering one parameter at a time, the highest classification accuracies were obtained using BBB_p, T_1, and T_2 (74 %, 69 %, and 65.8 %, respectively). During spontaneous seizures, accuracies based on ADC, BBB_p, BVf were 77.6 %, 63.7 %, and 60 %, respectively. Combination of all MRI parameters did not improve the classification accuracy. However, the multiparametric approach using the combination of T_2, BVf, VSI, StO_2 and BBB_p delivered a 90.5 % accuracy post-KA, while the combination of T_1, ADC and BVf lead to an 85 % accuracy in segregating the three experimental conditions

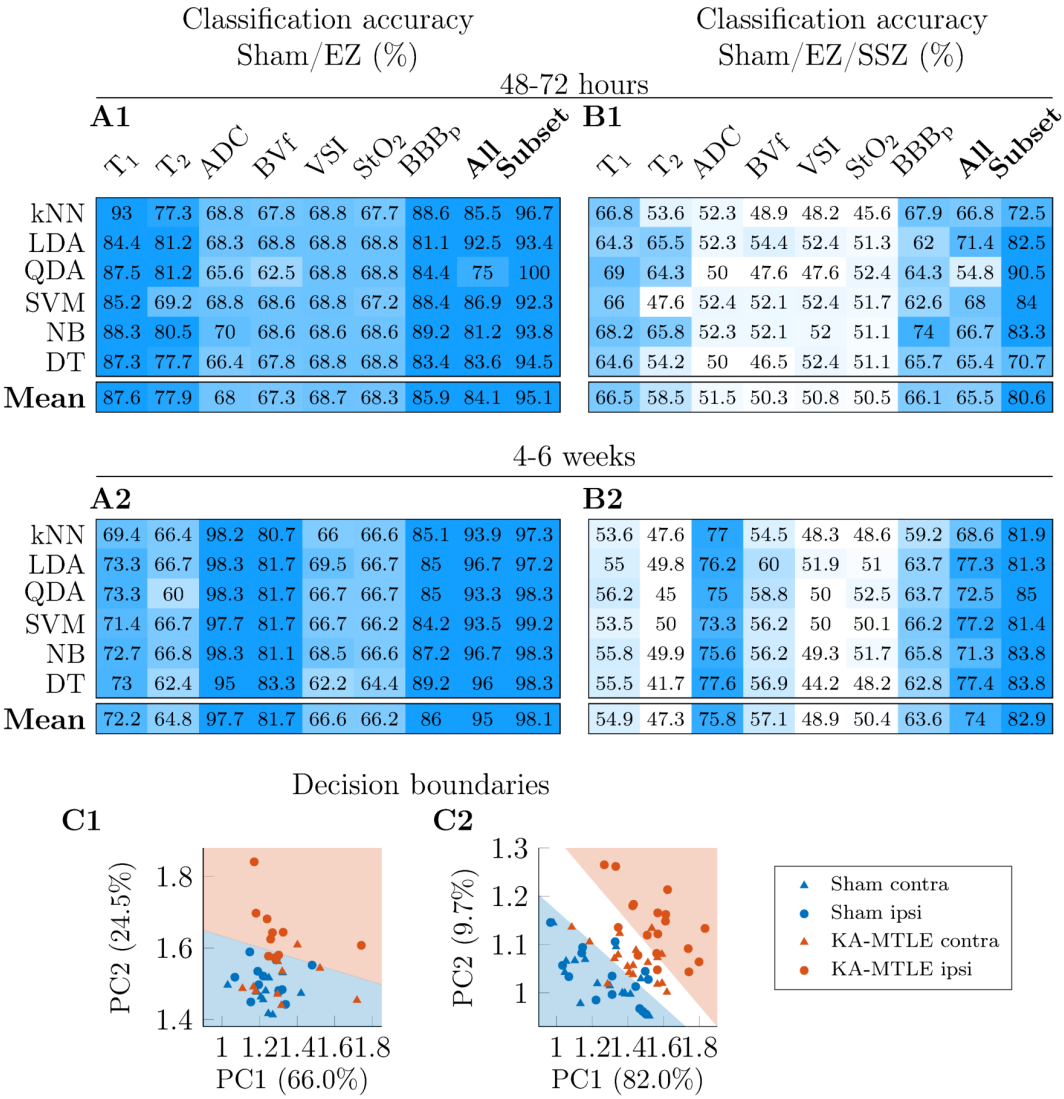

Figure 5.8 – Classification accuracy scores using one, all, or the best parameter subset. (**A1**, **A2**) show mean accuracy scores (obtained from 20 repetitions) for 2-class (sham and KA-MTLE ipsilateral) classification by (top-down): kNN: k-nearest neighbors, LDA/QDA: linear/quadratic discriminant analysis, SVM: support vector machines, NB: naive Bayes, and DT: decision tree. These classifications are performed (left-right) using a single parameter indicated at the top of the column, (All) using all seven parameters or (Subset) using the optimal subset of parameters. (**B1**, **B2**) show accuracy scores 3-class classification: sham contra- and ipsilateral hippocampi, KA-MTE contralateral hippocampus and KA-MTLE ipsilateral hippocampus. (**C1**, **C2**) show 2D representations of classes. PC1 and PC2 correspond to the two first principal components of the seven MRI normalized parameters assigned to each region of interest. The variance explained by each component is mentioned between parentheses. In (**C1**, **C2**), the orange area corresponds to the expected location of KA-MTLE ipsi, the blue area to that of sham (ipsi and contra), and the white area to the KA-MTLE contra, using the SVM classification. Note that in (**C1**), the white area is not visible on this 2D projection.

during spontaneous seizures. These results were obtained using QDA and the variability between the classification methods was low ($3.13 \pm 2.01\,\%$). Furthermore, figure 5.8 C2 shows contralateral MTLE data (red triangles) positioned between sham (blue triangles and circles) and ipsilateral MTLE data (red circles). Altogether, our neurovascular multiparametric analysis fully defines the epileptogenic hippocampus and it provides novel MRI identifiers for the contralateral hippocampi, a seizure spreading region in experimental MTLE.

5.3.3 Dictionary-based learning vs. steady-state methods

This section is a parenthesis to compare the impact of the DB-SL quantification compared to CEF quantification on vascular parameters estimation and resulting classification accuracy. We compare values obtained in five different brain regions and both hemispheres in figure 5.9. For VSI, we do not consider VSI values above 20 µm as it shown very high estimate errors using CEF method (section 3.4.2.1).

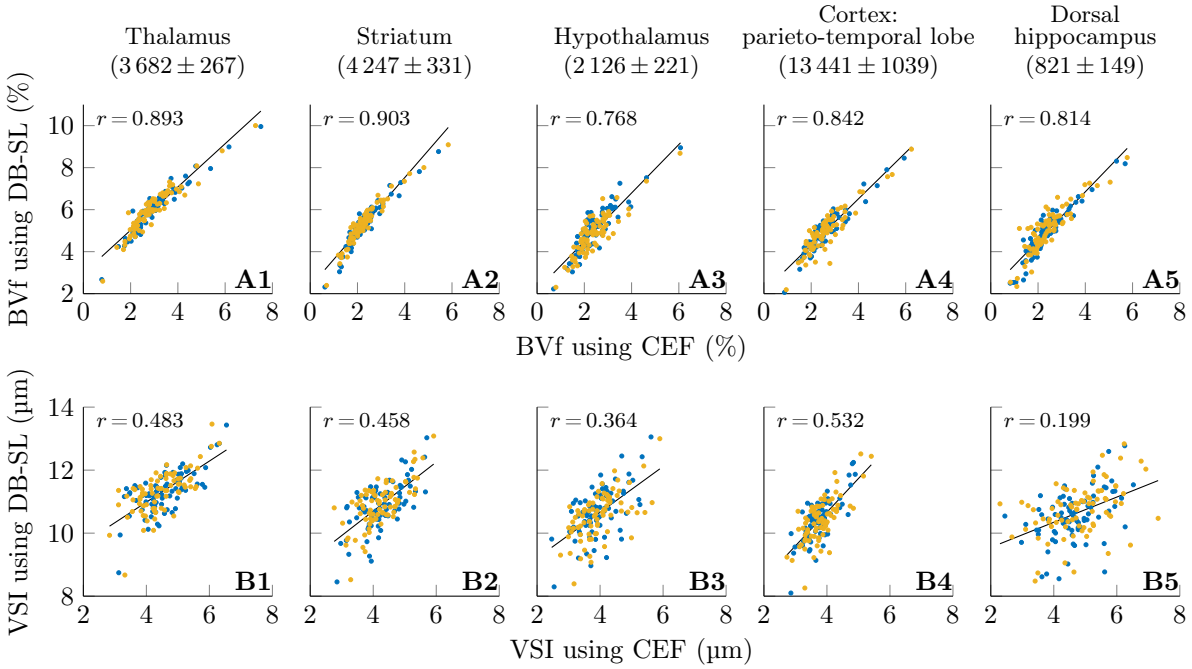

Figure 5.9 – Blood volume fractions and vessel size indexes in different brain regions, using two different reconstruction methods.
(**A1-A5**) Blood volume fraction (BVf) and (**B1-B5**) vessels size index (VSI) in five different brain regions, from (**A1**, **B1**) to (**A5**, **B5**): thalamus, striatum, hypothalamus, cortex and dorsal hippocampus. Mean volumes and standard deviation of each regions (in pixels) is reported above columns. Blue and yellow marks correspond to contralateral and ipsilateral hippocampi, respectively. Pearson correlation coefficient r is indicated in the top left corner.

Regarding BVf estimates, we observe correlation values between 0.768 and 0.903 indicating a high similarity of estimates. Regarding VSI estimates, correlation values are smaller, between 0.199 and 0.532. These results are in agreement with section 3.4.2.1 indicating low BVf estimates error for both methods but larger VSI estimates error.

Considering the classifications, we do not observe significant classification changes using CEF method. We interpret this minor difference by the fact that this method was applied to only three of the seven MRI parameters and that among these parameters one is not discriminant (StO_2) and the two others (BVf and VSI) are strongly correlated. Further investigations applying DBL analysis to quantify more parameters could have a greater impact.

5.4 Discussion, conclusion and perspectives

Our study effectively identifies and mathematically elaborates a suite of MRI cellular and cerebrovascular parameters over time and within a precise experimental MTLE setting. We successfully applied a quantitative, multiparametric, MRI acquisition and data processing pipeline to differentiate with high accuracy 1) epileptogenic hippocampi from sham and 2) the epileptogenic from the contralateral seizure spreading region. We confirmed coherence between neurovascular MRI identifiers and specific histological outputs within the same regions of interest during spontaneous seizures, and we propose this approach for a better identification of brain regions involved in seizure spreading. Our method could be integrated in current clinical MRI pre-surgical examinations with the goal of potentially improve mapping of the epileptic networks.

5.4.1 Multiparametric MRI to map the epileptic networks: clinical and experimental evidence

Our pre-clinical study indicates QDA as the most efficient method for MRI data set classification. Furthermore, all multi-parametric methods outperformed the mono-parametric analysis. Clinically, SVM was previously used to classify TLE patients by means of T_1-weighted [216] or diffusion images [217]. SVM achieved a prediction accuracy of 71 % for whole-brain and 81 % when focusing on the hemisphere ipsilateral to the hippocampal sclerosis [216]. A 69.4-77.8 % classification accuracy was also reported when using SVM to analyse the individual parameters T_1, T_2, ADC and fractional anisotropy in 17 TLE patients and 19 control volunteers [218]. When pre-processing the data (e.g. using feature

selection, dimensionality reduction) prior to the classification, the accuracy increased to 80.6 %. A focus on the ipsilateral hemisphere (2-class analysis) further improved accuracies within 88.9-100 % [218]. To the best of our knowledge, our study is the first one applying multi-parametric MRI analysis to a pre-clinical model of MTLE. The epileptogenic hippocampi were identified and distinguished from sham with a 98.3 % accuracy during spontaneous seizures and 100 % accuracy 48-72 hours post-KA. When reapplying the analysis to classify sham, seizure spreading and epileptogenic hippocampi, we maintained a high accuracy of 85 % and 90.5 % during spontaneous seizures and post-KA, respectively (figure 5.8). These results are relevant offering a novel MRI toolkit, based on neurovascular read out, to better outline the epileptic networks with the inclusion of propagating regions, perhaps also applicable to cases of non-lesional epilepsies.

5.4.2 Integrating imaging and histological evidence of neurovascular damage in MTLE

Single analysis of specific MRI read outs have previously been described. For instance, hyperintense T_2-weighted signal 1 hour to 7 days post-KA were previously reported in the MTLE model used herein [99] and in a pilocarpine-induced status epilepticus in rats [91]. In the latter study, T_2 values return to baseline 1 week after status epilepticus [91]. The T_1 changes observed in our study are also consistent with the T_1 increase 1 to 3 days after pilocarpine-induced status epilepticus and the return to baseline 2 weeks after [91]. At 4-6 weeks post-KA, the observed increased ADC is in line with the increased ADC observed 7 to 84 days after KA-induced status epilepticus in rats,while ADC remains normal 1 to 3 days after KA [219] and 23 days after electrical stimulation [94]. In [95], normal BVf was reported 2 days after status epilepticus and a trend increase in BVf 14 days after status epilepticus, although increased vessel density was reported by immunohistochemistry [202].

Our BBB permeability findings are consistent with [97], although we here used a clinically relevant contrast agent bolus injection followed by a 10 minutes tracking acquisition in place of a long-lasting infusion. Clinically, calculating the differential T_1 relaxation pre- and post-interictally was successfully used to spatially localize the epileptic foci in patients by detecting blood-brain barrier permeability [107]. Previously, we showed histological BBB leakage by analysing parenchymal fluorescein in the ipsilateral hippocampus in this MTLE model [84], an outcome consistent with the MRI data reported

here. Here, we report histological evidence of glio-vascular modifications that echoes the MRI data, specifically the ADC and BVf increase in the ipsilateral and contralateral hippocampi. The histological analyses of the contralateral hippocampi in MTLE mice reveals subtle cellular modifications possibly associated with seizures spreading [85, 207, 220]. Furthermore, some alterations were also observed by MRI in the cortex, but minor as compared to the contralateral hippocampus. In summary, contralateral seizures spreading regions could be further investigated for (sub)cellular or molecular changes and our MRI and histological studies comfort this line of reasoning [215, 221].

5.4.3 Study limitations and conclusions

Our study has limitations. From a technical standpoint, we experienced a typical slight signal decay from the cortex (located close the MRI coil, figure 5.4) towards the lower part of the brain (away from the MRI coil), which can be observed on anatomical, T_2 and BBB permeability maps (figure 5.4 A1-A4, C4, H1-H4). However, these intrinsic patterns were similar in all groups, not affecting our analyses. Our investigation did not include functional MRI [222, 223] or MR spectroscopy (e.g. Glutamate, GABA), two important technical approaches generating potentially complementary information. Furthermore, the diffusion acquisition protocol used in this work could be refined to analyze fractional anisotropy of diffusion kurtosis. In general, our multiparametric MRI analysis could be extended to include additional imaging measures, thereby refining classification accuracy. Here, we acknowledge that EEG recordings were not performed during MRI investigations long-term. This technical pitfall has impeded an MRI read-out classification based on quantifiable seizure activity in each mouse. By overcoming this technical challenge, we will continue the research initiated here. We also recognize that performing the proposed MRI protocol may be time consuming. Upon technical optimization, exploration in each mouse required approximately 45 minutes. This time frame could be shortened by eliminating specific sequences as, for example, we observed that StO_2 mapping did not significantly improve our results. We also acknowledge that, to define the epileptogenic and seizure propagating hippocampi we used reference data obtained from sham animals. This approach raises the significant issue of availability of reference data for humans. While T_1, T_2, and diffusion data exist [224–226], reference perfusion and BBB permeability data are not available. The latter represents a stumbling block, negatively impacting a pre-clinical to clinical transition. Generating imaging templates for the healthy human brain would be significant to develop statistical approach and to obtain maps of abnormal tissues, as performed for example for tumour identification [191]. An alternative to atlases

would searching for asymmetries in parameter maps between left and right hemispheres, as typically performed in current neuroradiology.

In summary, a multi-parametric quantitative MRI acquisition combining an optimal array of neurovascular read-outs may improve the identification of the epileptogenic and seizures spreading regions. Further pre-clinical trials are required to validate next application to specific clinical settings.

Chapter 6

Conclusion and perspectives

This thesis was articulated on three main topics: 1) methodological developments in MRF and 2) pre-clinical MRI data acquisitions and processing on experimental models of epilepsy. In parallel, to make full use of the first two contributions, 3) original software solutions have been developed.

Regarding the methodological developments, it was shown that the dictionary-based methods relying on more sophisticated biophysical models than the closed-form expression fitting, could improve the estimation of parameters, in our case vascular parameters. In particular, the simulation tools can take into account system imperfections, which are often disregarded in expressions based on simplifying assumptions. However, dictionary-based analysis requires by construction the management of a large dictionary that results in extensive time and memory requirements.

The MRF framework is particularly suitable for vascular application because simple models cannot take into account static and dynamic interactions within a pixel, as opposed to simulation tools. The simulation of this complex vascular environment results in extremely large simulation times that also have to be managed, especially as even more complex simulations could further improve the quality of the modeling. A realistic 3D voxel simulation tool in development under an ANR project (see examples in figure 6.1), should

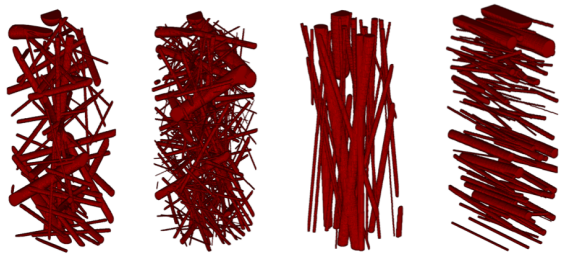

Figure 6.1 – 3D vascular simulation.
Four examples of 3D voxel, spatial resolution is $136 \times 136 \times 800\,\mu m^3$.

provides signal highly sensitive to vascular parameters based on *ex vivo* angiogram imaging and optimal signal patterns [227]. The tool exhibits a single signal simulation times of approximately 15 minutes (about 10 seconds for current 2D tool). We can also speculate that reducing a real vascular geometry to a few parameters would be too simplistic and taking into account a larger number of parameters is necessary e.g. the anisotropy, tortuosity, vessel orientations, etc. One may also want to simulate signals several minutes after contrast agent injections such as in dynamic contrast enhancement. In these cases, dictionary-based methods that allow a continuous representation of a large set of parameters from a small number of dictionary entries are highly desirable to limit simulation cost.

There has been several attempt to learn a continuous representation of the dictionary, all based on neural networks. We propose a statistical method that provides an high estimation accuracy compared to neural networks. Despite their high performance, neural network methods have some weaknesses, including difficulties in generalizing beyond the learning dictionary and potential instability in case of new dictionary entries (section 4.3.1.4, page 114), low robustness to both thermal and aliasing high noise levels (sections 4.3.2.1 and 4.3.2.2), and a significant interpretability of the estimates obtained. Indeed, *black box* machine learning models, i.e. functions that are too complicated for any human to comprehend, are currently being used for high stakes decision making such as in healthcare. Eventually methods are applied to explain these black box models. More complex models does not necessary mean more accurate, this is often not true, particularly when the data are structured, with a good representation in terms of naturally meaningful features [228].

Instead of creating methods to explain black box models, creating models that are inherently interpretable/explainable is an alternative way, as chosen in this work for DB-SL method. We demonstrated that relying on our statistical method, the interpretability of the model has resulted in the production of a confidence index. Other possibilities have been explored such as, for example, the inclusion of spatial considerations to constrain the model, which had previously been presented on hyper-spectral imaging [229]. This feature is part of the software package. Further investigations would be necessary to produce an effective spatially-constrained dictionary-based learning method in MRF. Among the possible improvements, a method for complex-valued data could be an important step forward. The benefits of a complex-valued neural network have been shown by [168] and in particular, the benefit of the complex-valued framework over the split of the real and imaginary parts into two channels, which is the usual technique. Finally, we saw that

each method has its own strengths and weaknesses (table 4.1, page 120) and the specific application will determine the use of one or the other, or even considering combining them for better results.

Ensemble learning typically refers to methods that generate several models that are combined to make a prediction, either in classification or regression problems [193]. In this multi-model study, we therefore considered a combination of methods that would improve accuracy. The preliminary results focused on dictionary-based learning methods combination, clearly shown the increase of estimates accuracy (section 4.3.4). One can also combine matching and the proposed learning method. The mean and standard deviation of the estimated posterior distribution (used in the actual framework as estimate and confidence index, respectively) could be used to compute the distance between them and those of the dictionary signals, i.e. the summary statistics of an approximate Bayesian computation (ABC, for more details, see [230]). This would provide a compression of the dictionary signals to two values and then avoid extensive time and memory requirements. In fact, ABC can be seen as a matching procedure, if we only consider the simulation entry that provided the minimum distance and reject others. One can also imagine using the entire posterior distribution and compute distance between distributions [231] to further improve estimate accuracy.

Related findings have been presented in several conferences: in 2018 at the annual congress of the *International Society for Magnetic Resonance in Medicine* (ISMRM) [9], and in 2019 at the French national congress of life imaging [10] and at the annual congress of the *French Society of Magnetic Resonance in Biology and Medicine* [11]. A comparison of the proposed and neural network approaches has been performed at the ISMRM this year [13] and a full paper is in revision [170].

Regarding the evaluation of epilepsy, the project was based on the use of experimental models to investigate the localization of regions involved in the epilepsy network. In Humans it may be difficult to identify these regions, both the epileptic foci and regions of epileptic seizure spread. We explored two different models of MTLE, one induced by intraperitoneal injection and the other one by intracerebral kainate injection. Results concerning the first one are documented in appendix D but were not presented in this thesis since we focused on the data corresponding to the second model (chapter 5). In fact, intraperitoneal injection model exhibits greater extent of neuronal damage but does not reproduce hippocampal sclerosis. Several practical issues were also addressed during this thesis but are not reported in this manuscript e.g. catheter installation for injection

of contrast agents into the scanner, stabilization of physiological parameters and scaling of the protocol on mice at 9.4 T. Issues remain, in particular, the ASL acquisition of blood flow in the absence of a dedicated labeling coil, remain. The MRI protocol could thus be improved: it could be more complete. MRF could be further used to accelerate acquisition and/or improve accuracy on the other vascular parameters evaluated in this study.

The study on MTLE model induced by intraperitoneal kainate injection, showed that a multi-parameter approach could improve the identification of epileptic zones but also of the regions in which the seizures spread. Since the data have been acquired and revealed a possible discrimination of epileptic hippocampus compared to healthy hippocampus, it would be valuable to investigate methods allowing discrimination at the voxel scale. As we have seen, depending on patient, areas within the hippocampus are inhomogeneously affected in humans (figure 2.7, page 27) The proposed approach could thus be used to refine the localization of altered tissues. Such methods have already been used to characterize tumor tissues in rats [191] but in this pathology the cellular and vascular changes induced are substantial and cover a large region. It is therefore obvious to localize the tumor in an image, even for unexperimented eyes. In epilepsy, these changes are small and are not detectable by eyes. An atlas of quantitative normal values could help detect local anomalies. Alternatively, asymmetry ratios may be used, a standard practice in radiology.

The protocol and analysis could be used with other experimental models of epilepsy to identify eventually a shared signature of MRI changes (e.g. intraperitoneal injection model). One could also investigate the impact of treatment on this MRI signature and thus determine whether it would be possible to identify the regions involved in epilepsy in treated patients. As it stands, the protocol is not compatible with a routine clinical examination and adjustments would be necessary, mainly in reducing the acquisition time. Findings are currently in preparation for submission.

An effort in this work has been made to provide a tool to easily apply the analysis methods (ours and competitors') to MRI data. Compare to standard MRF, dictionary-based learning methods can easily be computed on a desktop computer even for large dictionaries. We showed that NN based methods are faster (section 4.3.1.2, page 112), speed mainly relying on mini-batch algorithms combined to GPU implementation. The proposed method could be greatly accelerated by using the same algorithms, mini-batch [232]. Currently, the algorithm could already be optimized in its current implementation for moderate

speed gain (e.g. parallelization of local Gaussian computation) and implementations in other programming languages might be more suitable (e.g. in Python: GLLiM). I actually had the opportunity to support two clinicians in the use of the tools during their one-year research project.

We interfaced the proposed package with the *medical software for processing multi-parametric images pipelines* for an extended use to an audience not necessarily familiar with programming, accepted work [185]. With open science in mind, protocols, data and code will be shared.

Bibliography

[1] World Health Organization. *Epilepsy: a public health imperative*. Organization, World Health, 2019. https://www.who.int/mental_health/neurology/epilepsy/report_2019/en/.

[2] Kristina Malmgren, Sallie Baxendale, and J. Helen Cross. Long-term outcomes of epilepsy surgery in adults and children. *Long-Term Outcomes of Epilepsy Surgery in Adults and Children*, 7(6):1–283, 2015, DOI:10.1007/978-3-319-17783-0.

[3] Christian E. Elger and Dieter Schmidt. Modern management of epilepsy: A practical approach. *Epilepsy and Behavior*, 12(4):501–539, 2008, DOI:10.1016/j.yebeh.2008.01.003.

[4] William H Theodore and Robert S Fisher. Brain stimulation for epilepsy. *The Lancet Neurology*, 3(2):111–118, 2004, DOI:10.1016/S1474-4422(03)00664-1.

[5] Shlomo Shinnar. The risk of seizure recurrence following a first unprovoked seizure: A quantitative review. *Neurology*, 41(7):965–972, 1991, DOI:10.1212/wnl.41.7.965.

[6] Ettore Beghi, Arturo Carpio, Lars Forsgren, Dale C. Hesdorffer, Kristina Malmgren, Josemir W. Sander, Torbjorn Tomson, and W. Allen Hauser. Recommendation for a definition of acute symptomatic seizure. *Epilepsia*, 51(4):671–675, 2010, DOI:10.1111/j.1528-1167.2009.02285.x.

[7] Soheyl Noachtar and Jan Rémi. The role of EEG in epilepsy: A critical review. *Epilepsy and Behavior*, 15(1):22–33, 2009, DOI:10.1016/j.yebeh.2009.02.035.

[8] Ingrid E. B. Tuxhorn, Reinhard Schulz, and Bernd Kruse. Invasive EEG in the definition of the seizure onset zone: subdural electrodes. *Handbook of Clinical Neurophysiology*, 3(C):97–108, 2003, DOI:10.1016/S1567-4231(03)03008-9.

[9] Fabien Boux, Florence Forbes, Julyan Arbel, and Emmanuel L. Barbier. Dictionary-free MR fingerprinting parameter estimation via inverse regression. In *Proceedings of the 26th Annual Meeting, ISMRM, Paris*, page 4259, 2016. HAL:01941630.

[10] Fabien Boux, Florence Forbes, Julyan Arbel, and Emmanuel Barbier. Dicionary learning via regression: vascular MRI application. In *3e Congrès National d'Imagerie du Vivant (CNIV)*, 2019. HAL:02428647.

[11] Fabien Boux, Florence Forbes, Julyan Arbel, and Emmanuel Barbier. Estimation de paramètres IRM en grande dimension via une régression inverse. In *4e congrés de la Société Française de Résonance Magnétique en Biologie et Médecine (SFRMBM)*, 2019. HAL:02428679.

[12] Aurélien Delphin. MRI Signals Simulation for Validation of a New Microvascular Characterization, 2019. DiVA:1355024.

[13] Fabien Boux, Florence Forbes, Julyan Arbel, Aurélien Delphin, Thomas Christen, and Emmanuel Barbier. Dictionary-based Learning in MR Fingerprinting: Statistical Learning versus Deep Learning. In *International Society for Magnetic Resonance in Medicine (ISMRM), 2020.*, 2020. HAL:02922858.

[14] Hermann Ackermann. Cerebellar contributions to speech production and speech perception: psycholinguistic and neurobiological perspectives. *Trends in Neurosciences*, 31(6):265–272, 2008, DOI:10.1016/j.tins.2008.02.011.

[15] S. Blease, M. Griffiths, and J. Bradshaw. Anatomy of the brain, 2001. https://mayfieldclinic.com/pe-anatbrain.htm.

[16] A. Dorr, J. G. Sled, and N. Kabani. Three-dimensional cerebral vasculature of the CBA mouse brain: A magnetic resonance imaging and micro computed tomography study. *NeuroImage*, 35(4):1409–1423, 2007, DOI:10.1016/j.neuroimage.2006.12.040.

[17] R. S. Sellers. *Book Review: Comparative Anatomy and Histology: A Mouse and Human Atlas*, volume 49. Press, Academic, 2012.

[18] Julius Fridriksson, Paul Fillmore, Dazhou Guo, and Chris Rorden. Chronic Broca's aphasia is caused by damage to Broca's and wernicke's areas. *Cerebral Cortex*, 25(12):4689–4696, 2015, DOI:10.1093/cercor/bhu152.

[19] Jeffrey R. Binder. The Wernicke area. *Neurology*, 85(24):2170–2175, 2015, DOI:10.1212/WNL.0000000000002219.

[20] Tim Czopka, Charles Ffrench-Constant, and David A. Lyons. Individual oligodendrocytes have only a few hours in which to generate new myelin sheaths in vivo. *Developmental Cell*, 25(6):599–609, 2013, DOI:10.1016/j.devcel.2013.05.013.

[21] Jochen Gehrmann, Yoh Matsumoto, and Georg W. Kreutzberg. Microglia: Intrinsic immuneffector cell of the brain. *Brain Research Reviews*, 20(3):269–287, 1995, DOI:10.1016/0165-0173(94)00015-H.

[22] Konstantinos Meletis, Fanie Barnabé-Heider, Marie Carlén, Emma Evergren, Nikolay Tomilin, Oleg Shupliakov, and Jonas Frisén. Spinal cord injury reveals multilineage differentiation of ependymal cells. *PLoS Biology*, 6(7):1494–1507, 2008, DOI:10.1371/journal.pbio.0060182.

[23] J. A. Ramos-Vara and M. A. Miller. When Tissue Antigens and Antibodies Get Along: Revisiting the Technical Aspects of Immunohistochemistry-The Red, Brown, and Blue Technique. *Veterinary Pathology*, 51(1):42–87, 2014, DOI:10.1177/0300985813505879.

[24] Deepa B. Rao, Peter B. Little, and Robert C. Sills. Subsite awareness in neuropathology evaluation of National Toxicology Program (NTP) studies: A review of select neuroanatomical structures with their functional significance in rodents. *Toxicologic Pathology*, 42(3):487–509, 2014, DOI:10.1177/0192623313501893.

[25] Samar Deb and Samar Deb. Blood Supply of Brain and Spinal Cord. *Easy and Interesting Approach to Human Neuroanatomy (Clinically Oriented)*, 2:228–228, 2014, DOI:10.5005/jp/books/12107_15.

[26] Frederic Lauwers, Francis Cassot, Valerie Lauwers-Cances, Prasanna Puwanarajah, and Henri Duvernoy. Morphometry of the human cerebral cortex microcirculation: General characteristics and space-related profiles. *NeuroImage*, 39(3):936–948, 2008, DOI:10.1016/j.neuroimage.2007.09.024.

[27] Kurt E. Schlageter, Peter Molnar, Gregory D. Lapin, and Dennis R. Groothuis. Microvessel organization and structure in experimental brain tumors: Microvessel populations with distinctive structural and functional properties. *Microvascular Research*, 58(3):312–328, 1999, DOI:10.1006/mvre.1999.2188.

[28] Hartmut Vatter, Erdem Gueresir, and Volker Seifert. Blood injection subarachnoid hemorrhage rat model. 2009, DOI:10.1007/978-1-60327-185-1_22.

[29] Berislav V. Zlokovic. Neurovascular mechanisms of Alzheimer's neurodegeneration. *Trends in Neurosciences*, 28(4):202–208, 2005, DOI:10.1016/j.tins.2005.02.001.

[30] Amy J. Bastian and W. Thomas Thach. Structure and function of the cerebellum. *The Cerebellum and its Disorders*, 37(1):49–66, 2010, DOI:10.1017/cbo9780511666469.007.

[31] Karen K. Hirschi and Patricia A. D'Amore. Pericytes in the microvasculature. *Cardiovascular Research*, 32(4):687–698, 1996, DOI:10.1016/0008-6363(96)00063-6.

[32] Annika Armulik, Guillem Genové, Maarja Mäe, Maya H. Nisancioglu, Elisabet Wallgard, Colin Niaudet, Liqun He, Jenny Norlin, Per Lindblom, Karin Strittmatter, Bengt R. Johansson, and Christer Betsholtz. Pericytes regulate the blood-brain barrier. *Nature*, 468(7323):557–561, 2010, DOI:10.1038/nature09522.

[33] Brian T. Hawkins and Thomas P. Davis. The blood-brain barrier/neurovascular unit in health and disease. *Pharmacological Reviews*, 57(2):173–185, 2005, DOI:10.1124/pr.57.2.4.

[34] Amy R. Nelson, Melanie D. Sweeney, Abhay P. Sagare, and Berislav V. Zlokovic. Neurovascular dysfunction and neurodegeneration in dementia and Alzheimer's disease. *Biochimica et Biophysica Acta - Molecular Basis of Disease*, 1862(5):887–900, 2016, DOI:10.1016/j.bbadis.2015.12.016.

[35] Stefanie Robel, Benedikt Berninger, and Magdalena Götz. The stem cell potential of glia: Lessons from reactive gliosis. *Nature Reviews Neuroscience*, 12(2):88–104, 2011, DOI:10.1038/nrn2978.

[36] Michael V. Sofroniew and Harry V. Vinters. Astrocytes: Biology and pathology. *Acta Neuropathologica*, 119(1):7–35, 2010, DOI:10.1007/s00401-009-0619-8.

[37] Mark A. Anderson, Yan Ao, and Michael V. Sofroniew. Heterogeneity of reactive astrocytes. *Neuroscience Letters*, 565:23–29, 2014, DOI:10.1016/j.neulet.2013.12.030.

[38] Randolph N. Christensen, Byeong Keun Ha, Fang Sun, Jacqueline C. Bresnahan, and Michael S. Beattie. Kainate induces rapid redistribution of the actin cytoskeleton in ameboid microglia. *Journal of Neuroscience Research*, 84(1):170–181, 2006, DOI:10.1002/jnr.20865.

[39] Engin Gonul, Bülent Duz, Serdar Kahraman, Hakan Kayali, Ayhan Kubar, and Erdener Timurkaynak. Early pericyte response to brain hypoxia in cats: An ultrastructural study. *Microvascular Research*, 64(1):116–119, 2002, DOI:10.1006/mvre.2002.2413.

[40] Paula Dore-Duffy, Cheri Owen, Roumen Balabanov, Sharon Murphy, Thomas Beaumont, and José A. Rafols. Pericyte migration from the vascular wall in response to traumatic brain injury. *Microvascular Research*, 60(1):55–69, 2000, DOI:10.1006/mvre.2000.2244.

[41] Gesa Rascher, Arne Fischmann, Stephan Kröger, Frank Duffner, Ernst H. Grote, and Hartwig Wolburg. Extracellular matrix and the blood-brain barrier in glioblastoma

multiforme: Spatial segregation of tenascin and agrin. *Acta Neuropathologica*, 104(1):85–91, 2002, DOI:10.1007/s00401-002-0524-x.

[42] Giovanni Savettieri, Italia Di Liegro, Caterina Catania, Luana Licata, Giovanna Laura Pitarresi, Stefania D'Agostino, Gabriella Schiera, Viviana De Caro, Giulia Giandalia, Libero Italo Giannola, and Alessandro Cestelli. Neurons and ECM regulate occludin localization in brain endothelial cells. *NeuroReport*, 11(5):1081–1084, 2000, DOI:10.1097/00001756-200004070-00035.

[43] Jerome Engel. A proposed diagnostic scheme for people with epileptic seizures and with epilepsy: Report of the ILAE task force on classification and terminology. *Epilepsia*, 42(6):796–803, 2001, DOI:10.1046/j.1528-1157.2001.10401.x.

[44] Jerome Engel. ILAE classification of epilepsy syndromes. *Epilepsy Research*, 70(SUPPL.1):5–10, 2006, DOI:10.1016/j.eplepsyres.2005.11.014.

[45] Gregory D. Cascino and Joseph I. Sirven. Adult Epilepsy. *Adult Epilepsy*, 367(9516):1087–1100, 2011, DOI:10.1002/9780470975039.

[46] M. J. During and D. D. Spencer. Extracellular hippocampal glutamate and spontaneous seizure in the conscious human brain. *The Lancet*, 341(8861):1607–1610, 1993, DOI:10.1016/0140-6736(93)90754-5.

[47] Matthew J. During, Kathryn M. Ryder, and Dennis D. Spencer. Hippocampal GABA transporter function in temporal-lobe epileps. *Nature*, 376(6536):174–177, 1995, DOI:10.1038/376174a0.

[48] David M. Treiman. GABAergic mechanisms in epilepsy. *Epilepsia*, 42(SUPPL. 3):8–12, 2001, DOI:10.1046/j.1528-1157.2001.042Suppl.3008.x.

[49] Solomon L. Moshé, Emilio Perucca, Philippe Ryvlin, and Torbjörn Tomson. Epilepsy: New advances. *The Lancet*, 385(9971):884–898, 2015, DOI:10.1016/S0140-6736(14)60456-6.

[50] Marco De Curtis and Giuliano Avanzini. Interictal spikes in focal epileptogenesis. *Progress in Neurobiology*, 63(5):541–567, 2001, DOI:10.1016/S0301-0082(00)00026-5.

[51] C. S. Herrmann and T. Demiralp. Human EEG gamma oscillations in neuropsychiatric disorders. *Clinical Neurophysiology*, 116(12):2719–2733, 2005, DOI:10.1016/j.clinph.2005.07.007.

[52] J. Talairach, J. Bancaud, A. Bonis, G. Szikla, and P. Tournoux. Functional stereotaxic exploration of epilepsy. *Confinia neurologica*, 22(1):328–331, 1962, DOI:10.1159/000104378.

[53] Greg A. Worrell, Landi Parish, Stephen D. Cranstoun, Rachel Jonas, Gordon Baltuch, and Brian Litt. High-frequency oscillations and seizure generation in neocortical epilepsy. *Brain*, 127(7):1496–1506, 2004, DOI:10.1093/brain/awh149.

[54] Vadym Gnatkovsky, Stefano Francione, Francesco Cardinale, Roberto Mai, Laura Tassi, Giorgio Lo Russo, and Marco De Curtis. Identification of reproducible ictal patterns based on quantified frequency analysis of intracranial EEG signals. *Epilepsia*, 52(3):477–488, 2011, DOI:10.1111/j.1528-1167.2010.02931.x.

[55] Shelagh J. M. Smith. EEG in the diagnosis, classification, and management of patients with epilepsy. *Neurology in Practice*, 76(2):ii2—-ii7, 2005, DOI:10.1136/jnnp.2005.069245.

[56] Olivier David, Thomas Blauwblomme, Anne Sophie Job, Stéphan Chabards, Dominique Hoffmann, Lorella Minotti, and Philippe Kahane. Imaging the seizure onset zone with stereo-electroencephalography. *Brain*, 134(10):2898–2911, 2011, DOI:10.1093/brain/awr238.

[57] Gary W. Mathern, Thomas L. Babb, Barbara G. Vickrey, Maria Melendez, and James K. Pretorius. The clinical-pathogenic mechanisms of hippocampal neuron loss and surgical outcomes in temporal lobe epilepsy. *Brain*, 118(1):105–118, 1995, DOI:10.1093/brain/118.1.105.

[58] Ingmar Blümcke, Maria Thom, Eleonora Aronica, Dawna D. Armstrong, Fabrice Bartolomei, Andrea Bernasconi, Neda Bernasconi, Christian G. Bien, Fernando Cendes, Roland Coras, J. Helen Cross, Thomas S. Jacques, Philippe Kahane, Gary W. Mathern, Haijme Miyata, Solomon L. Moshé, Buge Oz, Çiğdem Özkara, Emilio Perucca, Sanjay Sisodiya, Samuel Wiebe, and Roberto Spreafico. International consensus classification of hippocampal sclerosis in temporal lobe epilepsy: A Task Force report from the ILAE Commission on Diagnostic Methods. *Epilepsia*, 54(7):1315–1329, 2013, DOI:10.1111/epi.12220.

[59] Orrin Devinsky, Annamaria Vezzani, Souhel Najjar, Nihal C. De Lanerolle, and Michael A. Rogawski. Glia and epilepsy: Excitability and inflammation. *Trends in Neurosciences*, 36(3):174–184, 2013, DOI:10.1016/j.tins.2012.11.008.

[60] Jonathon Wetherington, Geidy Serrano, and Ray Dingledine. Astrocytes in the Epileptic Brain. *Neuron*, 58(2):168–178, 2008, DOI:10.1016/j.neuron.2008.04.002.

[61] Teresa Ravizza, Barbara Gagliardi, Francesco Noé, Karin Boer, Eleonora Aronica, and Annamaria Vezzani. Innate and adaptive immunity during epileptogenesis and spontaneous seizures: Evidence from experimental models and human temporal lobe epilepsy. *Neurobiology of Disease*, 29(1):142–160, 2008, DOI:10.1016/j.nbd.2007.08.012.

[62] Valérie Rigau, Mélanie Morin, Marie Claude Rousset, Frédéric De Bock, Aurore Lebrun, Philippe Coubes, Marie Christine Picot, Michel Baldy-Moulinier, Joël Bockaert, Arielle Crespel, and Mireille Lerner-Natoli. Angiogenesis is associated with blood-brain barrier permeability in temporal lobe epilepsy. *Brain*, 130(7):1942–1956, 2007, DOI:10.1093/brain/awm118.

[63] Nicola Marchi, Lilyana Angelov, Thomas Masaryk, Vincent Fazio, Tiziana Granata, Nadia Hernandez, Kerri Hallene, Tammy Diglaw, Linda Franic, Imad Najm, and Damir Janigro. Seizure-promoting effect of blood-brain barrier disruption. *Epilepsia*, 48(4):732–742, 2007, DOI:10.1111/j.1528-1167.2007.00988.x.

[64] Nicola Marchi, Tiziana Granata, Chaitali Ghosh, and Damir Janigro. Blood-brain barrier dysfunction and epilepsy: Pathophysiologic role and therapeutic approaches. *Epilepsia*, 53(11):1877–1886, 2012, DOI:10.1111/j.1528-1167.2012.03637.x.

[65] Arielle Crespel, Philippe Coubes, Marie Claude Rousset, Corinne Brana, Alain Rougier, Gérard Rondouin, Joël Bockaert, Michel Baldy-Moulinier, and Mireille Lerner-Natoli. Inflammatory reactions in human medial temporal lobe epilepsy with hippocampal sclerosis. *Brain Research*, 952(2):159–169, 2002, DOI:10.1016/S0006-8993(02)03050-0.

[66] E. A. Van Vliet, S. Da Costa Araújo, S. Redeker, R. Van Schaik, E. Aronica, and J. A. Gorter. Blood-brain barrier leakage may lead to progression of temporal lobe epilepsy. *Brain*, 130(2):521–534, 2007, DOI:10.1093/brain/awl318.

[67] A. Depaulis and S. Hamelin. Animal models for mesiotemporal lobe epilepsy: The end of a misunderstanding? *Revue Neurologique*, 171(3):217–226, 2015, DOI:10.1016/j.neurol.2015.01.558.

[68] Graham V. Goddard. Development of epileptic seizures through brain stimulation at low intensity. *Nature*, 214(5092):1020–1021, 1967, DOI:10.1038/2141020a0.

[69] Kiyoshi Morimoto, Margaret Fahnestock, and Ronald J. Racine. Kindling and status epilepticus models of epilepsy: Rewiring the brain. *Progress in Neurobiology*, 73(1):1–60, 2004, DOI:10.1016/j.pneurobio.2004.03.009.

[70] Y. Ben-Ari and J. Lagowska. Action épileptogène induite par des injections intraamygdaliennes d'acide kainique. *Comptes rendus hebdomadaires des seances de l"Academie des sciences. Serie D: Sciences naturelles*, 287(8):813–816, 1978. PMID:103652.

[71] Waldemar A. Turski, Esper A. Cavalheiro, Michael Schwarz, Stanisław J. Czuczwar, Zdzisław Kleinrok, and Lechosław Turski. Limbic seizures produced by pilocarpine in

rats: Behavioural, electroencephalographic and neuropathological study. *Behavioural Brain Research*, 9(3):315–335, 1983, DOI:10.1016/0166-4328(83)90136-5.

[72] Maxime Lévesque and Massimo Avoli. The kainic acid model of temporal lobe epilepsy. *Neuroscience and Biobehavioral Reviews*, 37(10):2887–2899, 2013, DOI:10.1016/j.neubiorev.2013.10.011.

[73] Andrew White, Philip A. Williams, Jennifer L. Hellier, Suzanne Clark, F. Edward Dudek, and Kevin J. Staley. EEG spike activity precedes epilepsy after kainate-induced status epilepticus. *Epilepsia*, 51(3):371–383, 2010, DOI:10.1111/j.1528-1167.2009.02339.x.

[74] Doodipala Samba Reddy and Ramkumar Kuruba. Experimental models of status epilepticus and neuronal injury for evaluation of therapeutic interventions. *International Journal of Molecular Sciences*, 14(9):18284–18318, 2013, DOI:10.3390/ijms140918284.

[75] Luiz E. A. M. Mello, Esper A. Cavalheiro, Aiko M. Tan, William R. Kupfer, James K. Pretorius, Thomas L. Babb, and David M. Finch. Circuit Mechanisms of Seizures in the Pilocarpine Model of Chronic Epilepsy: Cell Loss and Mossy Fiber Sprouting. *Epilepsia*, 34(6):985–995, 1993, DOI:10.1111/j.1528-1157.1993.tb02123.x.

[76] Muddanna S. Rao, Bharathi Hattiangady, Doodipala S. Reddy, and Ashok K. Shetty. Hippocampal neurodegeneration, spontaneous seizures, and mossy fiber sprouting in the F344 rat model of temporal lobe epilepsy. *Journal of Neuroscience Research*, 83(6):1088–1105, 2006, DOI:10.1002/jnr.20802.

[77] Paul S. Buckmaster, Guo Feng Zhang, and Ruth Yamawaki. Axon sprouting in a model of temporal lobe epilepsy creates a predominantly excitatory feedback circuit. *Journal of Neuroscience*, 22(15):6650–6658, 2002, DOI:10.1523/jneurosci.22-15-06650.2002.

[78] Robert S. Sloviter. The neurobiology of temporal lobe epilepsy: Too much information, not enough knowledge. *Comptes Rendus - Biologies*, 328(2):143–153, 2005, DOI:10.1016/j.crvi.2004.10.010.

[79] Marcio A. De Furtado, Glaucia K. Braga, José A. C. Oliveira, Flavio Del Vecchio, and Norberto Garcia-Cairasco. Behavioral, morphologic, and electroencephalographic evaluation of seizures induced by intrahippocampal microinjection of pilocarpine. *Epilepsia*, 43(SUPPL. 5):37–39, 2002, DOI:10.1046/j.1528-1157.2002.043s2037.x.

[80] V. Bouilleret, V. Ridoux, A. Depaulis, C. Marescaux, A. Nehlig, and G. Le Gal La Salle. Recurrent seizures and hippocampal sclerosis following intrahippocampal kainate injection in adult mice: Electroencephalography, histopathology and synaptic reorganization similar

to mesial temporal lobe epilepsy. *Neuroscience*, 89(3):717–729, 1999, DOI:10.1016/S0306-4522(98)00401-1.

[81] Y. Ben-Ari, E. Tremblay, and O. P. Ottersen. Injections of kainic acid into the amygdaloid complex of the rat: An electrographic, clinical and histological study in relation to the pathology of epilepsy. *Neuroscience*, 5(3):515–528, 1980, DOI:10.1016/0306-4522(80)90049-4.

[82] C. Cepeda, T. Tanaka, D. Riche, and R. Naquet. Limbic status epilepticus: behaviour and sleep alterations after intra-amygdaloid kainic acid microinjections in Papio papio baboons. *Electroencephalography and Clinical Neurophysiology*, 54(6):603–613, 1982, DOI:10.1016/0013-4694(82)90114-6.

[83] Marta Rattka, Claudia Brandt, and Wolfgang Löscher. The intrahippocampal kainate model of temporal lobe epilepsy revisited: Epileptogenesis, behavioral and cognitive alterations, pharmacological response, and hippoccampal damage in epileptic rats. *Epilepsy Research*, 103(2-3):135–152, 2013, DOI:10.1016/j.eplepsyres.2012.09.015.

[84] Wendy Klement, Marine Blaquiere, Emma Zub, Frederic DeBock, Fabien Boux, Emmanuel Barbier, Etienne Audinat, Mireille Lerner-Natoli, and Nicola Marchi. A pericyte-glia scarring develops at the leaky capillaries in the hippocampus during seizure activity. *Epilepsia*, 60(7):1399–1411, jul 2019, DOI:10.1111/epi.16019.

[85] V. Riban, V. Bouilleret, B. T. Pham-Lê, J. M. Fritschy, C. Marescaux, and A. Depaulis. Evolution of hippocampal epileptic activity during the development of hippocampal sclerosis in a mouse model of temporal lobe epilepsy. *Neuroscience*, 112(1):101–111, 2002, DOI:10.1016/S0306-4522(02)00064-7.

[86] Khichar Shubhakaran and Rekha Jakhar Khichar. Neuroimaging of first-ever seizure: Contribution of MRI if CT is normal. *Neurology: Clinical Practice*, 4(5):372, 2014, DOI:10.1212/01.CPJ.0000455828.60011.1d.

[87] Nitin K. Sethi and Shinnar. Evidence-based guideline: Management of an unprovoked first seizure in adults: Report of the Guideline Development Subcommittee of the American Academy of Neurology and the American Epilepsy Society. *Neurology*, 85(17):1525, 2015, DOI:10.1212/WNL.0000000000002093.

[88] R. A. Bronen. Epilepsy: The role of MR imaging. *American Journal of Roentgenology*, 159(6):1165–1174, 1992, DOI:10.2214/ajr.159.6.1442376.

[89] Maarten G. Lansberg, M. W. O'Brien, A. M. Norbash, M. E. Moseley, M. Morrell, and G. W. Albers. MRI abnormalities associated with partial status epilepticus. *Neurology*, 52(5):1021–1027, 1999, DOI:10.1212/wnl.52.5.1021.

[90] M. D. King, N. Van Bruggen, R. G. Ahier, J. E. Cremer, J. V. Hajnal, S. R. Williams, and M. Doran. Diffusion-weighted imaging of kainic acid lesions in the rat brain. *Magnetic Resonance in Medicine*, 1991, DOI:10.1002/mrm.1910200117.

[91] Man Kin Choy, King K. Cheung, David L. Thomas, David G. Gadian, Mark F. Lythgoe, and Rod C. Scott. Quantitative MRI predicts status epilepticus-induced hippocampal injury in the lithium-pilocarpine rat model. *Epilepsy Research*, 88(2-3):221–230, 2010, DOI:10.1016/j.eplepsyres.2009.11.013.

[92] Yang Wang, Anthony Majors, Imad Najm, Min Xue, Youssef Comair, Michael Modic, and Thian C. Ng. Postictal alteration of sodium content and apparent diffusion coefficient in epileptic rat brain induced by kainic acid. *Epilepsia*, 37(10):1000–1006, 1996, DOI:10.1111/j.1528-1157.1996.tb00539.x.

[93] T. Engelhorn, J. Weise, T. Hammen, I. Bluemcke, A. Hufnagel, and A. Doerfler. Early diffusion-weighted MRI predicts regional neuronal damage in generalized status epilepticus in rats treated with diazepam. *Neuroscience Letters*, 417(3):275–280, 2007, DOI:10.1016/j.neulet.2007.02.072.

[94] Jaak Nairismägi, Olli H. J. Gröhn, Mikko I. Kettunen, Jari Nissinen, Risto A. Kauppinen, and Asla Pitkänen. Progression of brain damage after status epilepticus and its association with epileptogenesis: A quantitative MRI study in a rat model of temporal lobe epilepsy. *Epilepsia*, 45(9):1024–1034, 2004, DOI:10.1111/j.0013-9580.2004.08904.x.

[95] Nick M. E. A. Hayward, Xavier Ekolle Ndode-Ekane, Nino Kutchiashvili, Olli Gröhn, and Asla Pitkänen. Elevated cerebral blood flow and vascular density in the amygdala after status epilepticus in rats. *Neuroscience Letters*, 484(1):39–42, 2010, DOI:10.1016/j.neulet.2010.08.013.

[96] Guy Bar-Klein, Svetlana Lublinsky, Lyn Kamintsky, Iris Noyman, Ronel Veksler, Hotjensa Dalipaj, Vladimir V. Senatorov, Evyatar Swissa, Dror Rosenbach, Netta Elazary, Dan Z. Milikovsky, Nadav Milk, Michael Kassirer, Yossi Rosman, Yonatan Serlin, Arik Eisenkraft, Yoash Chassidim, Yisrael Parmet, Daniela Kaufer, and Alon Friedman. Imaging blood-brain barrier dysfunction as a biomarker for epileptogenesis. *Brain*, 140(6):1692–1705, 2017, DOI:10.1093/brain/awx073.

[97] E. A. van Vliet, W. M. Otte, J. A. Gorter, R. M. Dijkhuizen, and W. J. Wadman. Longitudinal assessment of blood-brain barrier leakage during epileptogenesis in rats. A quantitative MRI study. *Neurobiology of Disease*, 63:74–84, mar 2014, DOI:10.1016/j.nbd.2013.11.019.

[98] Catherine Roch, Claire Leroy, Astrid Nehlig, and Izzie J. Namer. Magnetic resonance imaging in the study of the lithium-pilocarpine model of temporal lobe epilepsy in adult rats. *Epilepsia*, 43(4):325–335, 2002, DOI:10.1046/j.1528-1157.2002.11301.x.

[99] Viviane Bouilleret, Astrid Nehlig, Christian Marescaux, and Izzie J. Namer. Magnetic resonance imaging follow-up of progressive hippocampal changes in a mouse model of mesial temporal lobe epilepsy. *Epilepsia*, 41(6):642–650, 2000, DOI:10.1111/j.1528-1157.2000.tb00223.x.

[100] Boris C. Bernhardt, Fatemeh Fadaie, Reinder Vos de Wael, Seok Jun Hong, Min Liu, Marie C. Guiot, David A. Rudko, Andrea Bernasconi, and Neda Bernasconi. Preferential susceptibility of limbic cortices to microstructural damage in temporal lobe epilepsy: A quantitative T1 mapping study. *NeuroImage*, 182:294–303, 2018, DOI:10.1016/j.neuroimage.2017.06.002.

[101] Lionel Thivard, Stéphane Lehéricy, Alexandre Krainik, Claude Adam, Didier Dormont, Jacques Chiras, Michel Baulac, and Sophie Dupont. Diffusion tensor imaging in medial temporal lobe epilepsy with hippocampal sclerosis. *NeuroImage*, 28(3):682–690, 2005, DOI:10.1016/j.neuroimage.2005.06.045.

[102] S. Flacke, U. Wüllner, E. Keller, F. Hamzei, and H. Urbach. Reversible changes in echo planar perfusion- and diffusion-weighted MRI in status epilepticus. *Neuroradiology*, 42(2):92–95, 2000, DOI:10.1007/s002340050021.

[103] P. F. Fabene, P. Marzola, A. Sbarbati, and M. Bentivoglio. Magnetic resonance imaging of changes elicited by status epilepticus in the rat brain: Diffusion-weighted and T2-weighted images, regional blood volume maps, and direct correlation with tissue and cell damage. *NeuroImage*, 18(2):375–389, 2003, DOI:10.1016/S1053-8119(02)00025-3.

[104] Ren H. Wu, Roland Bruening, Sami Noachtar, Stephan Arnold, Christian Berchtenbreiter, Peter Bartenstein, Alexander Drzezga, Klaus Tatsch, and Maximilian Reiser. MR measurement of regional relative cerebral blood volume in epilepsy. *Journal of Magnetic Resonance Imaging*, 9(3):435–440, 1999, DOI:10.1002/(SICI)1522-2586(199903)9:3<435::AID-JMRI11>3.0.CO;2-J.

[105] Jerome Aellen, Eugenio Abela, Sarah E. Buerki, Raimund Kottke, Elisabeth Springer, Kaspar Schindler, Christian Weisstanner, Marwan El-Koussy, Gerhard Schroth, Roland Wiest, Jan Gralla, and Rajeev K. Verma. Focal hemodynamic patterns of status epilepticus detected by susceptibility weighted imaging (SWI). *European Radiology*, 24(11):2980–2988, 2014, DOI:10.1007/s00330-014-3284-9.

[106] Xinyang Feng, Marla J. Hamberger, Hannah C. Sigmon, Jia Guo, Scott A. Small, and Frank A. Provenzano. Temporal lobe epilepsy lateralization using retrospective cerebral blood volume MRI. *NeuroImage: Clinical*, 19:911–917, 2018, DOI:10.1016/j.nicl.2018.05.012.

[107] Theodor Rüber, Bastian David, Guido Lüchters, Robert D. Nass, Alon Friedman, Rainer Surges, Tony Stöcker, Bernd Weber, Ralf Deichmann, Gottfried Schlaug, Elke Hattingen, and Christian E. Elger. Evidence for peri-ictal blood-brain barrier dysfunction in patients with epilepsy. *Brain*, 141(10):2952–2965, 2018, DOI:10.1093/brain/awy242.

[108] A. D. Elster. Questions and Answers in MRI, 2017. http://mriquestions.com.

[109] IMAIOS. L'IRM pas à pas, cours interactif sur l'imagerie par résonance magnétique, 2011. http://www.imaios.com/fr/e-Cours/e-MRI.

[110] H. H. Mitchell, T. S. Hamilton, F. R. Steggerda, and H. W. Bean. The Chemical Composition of the Adult Human Body and Its Bearing on the Biochemistry of Growth. *Journal of Biological Chemistry*, 158(3):625–637, 1945. https://www.jbc.org/content/158/3/625.full.pdf.

[111] F. Bloch. Nuclear induction. *Physica*, 17(3-4):272–281, 1951, DOI:10.1016/0031-8914(51)90068-7.

[112] Mark A. Brown and Richard C. Semelka. *MRI: basic principles and applications*. Sons, John Wiley &, 2011. ISBN:978-1-119-01305-1.

[113] Gary H Glover and John M Pauly. Projection reconstruction techniques for reduction of motion effects in mri. *Magnetic resonance in medicine*, 28(2):275–289, 1992, DOI:10.1002/mrm.1910280209.

[114] Jesse Hamilton, Dominique Franson, and Nicole Seiberlich. Recent advances in parallel imaging for MRI. *Progress in Nuclear Magnetic Resonance Spectroscopy*, 101:71–95, 2017, DOI:10.1016/j.pnmrs.2017.04.002.

[115] Albert Macovski. Noise in MRI. *Magnetic Resonance in Medicine*, 1996, DOI:10.1002/mrm.1910360327.

[116] J. B. Johnson. Thermal agitation of electricity in conductors. *Physical Review*, 32(1):97–109, 1928, DOI:10.1103/PhysRev.32.97.

[117] Assaf Tal. Lecture 9: SNR, 2014. https://www.weizmann.ac.il/chemphys/assaf_tal/sites/chemphys.assaf_tal/files/uploads/lecture_9_snr.pdf.

[118] Adolf Fick. Ueber Diffusion. *Annalen der Physik*, 170(1):59–86, 1855, DOI:10.1002/andp.18551700105.

[119] E. O. Stejskal and J. E. Tanner. Spin diffusion measurements: Spin echoes in the presence of a time-dependent field gradient. *The Journal of Chemical Physics*, 42(1):288–292, 1965, DOI:10.1063/1.1695690.

[120] H. C. Torrey. Bloch equations with diffusion terms. *Physical Review*, 104(3):563–565, 1956, DOI:10.1103/PhysRev.104.563.

[121] D. Le Bihan. Molecular diffusion nuclear magnetic resonance imaging. *Magnetic resonance quarterly*, 7(1):1–30, 1991. PMID:2043461.

[122] Emmanuel L. Barbier, Laurent Lamalle, and Michel Décorps. Methodology of brain perfusion imaging. *Journal of Magnetic Resonance Imaging*, 13(4):496–520, 2001, DOI:10.1002/jmri.1073.

[123] Donald S. Williams, Donald J. Grandis, Weiguo Zhang, and Alan P. Koretsky. Magnetic resonance imaging of perfusion in the isolated rat heart using spin inversion of arterial water. *Magnetic Resonance in Medicine*, 30(3):361–365, 1993, DOI:10.1002/mrm.1910300314.

[124] Wen Chau Wu, María Fernández-Seara, John A. Detre, Felix W. Wehrli, and Jiongjiong Wang. A theoretical and experimental investigation of the tagging efficiency of pseudocontinuous arterial spin labeling. *Magnetic Resonance in Medicine*, 58(5):1020–1027, 2007, DOI:10.1002/mrm.21403.

[125] Weiying Dai, Dairon Garcia, Cedric De Bazelaire, and David C. Alsop. Continuous flow-driven inversion for arterial spin labeling using pulsed radio frequency and gradient fields. *Magnetic Resonance in Medicine*, 60(6):1488–1497, 2008, DOI:10.1002/mrm.21790.

[126] Lydiane Hirschler, Clément S. Debacker, Jérôme Voiron, Sascha Köhler, Jan M. Warnking, and Emmanuel L. Barbier. Interpulse phase corrections for unbalanced pseudo-continuous arterial spin labeling at high magnetic field. *Magnetic Resonance in Medicine*, 79(3):1314–1324, 2018, DOI:10.1002/mrm.26767.

[127] CheMatech. P00449 – Gd-DOTA. https://www.chematech-mdt.com/produit/p00449-gd-dota/.

[128] CheMatech. P904 – USPIO. https://www.chematech-mdt.com/produit/p904-uspio/.

[129] Sagar Buch, Ying Wang, Min-Gyu Park, Pavan K Jella, Jiani Hu, Yongsheng Chen, Kamran Shah, Yulin Ge, and E Mark Haacke. Subvoxel vascular imaging of the midbrain using uspio-enhanced mri. *NeuroImage*, 220:117106, 2020, DOI:10.1016/j.neuroimage.2020.117106.

[130] Jerrold L Boxerman, Leena M Hamberg, Bruce R Rosen, and Robert M Weisskoff. Mr contrast due to intravascular magnetic susceptibility perturbations. *Magnetic resonance in medicine*, 34(4):555–566, 1995, DOI:10.1002/mrm.1910340412.

[131] Irene Troprès, Laurent Lamalle, M Peoc'h, Régine Farion, Yves Usson, Michel Décorps, and C Remy. In vivo assessment of tumoral angiogenesis. *Magnetic Resonance in Medicine: An Official Journal of the International Society for Magnetic Resonance in Medicine*, 51(3):533–541, 2004, DOI:10.1002/mrm.20017.

[132] Irène Troprès, Stephan Grimault, Albert Vaeth, Emmanuelle Grillon, Cécile Julien, Jean François Payen, Laurent Lamalle, and Michel Décorps. Vessel size imaging. *Magnetic Resonance in Medicine*, 45(3):397–408, 2001, DOI:10.1002/1522-2594(200103)45:3<397::AID-MRM1052>3.0.CO;2-3.

[133] Thomas Christen, Pierre Bouzat, Nicolas Pannetier, Nicolas Coquery, Anaïck Moisan, Benjamin Lemasson, Sébastien Thomas, Emmanuelle Grillon, Olivier Detante, Chantal Rémy, Jean François Payen, and Emmanuel Luc Barbier. Tissue oxygen saturation mapping with magnetic resonance imaging. *Journal of Cerebral Blood Flow and Metabolism*, 34(9):1550–1557, 2014, DOI:10.1038/jcbfm.2014.116.

[134] Thomas Christen, Benjamin Lemasson, Nicolas Pannetier, Régine Farion, Christoph Segebarth, Chantal Rémy, and Emmanuel L. Barbier. Evaluation of a quantitative blood oxygenation level-dependent (qBOLD) approach to map local blood oxygen saturation. *NMR in Biomedicine*, 24(4):393–403, 2011, DOI:10.1002/nbm.1603.

[135] Fahmi Khalifa, Ahmed Soliman, Ayman El-Baz, Mohamed Abou El-Ghar, Tarek El-Diasty, Georgy Gimel'Farb, Rosemary Ouseph, and Amy C. Dwyer. Models and methods for analyzing DCE-MRI: A review. *Medical Physics*, 41(12):124301, 2014, DOI:10.1118/1.4898202.

[136] Hai Ling Margaret Cheng. Improved correlation to quantitative DCE-MRI pharmacokinetic parameters using a modified initial area under the uptake curve (mIAUC) approach. *Journal of Magnetic Resonance Imaging*, 30(4):864–872, 2009, DOI:10.1002/jmri.21916.

[137] Dan Ma, Vikas Gulani, Nicole Seiberlich, Kecheng Liu, Jeffrey L. Sunshine, Jeffrey L. Duerk, and Mark A. Griswold. Magnetic resonance fingerprinting. *Nature*, 495(7440):187–192, 2013, DOI:10.1038/nature11971.

[138] Ananya Panda, Bhairav B. Mehta, Simone Coppo, Yun Jiang, Dan Ma, Nicole Seiberlich, Mark A. Griswold, and Vikas Gulani. Magnetic resonance fingerprinting – An overview. *Current Opinion in Biomedical Engineering*, 3:56–66, 2017, DOI:10.1016/j.cobme.2017.11.001.

[139] Debra F. McGivney, Rasim Boyacıoğlu, Yun Jiang, Megan E. Poorman, Nicole Seiberlich, Vikas Gulani, Kathryn E. Keenan, Mark A. Griswold, and Dan Ma. Magnetic resonance fingerprinting review part 2: Technique and directions. *Journal of Magnetic Resonance Imaging*, 51(4):993–1007, 2020, DOI:10.1002/jmri.26877.

[140] Jorge J. Moré. The Levenberg-Marquardt algorithm: Implementation and theory. *Numerical analysis*, pages 105–116, 1978, DOI:10.1007/bfb0067700.

[141] Dan Ma, Eric Y. Pierre, Yun Jiang, Mark D. Schluchter, Kawin Setsompop, Vikas Gulani, and Mark A. Griswold. Music-based magnetic resonance fingerprinting to improve patient comfort during MRI examinations. *Magnetic Resonance in Medicine*, 75(6):2303–2314, 2016, DOI:10.1002/mrm.25818.

[142] Yun Jiang, Dan Ma, Nicole Seiberlich, Vikas Gulani, and Mark A. Griswold. MR fingerprinting using fast imaging with steady state precession (FISP) with spiral readout. *Magnetic Resonance in Medicine*, 74(6):1621–1631, 2015, DOI:10.1002/mrm.25559.

[143] Jakob Assländer, Steffen J. Glaser, and Jürgen Hennig. Pseudo Steady-State Free Precession for MR-Fingerprinting. *Magnetic Resonance in Medicine*, 77(3):1151–1161, 2017, DOI:10.1002/mrm.26202.

[144] Benedikt Rieger, Fabian Zimmer, Jascha Zapp, Sebastian Weingärtner, and Lothar R. Schad. Magnetic resonance fingerprinting using echo-planar imaging: Joint quantification of T1 and T2 relaxation times. *Magnetic Resonance in Medicine*, 78(5):1724–1733, 2017, DOI:10.1002/mrm.26561.

[145] Megan E. Poorman, Michele N. Martin, Dan Ma, Debra F. McGivney, Vikas Gulani, Mark A. Griswold, and Kathryn E. Keenan. Magnetic resonance fingerprinting Part 1: Potential uses, current challenges, and recommendations. *Journal of Magnetic Resonance Imaging*, 51(3):675–692, 2020, DOI:10.1002/jmri.26836.

[146] Pan Su, Deng Mao, Peiying Liu, Yang Li, Marco C. Pinho, Babu G. Welch, and Hanzhang Lu. Multiparametric estimation of brain hemodynamics with MR fingerprinting ASL. *Magnetic Resonance in Medicine*, 78(5):1812–1823, 2017, DOI:10.1002/mrm.26587.

[147] T. Christen, N. A. Pannetier, W. W. Ni, D. Qiu, M. E. Moseley, N. Schuff, and G. Zaharchuk. MR vascular fingerprinting: A new approach to compute cerebral blood volume, mean vessel radius, and oxygenation maps in the human brain. *NeuroImage*, 89:262–270, 2014, DOI:10.1016/j.neuroimage.2013.11.052.

[148] Matthias Weigel. Extended phase graphs: Dephasing, RF pulses, and echoes - Pure and simple. *Journal of Magnetic Resonance Imaging*, 41(2):266–295, 2015, DOI:10.1002/jmri.24619.

[149] Dong Wang, Jason Ostenson, and David S. Smith. snapMRF: GPU-accelerated magnetic resonance fingerprinting dictionary generation and matching using extended phase graphs. *Magnetic Resonance Imaging*, 66:248–256, 2020, DOI:10.1016/j.mri.2019.11.015.

[150] Shaihan J. Malik, Rui Pedro A. G. Teixeira, and Joseph V. Hajnal. Extended phase graph formalism for systems with magnetization transfer and exchange. *Magnetic Resonance in Medicine*, 80(2):767–779, 2018, DOI:10.1002/mrm.27040.

[151] Martijn A. Cloos, Florian Knoll, Tiejun Zhao, Kai T. Block, Mary Bruno, Graham C. Wiggins, and Daniel K. Sodickson. Multiparametric imaging with heterogeneous radiofrequency fields. *Nature Communications*, 7:12445, 2016, DOI:10.1038/ncomms12445.

[152] Nicolas Adrien Pannetier, Clément Stéphan Debacker, Franck Mauconduit, Thomas Christen, and Emmanuel Luc Barbier. A Simulation Tool for Dynamic Contrast Enhanced MRI. *PLoS ONE*, 8(3), 2013, DOI:10.1371/journal.pone.0057636.

[153] Philippe Pouliot, Louis Gagnon, Tina Lam, Pramod K. Avti, Chris Bowen, Michèle Desjardins, Ashok K. Kakkar, Eric Thorin, Sava Sakadzic, David A. Boas, and Frédéric Lesage. Magnetic resonance fingerprinting based on realistic vasculature in mice. *NeuroImage*, 149:436–445, 2017, DOI:10.1016/j.neuroimage.2016.12.060.

[154] B. Lemasson, N. Pannetier, N. Coquery, Ligia S. B. Boisserand, Nora Collomb, N. Schuff, M. Moseley, G. Zaharchuk, E. L. Barbier, and T. Christen. MR vascular fingerprinting in stroke and brain tumors models. *Scientific Reports*, 6:37071, 2016, DOI:10.1038/srep37071.

[155] Jakob Assländer. A Perspective on MR Fingerprinting. *Journal of Magnetic Resonance Imaging*, pages 1–10, 2020, DOI:10.1002/jmri.27134.

[156] Debra F. McGivney, Eric Pierre, Dan Ma, Yun Jiang, Haris Saybasili, Vikas Gulani, and Mark A. Griswold. SVD compression for magnetic resonance fingerprinting in the time domain. *IEEE Transactions on Medical Imaging*, 33(12):2311–2322, 2014, DOI:10.1109/TMI.2014.2337321.

[157] Jakob Assländer, Martijn A. Cloos, Florian Knoll, Daniel K. Sodickson, Jürgen Hennig, and Riccardo Lattanzi. Low rank alternating direction method of multipliers reconstruction for MR fingerprinting. *Magnetic Resonance in Medicine*, 79(1):83–96, 2018, DOI:10.1002/mrm.26639.

[158] Bo Zhao, Kawin Setsompop, Elfar Adalsteinsson, Borjan Gagoski, Huihui Ye, Dan Ma, Yun Jiang, P. Ellen Grant, Mark A. Griswold, and Lawrence L. Wald. Improved magnetic resonance fingerprinting reconstruction with low-rank and subspace modeling. *Magnetic Resonance in Medicine*, 79(2):933–942, 2018, DOI:10.1002/mrm.26701.

[159] Gal Mazor, Lior Weizman, Assaf Tal, and Yonina C. Eldar. Low-rank magnetic resonance fingerprinting. *Medical Physics*, 45(9):4066–4084, 2018, DOI:10.1002/mp.13078.

[160] Mingrui Yang, Dan Ma, Yun Jiang, Jesse Hamilton, Nicole Seiberlich, Mark A. Griswold, and Debra McGivney. Low rank approximation methods for MR fingerprinting with large scale dictionaries. *Magnetic Resonance in Medicine*, 79(4):2392–2400, 2018, DOI:10.1002/mrm.26867.

[161] Stephen F. Cauley, Kawin Setsompop, Dan Ma, Yun Jiang, Huihui Ye, Elfar Adalsteinsson, Mark A. Griswold, and Lawrence L. Wald. Fast group matching for MR fingerprinting reconstruction. *Magnetic Resonance in Medicine*, 74(2):523–528, 2015, DOI:10.1002/mrm.25439.

[162] Mike Davies, Gilles Puy, Pierre Vandergheynst, and Yves Wiaux. A compressed sensing framework for magnetic resonance fingerprinting. *SIAM Journal on Imaging Sciences*, 7(4):2623–2656, 2014, DOI:10.1137/130947246.

[163] Tao Zhang, John M. Pauly, and Ives R. Levesque. Accelerating parameter mapping with a locally low rank constraint. *Magnetic Resonance in Medicine*, 73(2):655–661, 2015, DOI:10.1002/mrm.25161.

[164] Bo Zhao, Kawin Setsompop, Huihui Ye, Stephen F. Cauley, and Lawrence L. Wald. Maximum Likelihood Reconstruction for Magnetic Resonance Fingerprinting. *IEEE Transactions on Medical Imaging*, 35(8):1812–1823, 2016, DOI:10.1109/TMI.2016.2531640.

[165] Ouri Cohen, Bo Zhu, and Matthew S. Rosen. MR fingerprinting Deep RecOnstruction NEtwork (DRONE). *Magnetic Resonance in Medicine*, 80(3):885–894, 2018, DOI:10.1002/mrm.27198.

[166] Elisabeth Hoppe, Gregor Körzdörfer, Tobias Würfl, Jens Wetzl, Felix Lugauer, Josef Pfeuffer, and Andreas Maier. Deep learning for magnetic resonance fingerprinting: A new approach for predicting quantitative parameter values from time series. In *Studies in Health Technology and Informatics*, volume 243, pages 202–206, 2017, DOI:10.3233/978-1-61499-808-2-202.

[167] Elisabeth Hoppe, Florian Thamm, Gregor Körzdörfer, Christopher Syben, Franziska Schirrmacher, Mathias Nittka, Josef Pfeuffer, Heiko Meyer, and Andreas Maier. Abstract: Rinq fingerprinting: recurrence-informed quantile networks for magnetic resonance fingerprinting. In *Informatik aktuell*, page 184. Springer, 2020, DOI:10.1007/978-3-658-29267-6_38.

[168] Patrick Virtue, Stella X. Yu, and Michael Lustig. Better than real: Complex-valued neural nets for MRI fingerprinting. In *Proceedings - International Conference on Image Processing, ICIP*, volume 2017-Septe, pages 3953–3957. IEEE, 2018, DOI:10.1109/ICIP.2017.8297024.

[169] Marco Barbieri, Leonardo Brizi, Enrico Giampieri, Francesco Solera, Gastone Castellani, Claudia Testa, and Daniel Remondini. Circumventing the Curse of Dimensionality in Magnetic Resonance Fingerprinting through a Deep Learning Approach. *arXiv preprint arXiv:1811.11477*, 2018. arXiv:1811.11477.

[170] Fabien Boux, Florence Forbes, Julyan Arbel, Benjamin Lemasson, and Emmanuel Barbier. Bayesian inverse regression for vascular magnetic resonance fingerprinting. *HAL preprint*, 2020. HAL:02314026v2.

[171] Bhairav Bipin Mehta, Simone Coppo, Debra Frances McGivney, Jesse Ian Hamilton, Yong Chen, Yun Jiang, Dan Ma, Nicole Seiberlich, Vikas Gulani, and Mark Alan Griswold. Magnetic resonance fingerprinting: a technical review. *Magnetic Resonance in Medicine*, 81(1):25–46, 2019, DOI:10.1002/mrm.27403.

[172] Gopal Nataraj, Jon Fredrik Nielsen, Clayton Scott, and Jeffrey A. Fessler. Dictionary-Free MRI PERK: Parameter Estimation via Regression with Kernels. *IEEE Transactions on Medical Imaging*, 37(9):2103–2114, 2018, DOI:10.1109/TMI.2018.2817547.

[173] Fabian Balsiger, Amaresha Shridhar Konar, Shivaprasad Chikop, Vimal Chandran, Olivier Scheidegger, Sairam Geethanath, and Mauricio Reyes. Magnetic resonance fingerprinting

reconstruction via spatiotemporal convolutional neural networks. In *Lecture Notes in Computer Science (including subseries Lecture Notes in Artificial Intelligence and Lecture Notes in Bioinformatics)*, volume 11074 LNCS, pages 39–46. Springer, 2018, DOI:10.1007/978-3-030-00129-2_5.

[174] Pingfan Song, Yonina C. Eldar, Gal Mazor, and Miguel R. D. Rodrigues. HYDRA: Hybrid deep magnetic resonance fingerprinting. *Medical Physics*, 46(11):4951–4969, 2019, DOI:10.1002/mp.13727.

[175] Mohammad Golbabaee, Dongdong Chen, Pedro A. Gomez, Marion I. Menzel, and Mike E. Davies. Geometry of Deep Learning for Magnetic Resonance Fingerprinting. In *ICASSP, IEEE International Conference on Acoustics, Speech and Signal Processing - Proceedings*, volume 2019-May, pages 7825–7829. IEEE, 2019, DOI:10.1109/ICASSP.2019.8683549.

[176] Antoine Deleforge, Florence Forbes, and Radu Horaud. High-dimensional regression with gaussian mixtures and partially-latent response variables. *Statistics and Computing*, 25(5):893–911, 2015, DOI:10.1007/s11222-014-9461-5.

[177] Ker Chau Li. Sliced inverse regression for dimension reduction. *Journal of the American Statistical Association*, 86(414):316–327, 1991, DOI:10.1080/01621459.1991.10475035.

[178] R. Dennis Cook and Liliana Forzani. Partial least squares prediction in high-dimensional regression. *Annals of Statistics*, 47(2):884–908, 2019, DOI:10.1214/18-AOS1681.

[179] Hien D. Nguyen, Faicel Chamroukhi, and Florence Forbes. Approximation results regarding the multiple-output Gaussian gated mixture of linear experts model. *Neurocomputing*, 366:208–214, 2019, DOI:10.1016/j.neucom.2019.08.014.

[180] Salvatore Ingrassia, Simona C. Minotti, and Giorgio Vittadini. Local Statistical Modeling via a Cluster-Weighted Approach with Elliptical Distributions. *Journal of Classification*, 29(3):363–401, 2012, DOI:10.1007/s00357-012-9114-3.

[181] Bruce Jay Collings and Harald Niederreiter. Random Number Generation and Quasi-Monte Carlo Methods. 88(422):699, 1993, DOI:10.2307/2290359.

[182] Art B. Owen. Randomly Permuted (t,m,s)-Nets and (t,s)-Sequences. pages 299–317, 1995, DOI:10.1007/978-1-4612-2552-2_19.

[183] Paul Bratley and Bennett L. Fox. Algorithm 659: Implementing Sobol's Quasirandom Sequence Generator. *ACM Transactions on Mathematical Software (TOMS)*, 14(1):88–100, 1988, DOI:10.1145/42288.214372.

[184] J. Matouseˇk. On the l_2-discrepancy for Anchored Boxes. *Journal of Complexity*, 14(4):527–556, 1998. Corpus:15895395.

[185] Clément Brossard, Olivier Montigon, Fabien Boux, Aurélien Delphin, Thomas Christen, Emmanuel Barbier, Benjamin Lemasson, and Emmanuel L. Barbier. MP3: Medical software for Processing multi-Parametric images Pipelines. 2020. HAL:02937866.

[186] M. J. Sáiz-Abajo, B. H. Mevik, V. H. Segtnan, and T. Næs. Ensemble methods and data augmentation by noise addition applied to the analysis of spectroscopic data. *Analytica Chimica Acta*, 533(2):147–159, 2005, DOI:10.1016/j.aca.2004.10.086.

[187] Irène Troprès, Nicolas Pannetier, Sylvie Grand, Benjamin Lemasson, Anaïck Moisan, Michel Péoc'h, Chantal Rémy, and Emmanuel L. Barbier. Imaging the microvessel caliber and density: Principles and applications of microvascular MRI. *Magnetic Resonance in Medicine*, 73(1):325–341, 2015, DOI:10.1002/mrm.25396.

[188] Benjamin Lemasson, Thomas Christen, Raphaël Serduc, Cécile Maisin, Audrey Bouchet, Géraldine Le Duc, Chantal Rémy, and Emmanuel L. Barbier. Evaluation of the relationship between MR estimates of blood oxygen saturation and hypoxia: Effect of an antiangiogenic treatment on a gliosarcoma model. *Radiology*, 265(3):743–752, 2012, DOI:10.1148/radiol.12112621.

[189] Hirotogu Akaike. Information Theory and an Extension of the Maximum Likelihood Principle. pages 199–213, 1998, DOI:10.1007/978-1-4612-1694-0_15.

[190] Gideon Schwarz. Estimating the Dimension of a Model. *The Annals of Statistics*, 6(2):461–464, 1978, DOI:10.1214/aos/1176344136.

[191] Alexis Arnaud, Florence Forbes, Nicolas Coquery, Nora Collomb, Benjamin Lemasson, and Emmanuel L. Barbier. Fully Automatic Lesion Localization and Characterization: Application to Brain Tumors Using Multiparametric Quantitative MRI Data. *IEEE Transactions on Medical Imaging*, 37(7):1678–1689, jul 2018, DOI:10.1109/TMI.2018.2794918.

[192] Danielle Kara, Mingdong Fan, Jesse Hamilton, Mark Griswold, Nicole Seiberlich, and Robert Brown. Parameter map error due to normal noise and aliasing artifacts in MR fingerprinting. *Magnetic Resonance in Medicine*, 81(5):3108–3123, 2019, DOI:10.1002/mrm.27638.

[193] João Mendes-Moreira, Carlos Soares, Alípio Mário Jorge, and Jorge Freire De Sousa. Ensemble approaches for regression: A survey. 2012, DOI:10.1145/2379776.2379786.

[194] Zhenghan Fang, Yong Chen, Weili Lin, and Dinggang Shen. Quantification of relaxation times in MR Fingerprinting using deep learning. In *Proceedings of the International Society for Magnetic Resonance in Medicine. Scientific Meeting and Exhibition*, volume 25. NIH Public Access, 2017. PMID: 29681776.

[195] Zhenghan Fang, Yong Chen, Mingxia Liu, Lei Xiang, Qian Zhang, Qian Wang, Weili Lin, and Dinggang Shen. Deep Learning for Fast and Spatially Constrained Tissue Quantification from Highly Accelerated Data in Magnetic Resonance Fingerprinting. *IEEE Transactions on Medical Imaging*, 38(10):2364–2374, 2019, DOI:10.1109/TMI.2019.2899328.

[196] Ilkay Oksuz, Gastao Cruz, James Clough, Aurelien Bustin, Nicolo Fuin, Rene M. Botnar, Claudia Prieto, Andrew P. King, and Julia A. Schnabel. Magnetic resonance fingerprinting using recurrent neural networks. In *Proceedings - International Symposium on Biomedical Imaging*, volume 2019-April, pages 1537–1540. IEEE, 2019, DOI:10.1109/ISBI.2019.8759502.

[197] Alon Friedman. Blood-brain barrier dysfunction, status epilepticus, seizures, and epilepsy: A puzzle of a chicken and egg? *Epilepsia*, 52(SUPPL. 8):19–20, oct 2011, DOI:10.1111/j.1528-1167.2011.03227.x.

[198] E. A. van Vliet, E. Aronica, and J. A. Gorter. Blood-brain barrier dysfunction, seizures and epilepsy. 38:26–34, feb 2015, DOI:10.1016/j.semcdb.2014.10.003.

[199] Nicola Marchi, William Tierney, Andreas V. Alexopoulos, Vikram Puvenna, Tiziana Granata, and Damir Janigro. The etiological role of blood-brain barrier dysfunction in seizure disorders. *Cardiovascular Psychiatry and Neurology*, 2011, 2011, DOI:10.1155/2011/482415.

[200] Margarita Arango-Lievano, Badreddine Boussadia, Lucile Du Trieu De Terdonck, Camille Gault, Pierre Fontanaud, Chrystel Lafont, Patrice Mollard, Nicola Marchi, and Freddy Jeanneteau. Topographic Reorganization of Cerebrovascular Mural Cells under Seizure Conditions. *Cell Reports*, 23(4):1045–1059, apr 2018, DOI:10.1016/j.celrep.2018.03.110.

[201] Ofer Prager, Lyna Kamintsky, Luisa A. Hasam-Henderson, Karl Schoknecht, Vera Wuntke, Ismini Papageorgiou, Jutta Swolinsky, Valeria Muoio, Guy Bar-Klein, Udi Vazana, Uwe Heinemann, Alon Friedman, and Richard Kovács. Seizure-induced microvascular injury is associated with impaired neurovascular coupling and blood–brain barrier dysfunction. *Epilepsia*, 60(2):322–336, feb 2019, DOI:10.1111/epi.14631.

[202] Sebastien Milesi, Badreddine Boussadia, Clement Plaud, Matthias Catteau, Marie Claude Rousset, Frederic De Bock, Marie Schaeffer, Mireille Lerner-Natoli, Valerie Rigau, and

Nicola Marchi. Redistribution of PDGFRβ cells and NG2DsRed pericytes at the cerebrovasculature after status epilepticus. *Neurobiology of Disease*, 71:151–158, 2014, DOI:10.1016/j.nbd.2014.07.010.

[203] Annamaria Vezzani, Silvia Balosso, and Teresa Ravizza. Neuroinflammatory pathways as treatment targets and biomarkers in epilepsy. In *Nature Reviews Neurology*, volume 15, pages 459–472. Nature Publishing Group, aug 2019, DOI:10.1038/s41582-019-0217-x.

[204] Erwin A. Van Vliet, Willem M. Otte, Wytse J. Wadman, Eleonora Aronica, Gijs Kooij, Helga E. De Vries, Rick M. Dijkhuizen, and Jan A. Gorter. Blood-brain barrier leakage after status epilepticus in rapamycin-treated rats I: Magnetic resonance imaging. *Epilepsia*, 57(1):59–69, jan 2016, DOI:10.1111/epi.13246.

[205] Yuji Hamamoto, Daisuke Hasegawa, Shunta Mizoguchi, Yoshihiko Yu, Masae Wada, Takayuki Kuwabara, Aki Fujiwara-Igarashi, and Michio Fujita. Changes in the interictal and early postictal diffusion and perfusion magnetic resonance parameters in familial spontaneous epileptic cats. *Epilepsy Research*, 133(April):76–82, 2017, DOI:10.1016/j.eplepsyres.2017.04.015.

[206] Christophe Heinrich, Naoki Nitta, Armin Flubacher, Martin Müller, Alexander Fahrner, Matthias Kirsch, Thomas Freiman, Fumio Suzuki, Antoine Depaulis, Michael Frotscher, and Carola A. Haas. Reelin deficiency and displacement of mature neurons, but not neurogenesis, underlie the formation of granule cell dispersion in the epileptic hippocampus. *Journal of Neuroscience*, 26(17):4701–4713, 2006, DOI:10.1523/JNEUROSCI.5516-05.2006.

[207] Fabien Pernot, Christophe Heinrich, Laure Barbier, André Peinnequin, Pierre Carpentier, Franck Dhote, Valérie Baille, Claire Beaup, Antoine Depaulis, and Frédéric Dorandeu. Inflammatory changes during epileptogenesis and spontaneous seizures in a mouse model of mesiotemporal lobe epilepsy. *Epilepsia*, 52(12):2315–2325, dec 2011, DOI:10.1111/j.1528-1167.2011.03273.x.

[208] Itamar Ronen and Dae Shik Kim. *Principles of magnetic resonance imaging*. 2008.

[209] Emma Zub, Geoffrey Canet, Rita Garbelli, Marine Blaquiere, Laura Rossini, Chiara Pastori, Madeeha Sheikh, Chris Reutelingsperger, Wendy Klement, Frederic de Bock, Etienne Audinat, Laurent Givalois, Egle Solito, and Nicola Marchi. The GR-ANXA1 pathway is a pathological player and a candidate target in epilepsy. *FASEB journal : official publication of the Federation of American Societies for Experimental Biology*, 33(12):13998–14009, 2019, DOI:10.1096/fj.201901596R.

[210] G. D. Jackson, S. F. Berkovic, J. S. Duncan, and A. Connelly. Optimizing the diagnosis of hippocampal sclerosis using MR imaging. *American Journal of Neuroradiology*, 14(3):753–762, 1993. PMID:8517369.

[211] Amanpreet Badhwar, Jason P. Lerch, Edith Hamel, and John G. Sled. Impaired structural correlates of memory in Alzheimer's disease mice. *NeuroImage: Clinical*, 3:290–300, jan 2013, DOI:10.1016/j.nicl.2013.08.017.

[212] B. B. Avants, C. L. Epstein, M. Grossman, and J. C. Gee. Symmetric diffeomorphic image registration with cross-correlation: Evaluating automated labeling of elderly and neurodegenerative brain. *Medical Image Analysis*, 12(1):26–41, 2008, DOI:10.1016/j.media.2007.06.004.

[213] Marine Beaumont, Benjamin Lemasson, Régine Farion, Christoph Segebarth, Chantal Rémy, and Emmanuel L Barbier. Characterization of tumor angiogenesis in rat brain using iron-based vessel size index mri in combination with gadolinium-based dynamic contrast-enhanced mri. *Journal of Cerebral Blood Flow & Metabolism*, 29(10):1714–1726, 2009, DOI:10.1038/jcbfm.2009.86.

[214] Samuel Valable, Benjamin Lemasson, Régine Farion, Marine Beaumont, Christoph Segebarth, Chantal Remy, and Emmanuel L. Barbier. Assessment of blood volume, vessel size, and the expression of angiogenic factors in two rat glioma models: A longitudinal in vivo and ex vivo study. *NMR in Biomedicine*, 21(10):1043–1056, 2008, DOI:10.1002/nbm.1278.

[215] Ralph Meier, Ute Häussler, Ad Aertsen, Colin Deransart, Antoine Depaulis, and Ulrich Egert. Short-term changes in bilateral hippocampal coherence precede epileptiform events. *NeuroImage*, 38(1):138–149, 2007, DOI:10.1016/j.neuroimage.2007.07.016.

[216] Jeffrey D. Rudie, John B. Colby, and Noriko Salamon. Machine learning classification of mesial temporal sclerosis in epilepsy patients. *Epilepsy Research*, 117:63–69, 2015, DOI:10.1016/j.eplepsyres.2015.09.005.

[217] John Del Gaizo, Neda Mofrad, Jens H. Jensen, David Clark, Russell Glenn, Joseph Helpern, and Leonardo Bonilha. Using machine learning to classify temporal lobe epilepsy based on diffusion MRI. *Brain and Behavior*, 7(10):1–7, 2017, DOI:10.1002/brb3.801.

[218] Diego Cantor-Rivera, Ali R. Khan, Maged Goubran, Seyed M. Mirsattari, and Terry M. Peters. Detection of temporal lobe epilepsy using support vector machines in multi-parametric quantitative MR imaging. 41:14–28, 2015, DOI:10.1016/j.compmedimag.2014.07.002.

[219] Takaaki Tokumitsu, Anthony Mancuso, Philip R. Weinstein, Michael W. Weiner, Shoji Naruse, and Andrew A. Maudsley. Metabolic and pathological effects of temporal lobe epilepsy in rat brain detected by proton spectroscopy and imaging. 744(1):57–67, 1997, DOI:10.1016/S0006-8993(96)01071-2.

[220] Dimitrula Arabadzisz, Károly Antal, Franziska Parpan, Zsuzsa Emri, and Jean Marc Fritschy. Epileptogenesis and chronic seizures in a mouse model of temporal lobe epilepsy are associated with distinct EEG patterns and selective neurochemical alterations in the contralateral hippocampus. *Experimental Neurology*, 194(1):76–90, 2005, DOI:10.1016/j.expneurol.2005.01.029.

[221] Johan Pallud, Ute Häussler, Mélanie Langlois, Sophie Hamelin, Bertrand Devaux, Colin Deransart, and Antoine Depaulis. Dentate gyrus and hilus transection blocks seizure propagation and granule cell dispersion in a mouse model for mesial temporal lobe epilepsy. *Hippocampus*, 21(3):334–343, 2011, DOI:10.1002/hipo.20795.

[222] Antti M. Airaksinen, Juha Pekka Niskanen, Ryan Chamberlain, Joanna K. Huttunen, Jari Nissinen, Michael Garwood, Asla Pitkänen, and Olli Gröhn. Simultaneous fMRI and local field potential measurements during epileptic seizures in medetomidine-sedated rats using RASER pulse sequence. *Magnetic Resonance in Medicine*, 64(4):1191–1199, 2010, DOI:10.1002/mrm.22508.

[223] Hal Blumenfeld. Functional MRI studies of animal models in epilepsy. *Epilepsia*, 48(SUPPL. 4):18–26, sep 2007, DOI:10.1111/j.1528-1167.2007.01238.x.

[224] David Alexander Dickie, Susan D. Shenkin, Devasuda Anblagan, Juyoung Lee, Manuel Blesa Cabez, David Rodriguez, James P. Boardman, Adam Waldman, Dominic E. Job, and Joanna M. Wardlaw. Whole brain magnetic resonance image atlases: A systematic review of existing atlases and caveats for use in population imaging. 11:1, jan 2017, DOI:10.3389/fninf.2017.00001.

[225] Khader M. Hasan, Indika S. Walimuni, Larry A. Kramer, and Ponnada A. Narayana. Human brain iron mapping using atlas-based T2 relaxometry. *Magnetic Resonance in Medicine*, 67(3):731–739, mar 2012, DOI:10.1002/mrm.23054.

[226] Shengwei Zhang and Konstantinos Arfanakis. Evaluation of standardized and study-specific diffusion tensor imaging templates of the adult human brain: Template characteristics, spatial normalization accuracy, and detection of small inter-group FA differences. *NeuroImage*, 172:40–50, may 2018, DOI:10.1016/j.neuroimage.2018.01.046.

[227] Aurélien Delphin, Fabien Boux, Clément Brossard, Jan Warnking, Benjamin Lemasson, Emmanuel Luc Barbier, and Thomas Christen. Optimizing signal patterns for mr vascular fingerprinting. In *ISMRM & SMRT Virtual Conference & Exhibition*, 2020. HAL:02926840.

[228] Cynthia Rudin. Stop explaining black box machine learning models for high stakes decisions and use interpretable models instead. *Nature Machine Intelligence*, 1(5):206–215, 2019, DOI:10.1038/s42256-019-0048-x.

[229] Antoine Deleforge, Florence Forbes, Sileye Ba, and Radu Horaud. Hyper-spectral image analysis with partially latent regression and spatial Markov dependencies. *IEEE Journal on Selected Topics in Signal Processing*, 9(6):1037–1048, 2015, DOI:10.1109/JSTSP.2015.2416677.

[230] Paul Fearnhead and Dennis Prangle. Constructing summary statistics for approximate Bayesian computation: Semi-automatic approximate Bayesian computation. *Journal of the Royal Statistical Society. Series B: Statistical Methodology*, 74(3):419–474, 2012, DOI:10.1111/j.1467-9868.2011.01010.x.

[231] Bai Jiang, Tung Yu Wu, and Wing Hung Wong. Approximate Bayesian computation with Kullback-Leibler divergence as data discrepancy. In *International Conference on Artificial Intelligence and Statistics, AISTATS 2018*, pages 1711–1721, 2018. PMLR:84:1711-1721.

[232] Hien D. Nguyen, Florence Forbes, and Geoffrey J. McLachlan. Mini-batch learning of exponential family finite mixture models. *Statistics and Computing*, 30(4):731–748, 2020, DOI:10.1007/s11222-019-09919-4.

[233] Bb Avants, Nick Tustison, and Gang Song. Advanced normalization tools (ants). *Insight j*, 2(365):1–35, 2009. http://stnava.github.io/ANTs/.

[234] Thibaud Crespy, Maxime Durost, Pierre Fricault, Benjamin Lemasson, Pierre Bouzat, Emmanuel L. Barbier, and Jean François Payen. Hypertonic Sodium Lactate to Alleviate Functional Deficits Following Diffuse Traumatic Brain Injury: An Osmotic or a Lactate-Related Effect? *Neurocritical Care*, pages 1–9, 2020, DOI:10.1007/s12028-020-01090-3.

Appendix A

Curriculum vitae

Fabien Boux, Ph.D. student

fabien.boux@univ-grenoble-alpes.fr
http://fabienboux.wordpress.com/
https://www.linkedin.com/in/fabien-boux-248626101/

Education

2017 – 2020 **Ph.D. Applied Mathematics** in Université Grenoble Alpes, France,
supervised by Florence Forbes (Inria) & Emmanuel Barbier (Grenoble Institute of Neurosciences), in collaboration with Julyan Arbel (Inria).
Thesis title: *Statistical methods for vascular magnetic resonance fingerprinting: application to imaging the epileptic brain.*

2013 – 2016 **M.Sc. Signal and Image processing, Communication systems, and Multimedia** in Phelma engineering school, Polytechnic Institute of Grenoble, France.

Employment History

2017 **Consultant engineer** in Schneider Electric, Grenoble, France.
Development of continuous automatic integration tools for implementing analytics and artificial intelligence solutions in python programming.

2016 **Engineer (6-month internship)** in Clinatec biomedical research centre (CEA), Grenoble, France.
Optimization of supervised machine learning algorithms to estimate movements imagined by a tetraplegic patient from brain ECoG recording, using a regularized partial least squares regression.

2015 **Assistant engineer (4-month internship)** in GIPSA-lab, Grenoble, France.
Development of an algorithm to characterize the spatial dynamic of an epileptic seizure from brain EEG recording, using time-frequency decomposition and independent component analysis.

Research Publications

Journal Articles

1. **Boux**, **F.**, Forbes, F., Arbel, J., Lemasson, B., & Barbier, E. (2020). Bayesian inverse regression for vascular magnetic resonance fingerprinting. *Submitted to IEEE Transactions on Medical Imaging*.
2. **Boux**, **F.**, Forbes, F., Collomb, N., Zub, E., Lucile, M., de Bock, F., Blaquiere, M., Stupar, V., Depaulis, A., Marchi, N., & Barbier, E. (2020). Neurovascular multiparametric MRI defines epileptogenic regions in experimental mesiotemporal lobe epilepsy. *In preparation*.
3. Brossard, C., Montigon, O., **Boux**, **F.**, Delphin, A., Thomas, C., Barbier, E. L., & Lemasson, B. (2020). MP3: Medical software for Processing multi-Parametric images Pipelines. *Submitted to Frontiers in Neuroinformatics*.
4. Klement, W., Blaquiere, M., Zub, E., Debock, F., **Boux**, **F.**, Barbier, E., Audinat, E., Lerner-Natoli, M., & Marchi, N. (2019). A pericyte-glia scarring develops at the leaky capillaries in the hippocampus during seizure activity. *Epilepsia*, *60*(7), 1399–1411.

Conference Proceedings

1. **Boux**, **F.**, Forbes, F., Arbel, J., & Barbier, E. (2020). Estimation de paramètres IRM en grande dimension via une régression inverse, In *4e congrés de la Société Française de Résonance Magnétique en Biologie et Médecine (SFRMBM)*.
2. **Boux**, **F.**, Forbes, F., Arbel, J., Delphin, A., Christen, T., & Barbier, E. (2020). Dictionary-based Learning in MR Fingerprinting: Statistical Learning versus Deep Learning, In *ISMRM & SMRT Virtual Conference & Exhibition*.
3. Delphin, A., **Boux**, **F.**, Brossard, C., Warnking, J., Lemasson, B., Barbier, E. L., & Christen, T. (2020). Optimizing signal patterns for MR vascular fingerprinting, In *ISMRM & SMRT Virtual Conference & Exhibition*.
4. **Boux**, **F.**, Forbes, F., Arbel, J., & Barbier, E. (2019). Dictionary learning via regression: vascular MRI application, In *3e Congrès National d'Imagerie du Vivant (CNIV)*.
5. **Boux**, **F.**, Forbes, F., Arbel, J., & Barbier, E. (2018). Dictionary-free MR fingerprinting parameter estimation via inverse regression, In *Joint annual meeting ISMRM-ESMRMB*.

Skills

Data science	Pre-proccesing, vizualisation, machine learning, supervised & unsupervised learning, classification & regression, statistical & deep learning.
Coding	Matlab, Python, R, C/C++.
MRI acquisition	Pre-clinical 9.4T Bruker scanner, relaxometry, diffusion, perfusion: arterial spin labelling, vascular MRI: dynamic contrast-enhanced & USPIO-enhanced.
MRI processing	Quantitative MRI, closed-form equation fitting, simulation-based magnetic resonance fingerprinting: matching & learning, multi-parametric pipeline management, mask extraction, atlas registration.
Misc.	Academic research, supervision, oral communication, typesetting and publishing.
Languages	Strong reading, writing and speaking competencies for English and French.

Miscellaneous Experience

Awards and Achievements

2020 **Educational stipend for attending the ISMRM 28th Annual Meeting & Exhibition**, awarded by the ISMRM committee on Trainee Stipends.

2018 **Qualified for the regional finals of "Ma thèse en 180 secondes" competition**, international competition for the scientific vulgarisation open to French-speaking doctoral students from all over the world.

SFRMBM stipend for attending the Joint Annual Meeting ISMRM-ESMRMB 2018, awarded by the SFRMBM committee.

Certification

2014 **Certification for Animal Experimentation levels 1 and 2**, certified by the University centre for Experimental Biology.

References

Available on Request

Appendix B

Co-supervision of a master's student internship

B.1 Context

Aurélien Delphin, an engineering student at the Polytechnic Institute of Grenoble, realized his 6-month internship in the laboratory. At this occasion, I co-supervised him on two missions: 1) to implement additional features to the simulation tool initially developed in the team by Pannetier et al. [152], and 2) to investigate the deployment of the simulation tool on the university's computing grids (CiGri).

In the remainder, we present a sample from his master's internship report, which can be consulted online [12]. Brackets indicate text added to the original report for clarity.

B.2 Abstract: validation of MRI simulations

This report addressed the improvement of an MR simulation tool intended to generate large dictionaries of signals for microvascular characterization. Two main objectives were at stake. The first one was to improve the quality of the simulations by allowing a more realistic and flexible geometry generation. The [field of view (FOV)] of the voxels simulated has been made constant, and the possibility to generate vessels with normally distributed radii was added, which opens the way to new parameters exploration [figure B.1]. In addition, error control options on the geometrical parameters were implemented to ensure the user that the result he obtains matches his requirements. This last addition yields a higher rate of fails when generating dictionaries of signals, but

eventually ensures a better coverage of the parameter space. Dictionaries using these new functionalities were generated to analyse data from mice brains. The results were encouraging but improvements are yet to be made. In particular, the normal distribution used for vessel generation is too limiting. A more realistic distribution should be implemented to take the full advantage of variable radii on the cerebral parameter estimation. The dictionaries generated contained about 10^5 signals, which is few compared to what is used in the literature. Adding more varying parameters such as field inhomogeneities could potentially lead to an improvement of the estimation. However this would result in much larger dictionaries.

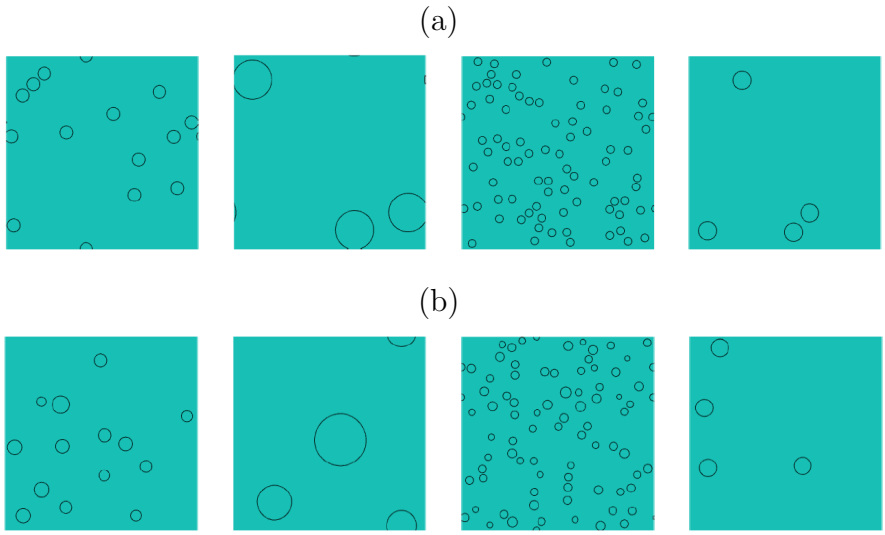

Figure B.1 – Geometry examples [using two vessel generation methods].
Four geometry obtained with (a) [the constant radii] method and (b) [the distributed radii] method with an FOV of 150 µm for different (BVf (%), [mean radius] (µm)) couples. From left to right: $(5, 5)$, $(10, 15)$, $(10, 3)$, $(2.5, 7)$. [For the second method, the variation coefficient that indicates the variance of the vessel normal distribution, is set to 20 %].

Eventually, generating 3D geometries would be optimal for the realism of the simulations. Implementing such geometries is complex and would greatly increase the computation time, but the team considers to put efforts towards this goal.

Comparing computational solutions to generate these dictionaries was the second objective of the internship. The team acquired a high-end server, and has access to a large number of computational cores on a grid provided by the Grenoble Alpes University. Parallel computation implementations were made to take advantage of the local server.

An unexpected behaviour was lately found in the solution proposed and a solution is currently under development to fix the problem and use the full power of this machine. All further developments of the tool will benefit from this finding. The computational grid was much more complex to use due to its specific functioning and asked for a lot of script writing. A satisfying workflow was developed and successfully tested [figure B.2]. However, limiting problems still exist in the use of compiled Matlab code, and in some errors linked with the grid. Support engineers work with us to solve these problems. Once it will be done the grid should be more powerful than the local server as more cores are theoretically available. Nevertheless one must keep in mind that it is a shared resource: performances largely depend on the number of people using it, and hence vary in time.

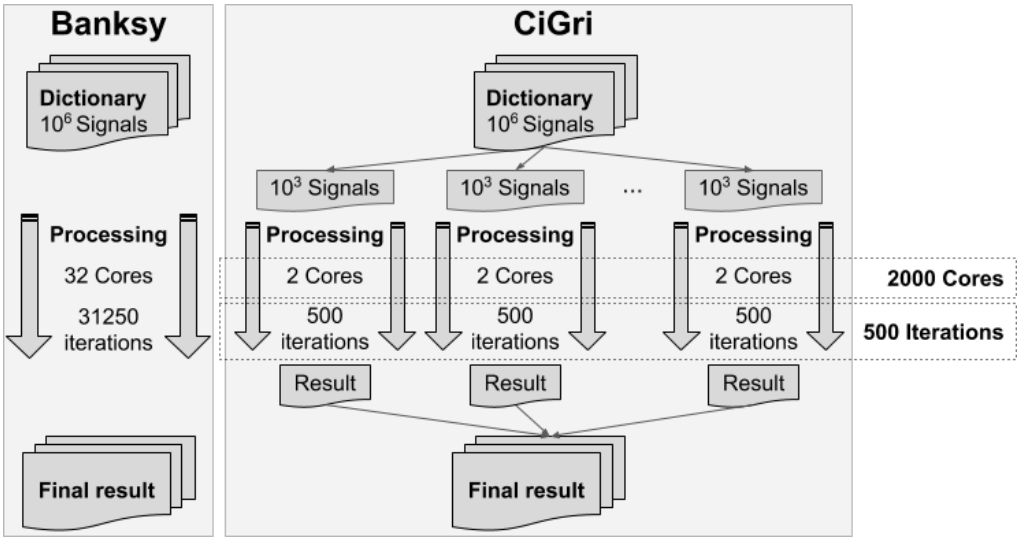

Figure B.2 – Comparison of a local server [Banksy] vs. a computation grid [CiGri] strategy.

Overall, this internship improved the tool by providing it with more possibilities, and put in light the difficulties yet to overcome to take the full advantage of the simulations in MRF. Future implementations are already planned to achieve this goal. Knowledge on the computational grid was acquired and transmitted to the team, and a solution to run efficiently MRVox2D on it was developed. The complete workflow was validated and proved to work, however errors are still to be fixed before having a truly convenient functioning.

Appendix C

Supplementary material - chapter 3

C.1 Bias-variance analysis

C.1.1 Frequentist analysis

The goal is to investigate the statistical properties of a proposed approach or equivalently of an estimator denoted by $\hat{\theta}$ of a quantity of interest θ. In statistics, an estimator is a function of the observations and is therefore random as observations are usually assumed random too. In practice however, the observations are only seen through a finite number of realizations, say $y_1, \ldots, y_I$.

For θ the true value of a parameter, we simulate I signals, using a given biophysical model and the same parameter θ, say, for $i = 1 : I$, $y_i = f(\theta) + \epsilon_i$, where ϵ_i is the realization of a given noise variable usually a centered Gaussian variable. From each of these I signals, we estimate the corresponding parameter value using the estimator $\hat{\theta}$, which leads to I values to approximate the same true θ, denoted by $\hat{\theta}_i$, for $i = 1 : I$.

The bias of an estimator with respect to a target value θ is

$$Bias(\hat{\theta}) = (E[\hat{\theta}] - \theta)$$

and usually appears squared as

$$Bias^2(\hat{\theta}) = (E[\hat{\theta}] - \theta)^2 \ .$$

Note that it does not involve an absolute value. The bias measures the performance of the estimator on average. Similarly the variance of an estimator is

$$Var(\hat{\theta}) = E[(\hat{\theta} - E[\hat{\theta}])^2] \ .$$

The variance measures the stability of the estimator or how much it moves around its mean performance. The variance depends only on the estimator and is not per se a measure of error as it does not involve the target θ. So in addition to the bias, another important quantity to measure the performance of an estimator is the Mean Square Error:

$$MSE(\hat{\theta}) = E[(\theta - \hat{\theta})^2].$$

It measures the average square error made by the estimator.

An important relationship between these quantities is referred to as the bias-variance trade-off or the bias-variance decomposition:

$$MSE(\hat{\theta}) = Bias^2(\hat{\theta}) + Var(\hat{\theta}).$$

In practice, the averages ($E[\cdot]$) are computed empirically on a given number of y_i for $i = 1:I$. Denoting $\hat{E}$ the empirical mean evaluated for the I simulations, and denoting $\hat{\theta}_i$ for $\hat{\theta}(y_i)$, we can therefore write ;

$$\frac{1}{I}\sum_{i=1}^{I}|\theta - \hat{\theta}_i|^2 = |\hat{E}[\hat{\theta}] - \theta|^2 + \frac{1}{I}\sum_{i=1}^{I}|\hat{\theta}_i - \hat{E}[\hat{\theta}]|^2$$

where

$$\hat{E}[\hat{\theta}] = \frac{1}{I}\sum_{i=1}^{I}\hat{\theta}_i.$$

The first two terms are measures of the deviation from the true θ while the last term is a constant intrinsic uncertainty due to the estimator. It depends on θ only through the y_i.

Note that the MSE is also the square RMSE by definition. In addition, it is common to use normalized quantities by dividing each term in the decomposition by θ^2.

Remark: Note that denomination and notation are slightly wrong in the bias-variance analysis of Zhao et al. [226]. What is called there the bias is in reality the so-called MAD for mean absolute deviation and there is a typo in the variance term where the first θ_n should be $\hat{\theta}_n$. The square MAD is probably not too far from the square bias but they differ due to the presence of the absolute value in the MAD. We are not aware of a similar decomposition using the MAD instead of the bias. For the MAD, the median should replace the mean.

$$MAD(\hat{\theta}) = E[|\theta - \hat{\theta}|]$$

while

$$Bias(\hat{\theta}) = (\theta - E[\hat{\theta}]) = E[(\theta - \hat{\theta})] \ .$$

C.1.2 Bayesian analysis

In the previous section, the goal was to analyze the performance of an estimator $\hat{\theta}(Y)$ considering the observations Y as a random variable so that the averages are taken over the observations, while the true θ to recover was considered as fixed. In this section, θ is assumed to be a random variable and averages are first taken with respect to θ and then with respect to both θ and Y.

Let p_0 be the true distribution of (Y, θ) both considered as random variables. We use a capital Y to denote the random Y while a small y denotes a realization of Y. The same holds for θ except that the notation is the same (oops) but the context should be clear...For a given y, then consider an estimator $\hat{\theta}(y)$ of θ. We have the following decomposition:

$$E_{p_0(\theta|y)}[(\hat{\theta}(y) - \theta)^2] = (\hat{\theta}(y) - E_{p_0(\theta|y)}[\theta])^2 + Var(p_0(\theta|y))$$

Let us denote by $p_{G,D}(\theta|y)$ the posterior provided by GLLiM which is hoped to be a good approximation of the true $p_0(\theta|y)$. Let also $\hat{\theta}_{G,D}(y)$ be the estimate of θ provided by GLLiM, which in practice is set to the mean of the GLLiM posterior. It follows that

$$E_{p_0(\theta|y)}[(\hat{\theta}_{G,D}(y) - \theta)^2] \quad = \quad (\hat{\theta}_{G,D}(y) - E_{p_0(\theta|y)}[\theta])^2 + Var(p_0(\theta|y)) \ . \tag{C.1}$$

If we consider now that Y is random, we can take the expectation of equation (C.1) with respect to Y. It comes:

$$E_{p_0(\theta,y)}[(\hat{\theta}_{G,D}(Y) - \theta)^2] \quad = \quad E_{p_0(y)}[(\hat{\theta}_{G,D}(Y) - E_{p_0(\theta|Y)}[\theta])^2] + E_{p_0(y)}[Var(p_0(\theta|Y))] \ .$$

The expectation in the left-hand side is now with respect to the joint $p_0(\theta, y)$ while the right-hand side was already independent of θ and just averaged over Y then. The left-hand side cannot be computed exactly in general but can be approximated by its empirical version using Monte Carlo simulations. Namely, consider i.i.d samples $\{(\theta_m, y_m), m = 1 \dots M\}$ distributed according to p_0. Equivalently, one can simulate θ_m according to some prior $p_0(\theta)$ and then y_m according to the physical model $p_0(y|\theta_m)$. From these samples, the left-hand side is approximated as

$$\frac{1}{M} \sum_{m=1}^{M} (\hat{\theta}_{G,D}(y_m) - \theta_m)^2,$$

which is the usual empirical MSE of $\hat{\theta}_{G,D}$.

Doing the same for the terms in the right-hand side, we get

$$\frac{1}{M}\sum_{m=1}^{M}(\hat{\theta}_{G,D}(y_m) - E_{p_0(\theta|y_m)}[\theta])^2 + \frac{1}{M}\sum_{m=1}^{M} Var(p_0(\theta|y_m)) \ .$$

Both $E_{p_0(\theta|y_m)}[\theta]$ and $Var(p_0(\theta|y_m))$ in the last expression are unknown and cannot be computed easily. It is actually the goal of methods like GLLiM to provide approximations for these quantities. GLLiM does so through an approximation $p_{G,D}(\theta|y_m)$ of the whole posterior $p_0(\theta|y_m)$.

If as expected, for all y_m, $E_{p_{G,D}(\theta|y_m)}[\theta] = \hat{\theta}_{G,D}(y_m)$ and $Var(p_{G,D}(\theta|y_m))$ are respectively good approximations of $E_{p_0(\theta|y_m)}[\theta]$ and $Var(p_0(\theta|y_m))$, meaning that $p_{G,D}(\theta|y_m)$ and $p_0(\theta|y_m)$ are close in terms of mean and variance, then the bias-variance decomposition above leads to

$$\frac{1}{M}\sum_{m=1}^{M}(\hat{\theta}_{G,D}(y_m) - \theta_m)^2 \approx \frac{1}{M}\sum_{m=1}^{M} Var(p_{G,D}(\theta|y_m)) = \frac{1}{M}\sum_{m=1}^{M} CI_m^2 \ .$$

Taking the square root, it comes

$$RMSE \approx \sqrt{\frac{1}{M}\sum_{m=1}^{M} CI_m^2} \ .$$

This later relationship is the one illustrated in figure 3.8, page 97. The figure showing a good relationship between both quantities indicates that the GLLiM approximation provides good first and second posterior moments. The slight deviation from equality when the SNR decreases is also consistent with the fact that the GLLiM performance may decrease as the noise increases.

Note that in figure 3.8, for each SNR level, 100 different samples of $\{(\theta_m, y_m), m = 1 \dots M\}$ with $M = 10\,000$ are simulated to check the above relationship.

As a conclusion the CI is a good indicator of the RMSE only if the learned GLLiM model is close to the true model in terms of mean and variance.

C.2 Data augmentation and noise modeling

This work has been submitted at the ISMRM congress 2020 but not accepted.

Data augmentation improves accuracy of dictionary-based learning methods for MR Fingerprinting

Fabien Boux Florence Forbes Julyan Arbel Emmanuel L. Barbier

November 2019

Summary of Main Findings: Dictionary augmentation using Gaussian noise improves the reconstruction accuracy of a dictionary-based learning approach by 50% without additional simulation or reconstruction cost.

Abstract

The dictionary-based learning (DBL) method, *i.e* the learning of a relationship between fingerprints and parameters spaces using an inverse regression, is faster, more accurate, and requires less simulations than the conventional dictionary-matching method. However, the DBL method is less robust to the noise level compared to the conventional dictionary-matching method. In this work, we investigate data augmentations by adding Gaussian noise to the dictionary fingerprints. We show that, at low SNR, data augmentation can increase estimates accuracy by more than 50%.

INTRODUCTION

To reduce simulation cost and reconstruction time, we recently proposed a dictionary-based learning (DBL) approach [1, 2], which uses a probabilistic model to learn the mapping from the dictionary fingerprint space to the parameters space. Interestingly, this approach also improves the accuracy on the final parameter estimates, compared to the standard dictionary matching method (DBM) [3]. However, compared to DBM, DBL appears to be less robust to fingerprints with low signal-to-noise ratio (SNR). To address this limitation, this work evaluates data augmentations by noise addition: first, we consider three data augmentation approaches, using various noise levels; second, we investigate the benefit of modeling the noise during the regression.

METHOD:

Experiments are designed as follows:

- **Dictionary design:** For P parameters and N entries, a matrix $\mathbf{X}_{dico} \in \mathbb{R}^{N\times P}$ is sampled according to a quasi-random strategy in the parameter space. Then, the matrix of fingerprints $\mathbf{Y}_{dico} \in \mathbb{R}^{N\times S}$ is simulated according to the function:

$$\mathbf{y}_{\text{toy}}\left(\mathbf{x}_{\text{toy}}\right) = \left| \sum_{i=1}^{N} \sin\left(\phi_i f_0\, \mathbf{t}\right) \exp\left(-\frac{\mathbf{t}}{x_i}\right) \right|,$$

  where $\mathbf{x}_{\text{toy}} = (x_1, x_2, \ldots, x_P) \in \mathbb{R}^P$ is the parameter vector, f_0 and $\boldsymbol{\phi} \in \mathbb{R}^P$ are constants and $\mathbf{t} \in \mathbb{R}^S$ is the sample vector. This choice of function allows the evaluation of various parameter dimensions.

- **Data augmentation:** The matrix $\mathbf{Y}_{augmented}$ is built from $\mathbf{Y}_{dico}$ according to one of the three following data augmentation procedure [4]:

1. The dictionary fingerprints $\mathbf{Y}_{dico}$ is substituted by its noisy version $\mathbf{Y}_{noisy1}$ according to SNR_{dico1}:

$$\mathbf{Y}_{augmented1} = \mathbf{Y}_{noisy1}.$$

2. $\mathbf{Y}_{dico}$ is doubled in size with the noisy fingerprints $\mathbf{Y}_{noisy1}$:

$$\mathbf{Y}_{augmented2} = \begin{pmatrix} \mathbf{Y}_{dico} \\ \mathbf{Y}_{noisy1} \end{pmatrix}.$$

3. $\mathbf{Y}_{dico}$ is augmented two times in size by noisy fingerprints $\mathbf{Y}_{noisy1}$ and $\mathbf{Y}_{noisy2}$ according to SNR_{dico1} and SNR_{dico2}:

$$\mathbf{Y}_{augmented3} = \begin{pmatrix} \mathbf{Y}_{dico} \\ \mathbf{Y}_{noisy1} \\ \mathbf{Y}_{noisy2} \end{pmatrix}.$$

Note that the size of $\mathbf{X}_{dico}$ is also augmented by replicating the matrix one or two times to match the length of $\mathbf{Y}_{augmented}$.

Noisy signals ($\mathbf{y}_{noisy}$) were computed from $\mathbf{y}$ using:

$$\mathbf{y}_{noisy} = |\mathbf{y} + \mathbf{n}|,$$

where $\mathbf{n}$ is a Gaussian noise. The dictionary signal SNR is SNR_{dico}.

- **Model learning:** A regression is performed to learn, from the dictionary, a model that handles the non-linear relationship between $\mathbf{X}_{augmented}$ and $\mathbf{Y}_{augmented}$ with a piece-wise linear model [2, 5].
- **Estimation:** The model is applied on the fingerprints $\mathbf{y}$ to compute the parameter estimates $\widehat{\mathbf{x}}$.
- **Performance evaluation:** The parameter space $\mathbf{X}_{test}$ is sampled and corresponding signals $\mathbf{Y}_{test}$ are simulated and used to compute $\widehat{\mathbf{X}}_{test}$. Gaussian noise is added on test signals according to SNR_{test}. Then, the root-mean-squared-error (RMSE) is computed between $\mathbf{X}_{test}$ and $\widehat{\mathbf{X}}_{test}$ and averaged over dimensions. For a given SNR_{dico}, SNR_{test}, and data augmentation method, the RMSE gain is the ratio between the RMSE obtained without and with data augmentation.

RESULTS:

Using data augmentation (1), three SNR_{dico} (10, 60, and a random SNR_{dico} vector between 10 and 60), and SNR_{test} between 3 and 100, we evaluate the RMSE gain in 4 experiment conditions (*i.e.* 3 and 5 parameters, 2 different dictionary sizes). For all SNR_{dico}, the data augmentation increases the robustness of the method (gain¿1) for SNR_{test} above 5 and below a cut-off value and deteriorates above. This cut-off depends SNR_{dico}, SNR_{test}, the number of parameters and the dictionary size. Cuttoffs (mean ± standard deviation) are: 73.9±16.3 for SNR_{dico}=60, 17.3±4.1 for SNR_{dico}=10 and 43.2±11.2 for $\text{SNR}_{dico} \in [10, 60]$. Accuracy gains before the cut-off are: 1.28±0.04, 1.22±0.05 and 1.26±0.04.

To search the optimal SNR_{dico} for the data augmentation (1), we evaluated values of SNR_{dico} between 10 and 250 for three SNR_{test} (15, 30 and 45). Figure 2 represents RMSE gains for the same conditions as that of Figure 1. As expected, gains are higher for noisy signals (low SNR_{test}); For high SNR_{dico}, the gain converges to 1. As RMSE gains depend on simulation conditions (*i.e.* dictionary design and SNR_{test}), there is no optimal SNR_{dico}. However, SNR_{dico}=60 always yields RMSE gains above 1 and average RMSE gain is 1.43 for the lowest SNR_{test}.

We compared data augmentations (1-3) with SNR_{dico1}=60 and SNR_{dico2}=10 (Figure 3). Data augmentations (1) and (2) provide similar results, except for large SNR_{test} for which the data augmentation (2) provides larger RMSE gains. Data augmentation (3) yields higher RMSE gains for SNR_{test} between 5 and 15 but lower elsewhere.

To model the noise, we incorporated SNR_{dico} as a new parameter ($\mathbf{X}_{dico} \in \mathbb{R}^{N\times(P+1)}$); for simulations, SNR_{dico} values were randomly picked between 10 and 60. SNR_{test} are well evaluated only between 3 and 10 (Figure 4). The combination of data augmentation (1) and noise modelling does not provide any benefit, however it reduces RMSE gains for low SNR (Figure 5).

DISCUSSION

Data augmentations based on noise addition reduces the RMSE on parameter estimates by more than 50%, in case of data with low SNR_{test}. Conversely, the accuracy on estimated parameters is decreased when using a noisy dictionary with high SNR_{test}. [values here]. Learning the noise does not provide significant benefit over adding noise to the dictionary. Several assumptions can be made regarding the mechanism behind noise augmentation including limit the overfitting during the learning phase (similar to what has been reported for deep learning) and produce fingerprints more similar to test signals (*e.g.* no true zero points). Further experiments are required to clarify these mechanisms.

CONCLUSION

Data augmentation using noise can readily be used to improve DBL reconstruction accuracy by 50% without additional simulation or reconstruction cost.

References

[1] Fabien Boux, Florence Forbes, Julyan Arbel, and Emmanuel L. Barbier. Dictionary-free mr fingerprinting parameter estimation via inverse regression. In *26th Annual Meeting ISMRM, Paris*, page 4259, 2018.

[2] Fabien Boux, Florence Forbes, Julyan Arbel, Benjamin Lemasson, and Emmanuel L. Barbier. Inverse regression in mr fingerprinting: reducing dictionary size while increasing parameters accuracy. *Submitted to Magnetic resonance in medicine*, 2019. Preprint: https://hal.archives-ouvertes.fr/hal-02314026/document.

[3] Dan Ma, Vikas Gulani, Nicole Seiberlich, Kecheng Liu, Jeffrey L Sunshine, Jeffrey L Duerk, and Mark A Griswold. Magnetic resonance fingerprinting. *Nature*, 495(7440):187, 2013.

[4] MJ Sáiz-Abajo, B-H Mevik, VH Segtnan, and T Næs. Ensemble methods and data augmentation by noise addition applied to the analysis of spectroscopic data. *Analytica chimica acta*, 533(2):147–159, 2005.

[5] Antoine Deleforge, Florence Forbes, and Radu Horaud. High-dimensional regression with gaussian mixtures and partially-latent response variables. *Statistics and Computing*, 25(5):893–911, 2015.

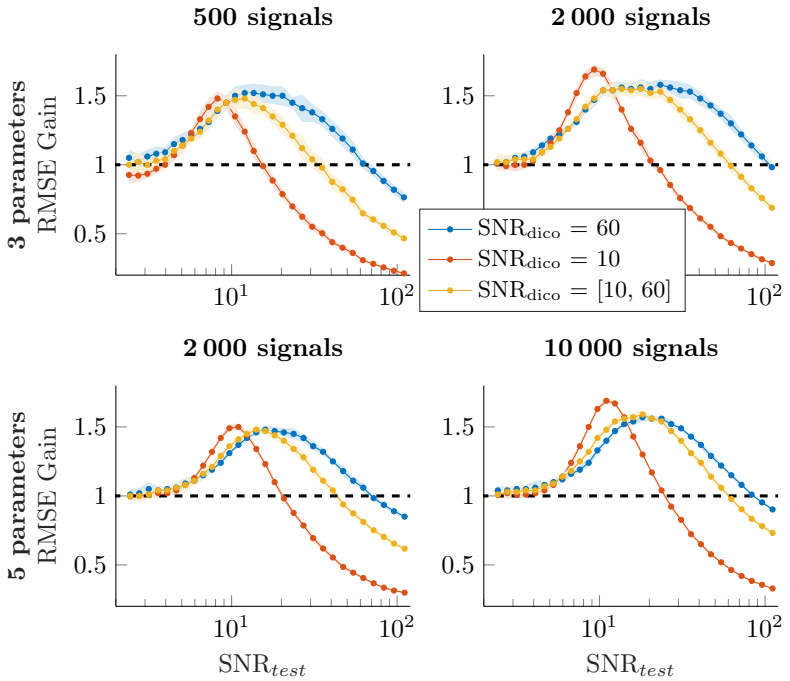

Figure 1: RMSE gains for different noise levels on test signals and three noise levels on dictionary signals: 10, 60 and random noise between these two values for each signal. The first row represents the 3 parameter experiments (500 and 2000 signals in the dictionary) and the second row represents the 5 parameter experiments (2000 and 10000 signals in the dictionary). The RMSE is computed for 10000 test signals and then, the experiment is repeated 20 times. Markers are the mean RMSE through these 20 repetitions and the area represents the standard deviation. The dashed line represents the symbolic gain equal to 1, above the line the error is smaller than without data augmentations and inversely below.

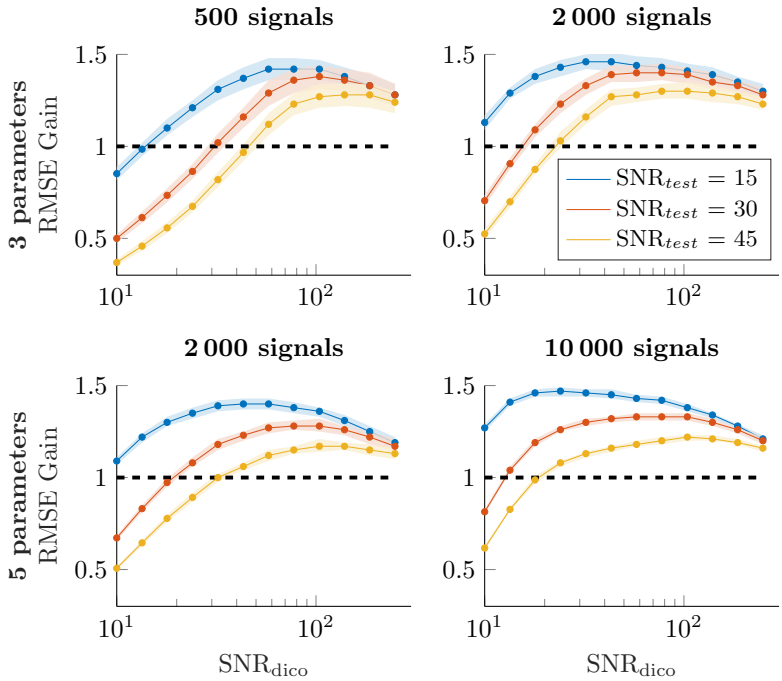

Figure 2: RMSE gains for different noise levels on dictionary signals and three different noise levels on test signals: 15, 30 and 45. The first row represents the 3 parameter experiments (500 and 2000 dictionary signals) and the second row represents the 5 parameter experiments (2000 and 10000 dictionary signals). RMSE are computed for 10000 test signals and 18 repetitions. Markers and areas are the mean and standard deviation of RMSE through these repetitions. The dashed line represents the gain equal to 1, above the error is smaller than without data augmentations and inversely below.

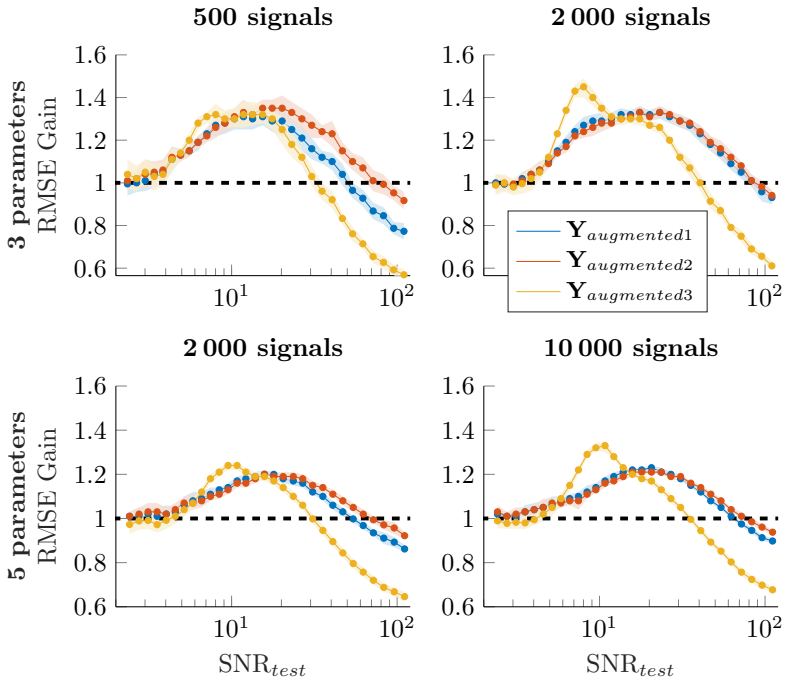

Figure 3: RMSE gains for three data augmentations and different noise levels on test signals. The first row represents the 3 parameter experiments (500 and 2000 dictionary signals) and the second row represents the 5 parameter experiments (2000 and 10000 dictionary signals). RMSE are computed for 10000 test signals and 20 repetitions. Markers and areas are the mean and standard deviation of RMSE through these repetitions. The dashed line represents the gain equal to 1, above the error is smaller than without data augmentations and inversely below.

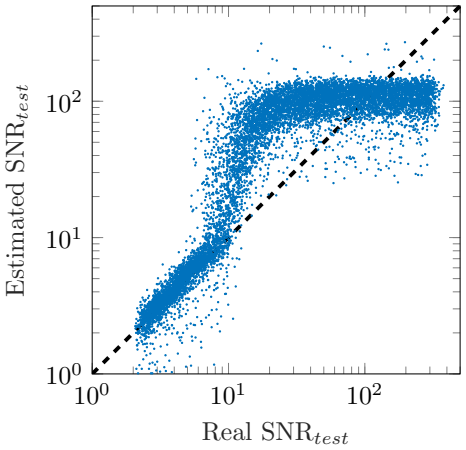

Figure 4: Estimated SNR$_{test}$ as a function of real SNR$_{test}$, using the dictionary-based learning (DBL) method. The dashed line represents the identity function (perfect estimation).

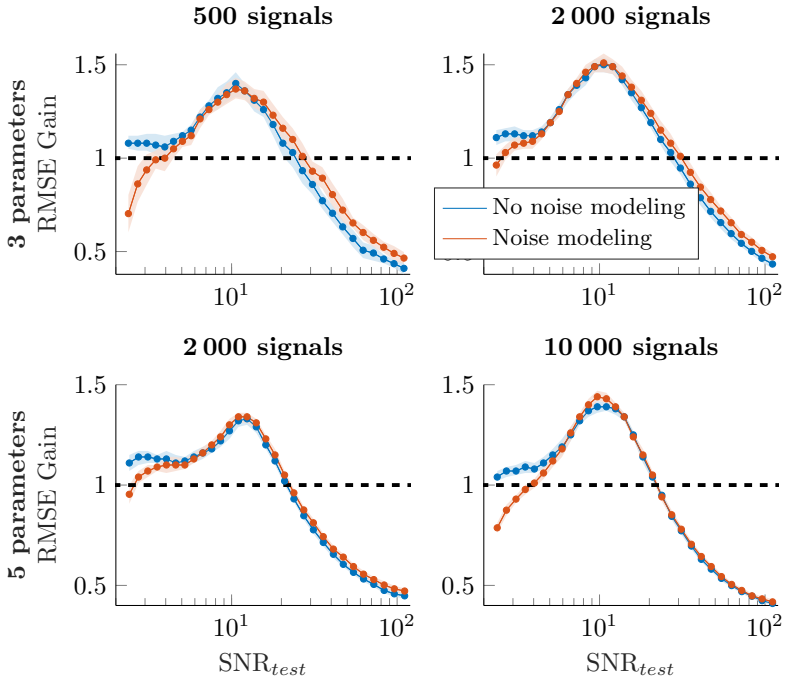

Figure 5: RMSE gains for data augmentation with and without noise modeling. The first row represents the 3 parameter experiments (500 and 2000 dictionary signals) and the second row represents the 5 parameter experiments (2000 and 10000 dictionary signals). RMSE are computed for 10000 test signals and 20 repetitions. Markers and areas are the mean and standard deviation of RMSE through these repetitions. The dashed line represents the gain equal to 1, above the error is smaller than without data augmentations and inversely below.

Appendix D

Supplementary material - chapter 5

During this work, we acquired MRI data on two experimental models of mesio-temporal lobe epilepsy (MTLE) in mice. The status epilepticus was induced by an administration of kainic acid, either using an intraperitoneal injection (IP model) or an intrahippocampal injection (IH model).

We are interested in 3 regions of interest: thalamus, hippocampus and cortex. For IH model, we only consider the contralateral cortex because of the lesion resulting from the cannula that passed through the cortex for intrahippocampal injection. For IH model, we also distinguish the contralateral and ipsilateral hippocampus.

In figures D.1 and D.2, we present the mean value obtained in each region of interest, for the eight following MRI parameters: relaxation times T_1 and T_2, diffusion (ADC), blood volume fraction (BVf), vessel size index (VSI), tissue oxygen saturation (StO_2), blood-brain-barrier permeability (BBB_p and cerebral blood flow (CBF).

Note that the data acquired with the IH model are those presented in chapter 5.

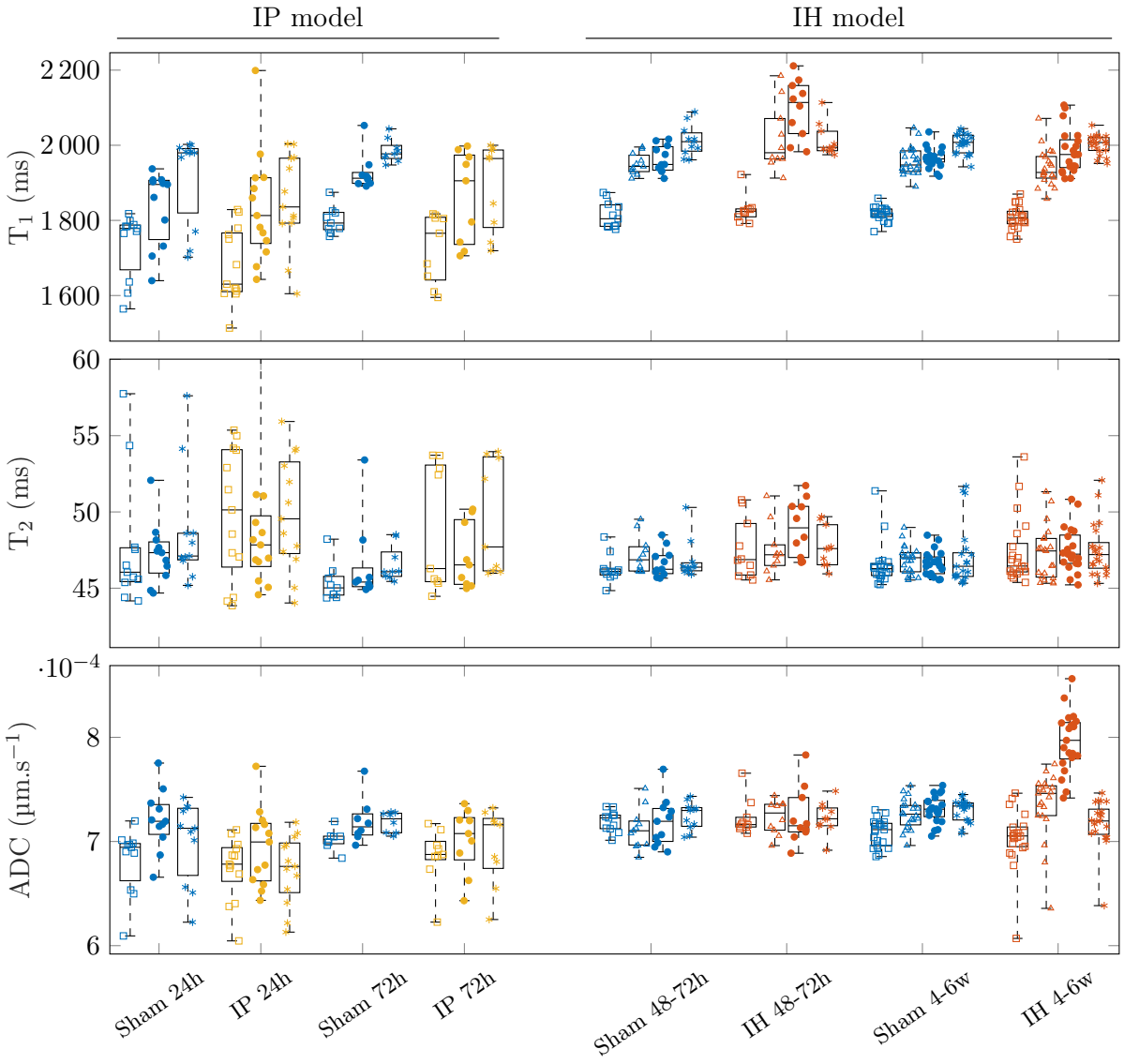

Figure D.1 – Cellular MRI parameters.
(*first row*) Relaxation time T_1, (*second row*) relaxation T_2, and (*last row*) apparent diffusion constant (ADC). Squares represent cortex values, triangles contralateral hippocampus, points ipsilateral hippocampus, and asterisks cortex for the 2 MTLE models. Note that for the IP model points represent the mean across the two hippomcapi. In total, 4 groups per model. For IP: sham and IP MTLE mice at 24 hours (sham n = 11; MTLE n = 13) and at 72 hours (sham n = 8; MTLE n = 9). For IH: sham and IH MTLE mice at 48-72 hours (sham n = 11; MTLE n = 10) and at 4-6 weeks (sham n = 20; MTLE n = 20). Sham are represented in blue, IP MTLE in yellow and IH MTLE in orange.

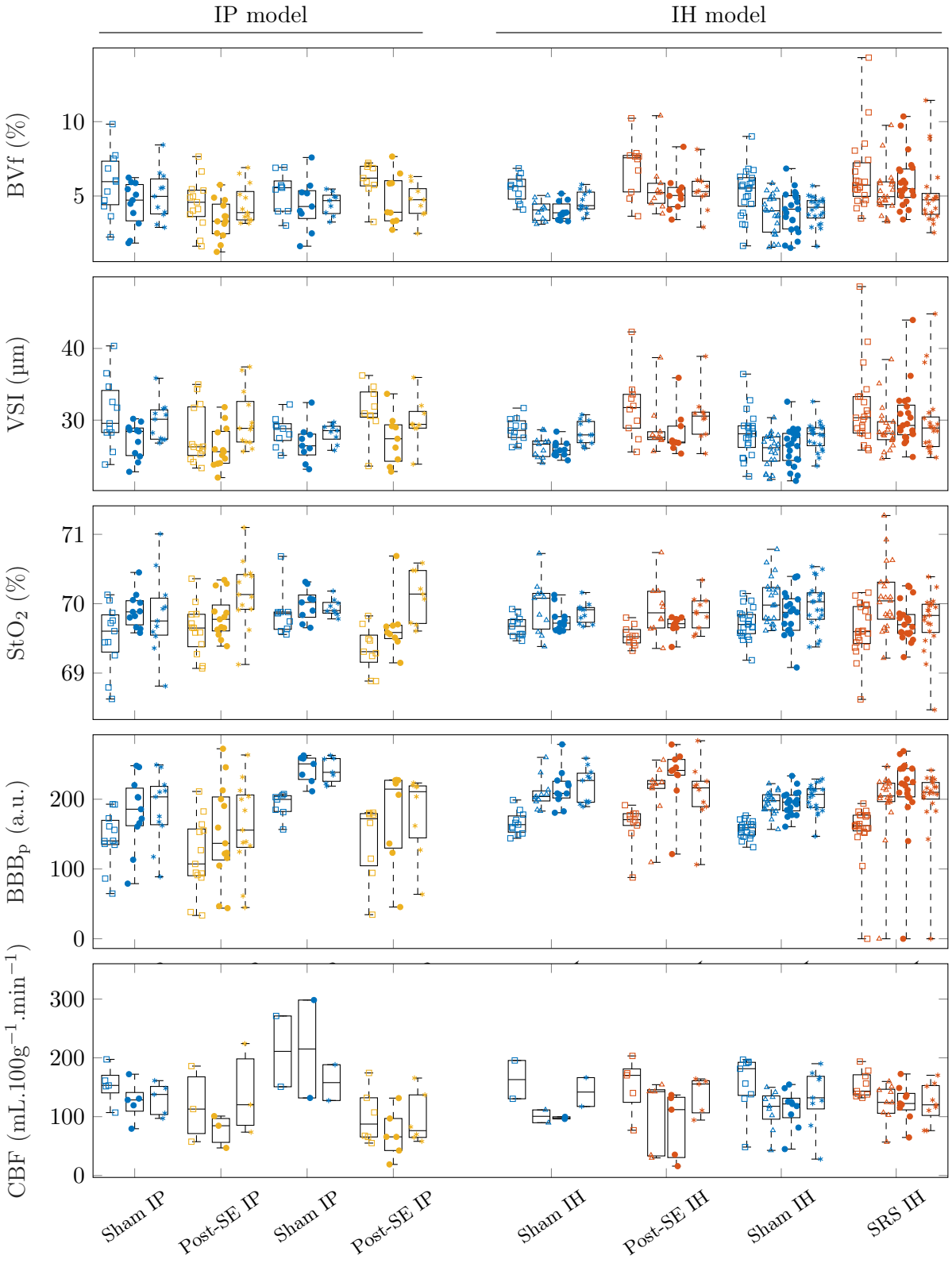

Figure D.2 – Vascular MRI parameters.
(*first row*) blood volume fraction (BVf), (*second row*) vessel size index (VSI), (*third row*) tissue oxygen saturation (StO_2), (*fourth row*) BBB permeability (BBB_p), and (*last row*) blood flow (CBF). See figure D.1 caption, for group description.

Appendix E

Software

E.1 Magnetic resonance fingerprinting package

The package containing the three dictionary-based methods compared in this work (i.e. the original dictionary-based matching [137], DBM; the dictionary-based deep learning [165], DB-DL; and the proposed dictionary-based statistical learning, DB-SL), can be found online: https://github.com/nifm-gin/DBL-qMRI. We provide an overview of the documentation that explains how to use the package in figure E.1. Note that most of the experiments realized in chapters 3 and 4 can be reproduced from associated scripts, see complete documentation online.

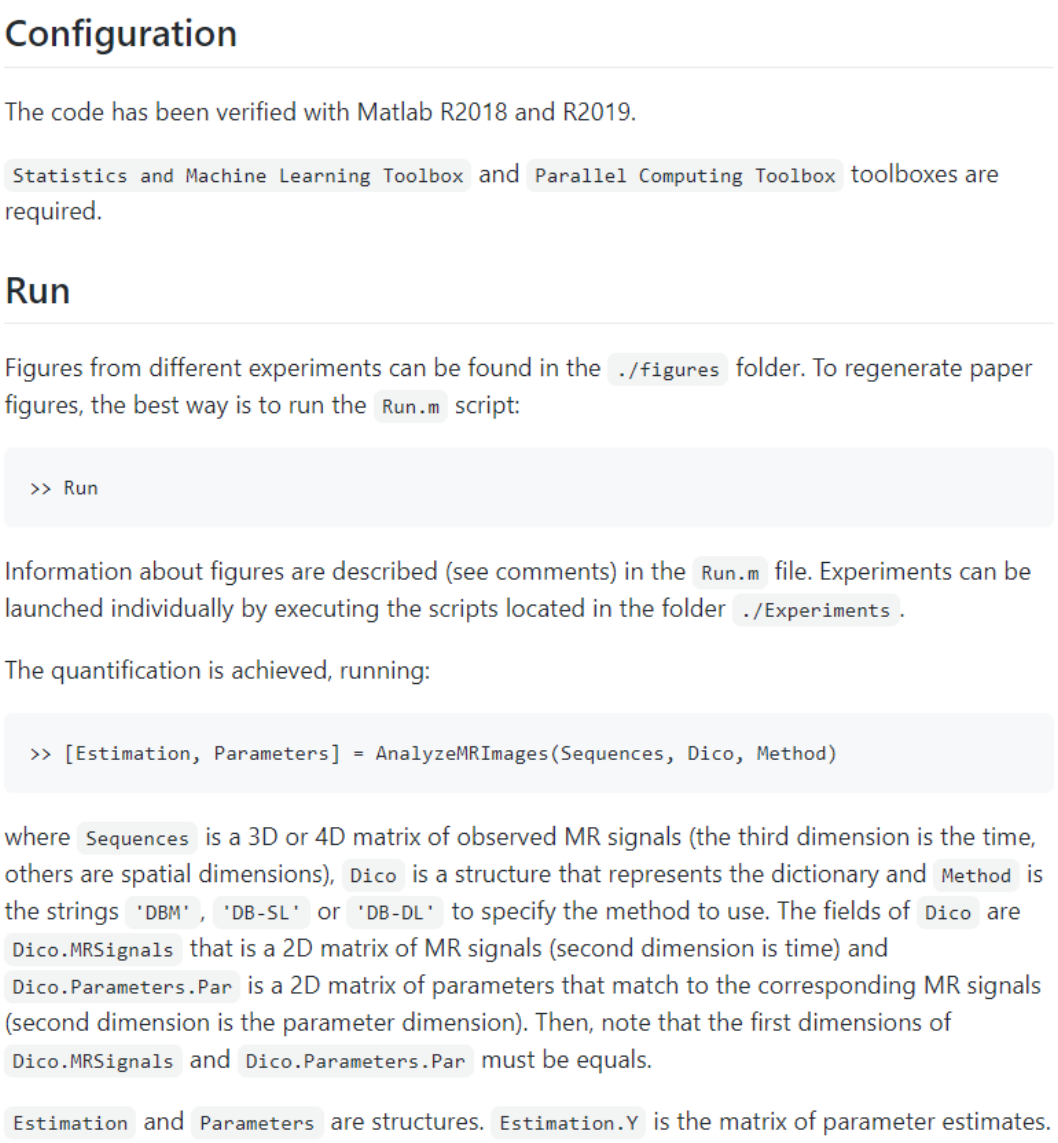

Configuration

The code has been verified with Matlab R2018 and R2019.

`Statistics and Machine Learning Toolbox` and `Parallel Computing Toolbox` toolboxes are required.

Run

Figures from different experiments can be found in the `./figures` folder. To regenerate paper figures, the best way is to run the `Run.m` script:

```
>> Run
```

Information about figures are described (see comments) in the `Run.m` file. Experiments can be launched individually by executing the scripts located in the folder `./Experiments`.

The quantification is achieved, running:

```
>> [Estimation, Parameters] = AnalyzeMRImages(Sequences, Dico, Method)
```

where `Sequences` is a 3D or 4D matrix of observed MR signals (the third dimension is the time, others are spatial dimensions), `Dico` is a structure that represents the dictionary and `Method` is the strings `'DBM'`, `'DB-SL'` or `'DB-DL'` to specify the method to use. The fields of `Dico` are `Dico.MRSignals` that is a 2D matrix of MR signals (second dimension is time) and `Dico.Parameters.Par` is a 2D matrix of parameters that match to the corresponding MR signals (second dimension is the parameter dimension). Then, note that the first dimensions of `Dico.MRSignals` and `Dico.Parameters.Par` must be equals.

`Estimation` and `Parameters` are structures. `Estimation.Y` is the matrix of parameter estimates.

Figure E.1 – GitHub Readme.
An overview of the complete documentation available online: GitHub.

E.2 MP3: Medical software for Processing multi-Parametric images Pipelines

This section introduces an open source software to convert, display and process medical images [185]. This software called *medical software for processing multi-parametric images pipelines* (MP3), is a collaborative development within the team initiated by Benjamin Lemasson and mainly achieved by Clément Brossard. It differentiates itself from the existing software by its ability to design complex processing pipelines and to wisely execute them on a large database. An MP3 pipeline can contain unlimited homemade or pre-existing processes called module, and can be carried out with a parallel execution system. As a viewer, MP3 allows to display up to four images together and to draw regions of interest (ROI), see figure E.2 B. MP3 is available at https://github.com/nifm-gin/MP3.

In this project, I was one of the principal developer and beta tester. Among others, here are some of my contributions:

- Implementation of the modules of vascular magnetic resonance fingerprinting, see section E.3.
- Implementation of a module running different scripts provided by Advanced Normalization Tools (ANTs) [233] to perform a co-registration of an anatomical image with a reference atlas image to automatically segment maps in different ROI. This module is supplemented by another module allowing to compute several statistics by ROI (e.g. mean, median, standard deviation,...).
- Design of a complete pipeline in mouse at 9.4 T, to generate maps, remove outliers, match atlas and extract summary statistics per ROI. This pipeline has been validated with a rat study at 4.7 T and the atlas matching procedure for human study.

I have also been involved in introducing the tool and providing support to several hospital clinicians and biologists. In particular, I have accompanied two hospital clinicians during their medical thesis project, providing support on the tool: Pierre Fricault in a pre-clinical MRI study on an experimental model of traumatic brain injury (part of the work in [234]) and Sarah Sintzel Strippoli in a clinical MRI study on brain damages after minor traumatic brain injury.

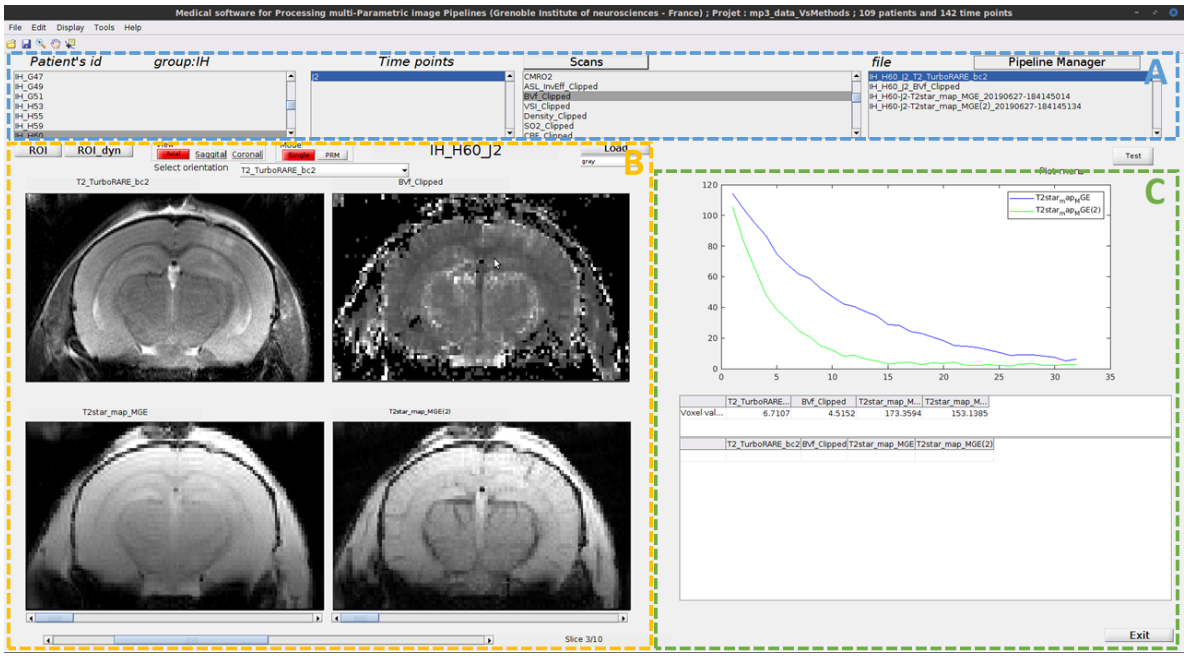

Figure E.2 – Overview of the main MP3 viewer.
(**A**) Database manager. (**B**) Images display. (**C**) Statistics display.

E.3 Vascular MRF module in MP3 software

The package introduced in section E.1 has been integrated into the MP3 software as a module named *Module_vascular_MRF*, following the nomenclature of the software.

Once the module is selected in the appropriate drop-down menu (figure E.3(a)), proceed as follows:

- Select in the database the MGEFIDSE acquisitions, i.e. pre- and post-USPIO injection.
- Indicate the folder containing the dictionary. In this folder, the dictionary can be in the form of two *.json* files containing the pre- and post-USPIO injection simulated signals and the file names must start with 'PRE_' and 'POST_', respectively. Another possibility is to directly use a *.mat* file that contains the vascular fingerprints, i.e. the pre-/post- ratio signal.
- *Prefix* option is used to name the output maps.
- Select parameters (at least one) you intend to estimate, see figure E.3(b).
- Select the method you intend to use, see figure E.3(c).
- *Method* option is used to apply a 3×3 spatial Gaussian filtering prior to the estimation. For example, this procedure has been used in [154]. Authors also

propose to remove the 8 last acquired echoes. Both these procedures aim at increasing the signal-noise-ratio (SNR). It was therefore decided to integrate this possibility into the module via the *Remove last echoes* option.

- If DB-SL or DB-DL methods are used, you can tune model properties (*not recommended*).

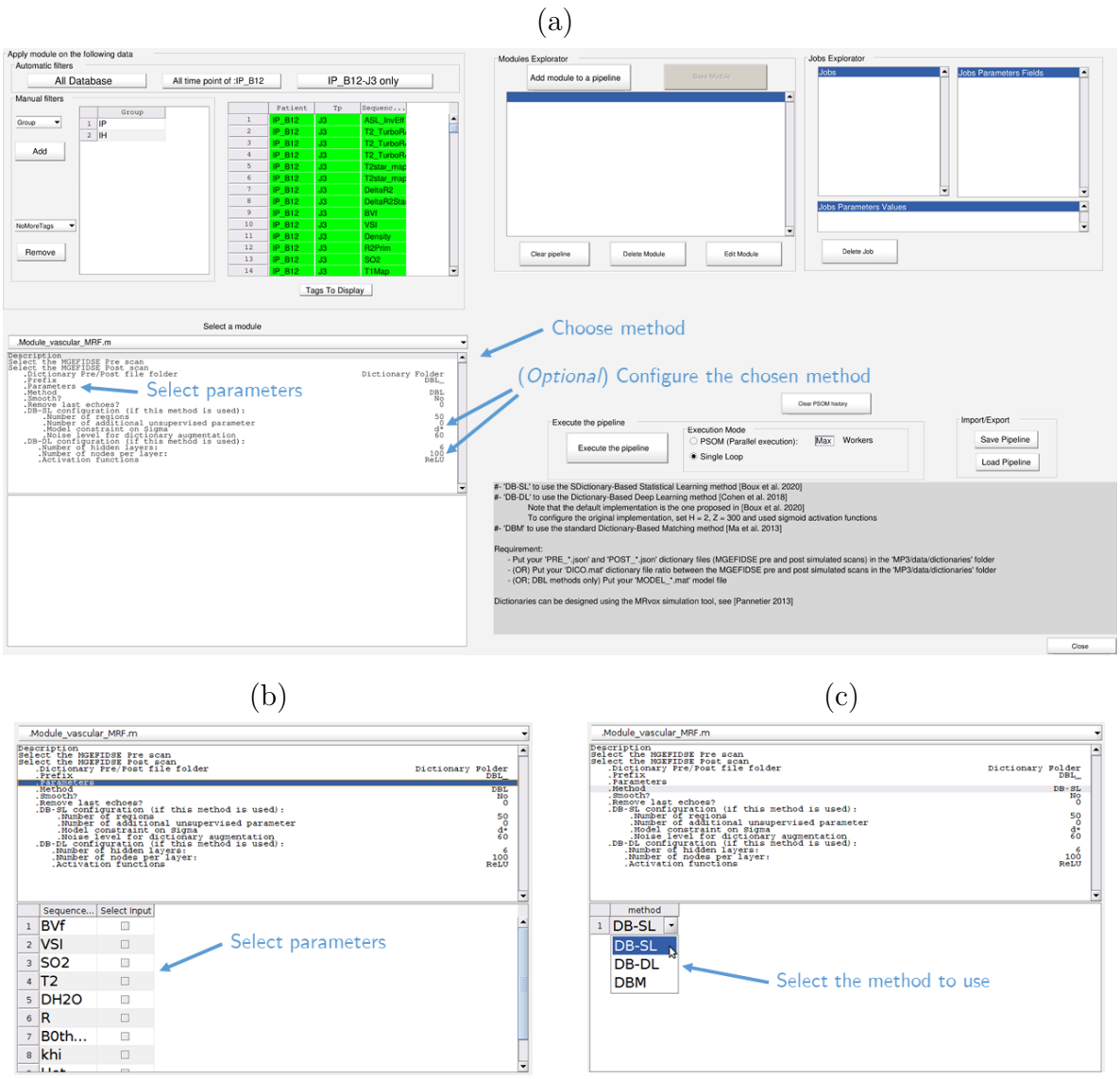

Figure E.3 – Procedure to configure the module *Module_vascular_MRF* in the MP3 pipeline manager.
(a) MP3 pipeline manager. (b,c) Two minimum steps required to configure the reconstruction. (b) Tick the boxes of the parameters you intend to estimate (at least one) using the selected dictionary based method in (c). Note that these parameters must be simulated in the dictionary.

Méthodes statistiques pour l'imagerie vasculaire par résonance magnétique : application au cerveau épileptique

L'objectif de ce travail de thèse est l'exploration de l'imagerie par résonance magnétique (IRM) pour l'identification et la localisation des régions du cerveau impliquées dans l'épilepsie mésio-temporale. Précisément, les travaux visent 1) à optimiser un protocole d'IRM vasculaire sur un modèle animal d'épilepsie et 2) à concevoir une méthode de quantification de cartes IRM vasculaires basée sur la modélisation de la relation entre signaux IRM et paramètres biophysiques. Les acquisitions IRM sur un modèle expérimental murin d'épilepsie mésio-temporale avec sclérose de l'hippocampe ont été effectuées sur un scanner 9.4 T. Les données collectées ont permis de quantifier sept cartes IRM cellulaires et vasculaires quelques jours après l'état de mal épileptique puis plus tard, lorsque les crises spontanées sont apparues. Ces paramètres ont été employés pour l'identification automatique des régions épileptogènes et des régions de propagation des crises. Afin d'augmenter la détection de petites variations des paramètres IRM chez les individus épileptiques, une méthode de quantification basée sur la résonance magnétique fingerprinting est développée. Cette méthode consiste à identifier, parmi un ensemble de signaux simulés, le plus proche du signal IRM acquis et peut être vue comme un problème inverse qui présente les difficultés suivantes : le modèle direct est non-linéaire et provient d'une série d'équations sans expression analytique simple; les signaux en entrée sont de grandes dimensions; les vecteurs des paramètres en sortie sont multidimensionnels. Pour ces raisons, nous avons utilisé une méthode de régression inverse afin d'apprendre à partir de simulation la relation entre l'espace des paramètres et celui des signaux. Dans un domaine largement dominé par les approches d'apprentissage profond, la méthode proposée se révèle très compétitive fournissant des résultats plus précis. De plus, la méthode permet pour la première fois de produire un indice de confiance associé à chacune des estimations. En particulier, cet indice permet de réduire l'erreur de quantification en rejetant les estimations associées à une faible confiance. Actuellement, aucun protocole clinique permettant de localiser avec précision le foyer épileptique ne fait consensus. La possibilité d'une identification non-invasive de ces régions est donc un premier pas vers un potentiel transfert clinique.

Statistical methods for vascular magnetic resonance fingerprinting: application to the epileptic brain

The objective of this thesis is the investigation of magnetic resonance imaging (MRI) for the identification and localization of brain regions involved in mesio-temporal lobe epilepsy (MTLE). Precisely, the work aims 1) at optimizing a vascular MRI protocol on an animal model of epilepsy and 2) at designing a method to quantify vascular MRI maps based on the modeling of the relationship between MRI signals and biophysical parameters. MRI acquisitions on an experimental mouse model of MTLE with hippocampal sclerosis were performed on a 9.4 T scanner. The data collected allowed the quantification of seven cellular and vascular MRI maps a few days after the epileptic condition and later when the spontaneous seizures emerged. These parameters were used for the automatic identification of epileptogenic regions and regions of seizure propagation. To enhance the detection of small variations in MRI parameters in epileptic subjects, a quantification method based on magnetic resonance fingerprinting has been developed. This method consists in identifying, among a set of simulated signals, the closest one to the acquired signal. It can be seen as an inverse problem that presents the following difficulties: the direct model is non-linear, as a complex series of equations or simulation tools; the inputs are high-dimensional signals; and the output is multidimensional. For these reasons, we used an appropriate inverse regression approach to learn a mapping between signal and biophysical parameter spaces. In a field widely dominated by deep learning approaches, the proposed method is very competitive and provides more accurate results. Moreover, the method allows for the first time to produce a confidence index associated with each estimate. In particular, this index allows to reduce the quantification error by discarding estimates associated with low confidence. So far no clinical protocol emerges as a consensus to accurately localize epileptic foci. The possibility of a non-invasive identification of these regions is therefore a first step towards a potential clinical transfer.